



İntrakraniyal Kanama Tespiti İçin Segmentasyon Algoritmalarının Karşılaştırmalı Bir Çalışması

Murat CANAYAZ^{1*} , Aysel MİLANLIOĞLU² , Sanem ŞEHRİBANOĞLU³ ,
Abdulsabır YALIN⁴ , Adem YOKUŞ⁵ 

¹Bilgisayar Mühendisliği Bölümü, Mühendislik Fakültesi, Van Yüzüncü Yıl Üniversitesi, Türkiye.

^{2,4}Nöroloji Bölümü, Tıp Fakültesi, Van Yüzüncü Yıl Üniversitesi, Türkiye.

³Ekonometri Bölümü, İktisadi ve İdari Bilimler Fakültesi, Van Yüzüncü Yıl Üniversitesi, Türkiye.

⁵Radyoloji Bölümü, Tıp Fakültesi, Van Yüzüncü Yıl Üniversitesi, Türkiye.

¹mcanayaz@yyu.edu.tr, ²ayselmilanlioglu@yyu.edu.tr, ³sanem@yyu.edu.tr, ⁴pamukkalet_@hotmail.com,
⁵ademyokus@yyu.edu.tr

Geliş Tarihi: 22.01.2024

Kabul Tarihi: 14.03.2024

Düzeltilme Tarihi: 10.03.2024

doi: <https://doi.org/10.62520/fujece.1423648>

Araştırma Makalesi

Alıntı: M. Canayaz, A. Milanlioğlu, S. Şehribanoğlu, A. Yalın ve A. Yokuş, "İntrakraniyal kanama tespiti için segmentasyon algoritmalarının karşılaştırmalı bir çalışması", Fırat Üni. Deny. ve Hes. Müh. Derg., vol. 3, no 2, pp. 75-94, Haziran 2024.

Öz

Tıp alanında segmentasyon özel bir öneme sahiptir. Segmentasyonun amaçlarından biri, herhangi bir organdaki hastalık tespiti sonrasında hastalıktan etkilenen bölgeyi görselleştirmektir. Son yıllarda, bu amaçla derin öğrenme modelleri ile etkili çalışmalar gerçekleştirilmiştir. Bu çalışmada, beyin parankimindeki kanama tespiti için 3 segmentasyon algoritması karşılaştırılmıştır. Bu algoritmalar, en bilinen U-net, LinkNet ve FPN algoritmalarıdır. Bu algoritmaların arka planında, derin öğrenme modellerinden oluşan 5 farklı ana yapı kullanılmıştır. Bu ana yapılar, Resnet34, ResNet50, ResNet169, EfficientNetB0 ve EfficientNet B1'dir. Çalışma için orijinal bir veri kümesi oluşturulmuştur. Çalışmadaki veri kümesi uzmanlar tarafından doğrulanmıştır. Çalışmada, tıp alanındaki en yaygın metrikler olan Dice katsayısı ve Jaccard indeksi, değerlendirme metrikleri olarak seçilmiştir. Algoritmaların performans sonuçları göz önüne alındığında, eğitim verisi için FPN mimarisi 0.9495 Dice katsayısı değeri ile en iyi sonuçları verirken, test verisi için LinkNet 0.9244 Dice katsayısı ile en iyi sonuçları vermiştir. Ayrıca, kullanılan ana yapılar arasında EfficientNetB1 en iyi sonuçları sağlamıştır. Elde edilen sonuçlar incelendiğinde, mevcut çalışmalara göre daha iyi bir segmentasyon performansı elde edilmiştir.

Anahtar kelimeler: Bölütleme, İntrakraniyal kanama, Derin öğrenme

*Yazışılan yazar

İntihal Kontrol: Evet – Turnitin

Şikayet: fujece@firat.edu.tr

Telif Hakkı ve Lisans: Dergide yayın yapan yazarlar, CC BY-NC 4.0 kapsamında lisanslanan çalışmalarının telif hakkını saklı tutar.



A Comparative Study of Segmentation Algorithms for Intracerebral Hemorrhage Detection

Murat CANAYAZ^{1*} , Aysel MİLANLIOĞLU² , Sanem ŞEHRİBANOĞLU³ ,
Abdulsabır YALIN⁴ , Adem YOKUŞ⁵ 

¹Department of Computer Engineering, Faculty of Engineering, Van Yuzuncu Yil University, Türkiye.

^{2,4}Department of Neurology, Faculty of Medicine, Van Yuzuncu Yil University, Türkiye.

³Department of Econometrics, Faculty of Economics and Administrative Sciences, Van Yuzuncu Yil University, Türkiye.

⁵Department of Radiology, Faculty of Medicine, Van Yuzuncu Yil University, Türkiye

¹mcanayaz@yyu.edu.tr, ²ayselmilanlioglu@yyu.edu.tr, ³sanem@yyu.edu.tr, ⁴pamukkalet_@hotmail.com,
⁵ademyokus@yyu.edu.tr

Received: 22.01.2024

Accepted: 14.03.2024

Revision: 10.03.2024

doi: <https://doi.org/10.62520/fujece.1423648>

Research Article

Citation: M. Canayaz, A. Milanlioğlu, S. Şehribanoğlu, A. Yalın and A. Yokuş, "A comparative study of segmentation algorithms for intracerebral hemorrhage detection", *Firat Univ. Jour. of Exper. and Comp. Eng.*, vol. 3, no 2, pp. 75-94, June 2024.

Abstract

Segmentation in the medical field has special importance. One of the purposes of segmentation is to visualize the area affected by the disease after disease detection in any organ. In recent years, efficient studies have been carried out for this purpose with deep learning models. In this study, three segmentation algorithms were compared for the detection of hemorrhage in brain parenchyma. These algorithms are the most familiar: U-net, LinkNet, and FPN algorithms. For the background of these algorithms, five backbones consisting of deep learning models were used. These backbones are Resnet34, ResNet50, ResNet169, EfficientNetB0, and EfficientNet B1. An original dataset was created for the study. The dataset in the study was verified by experts. In the study, the Dice coefficient and Jaccard index, which are the most common metrics in the medical field, were chosen as evaluation metrics. Considering the performance results of the algorithms, the FPN architecture with a 0.9495 Dice coefficient value for the training data and LinkNet with a 0.9244 Dice coefficient for the test data gave the best results. In addition, EfficientNetB1 provided the best results among the backbones used. When the results obtained were examined, better segmentation performance was obtained than in existing studies.

Keywords: Segmentation, Intracerebral hemorrhage, Deep learning

*Corresponding author

Plagiarism Checks: Yes – Turnitin

Complaints: fujece@firat.edu.tr

Copyright & License: Authors publishing with the journal retain the copyright to their work licensed under the CC BY-NC 4.0

1. Introduction

Radiological data are primarily chosen by specialists for the detection of diseases. In these detection processes, faster results have been obtained with artificial intelligence and deep learning applications in recent years. With tools designed to assist experts, studies in the medical field continue to develop rapidly. These tools perform many functions, such as examining a given image and locating, segmenting, and recognizing the disease. These tools are used in the detection of many diseases, such as brain tumors [1], lung cancer [2], melanoma skin cancer [3], and diabetic retinopathy [4]. Non-traumatic spontaneous intracerebral hemorrhage (SIH) is an emerging disease of vascular origin in the brain that can cause high mortality and very serious functional disability, with an annual incidence of 25/1,000,000, accounting for 10-15% of all stroke patients [5, 6]. Systemic arterial hypertension, amyloid angiopathy, vascular malformation, and anticoagulant drug use are the most common risk factors [7]. Chronic arterial hypertension in patients causes lipohyalinosis and degenerative changes in penetrating arterioles over time. Charcot-Bouchard aneurysms occur in the posterior fossa, pons, basal ganglia, and thalamus localizations [8], which are deep brain structures, whereas in amyloid angiopathy, more amyloid depositions accumulate in the vessel wall with hemorrhages occurring in many lobar areas in the brain [9]. Pathophysiologically, it was determined that intracerebral hemorrhage causes compression in the surrounding neuronal tissue by creating a sudden and rapid mass effect in brain tissue, and neuronal injury is caused by damage to the signal pathways between neurons [10]. Non-contrast computed tomography (CT) is the gold standard neuro-imaging modality for the diagnosis of SIH due to its easy accessibility and rapid performance [11]. Although there is no definite and specific treatment, aggressive and early medical support, blood pressure regulation, intracranial pressure monitoring and control, management of secondary brain injury, prevention of complications, and, in selected cases, surgical intervention have positive effects on prognosis [12].

Intracerebral hemorrhage, which is a common disease, is an important disease that causes death if it is not detected. Therefore, rapid detection of the disease will increase the chances of early intervention. In our study, the aim was to present a rapid approach for the detection of this disease. For this purpose, different parameters and models were trialed to determine which of several segmentation algorithms would provide better results. Although the U-net model was used for intraparenchymal hemorrhage segmentation in studies, segmentation algorithms such as LinkNet and FPN were not used, providing significant motivation to our study in terms of showing the performance of these algorithms. While ready-made datasets were used in other studies, data labeled by experts in the field was used in our study. For the reliability of success in measuring accurate performance, images related to this disease provided by RSNA [13] were included in our study, as well as our own dataset. The originality of our dataset, which is among the innovative aspects of our study, and the ability to detect disease with high accuracy rates by using multiple segmentation algorithms trained with different models are important criteria that distinguish our study from other studies. The contributions of our study to the field can be listed as follows:

- A new publicly available dataset showing expert-labeled intracranial intracerebral hemorrhage.
- Investigation of the performance of multiple segmentation algorithms and different backbones applied for the first time for this disease.

The organization of our study is as follows: in the second part, studies related to the disease are given. The methodology is given in the third section, and the results are given in the fourth section. The last sections contain the discussion and conclusion.

2. Related Works

In this section, firstly, segmentation studies on intracerebral hemorrhage detection and then classification studies are examined in detail. In the last part, studies in the medical field with the models we used in our study are given.

Accurate segmentation and quantification of intraparenchymal hematoma is very important to be able to diagnose patients more quickly and at a higher rate, to predict the outcomes for patients more accurately with the correct estimation of bleeding volume, and to decide on treatment options [14]. In recent years, studies

estimated bleeding volume very rapidly using segmentation algorithms, treatment strategies were developed, and more accurate and stable performances were achieved by using different methods [15–17]. Falk et al. presented an ImageJ plugin to analyze cell detection and shape measurements in U-net [18]. Hu et al. proposed an encoder-decoder convolutional neural network (ED-Net) for the detection of intracerebral hemorrhage (ICH). The model they propose makes extensive use of both low-level and high-level semantic knowledge. Although they achieved good results in their studies, they stated that their models still do not take into account spatial information, and this is a limitation of their work. It was stated in their studies that a dice coefficient of over 80% and a Jaccard index of over 75% were obtained [17]. Arab et al. attempted to develop a fast and fully automated deep learning method that applied deep supervised convolutional neural networks (CNN-DS) for hematoma segmentation and volume measurement in CT scans. They compared CNN-DS with three different methods and obtained the best result of 0.84 for CNN-DS. It was mentioned in their studies that more labeled data is needed for the detection of hematoma and that there may be human-induced errors while labeling. In our study, the tagged dataset was validated separately by three of our experts to minimize human-induced errors [19]. Jadon et al. used different image segmentation models (U-Net 2D, Inception-based UNet++ 2D model) to segment different phenotypes of hemorrhagic lesions in their study. In their study, they obtained a Dice coefficient of 0.94 for intraparenchymal hemorrhage (IPH) by using the Focal Tversky Loss Function in the UNet++ 2D model. This is a study showing the effect of the loss functions we used in our study on segmentation [20]. Cao et al. used the fuzzy C-means clustering method to separate the pixels on CT images and used the U-Net neural network they developed for auxiliary diagnosis of intracerebral hemorrhage. In the study, pixels in CT images are divided into four categories: white matter, gray matter, cerebrospinal fluid, and hemorrhage. The fact that this requires pre-processing before segmentation can be seen among the limits of the study. In the study, a 0.860 Dice coefficient value and a 0.712 Jaccard value were obtained [21]. Wang et al. proposed a modified U-Net and curriculum learning strategy to distinguish ICH subgroups on CT images. They emphasized that more training should be done with more data in their studies, where they obtained low values such as 0.67 Dice Coefficient and 0.50 Jaccard value [22]. Maya et al. classified the hemorrhage region into 3 types (epidural, subdural, and intraparenchymal hemorrhage) in their study using U-Net and CapsNet on CT images with stroke symptoms. In the study, first of all, some image processing methods were applied to the images. Then segmentation was done with U-net. In this segmentation, 75% Dice coefficient was obtained. Segmented images were classified with CapsNet. 92.1% validation accuracy was achieved with CapsNet [23]. Hssayeni et al. used an ICH segmentation method based on 5-fold cross-validation in their study, where they developed a deep fully connected network (FCN) named U-Net to segment ICH regions on CT scans in a fully automatic manner. It has been reported that a Dice coefficient of 0.31 was obtained in this segmentation process. They emphasized that this low dice coefficient value may be due to incorrect segmentation near the bone in grayscale images where the density is similar. They also stated that the model they developed in the study was not sufficient to detect small hemorrhages [24]. Abramova et al. used a 3D U-Net architecture with compression and excitation blocks to automatically segment hemorrhagic stroke lesions on CT scans, as well as restrictive patch sampling to alleviate the problem of class imbalance and resolve the issue of intraventricular hemorrhage not considered to be a stroke lesion. The average Dice coefficient value of 0.86 was reached in the study. It has been stated that the performance of U-net increases when used with squeeze-and-excitation blocks [25]. Liu et al. used the U-Net neural network model and contour recognition to extract the brain parenchymal region through intelligent tissue analysis of cerebral hemorrhage after segmentation to detect hypertensive intracerebral hemorrhages. It contributes to this field as a study that provides texture analysis after segmentation [26]. Manasa et al. used the U-Net algorithm for semantic segmentation in a study using 146 images for the detection of ICH [27].

He (2020) used SE-ResNeXt50 and EfficientNet-B3 to learn the classification for five subtypes of intracranial hemorrhage. The RNSA dataset, which is also included in our study, was used here. A classification has been made for all diseases in this dataset. As a result of classification, a 0.0548 loss score value was obtained in test sets [28]. Castro et al. used VGG-16 and CNN-4 for detection of intracranial hemorrhage (HIC). In their study, they made a classification that only states whether there is hemorrhage or not. For this binary classification, the accuracy rate they obtained with VGG-16 was 0.968, and the accuracy rate they obtained with CNN-4 was 0.981. As a result, they reported that CNN could be a useful tool for CT images in disease detection [29]. Burduja et al., in their intracranial hemorrhage detection study based on the RSNA 2019 dataset with CTs, used a lightweight deep neural network architecture consisting of a

convolutional neural network (CNN) and a long short-term memory (LSTM) network. In their studies, they tried to classify the feature vectors they obtained from the images. It has been stated that an accuracy of over 96% has been achieved. In the limitations of the study, they demonstrated that their system was able to predict the correct label for a particular bleeding subtype without considering all sites for the relevant subtype. They concluded that although this behavior produces very good accuracy rates, it is not optimal for visualizing all bleeding sites. In our application, an accurate visualization of the bleeding site is provided [30].

Araújo et al. used a melanoma segmentation method based on U-Net and LinkNet deep learning networks combined with transfer learning and fine-tuning techniques. Additionally, they evaluated the model's ability to learn to segment the dataset by merging the disease or just the datasets. The experiments were performed on three datasets (PH2, ISIC 2018, and DermIS), and they stated that they obtained more promising results with U-net, whose Dice values averaged 0.923 in the PH2 dataset, 0.893 in ISIC 2018, and 0.879 for DermIS, respectively. Although there is no ICH segmentation in the study, it is one of the studies in which the performance comparisons of U-net and LinkNet are included [3]. Ghosh et al. detected brain tumors by comparing two different U-Net architectures (U-Net: baseline and U-Net: ResNeXt50 backbone) and a feature pyramid network (FPN) based on segmentation. The U-Net architecture with the ResNeXt50 backbone achieved dice coefficients of 0.932, with values for basic U-Net and FPN of 0.846 and 0.899, respectively. In this study, U-net and FPN were used together. It is also seen that a better dice coefficient value can be obtained by using the ResNeXt50 backbone for U-net [31]. Sobhaninia et al. measured some biometric parameters, such as fetal head circumference (HC), to check the health and growth of the fetus. For this study, they used mini-LinkNet by modifying LinkNet as a multiscale light convolutional neural network. In this study, the effective structure of LinkNet is emphasized [32]. In their study using a cross-scale feature pyramid for OCT images, Fan et al. achieved an average sensitivity (mAP) of 85.02 for FPN for OCT lesion detection [33]. Dai et al. used cone-beam CT (CBCT)-based adaptive radiotherapy in their study, in which they automatically identified at-risk head and neck organs using dual pyramid networks. When the results of the patient images were examined, the best DSC was 0.96 for the oral cavity and 0.66 for the lowest optical chiasm [34]. Lo et al. proposed a deep learning (DL) framework for 2D fetal MRI segmentation using a cross-attention squeeze excitation network (CASE-Net) for research and clinical applications. The purpose of CASE-Net was to emphasize the localization of contextual information related to biomedical segmentation by combining attentional mechanisms with squeezing and excitation (SE) blocks. This was a retrospective study with 34 patients. In their experiments, they showed that the proposed CASE-Net outperformed other competitive segmentation architectures, achieving the highest segmentation Dice score of 87.36% [35]. Singh et al. used the ImageCLEF Med Tuberculosis 2019 dataset in their study about detecting tuberculosis lesions in the lungs using image segmentation. The dataset consisted of 3D CT images divided into 2D slices, and segmentation was applied to each slice using U-Net, FPN, and LinkNet architectures. In this study, three segmentation algorithms were compared, as in our study [36].

3. Methodology

3.1. Dataset

In our study, the data of 100 patients (44 males and 56 females) diagnosed with SIH who were hospitalized in the Neurology Department of Van Yüzüncü Yıl University were analyzed retrospectively. All permissions for the study were obtained from the hospital ethics committee. The mean age of the patients was 65.1 years (23–95 years). Patients with epidural, subdural, subarachnoid, ventricular hemorrhages, aneurysms, or hematomas secondary to vascular malformations were excluded from the study. In CT imaging, hematoma is easier to recognize because it appears brighter (hyperintense) than the surrounding brain tissue and cerebrospinal fluid. The ABC/2 formula, which is frequently used in clinical studies and daily practice, was used to calculate the hematoma volume. Using the ABC/2 formula, total hematoma volumes were calculated with perpendicular diameter measurements from CT images in both coronal and axial planes. These calculations were made independently by two neurologists in order to reduce observer variability and measure the hematoma volume as if it were larger than it is, especially in irregular hematomas. The hematoma volume average was 45.3 cm³ (0.49–273 cm³). For the segmentation process, both the images in the dataset and the contours of the hematoma on the CT images of the patients were manually marked with a red color by the neurologists using the cursor.

In order to contribute to the dataset in our study, 264 intracerebral hemorrhage images were identified from the RNSA [13] dataset. This dataset was created by four working groups consisting of Stanford University, Thomas Jefferson University, Unity Health Toronto, Universidade Federal de São Paulo (UNIFESP), and the American Society of Neuroradiology (ASNR) [13]. In the dataset, there are images of other intracranial hemorrhages. Among these, images that were confirmed as intracerebral hemorrhages were selected for use in our study. The selected images were again marked by our experts. Ground truth masks were removed from the marked images. Examples of images marked and unmasked by experts are given in Figure 1.

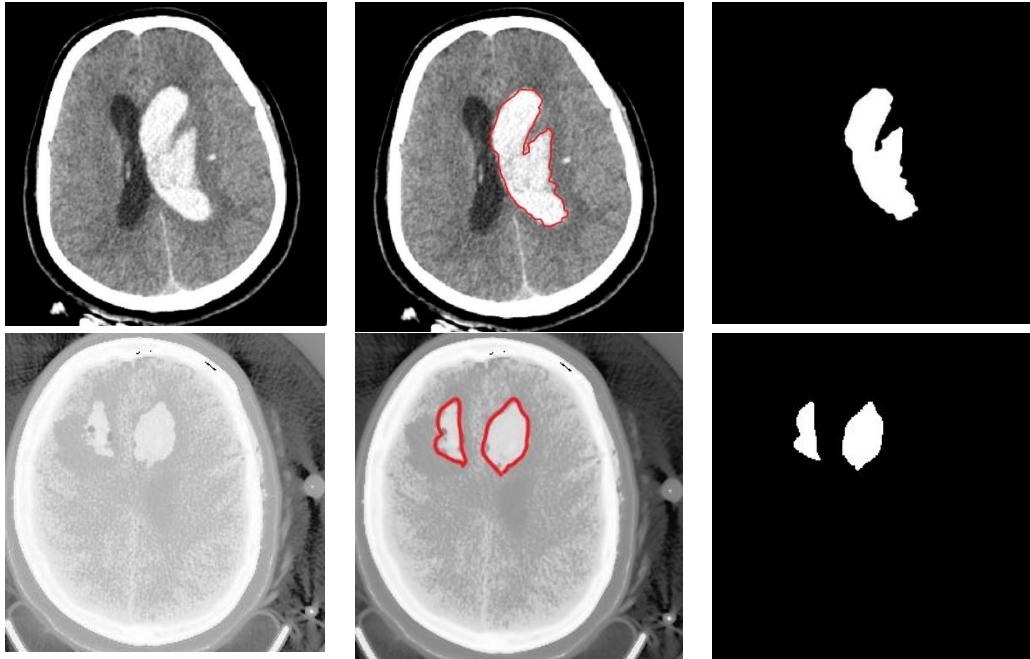


Figure 1. Samples from the Dataset

In Figure 1, the first row shows an example from the first dataset, and row 2 shows an example from the RNSA dataset. As can be seen, the second dataset has lower values in terms of both resolution and quality than the first dataset.

3.2. Segmentation Algorithms

3.2.1. U-Net

The architecture known as the Fully Convolutional Network (FCN) stands out as a remarkably successful and frequently employed foundational structure recommended for semantic segmentation [37]. U-Net, another architectural framework derived from FCN, was specifically devised for the semantic segmentation of medical images [38]. The network's structure comprises two distinct segments, namely the contraction and expansion paths [26, 38]. Operations conducted on the left side, the contraction path, aim to grasp contextual details of the image, effectively extracting features from it. These operations closely adhere to the established logic of classical CNN architecture.

Conversely, operations on the right side, the expansion path, precisely localize the segments within the image [38, 39]. The connection between the contraction and expansion paths employs a concatenation operator instead of summation, enhancing the direct application of spatial information to deeper layers and achieving a more precise segmentation outcome [40]. Unlike classical deep learning, which requires abundant examples and substantial computing resources, U-Net demonstrates adaptability with minimal training sets [39, 41]. Notably, this adaptability renders it particularly suitable for tasks involving the segmentation of medical images [39, 42].

U-Net's distinctive strategy, which sets it apart from other segmentation architectures, involves combining feature maps from the contraction phase with their symmetrical counterparts in the expansion phase. This innovative approach facilitates the dispersion of contextual information into high-resolution feature maps [3]. The structural depiction of U-Net is illustrated in Figure 2.

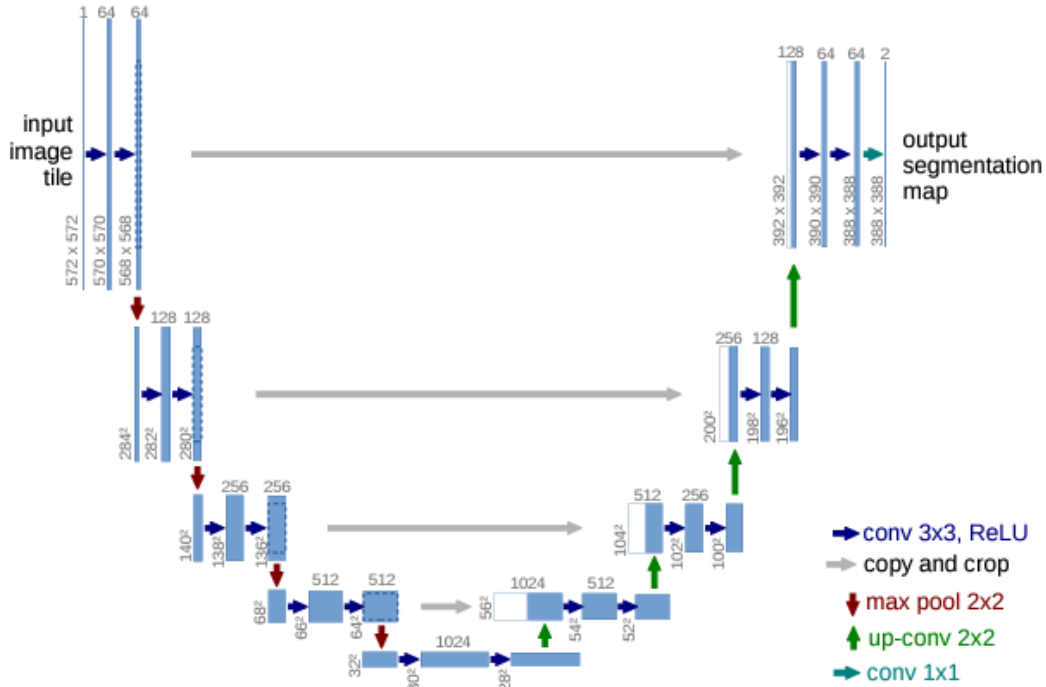


Figure 2. U-net Structure [38]

3.2.2. LinkNet

LinkNet features a streamlined deep neural network architecture that facilitates the acquisition of knowledge in semantic segmentation tasks without a notable surge in parameters. It bears resemblance to U-Net and other segmentation networks. Positioned on the left is an encoder, while on the right is a decoder [3]. The encoder operates by encoding data within the source space, and the decoder translates this data into spatial categorization to execute the segmentation [3, 43]. Unlike current neural network architectures, where encoders in segmentation processes perform multiple downsampling operations, LinkNet adopts a different approach. This deviation is crucial, as the conventional process tends to result in the loss of spatial information during cascading convolutions in the encoder segment [44]. Retrieving such lost information proves to be challenging [43].

In Link-Net, a distinctive feature is observed wherein the input of each encoder layer is concurrently assigned to the output of the corresponding decoder. The intent behind this mechanism is to reclaim spatial information that was lost, serving as a valuable resource for the decoder and the subsequent upsampling processes [43]. The utilization of fewer parameters is a noteworthy characteristic, attributed to the shared information learned by the encoder, facilitated by the decoder [36, 43]. Figure 3 illustrates the structural layout of LinkNet.

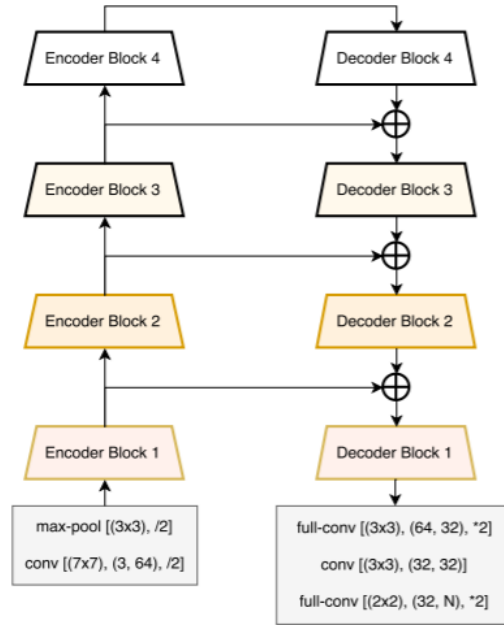


Figure 3. LinkNet Structure [43]

3.2.3. FPN

FPN utilizes the pyramidal hierarchy of deep convolutional networks to generate feature pyramids with minimal additional computational cost [45]. Image pyramids serve as a data structure specifically designed to facilitate convolution by employing downscaled versions of the original image at regular intervals. These downscaled copies effectively reduce both sample density and resolution [46]. The foundational concept of feature pyramids is established by image pyramids [47]. The pyramid framework is believed to offer a conceptual unification for representing and manipulating low-level visual information. It presents a versatile and convenient multi-resolution format that aligns with various scales present in visual scenes, mirroring the multiple processing scales within the human visual system [46]. FPN, functioning as a feature extractor grounded in the pyramid concept, excels in both accuracy and speed [47]. While ConvNets provide a high level of semantic understanding and resistance to variance, the inclusion of pyramids remains essential for achieving optimal accuracy. Specifying each level of an image pyramid yields a multi-scale feature representation where all levels, including those with high resolution, exhibit significant semantic strength. However, the drawback of employing an image pyramid lies in the increased extraction time [47].

FPN employs a comprehensive approach, combining features through bottom-up, top-down paths, and lateral connections to leverage the feature hierarchy, ultimately creating a robust feature pyramid [48]. The bottom-up path facilitates a top-down progression, rendering higher-resolution layers compared to the base layer. Each stage in this progression is identified as a pyramid level [46]. Among the reconstructed layers, the final layer output is selected as a feature map to construct the pyramid [47]. The top-down path is enriched by incorporating lateral links between feature maps [36]. This path creates spatially coarser yet semantically stronger feature maps with higher-resolution layers in a top-down manner. These features are further enhanced by integrating features from the bottom-up path through lateral links. Each lateral link connects feature maps with the same spatial dimensions from both the bottom-up and top-down paths [47]. The structural representation of FPN is visually depicted in Figure 4.

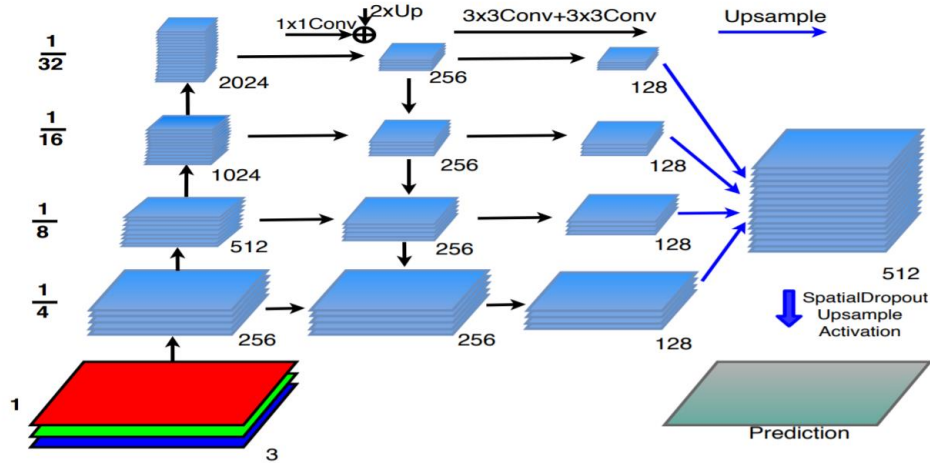


Figure 4. FPN Structure [45]

3.3. Backbones

3.3.1. ResNet

Residual Network (ResNet) [49] is a deep learning network architecture using residual layers that won first place in the ImageNet competition in 2015. In this model, it is thought that a faster model will be created by adding residual values between the linear and ReLU layers and the blocks that feed the next layers (residual blocks). For this reason, in network structures where the residual block structure is used, the data in one layer is given as input to the next layer and transmitted to the next layers in 2 or 3 layers. The single residual block structure is shown in Figure 5. The output of the residual block can be formulated as in Equation 1.

$$y = F(x) + x \quad (1)$$

where F is the residual function and x and y are the input and output of the residual function, respectively. The entire residual network consists of the first convolutional layer and a few basic blocks [50]. The structure of the ResNet 34 model is shown in Figure 6 [49].

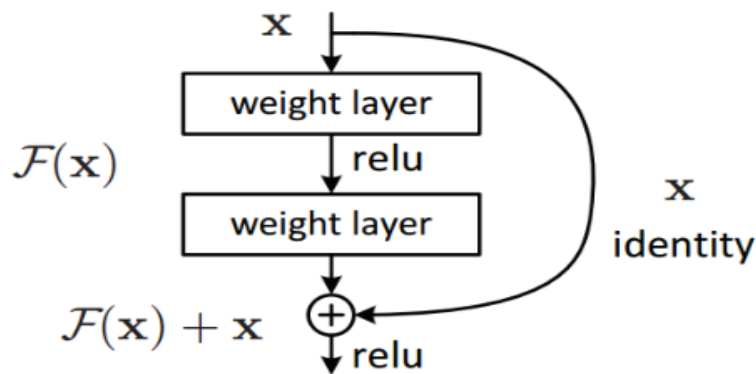


Figure. 5. Single residual block [49]

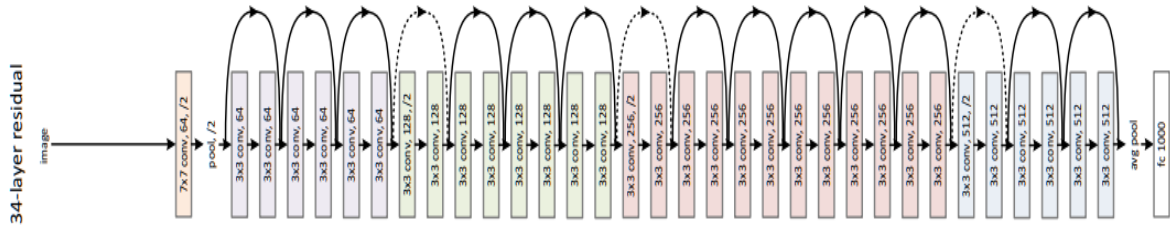


Figure 6. ResNet34 Structure

3.3.2. EfficientNet

EfficientNet is a deep learning model developed by the Google research team [51] in 2019. There are many different versions of this model, from B0 to B7, which were developed based on the hypothesis of increasing the width and resolution of the model as well as the depth of the model. As the number of parameters calculated in each version increased, the computational cost also increased. While performing EfficientNet, the ResNet model was used for the first performance comparisons. In our application, these models were selected as the backbones for segmentation algorithms, and performance comparisons were made. The three concepts this model considers are depth, breadth, and resolution. Depth refers to how deep the meshes are. In other words, it is equivalent to the number of layers. The width is the number of channels in the convolution layer. Resolution is the resolution of the image transmitted to the network. Researchers proposed a new scaling method that equally scales all dimensions of the network's depth, width, and resolution. We can summarize these concepts in Figure 7 [51].

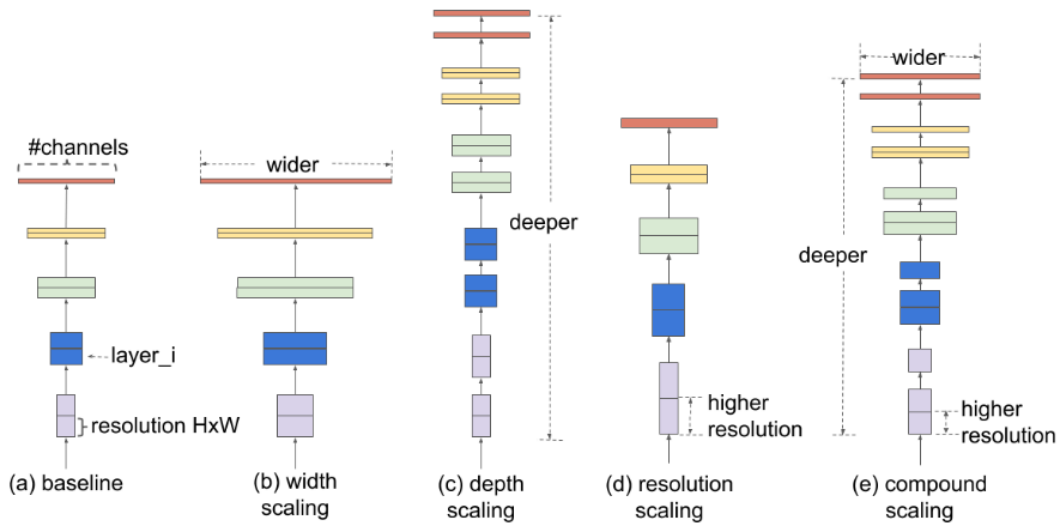


Figure 7. a) Basic network example, b)-d) traditional scalings that increase only one dimension of network width, depth or resolution, e) EfficientNet's composite scaling method

The EfficientNet B0 structure is shown in Figure 8. The main building block of this mesh is MBConv, to which compression and excitation optimization are added. These blocks create shortcuts between the beginning and end of a convolutional block. Input activation maps are expanded using 1x1 convolutions, increasing the depth of feature maps. The shortcut links used in this model connect narrow layers together, while wider layers are located between jump links. This structure helps reduce the model size as well as the total number of operations required. Other parameters used in this model are as follows: kernel_size is the kernel size for convolution, for example, 5 x 5; num_repeat specifies that the repeat count of a given block must be greater than zero; input_filters and output_filters are the number of filters; expand_ratio is the input filter expansion rate; id_skip determines whether to use link skipping; and se_ratio shows the spin rate for squeezing and excitation blocks.

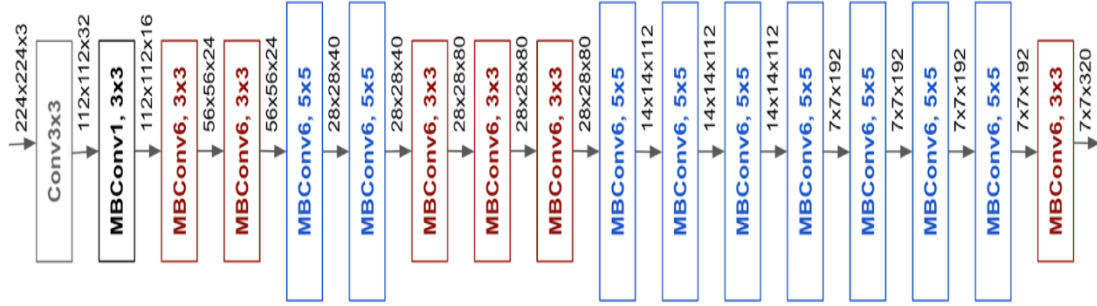


Figure 8. EfficientNet B0 Structure [51]

3.4. Application

The Python environment was used for the application. Before the application, 334 images in the dataset were reserved for model training, and 30 images were used for performance analysis after model training was completed. During the model training process, 20% of 334 images were used for validation. The dataset was run separately in each segmentation algorithm. Different backbones were tested in each run. At the end of the run, performance analysis was made for the models with test data. The parameter values used in the operation of the models are given in Table 1.

Table 1. Parameter Settings

Parameter	Value
Optimizer	Adam
Learning Rate	0.0005
Epoch	100
Batch Size	8
Input Size	(256,256,3)
Activation	Sigmoid
callbacks	ReduceLROnPlateau and ModelCheckPoint

4. Evaluation Metrics

The application was run on a workstation with an I7 processor and 16 GB of RAM. The workstation had a graphics card with a Geforce 1070 GPU. Evaluation metrics are covered in two different sections. The first of these is the segmentation metric that is needed to examine the segmentation results, while the second is the model metrics used to examine the accuracy of the models.

4.1. Segmentation Metrics

4.1.1. Jaccard Index

The Jaccard index is a metric that measures the similarity between the reference value and the predicted value in segmentation applications. For this metric value, similar features between the two values are divided into the union of the two sets; in other words, by taking the intersection of the two sets. The formula used for the Jaccard index is given in equation 2. This metric ranges from 0–1 (0–100%); 0 indicates no overlap, and 1 indicates perfectly overlapping segmentation.

$$J(Y, Y') = \frac{|Y \cap Y'|}{|Y| + |Y'| - |Y \cap Y'|} \quad (2)$$

Where Y is the ground truth and Y' is the prediction.

4.1.2. Dice Coefficient

This metric is very similar to the Jaccard index. There is a positive relationship between them. It is a well-known metric that measures the similarity between the reference value and the predicted value in segmentation. Like the Jaccard index, this metric has values between 0 and 1, where 0 indicates no overlap and 1 indicates perfectly overlapping segmentation. Equation 3 is used for the Dice coefficient.

$$J(Y, Y') = \frac{2|Y \cap Y'|}{|Y| + |Y'|} \quad (3)$$

Where Y is the ground truth and Y' is the prediction.

4.2. Model Metrics

4.2.1. Binary Cross Entropy Loss

This loss function is used in binary classification tasks. As is known, masks used consist of binary images as background 0 and foreground 1. Equation 4 is used for this function.

$$L_{BCE}(y, \hat{y}) = -(y \log(\hat{y}) + (1 - y) \log(1 - \hat{y})) \quad (4)$$

Here \hat{y} denotes the value predicted by the model and y is the target value.

4.2.2. Dice Loss

Dice is a loss function often used to evaluate success in biomedical images. Equation 5 is used for this function.

$$\text{DiceLoss} = -\frac{2}{|C|} \sum_i^C \frac{\sum_k S_i^k L_i^k}{\sum_k S_i^k + \sum_k L_i^k} \quad (5)$$

Where C is the number of classes, k is every pixel in the image, S is the prediction and L is the ground truth label.

4.2.3. Focal Loss

Loss of focus (FL) [52] attempts to reduce the contribution of easy examples so that CNN can focus more on difficult examples. It does this by giving more weight to samples that are difficult or easily misclassified. Focal loss is included in the literature as a more developed version of cross-entropy. Therefore, Equation 6 was used to calculate the focal loss.

$$FL(p_t) = -(1 - p_t)^\gamma \log(p_t) \quad (6)$$

As can be seen from the formula, it adds the factor $(1 - p_t)^\gamma$ to cross-entropy. Relative loss is reduced for samples classified well when $\gamma > 0$.

5. Results

It is possible to evaluate the results of our study as an ablation study. Two different threshold values were used for the Jaccard index and Dice coefficient values in the study. These are values of 0.5 and 0.6. The aim was to take the results into consideration if the intersection point between the estimated

and actual values was greater than these values. First, the results obtained from the 0.5 threshold value are given in Table 2.

Table 2. Results of models (threshold: 0.5)

U-net		Training Data		Test Data	
Model		Jaccard Index	Dice Coefficient	Jaccard Index	Dice Coefficient
resnet34		0.8976	0.9354	0.8563	0.9213
resnet50		0.8716	0.9075	0.8223	0.8872
resnet101		0.8939	0.9361	0.8449	0.9146
effnetb0		0.9028	0.9366	0.8554	0.9212
effnetb1		0.9078	0.9426	0.8579	0.9227

LinkNet		Training Data		Test Data	
Model		Jaccard Index	Dice Coefficient	Jaccard Index	Dice Coefficient
resnet34		0.876	0.9187	0.8498	0.9169
resnet50		0.8605	0.9028	0.839	0.9105
resnet101		0.8351	0.8866	0.8382	0.9099
effnetb0		0.8996	0.9363	0.8492	0.9176
effnetb1		0.903	0.9431	0.8611	0.9244

FPN		Training Data		Test Data	
Model		Jaccard Index	Dice Coefficient	Jaccard Index	Dice Coefficient
resnet34		0.9079	0.9429	0.8546	0.9202
resnet50		0.8994	0.9361	0.841	0.9116
resnet101		0.8511	0.9015	0.8403	0.911
effnetb0		0.8887	0.9278	0.8448	0.9145
effnetb1		0.914	0.9495	0.8589	0.9233

When we evaluate the table obtained for threshold value 0.5, it is possible to see the highest Jaccard index and dice coefficient values with the EfficientNet B1 backbone in all segmentation algorithms. If they are evaluated among themselves, FPN reached the highest Dice coefficient value with a value of 0.9495 for the training data. The Jaccard index here is 0.9140. When the values obtained for the test data are examined, the LinkNet algorithm obtains a 0.9244 Dice coefficient value and a 0.8611 Jaccard index value. In Table 3, the results obtained from threshold 0.6 are given.

In the table for threshold 0.6, a 0.9451 Dice coefficient value for training data and a 0.9096 Jaccard index were obtained for the ResNet34 backbone in the FPN model. This value is the highest value for training data. The highest values for the test data were also obtained with the FPN algorithm, but from the EfficientNet B1 backbone. These values are 0.9241 Dice coefficient and 0.8605 Jaccard index values.

Table 3. Results of models (threshold: 0.6)

U-net Model	Training Data		Test Data	
	Jaccard Index	Dice Coefficient	Jaccard Index	Dice Coefficient
resnet34	0.8663	0.9098	0.8364	0.9076
resnet50	0.8976	0.9328	0.8355	0.9081
resnet101	0.8682	0.9161	0.8282	0.9025
effnetb0	0.8995	0.939	0.8521	0.9191
effnetb1	0.8904	0.9295	0.8538	0.92

LinkNet Model	Training Data		Test Data	
	Jaccard Index	Dice Coefficient	Jaccard Index	Dice Coefficient
resnet34	0.8732	0.9127	0.8516	0.9187
resnet50	0.8592	0.9049	0.8288	0.9034
resnet101	0.877	0.9229	0.8511	0.9187
effnetb0	0.8807	0.921	0.8506	0.9178
effnetb1	0.8954	0.9359	0.8563	0.9218

FPN Model	Training Data		Test Data	
	Jaccard Index	Dice Coefficient	Jaccard Index	Dice Coefficient
resnet34	0.9096	0.9451	0.8538	0.9199
resnet50	0.8993	0.9311	0.8476	0.9164
resnet101	0.8695	0.9107	0.8371	0.9086
effnetb0	0.9011	0.9336	0.8535	0.9196
effnetb1	0.8983	0.9339	0.8605	0.9241

The highest results obtained from the training and test data for both threshold values are given in Table 4 and Table 5, respectively.

Table 4. Threshold results for training data

Threshold	Algorithm	Train Data		
		Model	Jaccard Index	Dice Coefficient
0.5	FPN	EfficientNetB1	0.914	0.9495
0.6	FPN	Resnet34	0.9096	0.9451

Table 5. Threshold results for test data

Threshold	Algorithm	Test Data		
		Model	Jaccard Index	Dice Coefficient
0.5	LinkNet	EfficientNetB1	0.8611	0.9244
0.6	FPN	EfficientNetB1	0.8605	0.9241

When we examine the table comparing the threshold values, the FPN algorithm with a 0.5 threshold and the EfficientNet B1 backbone training data obtained the highest values with a 0.9495 Dice coefficient and a 0.9140 Jaccard index. In the test data, the highest values were obtained at the 0.5 threshold. These values were obtained from the LinkNet algorithm and the EfficientNet B1 model. The resulting Jaccard index was 0.8611, and the Dice coefficient value was 0.9244. In Figure 9, the loss charts for the models that provided the best values in the test data are given.

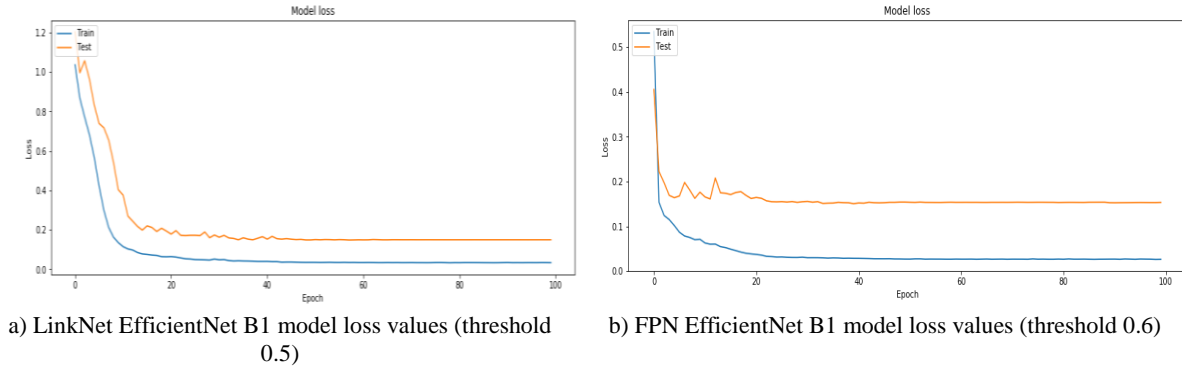


Figure 9. Loss function values of best models

In Figure 10, some examples of the segmentation results from the algorithms where these values were obtained are shown. The aim was to show the segmentation performance by obtaining segmentation results for the same samples in both models. The first line shows the hospital data, and the second line shows sample data from the RNSA dataset. As can be seen, the images obtained are clearer based on the device quality. Although the picture quality is low in the models we compared, successful results were obtained. While a 0.80 Jaccard index was obtained for LinkNet in the first line image, a 0.70 Jaccard index was obtained for the same image in FPN. For the picture in the second line, a 0.94 Jaccard index was obtained in LinkNet, while a 0.93 Jaccard index was obtained in FPN.

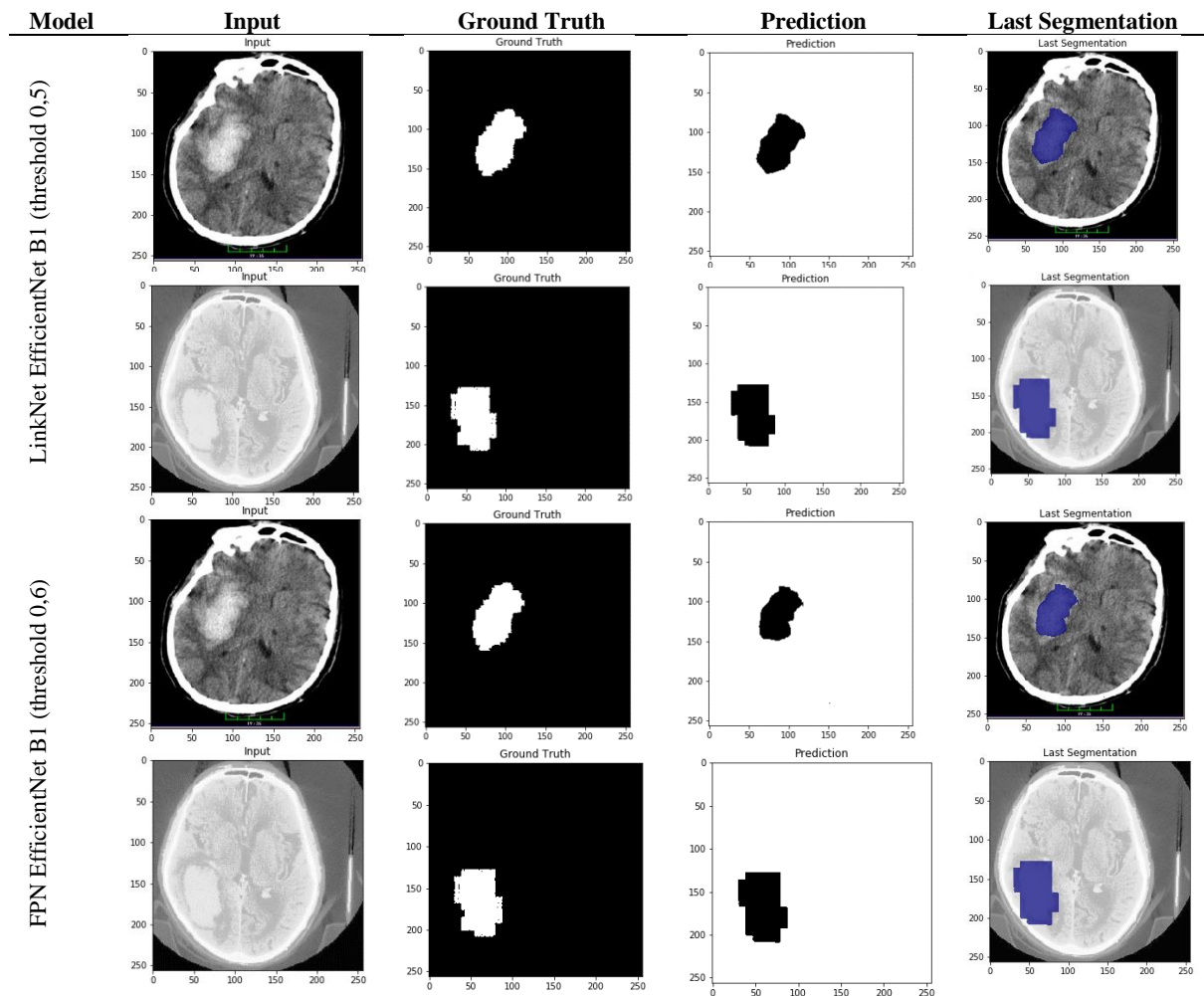


Figure 10. Results of the best models

6. Discussion

Our study started with marking images obtained from the hospital by experts and obtaining the masks with image preprocessing techniques. Cases where the obtained images may be insufficient for the performance of the segmentation algorithms are taken into account. For this reason, new images of intracerebral hemorrhages were taken from the Kaggle database and marked by our experts. The selection of this disease in our study is also important. As reported by the experts where we live, intracerebral hemorrhage is detected more frequently among intracranial hemorrhages. Carrying out the study with three segmentation algorithms is a preliminary process for the web-based software we plan to develop to detect this disease. With the use of our web-based software in hospitals, it will be a decision-support mechanism that will help experts make decisions more quickly.

For these purposes, a detailed examination of segmentation algorithms was made in our study. By adding backbones to the standard structure of these algorithms, it was seen that the features were better extracted, and thus they performed better. EfficientNet, which is used as a backbone in the study, is one of the state-of-the-art deep learning models. Although ResNet is not as new as EfficientNet, it is still a powerful model that is frequently used in studies. This algorithm takes its power from the residual layers of the layers, which provide information from the previous layer. With these layers, information transmission is provided between the layers. It is undesirable to have information lost in feature extraction in medical images. Again, EfficientNet is one of the current models that has found a solution to this problem. Therefore, in this study, we wanted to compare the strong results of the models over time by taking an old and a new model.

In Section 2, studies for ICH classification and segmentation are discussed separately. While examining the studies, explanations were given about their limitations and how our study dealt with these limitations. For example, in [24], it was reported that small hemorrhages could not be detected and an incorrect segmentation process occurred due to density similarity. In our study, it was reported that even small hemorrhages could be easily detected, according to the determination of our experts. Arab et al. reported that erroneous results may be obtained as a result of human-induced markings in the dataset [19]. We tried to minimize the error rate by labeling the datasets of the three experts in our study and validating them separately. In addition, in the studies we examined, after using image processing techniques on images, segmentation or classification was made. With the backbones we used and the extraction of features, there was no need for any image processing before the training.

When the results of our study are examined, looking at the values obtained from the three segmentation algorithms, it is possible to say that the FPN algorithm achieves better results than the other algorithms, considering the metrics accepted for intracerebral hemorrhage segmentation. As we know, many deep learning models are used as backbones in the background of these algorithms. In this study, we chose different versions of the ResNet and EfficientNet models as backbones. In summary, our study covers three segmentation algorithms and five backbones. Among these backbones, EfficientNet models achieved better results. Additionally, with the models developed, our approach will have the advantage of further speeding up the pre-processing step that requires an expert so that the patient can be intervened with more quickly.

In Section 2, where segmentation studies in different fields are examined, segmentation performance above 90% was not achieved in most of the studies related to ICH. In our study, there was a success rate of 0.9495. Considering the results obtained and the studies we examined in the literature, it was confirmed by our experts that better results were obtained in the detection of intracerebral hemorrhage with the models we developed. In addition, the segmentation architectures used in our study and studies using multiple backbones were not encountered in the literature at the time of this study. It motivated us to include different architectures in our study and to add the performance results of different backbones used with these architectures to the literature. Another result encountered while examining previous studies was that the studies were not used as software; in other words, they were not practically included in clinical studies. For this purpose, the necessary models were created for our web-based ICH detection software, which we will present in our future studies.

In addition, as mentioned in the dataset introduction, our work achieved successful results even with the RNSA dataset, which consists of low-quality images. This is noteworthy in terms of demonstrating the power of segmentation algorithms and their backbones. The dataset we labeled in the study will be shared publicly, and other researchers will benefit from it. We think that this will be another contribution of our study to the field.

As is known, deep learning applications have high computational costs. When GPU graphics cards are used, operations are performed in a very short time. If the calculation times in the study are investigated, each epoch lasted between 10 and 30 seconds in our study. The shorter this period, the earlier the disease can be detected, and thus the patient can be intervened in in a short time.

7. Conclusions

In this study, we attempted to demonstrate the performance of three different segmentation algorithms for the segmentation of intracerebral hemorrhage detection. An original dataset obtained from the hospital and marked by experts was prepared for the study. In addition, this dataset was enriched with images of this disease obtained from the Kaggle platform. For the backbone selection of the models, the ResNet and EfficientNet deep learning models were chosen. A total of five backbones were used. When the results were examined, the FPN model provided better results for the training data, and the LinkNet model provided better results for the test data. When a comparison is made between backbones, EfficientNet models give better results than ResNet models. The results were evaluated by experts, and it is predicted that it will be a decision-support mechanism that helps expert opinion in hospitals. It has led us to predict that our study can be used objectively in clinical applications after the results were verified separately by three experts. In addition to this foresight, we are aware that better models can emerge by making performance evaluations and receiving feedback with each new piece of data received. For this purpose, the aim is to transfer this study to a web platform for future studies and to continue testing in the hospital environment. We consider this original study a suitable option when rapid diagnosis or a second opinion is required for the detection of intracranial hemorrhage. With the publication of the dataset prepared for the application, a unique dataset will be included in the literature. In addition, we continue to work on other intracranial hemorrhage detection models.

8. Author Contribution Statement

Murat CANAYAZ: Methodology, Software, Validation, Investigation, Data curation, Writing - original draft, Visualization, Project administration, Conceptualization, Validation, Formal analysis, Resources, Writing - review & editing, Supervision, Visualization. Aysel Milanlioğlu: Writing - original draft, Visualization, Writing - review & editing, Validation, Resources, Formal analysis, Investigation. Sanem Şehribanoğlu: Visualization, Project administration, Conceptualization, Validation, Formal analysis, Resources, Writing - review & editing, Supervision, Visualization. Abdulsabır Yalın: Writing - original draft, Visualization, Writing - review & editing, Validation, Resources, Formal analysis, Investigation. Adem Yokuş: Writing - original draft, Visualization, Writing - review & editing, Validation, Resources, Formal analysis, Investigation.

9. Ethics Committee Approval and Conflict of Interest

In our study, the data of 100 patients (44 males, 56 females) diagnosed with SIH, who were hospitalized in the Neurology Department of Van Yuzuncu Yıl University, were analyzed retrospectively. All permissions for the study were obtained from the hospital ethics committee. There is no conflict of interest with any person/institution in the prepared article.

10. References

- [1] M.U. Rehman, S. Cho, J.H. Kim and K.T. Chong, "Bu-net: Brain tumor segmentation using modified u-net architecture", *Elect.*, 9, 1-12, 2020.
- [2] T. Lan, Y. Li, J.K. Murugi, Y. Ding and Z. Qin, "RUN:Residual U-Net for Computer-Aided Detection of Pulmonary Nodules without Candidate Selection", <http://arxiv.org/abs/1805.11856>, 2018.
- [3] R.L. Araújo, F.H.D. de Araújo and R.R.V. Silva, Automatic segmentation of melanoma skin cancer using transfer learning and fine-tuning, *Multimed. Syst.*, 2021.
- [4] Q. Chen, P. Liu, J. Ni, Y. Cao, B. Liu and H. Zhang, "Pseudo-Labeling for Small Lesion Detection on Diabetic Retinopathy Images", *Int. Jt. Conf. Neural Networks, IEEE*, pp. 1–8, 2020.
- [5] C.J. J van Asch, M.J. A Luitse, G.J. E Rinkel, I. van der Tweel, A. Algra and C.J. M Klijn, "Incidence, case fatality, and functional outcome of intracerebral haemorrhage over time, according to age, sex, and ethnic origin: a systematic review and meta-analysis", *Lancet Neurol.*, 9, 167–176, 2010.
- [6] M.T.C. Poon, A.F. Fonville and R. Al-Shahi Salman, "Long-term prognosis after intracerebral haemorrhage: systematic review and meta-analysis", *J. Neurol. Neur., Psych.*, 85, 660– 667, 2014.
- [7] M. Yamada, "Cerebral amyloid angiopathy: emerging concepts", *J. Stroke.* 17, 17–30, 2015.
- [8] W.C. Ziai and J.R. Carhuapoma, "Intracerebral Hemorrhage.", *Continuum (Minneap. Minn)*, 24, 1603–1622, 2018.
- [9] V. Aiyagari, "The clinical management of acute intracerebral hemorrhage", *Expert Rev. Neurother.* 15, 1421–1432, 2015.
- [10] A.I. Qureshi, S. Tuhim, J.P. Broderick, H.H. Batjer, H. Hondo and D.F. Hanley, "Spontaneous intracerebral hemorrhage", *N. Engl. J. Med.* 344, 1450–1460, 2001.
- [11] O. Flower and M. Smith, "The acute management of intracerebral hemorrhage", *Curr. Opin. Crit. Care.* 17, 106–114, 2011.
- [12] J.C. 3rd Hemphill, S.M. Greenberg, C.S. Anderson, K. Becker, B.R. Bendok, M. Cushman, G.L. Fung, J.N. Goldstein, R.L. Macdonald, P.H. Mitchell, P.A. Scott, M.H. Selim and D. Woo, "Guidelines for the Management of Spontaneous Intracerebral Hemorrhage: A Guideline for Healthcare Professionals From the American Heart Association/American Stroke Association", 46 2032–2060, 2015.
- [13] Kaggle, RSNA Intracranial Hemorrhage Detection, <https://www.kaggle.com/c/rsna-intracranial-hemorrhage-detection/data>, 2021.
- [14] M.I. Aguilar and T.G. Brott, "Update in intracerebral hemorrhage", *The Neurohosp.*, 1, 148–159, 2011.
- [15] A. Patel, F.H.B.M. Schreuder, C.J.M. Klijn, M. Prokop, B. van Ginneken, H.A. Marquering, Y.B.W.E.M. Roos, M.I. Baharoglu, F.J.A. Meijer and R. Manniesing, "Intracerebral haemorrhage segmentation in non-contrast CT. ", *Sci. Rep.* 9, 17858, 2019.
- [16] J. Xu, R. Zhang, Z. Zhou, C. Wu, Q. Gong, H. Zhang, S. Wu, G. Wu, Y. Deng, C. Xia and J. Ma, "Deep network for the automatic segmentation and quantification of intracranial hemorrhage on CT", *Front. Neurosci.* 14, 1084, 2021.
- [17] K. Hu, K. Chen, X. He, Y. Zhang, Z. Chen, X. Li and X. Gao, "Automatic segmentation of intracerebral hemorrhage in CT images using encoder–decoder convolutional neural network", *Infor. Process. & Manag.*, 57, 102352, 2020.
- [18] T. Falk, D. Mai, R. Bensch, Ö. Çiçek, A. Abdulkadir, Y. Marrakchi, A. Böhm, J. Deubner, Z. Jäckel, K. Seiwald, A. Dovzhenko, O. Tietz, C. Dal Bosco, S. Walsh, D. Saltukoglu, T.L. Tay, M. Prinz, K. Palme, M. Simons, I. Diester, T. Brox and O. Ronneberger, "U-Net: deep learning for cell counting, detection, and morphometry", *Nat. Methods.* 16, 67–70, 2019.
- [19] A. Arab, B. Chinda, G. Medvedev, W. Siu, H. Guo, T. Gu, S. Moreno, G. Hamarneh, M. Ester and X. Song, "A fast and fully-automated deep-learning approach for accurate hemorrhage segmentation and volume quantification in non-contrast whole-head CT", *Sci. Rep.* 10, 19389, 2020.
- [20] S. Jadon, O.P. Leary, I. Pan, T.J. Harder, D.W. Wright, L.H. Merck and D. Merck, "A comparative study of 2D image segmentation algorithms for traumatic brain lesions using CT data from the ProTECTIII multicenter clinical trial", in: T.M. Deserno, P.-H. Chen (Eds.), *Imaging Informatics*

- Heal. Res. Appl., SPIE, p. 48, 2020.
- [21] G. Cao, Y. Wang, X. Zhu, M. Li, X. Wang and Y. Chen, "Segmentation of Intracerebral Hemorrhage Based on Improved U-Net", in: 2020 IEEE Conf. Telecommun. Opt. Comput. Sci., IEEE, pp. 183–185, 2020.
- [22] J.L. Wang, H. Farooq, H. Zhuang and A.K. Ibrahim, "Segmentation of Intracranial Hemorrhage Using Semi-Supervised Multi-Task Attention-Based U-Net", *Appl. Sci.* 10, 2020.
- [23] B.S. Maya and T. Asha, "Segmentation and classification of brain hemorrhage using U-net and CapsNet", *J. Seybold Rep.* 1, 18–25, 2020.
- [24] M.D. Hssayeni, M.S. Croock, A. Al-Ani, H.F. Al-Khafaji, Z.A. Yahya and B. Ghoraani, "Intracranial Hemorrhage Segmentation Using Deep Convolutional Model, (n.d.).
- [25] V. Abramova, A. Clèrigues, A. Quiles, D.G. Figueredo, Y. Silva, S. Pedraza, A. Oliver and X. Lladó, "Hemorrhagic stroke lesion segmentation using a 3D U-Net with squeeze-and-excitation blocks", *Comput. Med. Imaging Graph.* 90, 101908, 2021.
- [26] Y. Liu, Q. Fang, A. Jiang, Q. Meng, G. Pang and X. Deng, "Texture analysis based on U-Net neural network for intracranial hemorrhage identification predicts early enlargement", *Comput. Methods Programs Biomed.* 206, 106140, 2021.
- [27] C. Sai Manasa and V. Bhavana, "Deep Learning Algorithms to Detect and Localize Acute Intracranial Hemorrhages", in: Sabu M. Thampi, Sri Krishnan, Rajesh M. Hegde, Domenico Ciuonzo, Thomas Hanne, Jagadeesh Kannan R. (Eds.), *Adv. Signal Process. Intell. Recognit. Syst.*, Springer, Singapore, 367–374, 2021.
- [28] J. He, "Automated Detection of Intracranial Hemorrhage on Head Computed Tomography with Deep Learning", in: *Proc. 2020 10th Int. Conf. Biomed. Eng. Technol.*, ACM, New York, NY, USA, 117–121, 2020.
- [29] S. Castro, Juan Sebastian Chabert, C. Saavedra and R. Salas, "Convolutional neural networks for detection intracranial hemorrhage in CT images", in: *CEUR Workshop Proc.*, 37–43, 2020.
- [30] M. Burduja, R.T. Ionescu and N. Verga, "Accurate and efficient intracranial hemorrhage detection and subtype classification in 3d ct scans with convolutional and long short-term memory neural networks", *Sensors.* 20, 5611, 2020.
- [31] S. Ghosh and K.C. Santosh, "Tumor Segmentation in Brain MRI: U-Nets versus Feature Pyramid Network", *IEEE 34th Int. Symp. Comput. Med. Syst.*, IEEE, 2021.
- [32] Z. Sobhaninia, A. Emami, N. Karimi and S. Samavi, "Localization of Fetal Head in Ultrasound Images by Multiscale View and Deep Neural Networks", *25th Int. Comput. Conf. Comput. Soc. Iran*, IEEE, 2020.
- [33] D. Fan, C. Zhang, B. Lv, L. Wang, G. Wang, M. Wang, C. Lv and G. Xie, "Positive-Aware Lesion Detection Network with Cross-scale Feature Pyramid for OCT Images", 2020.
- [34] X. Dai, Y. Lei, T. Wang, A.H. Dhabaan, M. McDonald, J.J. Beitler, W.J. Curran, J. Zhou, T. Liu and X. Yang, "Head-and-neck organs-at-risk auto-delineation using dual pyramid networks for CBCT-guided adaptive radiotherapy", *Phys. Med. Biol.* 66, 2021.
- [35] J. Lo, S. Nithiyantham, J. Cardinell, D. Young, S. Cho, A. Kirubarajan, M.W. Wagner, R. Azma, S. Miller, M. Seed, B. Ertl-Wagner and D. Sussman, "Cross Attention Squeeze Excitation Network (CASE-Net) for Whole Body Fetal MRI Segmentation", *Sensors.* 21, 4490, 2021.
- [36] J. Singh, A. Tripathy, P. Garg and A. Kumar, "Lung tuberculosis detection using anti-aliased convolutional networks", *Procedia Comput. Sci.* 173, 281–290, 2020.
- [37] J. Long, E. Shelhamer and T. Darrell, "Fully convolutional networks for semantic segmentation", *IEEE Conf. Comput. Vis. Pattern Recognit.*, IEEE, 2015.
- [38] O. Ronneberger, P. Fischer and T. Brox, "U-Net: Convolutional Networks for Biomedical Image Segmentation", N. Navab, J. Hornegger, W.M. Wells, A.F. Frangi (Eds.), *Med. Image Comput. Comput. Interv. – MICCAI 2015, Lecture Notes in Computer Science*, vol 9351. Springer, Munich, Germany, 234–241, 2015.
- [39] L. Jiao and J. Zhao, "A survey on the new generation of deep learning in image processing", *IEEE Access.* 7, 2019.
- [40] L. Li, M. Wei, B. Liu, K. Atchaneeyasakul, F. Zhou, Z. Pan, S.A. Kumar, J.Y. Zhang, Y. Pu, D.S. Liebeskind and F. Scalzo, "Deep learning for hemorrhagic lesion detection and segmentation on brain CT Images", *IEEE J. Biomed. Heal. Informatics.* 25, 2021.
- [41] G. Cao, Y. Wang, X. Zhu, M. Li, X. Wang and Y. Chen, "Segmentation of intracerebral hemorrhage

- based on improved U-Net, IEEE Conf. Telecommun. Opt. Comput. Sci., IEEE, pp. 183–185, 2020.
- [42] M.G. Oghli, A. Shabanzadeh, S. Moradi, N. Sirjani, R. Gerami, P. Ghaderi, M. Sanei Taheri, I. Shiri, H. Arabi and H. Zaidi, "Automatic fetal biometry prediction using a novel deep convolutional network architecture", *Phys. Medica.* 88, 127–137, 2021.
- [43] A. Chaurasia and E. Culurciello, "LinkNet: Exploiting Encoder Representations for Efficient Semantic Segmentation", 2017.
- [44] Z. Sobhaninia, S. Rezaei, N. Karimi, A. Emami and S. Samavi, "Brain Tumor Segmentation by Cascaded Deep Neural Networks Using Multiple Image Scales", 28th Iran. Conf. Electr. Eng., IEEE, 2020.
- [45] S.S. Seferbekov, V.I. Iglovikov, A. V. Buslaev and A.A. Shvets, "Feature Pyramid Network for Multi-Class Land Segmentation", <http://arxiv.org/abs/1806.03510>, 2018.
- [46] E.H. Adelson, C.H. Anderson, J.R. Bergen, P.J. Burt and J.M. Ogden, "Pyramid methods in image processing", *RCA Eng.* 29, 33–41. http://persci.mit.edu/pub_pdfs/RCA84.pdf, 1984.
- [47] T.-Y. Lin, P. Dollar, R. Girshick, K. He, B. Hariharan and S. Belongie, "Feature Pyramid Networks for Object Detection", IEEE Conf. Comput. Vis. Pattern Recognit., IEEE, pp. 936–944, 2017.
- [48] M. Hu, Y. Li, L. Fang and S. Wang, "A2-FPN: Attention Aggregation Based Feature Pyramid Network for Instance Segmentation", in: Proc. IEEE/CVF Conf. Comput. Vis. Pattern Recognit., pp. 15343–15352, 2021.
- [49] K. He, X. Zhang, S. Ren and J. Sun, "Deep Residual Learning for Image Recognition", arXiv:1512.03385v1 (n.d.) 1–12. <http://image-net.org/challenges/LSVRC/2015/>, 2021.
- [50] M. Gao, J. Chen, H. Mu, D. Qi, "A transfer residual neural network based on resnet-34 for detection of wood knot defects", *Fores.*, 12, 1–16, 2021.
- [51] M. Tan and Q. V. Le, "EfficientNet: Rethinking Model Scaling for Convolutional Neural Networks", arXiv:1905.11946v5, <http://arxiv.org/abs/1905.11946>, 2019.
- [52] T.Y. Lin, P. Goyal, R. Girshick, K. He and P. Dollar, "Focal loss for dense object detection", IEEE Trans. Pattern Anal. Mach. Intell. 42, 318–327, 2020.



Kemer Taşıyıcı Sistemli Yığma Taş Köprülerin Geometrik Özellikleri Üzerine Parametrik Çalışma

Suat Gökhan ÖZKAYA ^{1*}

¹İnşaat Teknolojileri Programı, Teknik Bilimler Meslek Yüksekokulu, Ardahan Üniversitesi, Ardahan, Türkiye.
¹suatgokhanozkaya@ardahan.edu.tr

Geliş Tarihi: 15.01.2024
Kabul Tarihi: 18.03.2024

Düzeltilme Tarihi: 12.02.2024

doi: <https://doi.org/10.62520/fujece.1419980>
Araştırma Makalesi

Alıntı: S. G. Özkaya, “Kemer taşıyıcı sistemli yığma taş köprülerin geometrik özellikleri üzerine parametrik çalışma”, Fırat Üni. Deny. ve Hes. Müh. Derg., vol. 3, no 2, pp. 95-115, Haziran 2024.

Öz

Bu araştırmada, açıklık boyutları, yükseklik ve kemer kalınlığı gibi ayırt edici özellikler göz önünde bulundurularak yığma kemerli köprülerin hesaplamalı modelleri oluşturulmaya çalışılmaktadır. Kemer genişliği modelleme süreci boyunca sabit bir parametre olarak tutulmuştur. Bu hesaplamalı temsillerin oluşturulması amacıyla sonlu elemanlar analiz yazılımı olan, ANSYS sürüm 16 kullanılmıştır. Bu köprülerin yapısal bütünlüğünü ve yük taşıma kabiliyetlerini değerlendirmek için, yükleme senaryoları hem köprünün orta bölümüne hem de kemer açıklığının dörtte birine uygulanmıştır. Bu amaçla benimsenen analitik metodoloji statik itme analizidir. Daha sonra, çalışmada kemerlerin geometrik özelliklerinin yük taşıma kapasiteleri üzerindeki etkisi derinlemesine incelenmiştir. Bu araştırmanın bulguları, tamamen yıkılmış ya da kısmen yıkılmış olan tarihi köprülerin tekrardan inşa edilebilmesine rehberlik etme ve bilgilendirme konusunda potansiyel fayda sağlamaktadır.

Anahtar kelimeler: Yığma, Kemer köprü, İtme analizi

*Yazışılan yazar

İntihal Kontrol: Evet – Turnitin

Şikayet: fujece@firat.edu.tr

Telif Hakkı ve Lisans: Dergide yayın yapan yazarlar, CC BY-NC 4.0 kapsamında lisanslanan çalışmalarının telif hakkını saklı tutar.



Parametric Study on The Geometric Properties of Masonry Stone Bridges with an Arch Carrier System

Suat Gokhan OZKAYA^{1*} 

^{1,2}Construction Technologies Program, Vocational School of Technical Sciences, Ardahan University, Türkiye.

¹suatgokhanozkaya@ardahan.edu.tr

Received: 15.01.2024

Accepted: 18.03.2024

Revision: 12.02.2024

doi: <https://doi.org/10.62520/fujece.1419980>

Research Article

Citation: Suat G. Ozkaya, "Parametric study on the geometric properties of masonry stone bridges with an arch carrier system", *Firat Univ. Jour. of Exper. and Comp. Eng.*, vol. 3, no 2, pp. 95-115, June 2024.

Abstract

In this research, computational models of masonry arch bridges were constructed, taking into account distinctive features such as span dimensions, height, and arch thickness, while the arch width was maintained as a constant parameter throughout the modeling process. The finite element analysis software, ANSYS version 16, was utilized to create these computational representations. To evaluate the structural integrity and load-carrying capabilities of these bridges, loading scenarios were applied to both the center section of the bridge and a quarter of the arch span. The analytical methodology adopted for this purpose was static thrust analysis. Subsequently, the study delved into the influence of the geometrical characteristics of the arches on their load-carrying capacity. The findings of this research hold potential utility in guiding and informing the reconstruction of historic bridges that have been completely or partially demolished.

Keywords: Masonry, Arch bridge, Pushover analysis

*Corresponding author

Plagiarism Checks: Yes – Turnitin

Complaints: fujece@firat.edu.tr

Copyright & License: Authors publishing with the journal retain the copyright to their work licensed under the CC BY-NC 4.0

1. Introduction

Built to cross natural obstacles such as rivers and valleys, arch bridges have played a vital role in various civilizations over the centuries. While some of the arch bridges, which form an integral part of transportation networks, have stood the test of time and continue to fulfill their intended functions, others have become a popular destination for visitors and can be visited with guided tours.

Today, the construction of new structures has become relatively easy, but the assessment and maintenance of existing structures pose significant challenges. The conservation and restoration of bridges, symbols of our historical heritage, requires complex calculations and assessments. For example, when assessing the mechanical properties of the constituent elements of a historic masonry structure, precise results can be obtained through experimental techniques. In contrast, non-destructive methods used to preserve the historical integrity of these structures provide imprecise material information.

Similarly, while experimental studies can provide precise information on structural behavior under varying loads, the use of finite element analysis through a number of emerging technological platforms provides preliminary insights into structural behavior. Given the inherent complexity of determining the stiffness and reliability of heterogeneous structures in a nonlinear system, finite element analysis plays an important role in facilitating and accelerating the evaluation of various load carrying scenarios.

Bridges are conventionally engineered and constructed to accommodate the anticipated service loads. The assessment of intricate vertical movements in existing arch bridges can be effectively achieved through the development of precise computational models. Among the methodologies employed for the investigation of arch bridges, finite element analysis stands out as a prominent technique. The analysis of masonry arch bridges has garnered significant attention from numerous researchers, with a comprehensive compilation of these studies presented in the accompanying Table 1 for reference.

Table 1. Literature review

A. C., Aydin, and S. G.(Özkaya, 2018) [1]	The authors of this study conducted a comprehensive investigation aimed at elucidating the structural response of single-span masonry arch bridges when subjected to specific loading conditions. This analysis was conducted utilizing the pushover analysis method, which enables the assessment of structural behavior under gradually increasing loads until failure or a predefined limit state is reached. To facilitate this analysis, finite element simulations were employed, leveraging the capabilities of the ANSYS software program.
Galasco et al. (2006) [2]	In their research, the authors employed the static pushover analysis method to meticulously monitor and record the magnitude of horizontal displacement exhibited by a masonry structure in a systematic and incremental manner. This method enables a detailed examination of the structure's response to progressively applied lateral forces, facilitating a comprehensive understanding of its behavior under such loading conditions.
S. Resemini, and S., Lagomarsino, (2007) [3]	Within their study, the authors undertook a comprehensive examination encompassing both pushover and dynamic analyses of a three-dimensional (3D) masonry bridge. The outcomes derived from the dynamic analyses served to corroborate and validate the findings obtained from the pushover analyses. This convergence of results between the two analytical methods underscores the robustness and consistency of their research outcomes.
M., Yazdani, and M. S. Marefat, (2013) [4]	In order to assess the seismic performance of a reinforced concrete bridge with an arch design, the authors employed a nonlinear static analysis method, commonly referred to as a pushover analysis. This analysis method was applied to the bridge structure, focusing on its response to lateral forces in the horizontal direction. Through this approach, the authors aimed to evaluate how the bridge would behave under seismic loading conditions, particularly emphasizing its resistance and deformation characteristics.

Table 1. Literature review (Continue)

Y. C. Loo, (1995) [5]	In their study, the authors investigated a nonlinear finite element approach suitable for the progressive collapse analysis of masonry arch bridges. Among the various material properties investigated in their case study, only the influence of the wall tensile strength σ_t and the (post-cracking) stress softening parameter N on the collapse behavior of the arch bridge was investigated.
Pelà et al. (2013) [6]	Within their research, the authors conducted a comparative assessment to gauge the efficacy of nonlinear static analysis in relation to a comprehensive suite of 84 nonlinear dynamic analyses. The examination was carried out with a particular focus on a critical node positioned at the center of mass of the bridge structure. The results of this investigation indicated that the selected node at the center of mass exhibited superior performance, highlighting its effectiveness in capturing the bridge's seismic behavior compared to the extensive set of nonlinear dynamic analyses.
Caglayan et al. (2012) [7]	In their study, the authors created a three-dimensional finite element model of the reinforced concrete bridge through the utilization of finite element analysis software. This model was meticulously calibrated by incorporating structural parameters derived from both dynamic and static tests. Subsequently, the calibrated finite element model was harnessed as a tool for conducting structural evaluations, enabling a comprehensive assessment of the bridge's behavior and performance characteristics.
Choo et al. (1990) [8]	In their research, the authors delved into an examination of the structural behavior of masonry arch bridges, employing the finite element method as their analytical approach. They further undertook a comparative analysis by juxtaposing the outcomes of their finite element simulations with empirical data obtained from experimental tests conducted on brick arch bridges. This investigative strategy allowed the authors to assess the accuracy and validity of their computational model by contrasting it with real-world experimental observations, thereby enhancing the comprehensiveness and reliability of their findings.
Çakır et al. (2015) [9]	In their study, the authors developed a new approach for determining the most suitable arch form for different loadings in the loading analysis performed with the help of finite element program.
A., Bencich, and R. Morbiducci, (2007) [10]	The authors endeavored to bridge the gap between ancient masonry arch bridges and contemporary scientific knowledge. In pursuit of this objective, they engaged in the modeling and analysis of these historical structures through the utilization of computer software. Their focus revolved around estimating the load-carrying capacities of bridges featuring diverse geometrical configurations, primarily by conducting vertical loading analyses. This approach allowed them to glean insights into the structural performance and capacity of these bridges, effectively aligning their historical significance with modern analytical methodologies.
Bayraktar et al. (2010) [11]	The authors of the study engaged in a comprehensive exploration of the dynamic properties of the masonry bridge, encompassing analytical and experimental predictions of key characteristics such as natural frequency, mode shapes, and damping ratio. To achieve this objective, they harnessed the finite element method as a computational tool. In their pursuit of accuracy, they refined their bridge models to minimize disparities between the results obtained from experimental modal analyses and their corresponding analytical counterparts. This iterative process of model improvement and validation allowed for a more precise and reliable assessment of the bridge's dynamic behavior.
S., Toker, and A.İ., Ünay, (2004) [12]	In their research, the authors endeavored to employ mathematical modeling techniques to simulate the response of an arch sample, designed to represent typical examples of arched stone bridges, when subjected to various load scenarios. Through these mathematical models, they sought to gain insights into how such bridges would behave under different types and magnitudes of loads, thereby contributing to a better understanding of their structural performance and resilience.

Table 1. Literature review (Continue)

Callaway et al. (2012) [13]	The authors of this study conducted an investigation to assess the influence of backfill on the load-bearing capacity of a masonry arch bridge. To carry out this examination, they utilized a set of 27 small-scale arch bridges in their experimental analyses. Subsequently, they compared the outcomes obtained through their experimental testing with the analysis results generated using Ring 3.0 analysis software. This comparative analysis enabled them to evaluate the correspondence between their empirical findings and the computational predictions, shedding light on the impact of backfill on the structural performance of masonry arch bridges.
T., Uçar and G., Şakar (2021) [14]	The authors present an approach to simplify the solution of arches under vertical loads and their modeling in computerized analysis programs has presented.
Boothby et al. (1998). [15]	In their study, the authors performed analyses to investigate the behavior of masonry arch bridges under truck load. Their analyses with finite element program It has been guiding in modeling masonry arch structures, determining material properties for infill and selecting stiffnesses.
Ş., Sözen M., Çavuş (2020). [16]	In their study, the authors investigated the earthquake performance of a sample bridge that has undergone geometric form changes over time using ANSYS finite element program. They performed static and time domain analysis for both the old and the new state of the bridge and investigated the stress and deformation conditions. It is concluded that the change in geometric form has a positive effect on the earthquake performance of the bridge.
A., Özmen, and E., Sayın, (2020). [17]	In their study, the authors performed linear analyses to determine the behavior of a single span masonry bridge under earthquake action. The seismic response of the bridge was evaluated by using the acceleration records of the 2011 Simav and 2002 Sultandagi earthquakes in the solid model obtained using ANSYS finite element program.
E., Yılmaz, G., Sayın, E., Sayın, A., Özmen, (2022). [18]	In their study, the authors investigated the single span Murat Bey Bridge as a numerical application. A three-dimensional finite element model was created with SAP2000 finite element program. Time-history analysis method was applied for the seismic evaluation of the bridge. Acceleration records of 1998 Adana, 2003 Bingöl, 2011 Van and 2020 Elazığ earthquakes were used in the dynamic analysis, and the displacement and stress graphs obtained as a result of the analysis were analyzed.
Zampieri et al (2020) [19]	In this study, the authors conducted a study to evaluate the vertical load capacity of single span masonry bridges. The study was carried out for the retrofitting of the bridges considered. Analyses were performed for pre-strengthening and post-strengthening.

2. Material and Method

Numerous methodologies have been developed for assessing the performance of masonry arch bridges, with the finite element method being one of the prominent approaches. This method encompasses both linear elastic and nonlinear elastic analyses. Linear elastic finite element analysis allows for the calculation of deformations within masonry arch bridges but does not provide insights into the collapse mechanism or collapse load. Consequently, it primarily serves to estimate the structural behavior of the bridge.

In contrast, nonlinear static pushover analyses are employed to determine the maximum displacement and, consequently, the collapse load of the structure. This method, as described by M.S. Marefat et al. [20], was utilized in the study to assess the behavior of masonry arch bridges under vertical loading conditions. The capacity curves generated through pushover analyses furnish valuable information regarding the maximum load-bearing capacity and associated maximum displacement from initial cracking to the point of collapse. The material properties used in the computational models were derived from existing literature, ensuring accuracy and consistency in the analytical approach.

The material properties employed in the modeling of the bridges under investigation within the context of the study have been documented and are available in Table 2 of the work authored by Barış Sevim and colleagues. [21] This table likely provides essential details regarding the mechanical characteristics and properties of the materials used in the computational models, ensuring transparency and replicability in the research methodology.

Table 2. Material properties

Materials Properties	Modulus of Elasticity (MPa)	Poisson Ratio	Mass Density (kg/m ³)	Value of Cohesion (N/mm ²)	Angle of Friction	Compressive strength (N/mm ²)	Tensile strength (N/mm ²)
Arch Stone	3000	0.25	1600	-	-	5	0.03
Spandrel Walls	2500	0.20	1400	-	-	5	1
Backfill Material	1500	0.05	1300	0.03	34°	-	-
Foundation Rock	15000	0.20	2350	-	-	5	1
Loading Plate	-	200000	0.3	-	-	-	-

In the process of creating finite element models using ANSYS software for the masonry structures, an assumption was made that the material behavior of masonry is akin to that of concrete. Consequently, the concrete material model was chosen for the ANSYS finite element models. ANSYS offers a range of material properties suitable for reinforced concrete elements, and within this framework, the Willam-Warnke (1975) [22] criterion, employing a five-parameter SOLID65 element, was integrated into the software for the analysis. For boundary conditions, it was assumed that all degrees of freedom were constrained in all directions at the base or ground level of the bridge, which is a common approach in structural analysis to represent the bridge's connection to its foundation.

The Willam-Warnke model with five parameters was used as the material model. These parameters are given in Table 3.

Table 3. Willam-Warnke failure surface parameters

Parameter	Definition
f_t	Ultimate uniaxial tensile strength
f_c	Ultimate uniaxial compressive strength
f_{cb}	Ultimate biaxial compressive strength
f_1	Ultimate compressive strength for a state of biaxial compression superimposed on hydrostatic stress state (ζh)
f_2	Ultimate compressive strength for a state of uniaxial compression superimposed on hydrostatic stress state (ζh)

The Willam-Warnke model is based on the tensile and compressive strengths of the stone to study the fracture behavior of the material. This model shows the plastic behavior of single span masonry arch bridges more realistically. However, in the analysis of structural systems such as masonry structures, where it is reasonable to assume that materials exhibit negligible tensile strength under compressive loads, the application of the Willam-Warnke model alone may be considered appropriate as it avoids problems of stress localization between material elements. Figure 1 presents a uniaxial stress-strain relationship, providing a graphical representation of the material's behavior.

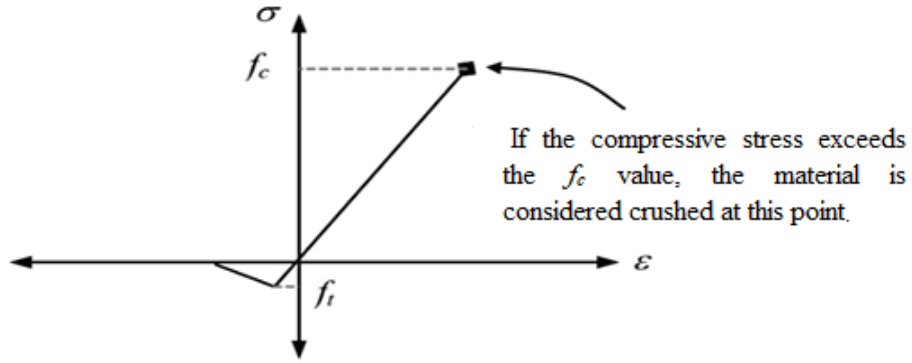


Figure 1. Willam-Warnke uniaxial stress state in ANSYS (version 16) [23]

The finite element software ANSYS (version 2016) [23] was utilized to conduct the structural analyses of the bridges.

Masonry structures exhibit variations based on construction techniques, material properties, and geometric characteristics. In this study, the width of the retaining walls (spandrel wall widths) and the width of the arches were held constant, while the arch span, arch height, and arch thickness were allowed to vary. Spandrel wall width and Arch width are the same in all models and are 0.3m and 2.6m respectively. Table 4 presents the geometrical properties of these bridges.

Table 4. Geometrical properties of the model bridges

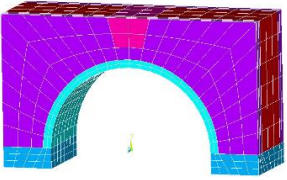
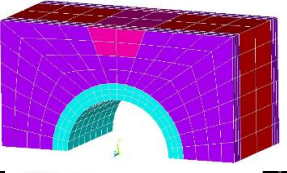
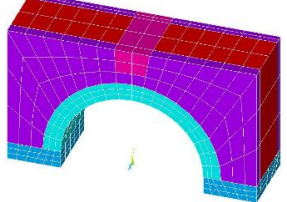
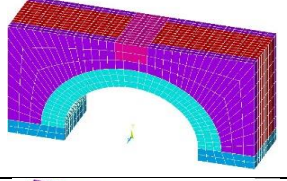
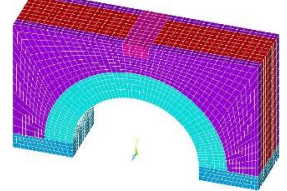
Bridge Model No	Arch radius(r)	Arch thickness(t)	Arch height(h)	Total length
Model 1a 	2m	0.2m	3.2m	4.4m
Model 1b 	2m	0.3m	3.3m	4.6m
Model 1c 	2m	0.5m	3.5m	5.0m
Model 1d 	2m	0.7m	3.7m	5.4m
Model 1e 	2m	0.9m	3.9m	5.8m

Table 4. Geometrical properties of the model bridges (Continue)

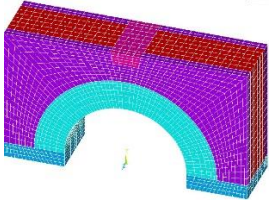
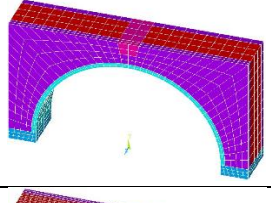
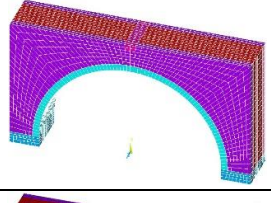
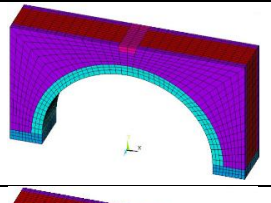
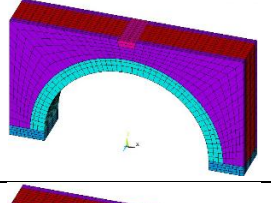
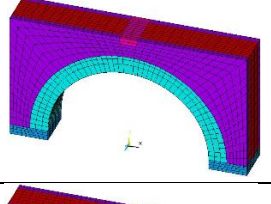
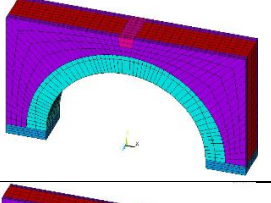
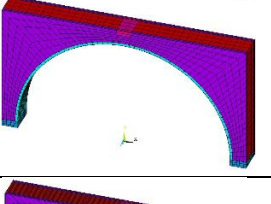
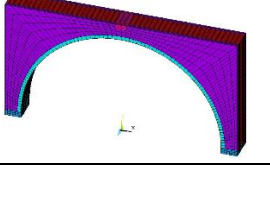
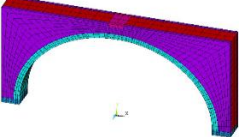
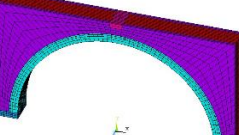
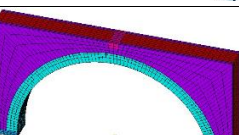
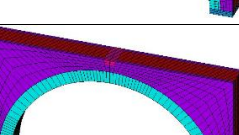
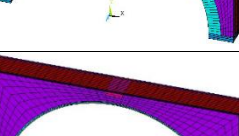
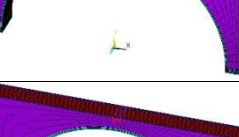

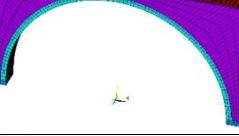
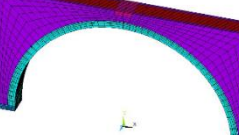
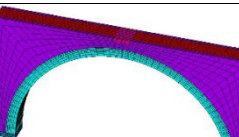
 Model 1f	2m	1.0m	4.0m	6.0m
 Model 2a	4m	0.2m	3.2m	4.4m
 Model 2b	4m	0.3m	3.3m	4.6m
 Model 2c	4m	0.5m	3.5m	5.0m
 Model 2d	4m	0.7m	3.7m	5.4m
 Model 2e	4m	0.9m	3.9m	5.8m
 Model 2f	4m	1.0m	4.0m	6.0m
 Model 3a	6m	0.2m	3.2m	4.4m
 Model 3b	6m	0.3m	3.3m	4.6m

Table 4. Geometrical properties of the model bridges (Continue)

Model 3c		6m	0.5m	3.5m	5.0m
Model 3d		6m	0.7m	3.7m	5.4m
Model 3e		6m	0.9m	3.9m	5.8m
Model 3f		6m	1.0m	4.0m	6.0m
Model 4a		8m	0.2m	3.2m	4.4m
Model 4b		8m	0.3m	3.3m	4.6m
Model 4c		8m	0.5m	3.5m	5.0m
Model 4d		8m	0.7m	3.7m	5.4m
Model 4e		8m	0.9m	3.9m	5.8m
Model 4f		8m	1.0m	4.0m	6.0m

3. Experimental Results

In accordance with findings from prior literature studies, specifically referencing the work of Cavicchi and Gambarotta [24], loading conditions were applied to two distinct locations on the arch of the bridges. A total of 24 bridge models were considered for analysis, and these loadings were implemented both at the center of the arch and at a position corresponding to one-quarter ($L/4$) of the arch span in the vertical direction. In order to calculate the vertical load capacity of the bridge, PD1, PD2 loads were applied as separate analysis cases as vertical displacement load at $L/4$ of the span length and at the midpoint of the arch, respectively. The reference displacement reading (control) point CP is shown in Figure 2.

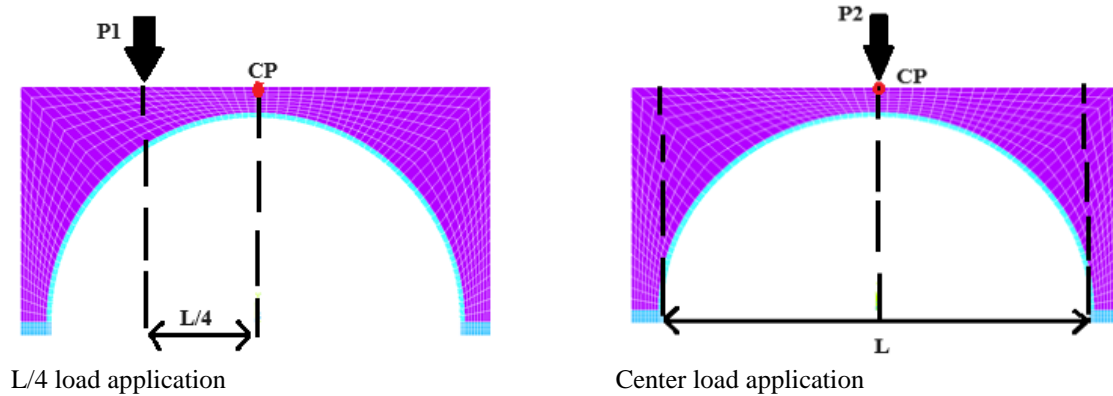


Figure 2. Finite element model and load application locations for vertical loads

The loading configurations applied at the center of the arch are visually represented in the Figures 3 below.

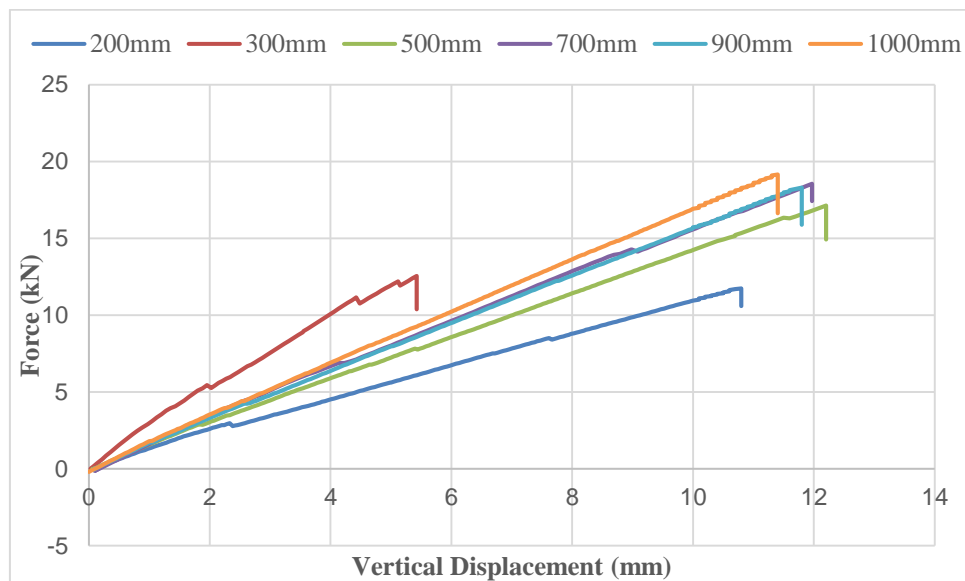


Figure 3. Loading at the center of the arch of a bridge with a radius of 2m

Based on the analyses conducted by applying vertical loads to the midsection of the arches, each with a radius of 2 meters and varying arch thicknesses ranging from 0.2 meters to 1.0 meter, several key findings were obtained:

Maximum Displacement: The largest vertical displacement observed in these analyses was 12.2 millimeters, and it occurred in the bridge with an arch thickness of 500 millimeters.

Maximum Load-Carrying Capacity: The bridge with an arch thickness of 1.0 meters demonstrated the highest total load-carrying capacity, reaching 19.15 kN.

Loading Method: The loads were applied by defining a steel plate in the area where the load was intended. These loads were applied in the form of displacement loads in the vertical direction.

Effect of Arch Thickness: Generally, it was observed that both the total displacement and the total load-carrying capacity increased as the arch thickness increased. This suggests that thicker arches exhibited greater stiffness and load-carrying capacity.

Crack Initiation and Progression: The initiation and progression of cracks were primarily observed in the region where the loading was applied, ultimately leading to the collapse of the bridge.

These findings underscore the importance of arch thickness in determining the structural behavior and load-carrying capacity of masonry arch bridges. Thicker arches tend to offer greater resistance to vertical loads, but eventual cracking and collapse may still occur under excessive loading conditions. The deformation of the bridge models in the 2m radius bridge models in the loading cases applied at the midpoint of the arch span is given in the Figure 4.

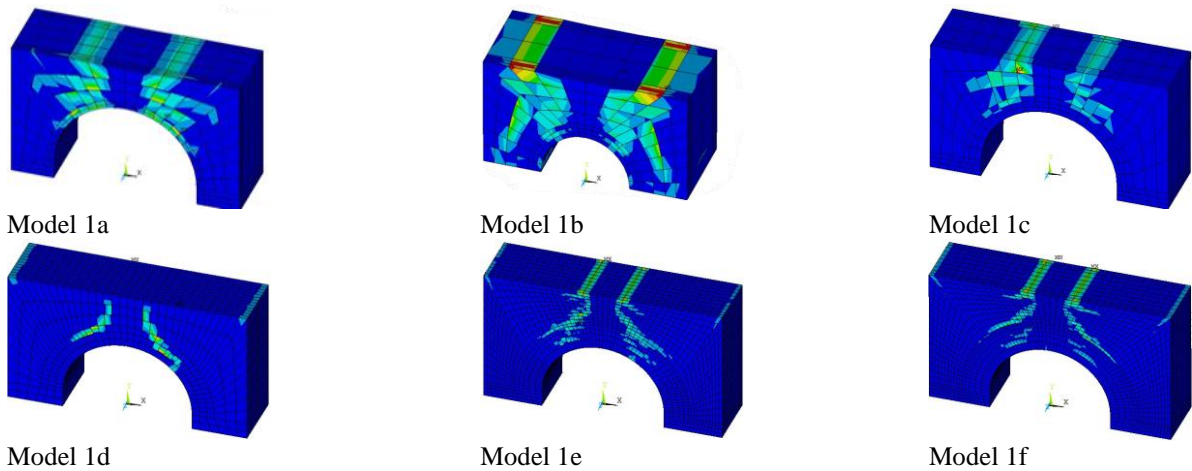


Figure 4. The deformation of the bridge models for midpoint loading case

In the study involving bridges with a larger radius of 4 meters (Figure 5), several notable findings were observed:

Maximum Displacement and Load Capacity: Among the bridges analyzed, the one with an arch thickness of 900 millimeters exhibited the largest displacement, measuring 20.13 millimeters. Additionally, this same bridge displayed the highest load-carrying capacity, with a value of 139.44 kN.

Crack Initiation and Propagation: Similar to the previous analysis, it was observed that crack initiation and propagation predominantly occurred in the region where the load was applied. This behavior is consistent with the earlier findings.

Comparative Displacements: Interestingly, the vertical displacements of the bridges with arch thicknesses 700 mm and 900 mm were nearly identical to each other. This suggests that the arch thickness within this range did not significantly affect the resulting displacements.

Impact of 1-Meter Arch Thickness: However, when the arch thickness increased to 1 meter, both the displacement and load-carrying capacity decreased. This indicates that a 1-meter arch thickness led to reduced structural performance compared to the 0.9-meter arch.

These findings underline the complexity of the relationship between arch thickness and bridge behavior. While thicker arches generally provide higher load capacity, there can be a point beyond which increasing thickness may lead to diminished performance. The specific behavior appears to be influenced by the interplay of multiple factors and structural characteristics.

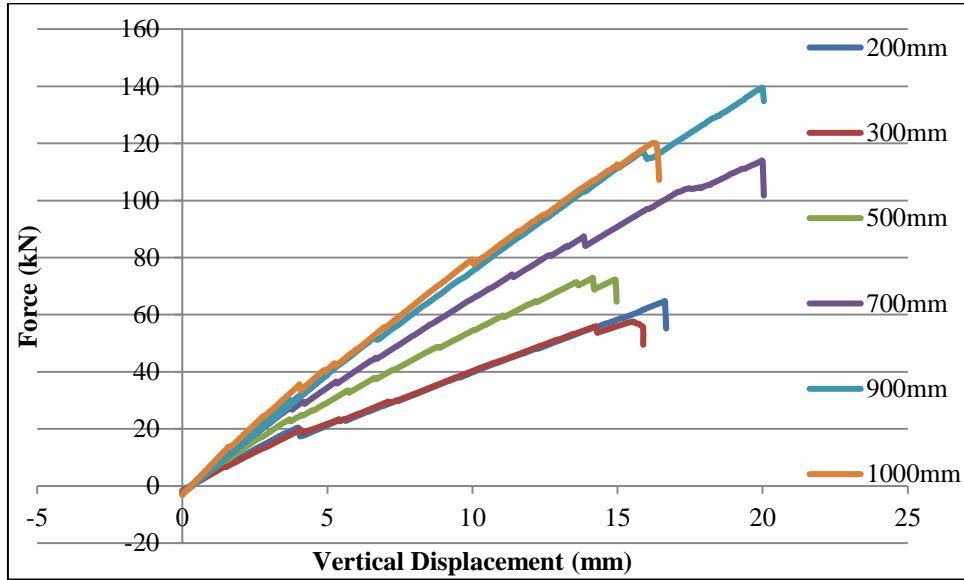


Figure 5. Loading at the center of the arch of a bridge with a radius of 4m

The deformation of the bridge models in the 4m radius bridge models in the loading cases applied at the midpoint of the arch span is given in the Figure 6.

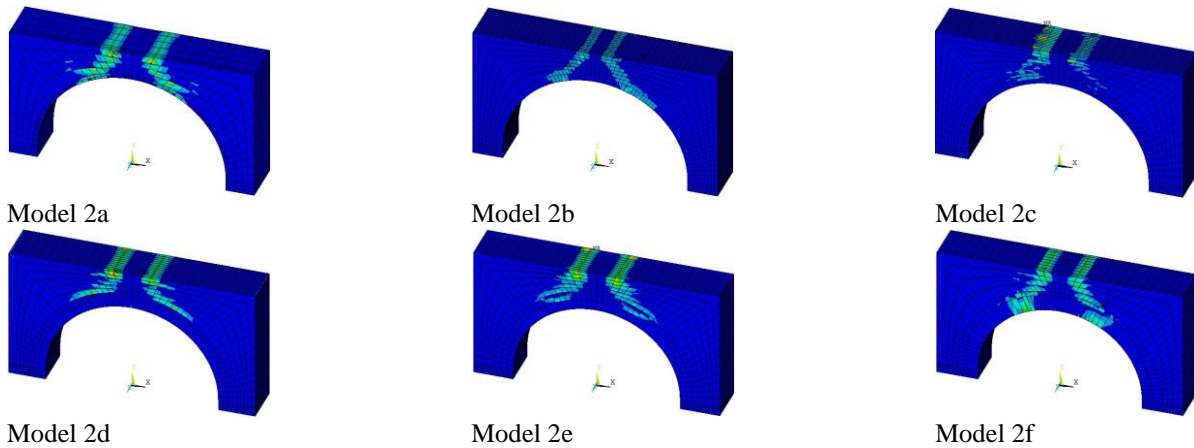


Figure 6. The deformation of the bridge models for midpoint loading case

In the study involving bridges with a larger radius of 6 meters (Figure 7), the following key observations were made:

Maximum Displacement and Load Capacity: Among the bridges analyzed, the one with an arch thickness of 500 millimeters exhibited the largest vertical displacement, measuring 35.23 millimeters. Additionally, this same bridge displayed the highest load-carrying capacity, with a value of 74.94 kN.

Crack Progression: It was noted that the crack propagation was consistent across all bridges, regardless of the specific arch thicknesses. The tensile stresses under vertical displacement load reached the permissible masonry tensile strength, especially in the upper sides of the arch, posing a risk for damage.

Collapse: Ultimately, all the bridges in this study experienced collapse, which was expected given the observed crack progression. The structural behavior reached a point where the bridges could no longer support the applied loads, leading to their collapse.

These findings emphasize that, in the context of bridges with a larger radius of 6 meters, arch thickness significantly influenced both displacement and load-carrying capacity. Thinner arches 500 mm exhibited higher load capacity but also experienced larger displacements before reaching the point of collapse. Additionally, it is noteworthy that the crack progression behavior remained consistent across all bridges, contributing to their eventual failure.

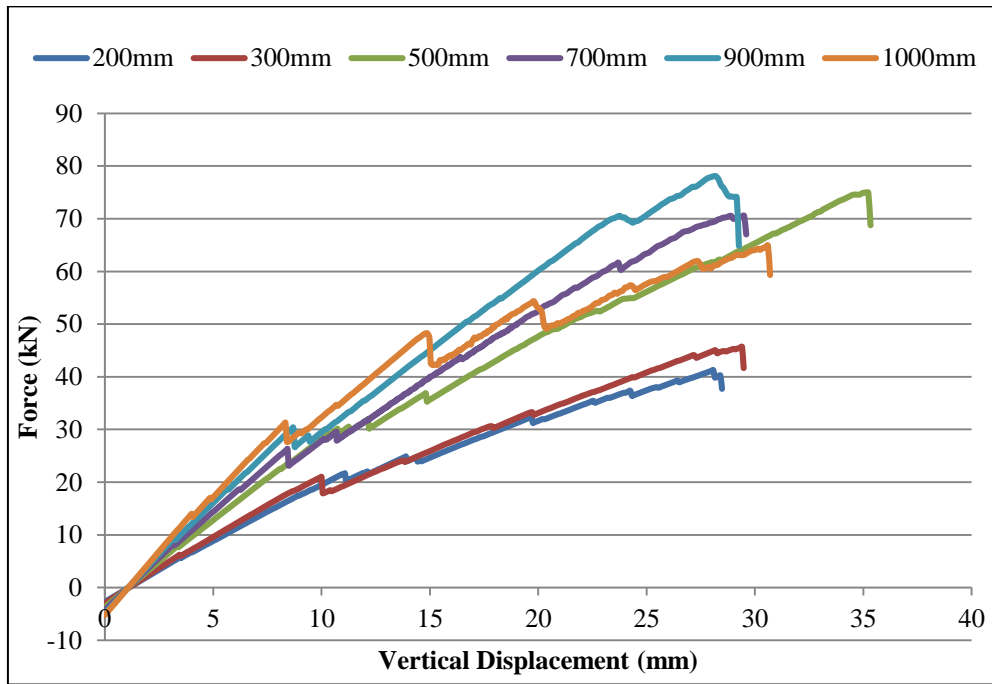


Figure 7. Loading at the center of the arch of a bridge with a radius of 6m

The deformation of the bridge models in the 6m radius bridge models in the loading cases applied at the midpoint of the arch span is given in the Figure 8.

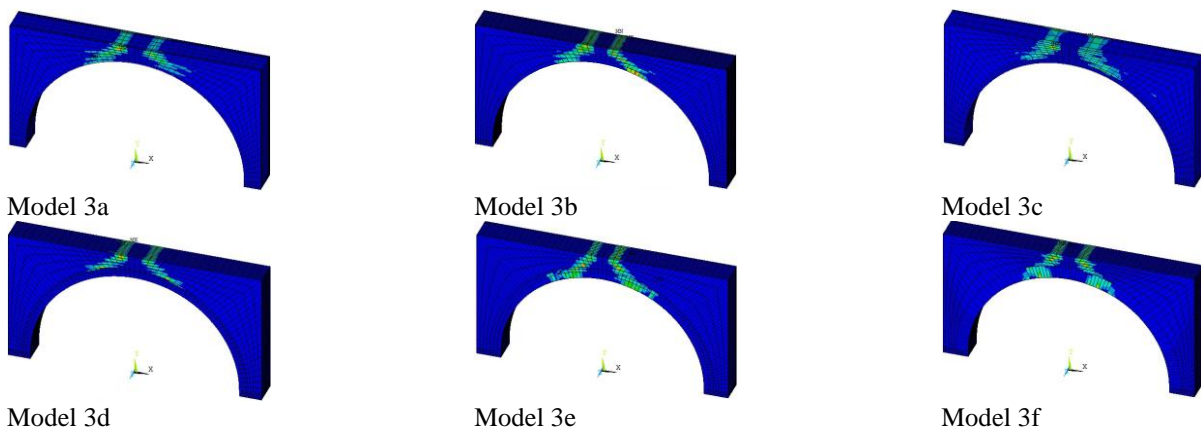


Figure 8. The deformation of the bridge models for midpoint loading case

In the study of bridges with a larger radius of 8 meters (Figure 9), several key findings were identified:

Maximum Displacement: The bridge with an arch thickness of 200 millimeters exhibited the largest vertical displacement, measuring 45.93 millimeters. This bridge had the highest displacement among the bridges analyzed in this study.

Maximum Load-Carrying Capacity: The bridge with an arch thickness of 900 millimeters demonstrated the highest load-carrying capacity, with a value of 89.36 kN. This bridge exhibited the greatest load-bearing capability among the bridges considered.

Consistent Crack Progression: Similar to previous observations, the progression of cracks was consistent across all bridges, irrespective of their specific arch thicknesses. Tensile stresses under vertical displacement load reached the permissible masonry tensile strength, especially in the upper sides of the arches, posing a risk for damage.

Failure Mechanism: In the vertical loading analyses, the failure mechanism was generally consistent across the bridges. This suggests that the load-induced structural failure had similar characteristics across different bridges.

Effect of Arch Radius and Height: It was noted that as the arch radius and arch height increased, both displacement and load-carrying capacity also increased. This trend indicates that larger arch dimensions resulted in greater structural performance and capacity to withstand vertical loads.

These findings highlight the influence of arch thickness, radius, and height on the structural behavior of masonry arch bridges. Thicker arches and larger arch dimensions generally contributed to higher load capacity and reduced displacement before reaching the point of collapse. The deformation of the bridge models in the 8m radius bridge models in the loading cases applied at the midpoint of the arch span is given in the Figure 10.

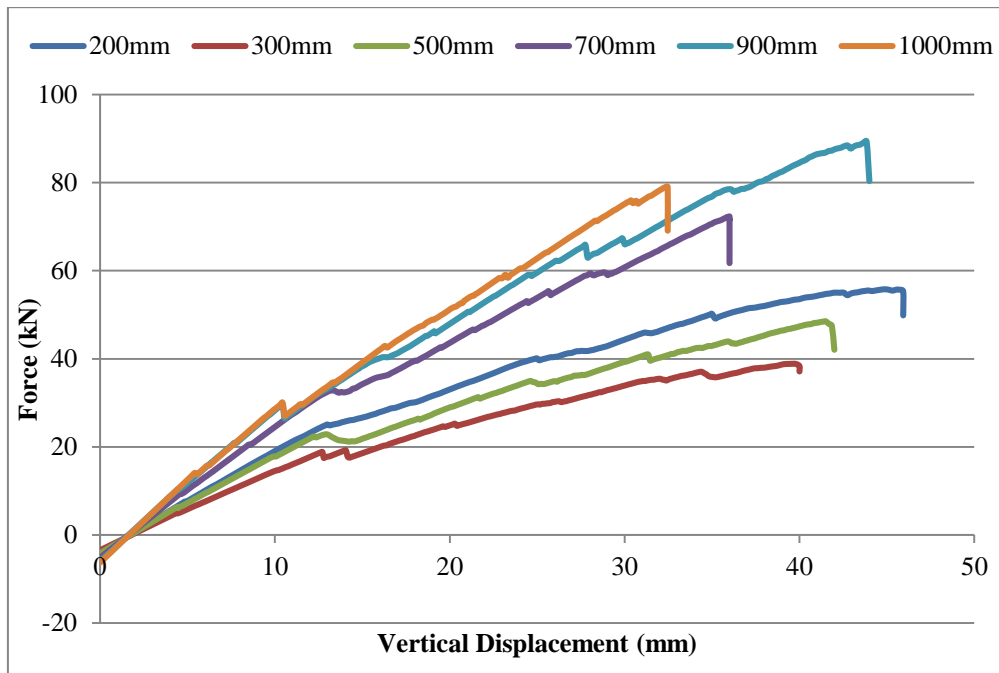


Figure 9. Loading at the center of the arch of a bridge with a radius of 8m

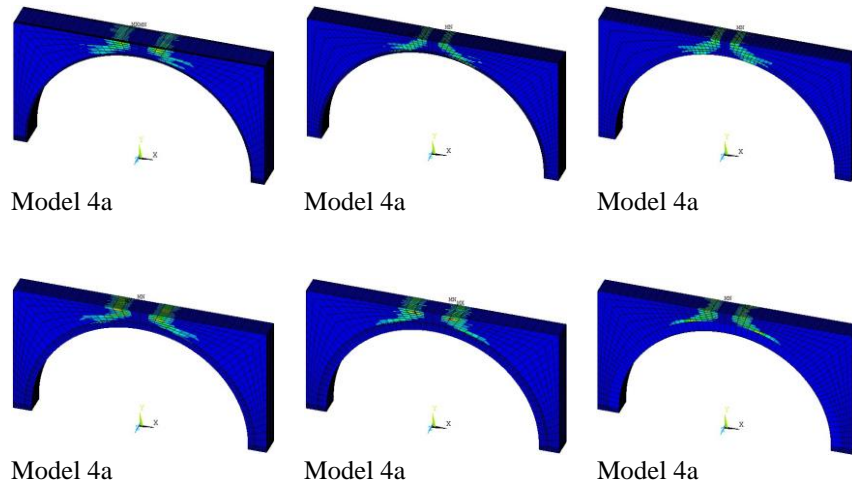


Figure 10. The deformation of the bridge models for midpoint loading case

In the study involving a bridge with an arch radius of 2 meters (Figure 11), the bridge with an arch thickness of 500 millimeters exhibited the following notable characteristics when subjected to loading at the L/4 part of the arch span:

Maximum Displacement: The bridge with an arch thickness of 500 millimeters demonstrated the largest vertical displacement, measuring 13.67 millimeters. This displacement value represents the greatest deflection observed among the bridges analyzed in this specific loading condition.

Maximum Load-Carrying Capacity: Additionally, the same bridge with an arch thickness of 500 millimeters exhibited the highest load-carrying capacity, with a value of 15.98 kN. This bridge demonstrated the greatest load-bearing capability among the considered bridges when loaded at the L/4 span point.

These findings emphasize the significance of arch thickness in determining the structural behavior and load-carrying capacity of masonry arch bridges, particularly under loading conditions applied at the L/4 part of the arch span. Thicker arches tend to provide greater stiffness and load capacity, resulting in reduced displacement and higher load-bearing capability.

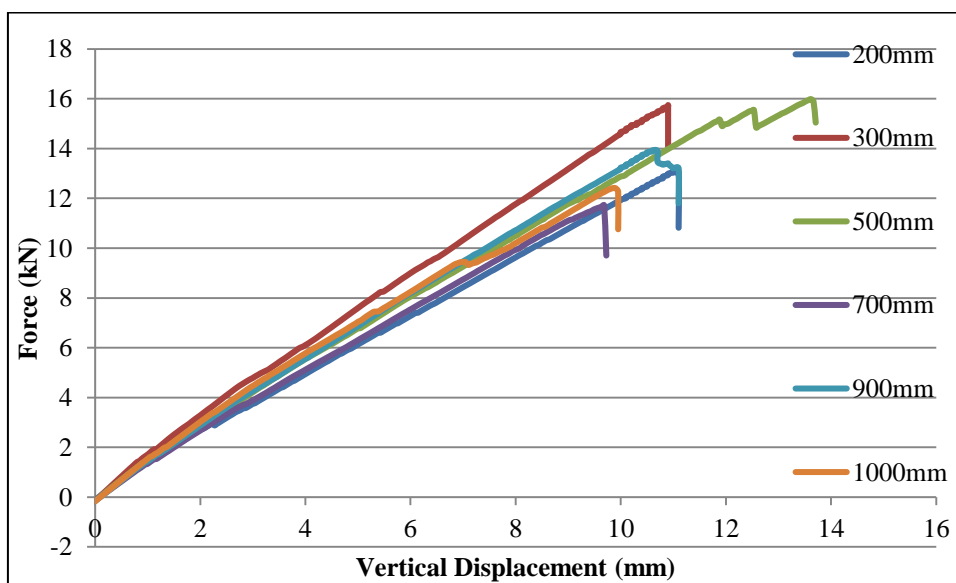


Figure 11. Loading condition of the arch L/4 span of the bridge with radius 2m

The deformations and stresses in the bridge models for L/4 span loading cases in 2m radius bridge models are given in the Figure 12.

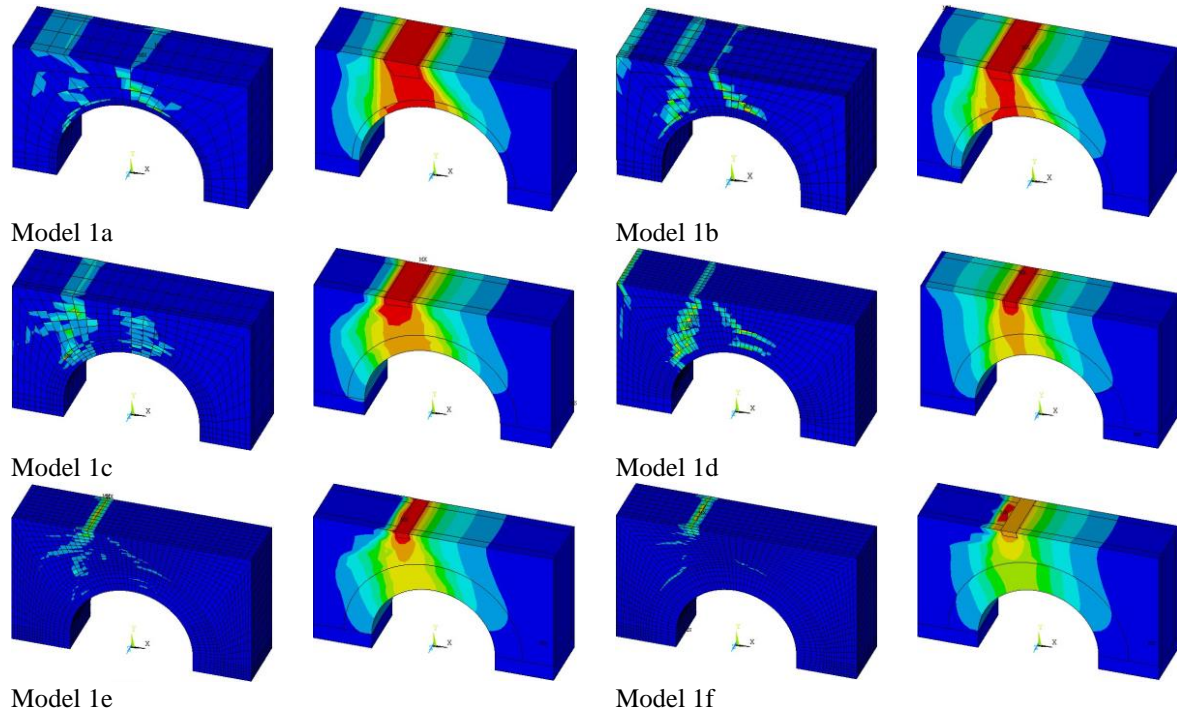


Figure 12. The deformations and stresses in the bridge models for L/4 span loading cases

In the study involving a bridge with an arch radius of 4 meters (Figure 13), the bridge with an arch thickness of 200 millimeters exhibited the following noteworthy characteristics when subjected to loading at the L/4 part of the arch span:

Maximum Displacement: The bridge with an arch thickness of 200 millimeters demonstrated the largest vertical displacement, measuring 16.12 millimeters. This displacement value represents the greatest deflection observed among the bridges analyzed in this specific loading condition.

Maximum Load-Carrying Capacity: Additionally, the same bridge with an arch thickness of 200 millimeters exhibited the highest load-carrying capacity, with a value of 106.22 kN. This bridge demonstrated the greatest load-bearing capability among the considered bridges when loaded at the L/4 span point.

These findings underscore the influence of arch thickness on the structural behavior and load-carrying capacity of masonry arch bridges, particularly under loading conditions applied at the L/4 part of the arch span. Thicker arches tend to offer enhanced stiffness and load capacity, resulting in reduced displacement and increased load-bearing capability.

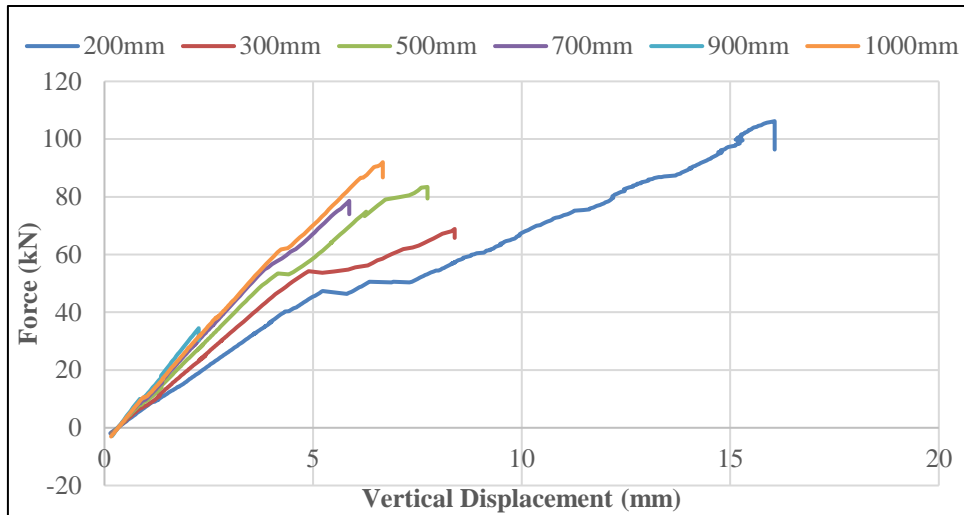


Figure 13. Loading condition of the arch L/4 span of the bridge with a radius of 4m

The deformations and stresses in the bridge models for L/4 span loading cases in 4m radius bridge models are given in the Figure 14.

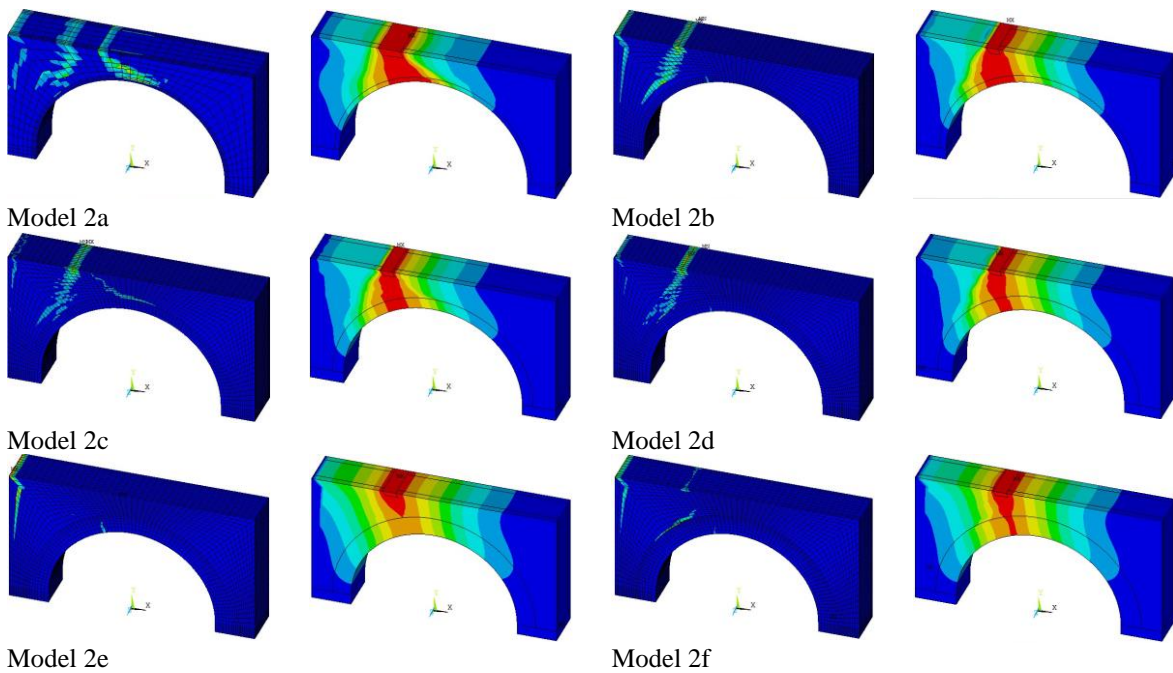


Figure 14. The deformations and stresses in the bridge models for L/4 span loading cases

In the study involving a bridge with an arch radius of 6 meters (Figure 15), several notable findings were identified for different arch thicknesses:

Maximum Displacement for 30 mm Thickness: Among the bridges analyzed, the one with an arch thickness of 30 millimeters exhibited the largest vertical displacement, measuring 11.72 millimeters. This bridge had the highest displacement among the bridges considered.

Maximum Load-Carrying Capacity for 700 mm Thickness: The bridge with an arch thickness of 700 millimeters demonstrated the highest load-carrying capacity, with a value of 94.84 kN. This bridge exhibited the greatest load-bearing capability among the analyzed bridges.

Collapse Mechanism Consistency: In general, the collapse mechanism was observed to be similar across the various bridges, indicating that the behavior leading to collapse was consistent in principle.

Crack Propagation Variation for 300 mm Thickness: Interestingly, it was noted that in the case where the arch thickness was 300 millimeters (0.3 meters), the progression of cracks differed from the other bridges. Instead of progressing uniformly, the crack propagation in this case moved toward the middle section of the arch.

These findings highlight the impact of arch thickness on the structural behavior and load-carrying capacity of masonry arch bridges with a 6-meter radius. Thicker arches tend to offer enhanced load capacity, while variations in crack propagation patterns can occur depending on the specific arch thickness. Tensile stresses have reached the permissible masonry tensile strength and pose a risk for damage.

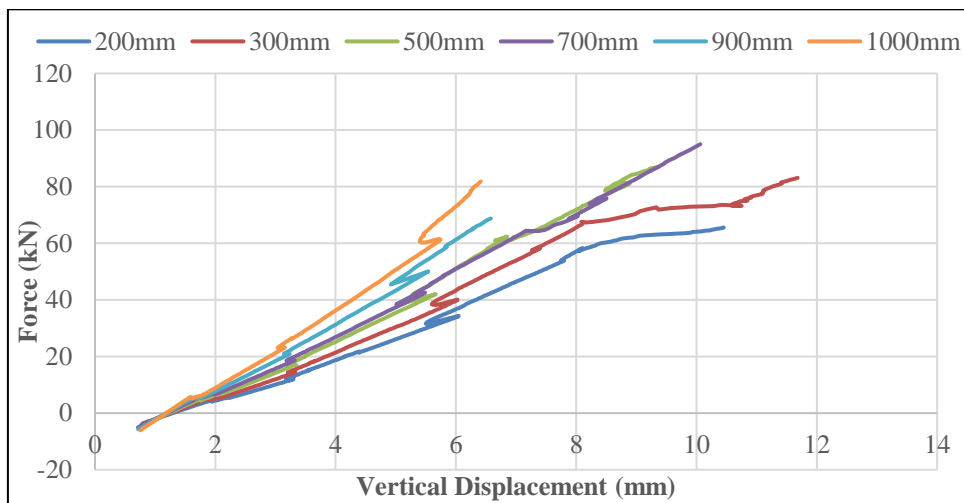


Figure 15. Loading condition of the arch L/4 span of the bridge with a radius of 6m

The deformations and stresses in the bridge models for L/4 span loading cases in 6m radius bridge models are given in the Figure 16.

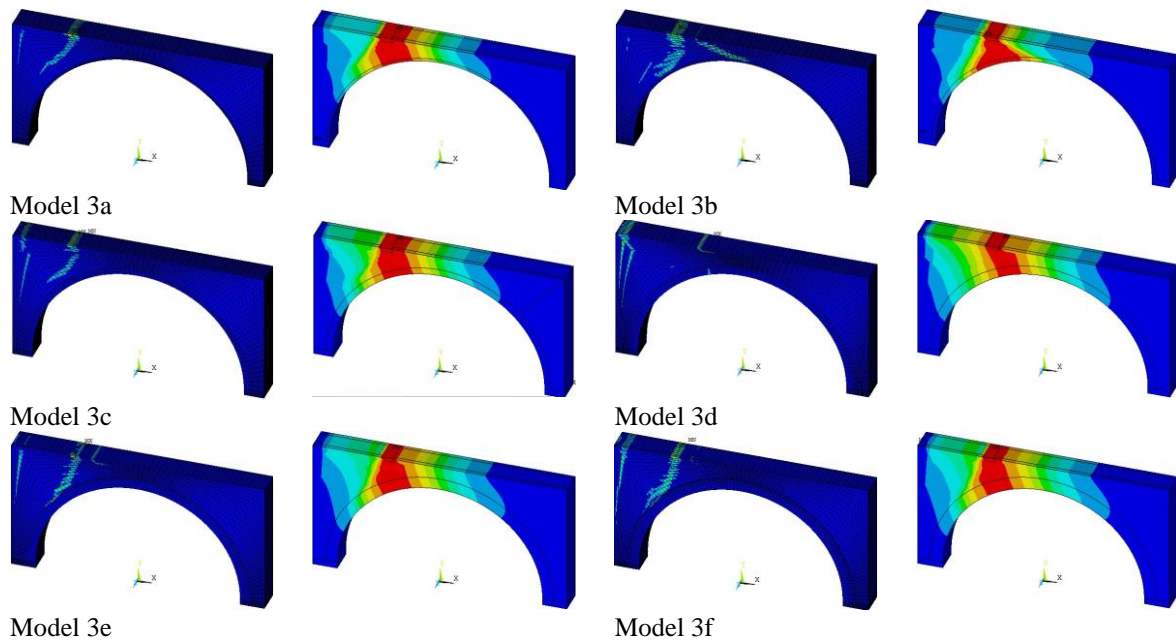


Figure 16. The deformations and stresses in the bridge models for L/4 span loading cases

In the study involving a bridge with an arch radius of 4 meters (Figure 17), the bridge with an arch thickness of 900 millimeters exhibited the following notable characteristics when subjected to loading at the L/4 part of the arch span:

Maximum Displacement: The bridge with an arch thickness of 900 millimeters displayed the largest vertical displacement, measuring 24.12 millimeters. This displacement value represents the greatest deflection observed among the bridges analyzed in this specific loading condition.

Maximum Load-Carrying Capacity: Additionally, the same bridge with an arch thickness of 900 millimeters exhibited the highest load-carrying capacity, with a value of 15.87 kN. This bridge demonstrated the greatest load-bearing capability among the considered bridges when loaded at the L/4 span point.

These findings underscore the significance of arch thickness and geometry, specifically the arch radius and height, in determining the structural behavior and load-carrying capacity of masonry arch bridges. It's observed that, in general, as the arch span and height increase, both displacement and load-carrying capacity tend to increase as well, indicating that larger arch dimensions contribute to improved structural performance. Additionally, it was noted that crack propagation patterns remained consistent among bridges with an 8-meter radius, suggesting similarities in the behavior of these bridges under the applied loads. The tensile stresses in the arch with 300mm arch stone thickness exceed the allowable masonry tensile strength and pose a risk for damage.

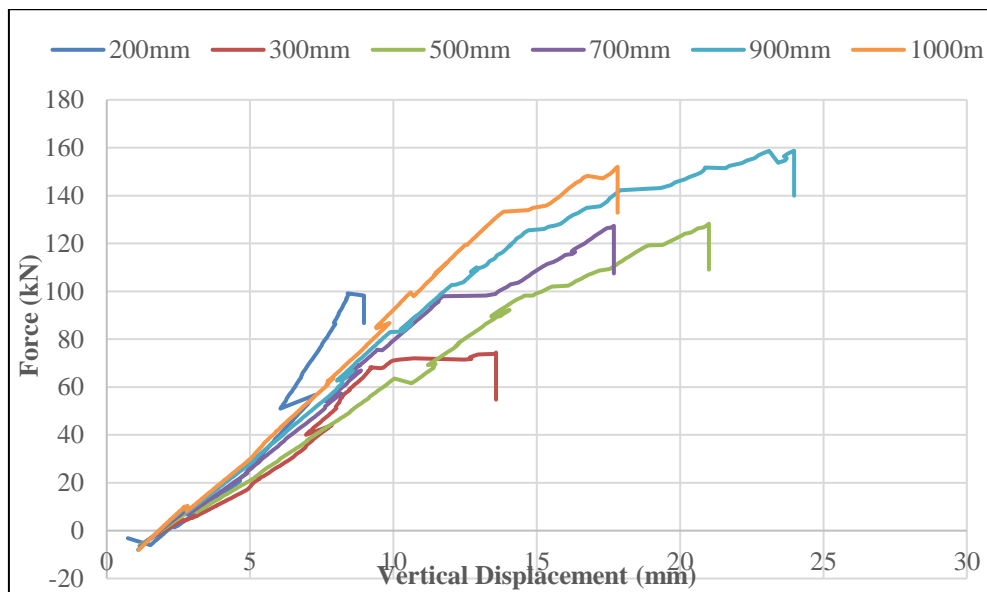


Figure 17. Loading condition of the arch L/4 span of the bridge with a radius of 8 m

The deformations and stresses in the bridge models for L/4 span loading cases in 8m radius bridge models are given in the Figure 18.

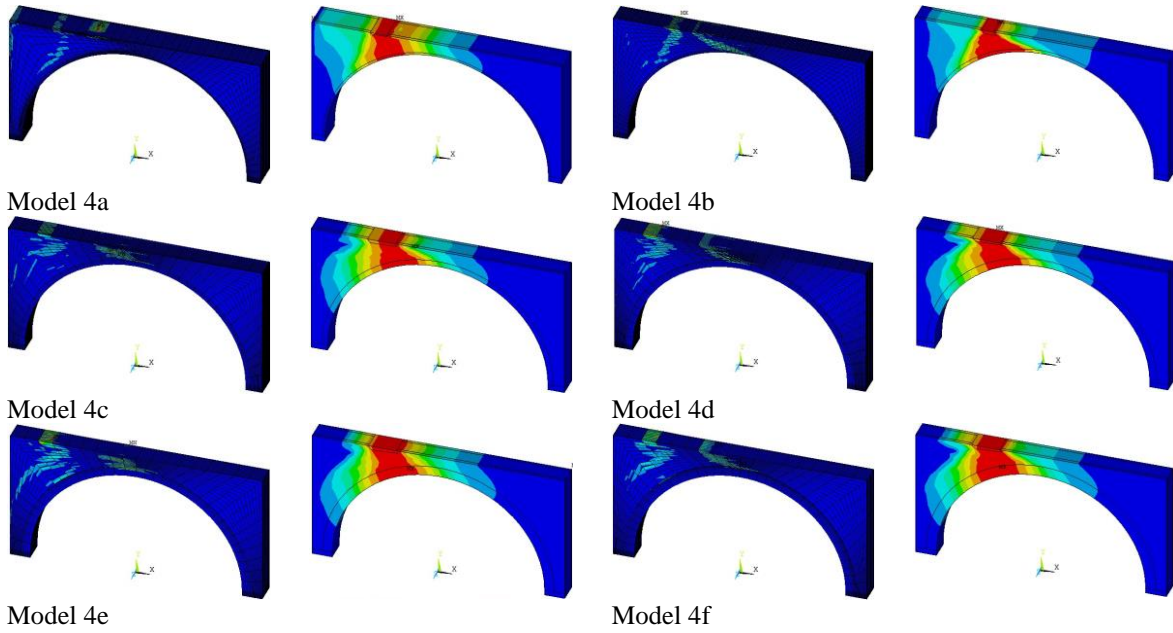


Figure 18. The deformations and stresses in the bridge models for $L/4$ span loading cases

4. Conclusions

The study carried out to evaluate the total load carrying capacity of bridges reveals a consistent trend where the increase in arch span and height corresponds to higher values for both displacement and load carrying capacity. This is true for both loading conditions considered in the study. In the analysis for both loading cases, it was determined that the most ideal bridge model has a radius of 8 m and an arch thickness of 900 mm.

These findings underline the importance of arch span and height as critical factors affecting the structural behavior of bridges using arch support systems. The observed relationship between these parameters and the load carrying capacity and displacement of the bridge provides valuable insights into the behavior of such historic arch bridges.

This study may be useful in providing preliminary information for the reconstruction of historical arch bridges that existed in the past but were destroyed by natural disasters over time and whose construction materials have survived to the present day.

5. Author Contribution Statement

In the study carried out, Author 1 contributed to the formation of the idea, making the design and literature review, evaluating the results obtained, obtaining the materials used and examining the results, spelling and checking the article in terms of content.

6. Ethics Committee Approval and Conflict of Interest

“There is no conflict of interest with any person/institution in the prepared article”

7. References

- [1] A. C. Aydin, and S. G. Özkaya, “The finite element analysis of collapse loads of single-spanned historic masonry arch bridges (Ordu, Sarpdere Bridge)”, *Eng. Fail. Analy.*, 84, 131-138, 2018.

- [2] A. Galasco, S. Lagomarsino, and A. Penna, “On the use of pushover analysis for existing masonry buildings”, In First European Conference on Earthquake Engineering and Seismology, 9, 1-10, 2006.
- [3] S. Resemini and S. Lagomarsino, “Displacement-based methods for the seismic assessment of masonry arch bridges”, 5th International Conference on Arch Bridges, 7, 441-450, 2007.
- [4] M. Yazdani, and M. S. Marefat, “Seismic assessment of six-meter spans plain concrete arch bridge”, Journ.of Seism. and Earthq. Eng., 15(1), 81-90, 2013.
- [5] Y. C. Loo, “Collapse load analysis of masonry arch bridges. In Arch bridges: proceedings of the first international conference on arch bridges held at bolton”, UK on 3–6, 167-174, Thomas Telford Publishing, 1995.
- [6] L. Pelà, A. Aprile, and A. Benedetti, “Comparison of seismic assessment procedures for masonry arch bridges”, Cons. and Buil. Mat., 38, 381-394, 2013.
- [7] B. O. Caglayan, K. Ozakgul, and O. Tezer, “Assessment of a concrete arch bridge using static and dynamic load tests” Struc.l Eng. and Mech., 41, 1, 83-94, 2012.
- [8] B. S. Choo, M. G. Coutie, and N. G. Gong, “The application of the finite element method to the study of cracking in masonry arch bridges”, Paper Presented at The International Conference on Applied Stress Analysis, Nottingham, UK, 1990.
- [9] F. Çakir, F. M. ÖzkaL, and H. Uysal, “Sonlu elemanlar yöntemi ile farklı yükleme durumları altındaki yığma kemerlerin yapısal başarımlarının incelenmesi”, 5. Tarihi Eserlerin Güçlendirilmesi ve Geleceğe Güvenle Devredilmesi Sempozyumu, 215-226, Erzurum, Turkey, 2015.
- [10] A. Brencich, and R. Morbiducci, “Masonry arches: historical rules and modern mechanics”, International Jour. of Archit. Herit., 1, 165–189, 2007.
- [11] A. Bayraktar, A.C. Altunisik, F. Birinci, B. Sevim and T. Turker, “Finite-element analysis and vibration testing of a two-span masonry arch bridge”, Jour. of Per Form.eo Const.Facil., 24, 1, 46-52, 2010.
- [12] S. Toker, and A.İ. Ünay, “Mathematical modeling and finite element analysis of masonry arch bridges”, Gazi Univ. Jour. of Sci., 17, 2, 129-139, 2004.
- [13] P. Callaway, M. Gilbert and C. C. Smith, “Influence of backfill on the capacity of masonry arch bridges”, Proceedings of The Institution of Civil Engineers: Bridge Engineering, 165, 147–158, 2012.
- [14] T. Uçar, G. Şakar, “Kemerlerin statik analizi için basitleştirilmiş bir yaklaşım”, Dumlupınar Üniver.Fen Bil. Enstit. Derg., 24, 37, 2011.
- [15] T. E. Boothby, D. E. Domalik, and V. A. Dalal, “Service load response of masonry arch bridges”, Jour.of Struc.Eng., 124, 1, 17-23, 1998.
- [16] Ş. Sözen, M. Çavuş, “Tek açıklıklı tarihi taş köprülerde form değişikliğinin köprünün sismik davranışına etkisinin değerlendirilmesi: niksar yılanlı (leylekli) köprü örneği”, Düzce Üniver. Bil. ve Tekn. Derg., 8, 1, 48-59, 2020.
- [17] A. Özmen, and E. Sayın, “Tarihi yığma bir köprünün deprem davranışının değerlendirilmesi”, Niğde Ömer Halisdemir Üniver. Müh. Bil. Derg., 9, 2, 956-965, 2020.
- [18] E. Yılmaz, G. Sayın, E. Sayın, A. Özmen, “Tarihi yığma köprülerin farklı depremler altında dinamik analizi: murat bey köprüsü örneği”, Turkish Jour. of Sci. and Tech., 2022.
- [19] P. Zampieri, N. Simoncello, J. Gonzalez-Libreros and C. Pellegrino, “Evaluation of the vertical load capacity of masonry arch bridges strengthened with FRCM or SFRM by limit analysis”, Eng. Struc, 225, 111135, 2020.
- [20] M.S. Marefat, M. Yazdani, and M. Jafari, “Seismic assessment of small to medium spans plain concrete arch bridges”, Europ. Jour. of Envir. and Civil Eng., 23, 7, 894-915, 2017.
- [21] B. Sevim, A. Bayraktar, A. C. Altunişik, S. Atamtürktür, and F. Birinci, “Finite element model calibration effects on the earthquake response of masonry arch bridges”, Fin. Elem. in Analy. and Des., 47, 7, 621–634, 2011.
- [22] K. Willam, E. Warnke, “Constitutive model for the triaxial behavior of concrete”, Inter. Assoc. for Brid., 1-30, 1975.
- [23] ANSYS Swanson Analysis System, USA, 2016.
- [24] A. Cavicchi and L. Gambarotta, “Collapse analysis of masonry bridges taking into account arch–fill interaction”, Eng. Struc., 27, 4, 605-615, 2005.



Derin Öğrenme ve Özellik Seçimi Yaklaşımları Kullanılarak Twitter Verilerinden COVID-19 Aşı Karşıtlığı Tespiti

Serdar ERTEM¹ , Erdal ÖZBAY^{2*} 

^{1,2}Bilgisayar Mühendisliği Bölümü, Mühendislik Fakültesi, Fırat Üniversitesi, Elazığ, Türkiye.

¹serdarertem01@gmail.com, ²erdalozbay@firat.edu.tr

Geliş Tarihi: 27.02.2024
Kabul Tarihi: 29.03.2024

Düzeltilme Tarihi: 19.03.2024

doi: <https://doi.org/10.62520/fujece.1443753>
Araştırma Makalesi

Alıntı: S. Ertem ve E. Özbay, “Derin öğrenme ve özellik seçimi yaklaşımları kullanılarak twitter verilerinden covid-19 aşı karşıtlığı tespiti”, Fırat Üni. Deny. ve Hes. Müh. Derg., vol. 3, no 2, pp. 116-133, Haziran 2024.

Öz

COVID-19 pandemisi, dünya genelinde sağlık, ekonomi ve toplumsal yaşamı derinden etkileyen bir krize dönüşmüştür. Bu kriz sırasında aşı karşıtlığı, salgının kontrolü ve aşılama kampanyalarının etkinliği açısından önemli bir engel oluşturmaktadır. Bu çalışmada, derin öğrenme ve özellik seçimi yaklaşımlarının birleşimi kullanılarak COVID-19 aşı karşıtlığının twitter verilerinden tespiti amaçlanmıştır. Önerilen yöntem, derin öğrenme modeli ile özellik seçimi tekniklerinin entegrasyonunu içermekte ve metin verilerindeki önemli özellikleri belirleyerek aşı karşıtlığını tanımlamaktadır. Özellik çıkarımı için TF-IDF ve N-gram yöntemleri hibrit kullanılmış, ardından Ki-kare özellik seçimi gerçekleştirilmiştir. Veri seti twitter text verilerinden ve iki etiketten oluşmaktadır. Etiketlerin dengelenmesi için Sentetik Azınlık Aşırı Örneklemleme Tekniği (SAAÖT) yöntemi uygulanmıştır. Sınıflandırma işlemi için derin öğrenme mimarilerinden Uzun Kısa-Sürelili Bellek (UKSB) kullanılmıştır. Önerilen özellik çıkarımı, özellik seçimi ve UKSB yöntemlerinin birlikte kullanılmasıyla elde edilen deneysel sonuçlara göre %99.23 ile en yüksek doğruluk değerine ulaşılmıştır. Bu sonuçlar, COVID-19 aşı karşıtlığının metin verileri üzerinde etkili bir şekilde tespit edilmesi için önerilen yöntemlerin başarılı bir şekilde kullanılabileceğini göstermektedir. Çalışmanın sonuçları, sağlık politikalarının ve kamuoyu bilgilendirme stratejilerinin geliştirilmesine yönelik değerli bilgiler sunabilmektedir. Bu bakımdan, aşılama kampanyaları ve halk sağlığı müdahaleleri planlanırken, aşı karşıtlığı belirlemede yeni ve güçlü bir araç geliştirilmiştir.

Anahtar kelimeler: COVID-19 aşı-karşıtlığı, Derin öğrenme, Özellik seçimi, UKSB, Metin sınıflandırma

*Yazışılan yazar

İntihal Kontrol: Evet – Turnitin
Şikayet: fujece@firat.edu.tr

Telif Hakkı ve Lisans: Dergide yayın yapan yazarlar, CC BY-NC 4.0 kapsamında lisanslanan çalışmalarının telif hakkını saklı tutar.



Detection of COVID-19 Anti-Vaccination from Twitter Data Using Deep Learning and Feature Selection Approaches

Serdar ERTEM¹ , Erdal ÖZBAY^{2*} 

^{1,2}Computer Engineering Department, Faculty of Engineering, Firat University, 23119, Elazig, Türkiye.

¹serdarterem01@gmail.com, ²erdalozbay@firat.edu.tr

Received: 27.02.2024
Accepted: 29.03.2024

Revision:19.03.2024

doi: <https://doi.org/10.62520/fujece.1443753>
Research Article

Citation: S. Ertem and E. Özbay, "Detection of covid-19 anti-vaccination from twitter data using deep learning and feature selection approaches", Firat Univ. Jour.of Exper. and Comp. Eng., vol. 3, no 2, pp. 116-133, June 2024.

Abstract

The COVID-19 pandemic has evolved into a crisis significantly impacting health, the economy, and social life worldwide. During this crisis, anti-vaccination sentiment poses a considerable obstacle to controlling the epidemic and the effectiveness of vaccination campaigns. This study aimed to detect COVID-19 anti-vaccination sentiment from Twitter data using a combination of deep learning and feature selection approaches. The proposed method integrates a deep learning model with feature selection techniques to identify anti-vaccination sentiment by pinpointing important features in text data. Hybrid TF-IDF and N-gram methods were utilized for feature extraction, followed by Chi-square feature selection. The dataset comprises Twitter text data and two labels. The Synthetic Minority Oversampling Technique (SMOTE) was applied to balance the labels. Long Short-Term Memory (LSTM), a deep learning architecture, was employed for the classification process. The experimental results, obtained by leveraging the proposed feature extraction, feature selection, and LSTM methods, achieved the highest accuracy value of 99.23%. These findings demonstrate the proposed methods' success in effectively detecting COVID-19 anti-vaccination sentiment in text data. The study's results can offer valuable insights for developing health policies and public information strategies, presenting a new and powerful tool for detecting anti-vaccine sentiment in planning vaccination campaigns and public health interventions.

Keywords: COVID-19 anti-vaccine, Deep learning, Feature selection, LSTM, Text classification

*Corresponding author

1. Introduction

The COVID-19 pandemic has demonstrated the profound effects of the global health crisis. In this process, the existence of an important problem such as society's anti-vaccination complicates the control of the epidemic and vaccination efforts. The causes and prevalence of anti-vaccine sentiment have been the subject of extensive research. In this context, social media platforms have become an important platform for people to express their thoughts, concerns, and attitudes [1].

In this study, a dataset consisting of Twitter text data was used to detect COVID-19 anti-vaccination. Twitter is a suitable source for this type of analysis because it has a large user base and is a platform where real-time opinions can be shared. Analysis of the tweets that make up our data set with deep learning and feature selection approaches was used as a tool to understand and define anti-vaccine sentiment [2].

Text classification holds significant importance in the field of natural language processing (NLP) due to the ever-increasing size of textual data. Additionally, the automatic labeling of data plays a crucial role. In NLP, transforming words into vectors—thereby converting them into numerical values comprehensible to computers—is a critical task. The techniques employed to convert words into numerical values are pivotal in text classification processes, as they considerably influence the accuracy of the system (model) to be developed. Hence, the vectors generated by these techniques should accurately represent the words, with the goal of producing vectors that enhance classification success. Improving the quality of vectors not only aids in representing words more accurately but also enriches the multifaceted relationships between words, contributing to better model performance [3].

Deep learning and machine learning approaches have been utilized to identify the negative sentiments associated with COVID-19 vaccines on social media. Typically, researchers categorize tweets concerning COVID-19 vaccines into two principal groups: those expressing negative sentiments about vaccines and those unrelated to such sentiments. Valid tweets are further classified into three subcategories: personal experiences, informational content, and advisory messages. In a particular study, four machine learning models were trained using the collected data: Support Vector Machine (SVM), Logistic Regression (LR), Long Short-Term Memory (LSTM), and Artificial Neural Networks (ANN). The LSTM model achieved the highest accuracy, with a rate of 97.64%. It was observed that the SVM model presented the lowest accuracy rate, at 80%, for the research conducted. Additionally, the researchers evaluated the performance of various natural language processing models in detecting anti-vaccine sentiments during the COVID-19 pandemic. They discovered that the BERT (Bidirectional Encoder Representations from Transformers) model surpassed the other models in terms of performance on the test set [5].

In this study, meaningful features were obtained from English tweets by using Term Frequency-Inverse Document Frequency (TF-IDF) and N-gram methods together for feature extraction from text data to detect anti-vaccination. Additionally, feature selection was made using the Chi-square method to select the most prominent among these features. Synthetic Minority Oversampling Technique (SMOTE) method was applied to balance the data set. Finally, tweets were classified using the Long Short Term Memory (LSTM) deep learning algorithm [6].

The contributions of this study are as follows:

- Different feature extraction techniques were applied to obtain meaningful features from text data.
- Feature selection was applied to the features extracted from text data using the Chi-square method.
- Using these features with the LSTM deep learning model, signs of anti-vaccination were detected.
- Experimental results showed that the combination of deep learning and feature selection methods was effective in detecting COVID-19 anti-vaccination.

The results of the study show the effectiveness of the proposed methods. The results obtained show that the detection of anti-vaccination has been successfully carried out with a high accuracy rate. This study highlights the importance of data-driven approaches to identifying and managing anti-vaccine sentiment.

2. Related Works

In recent years, vaccination efforts related to the COVID-19 pandemic have become one of the most important agenda items worldwide. However, anti-vaccine sentiment has been a factor that has significantly impacted these efforts. In the literature, research on anti-vaccination has increased and many studies have been conducted on this subject. These studies have created an important basis for understanding the causes, effects and spread mechanisms of anti-vaccination, and the current status of anti-vaccination in the literature has been examined.

Qorib et al. showed in their study that the combination of TextBlob + TF-IDF + LinearSVC achieved the best performance in classifying public sentiment as positive, neutral, or negative. This combination resulted in 96.75% accuracy, 96.92% sensitivity, 92.80% specificity, and 94.70% F1 score. Additionally, combining two vectorization methods such as CountVectorizer and TF-IDF has been found to reduce model accuracy [7].

In a study where an AI-based framework was developed to detect COVID-19 vaccine misinformation, the BERT model showed the best performance. In the evaluation performed on the test set, a 98% F1 score was obtained. These findings were found to show that artificial intelligence models are effective in detecting misinformation about COVID-19 vaccines on social media platforms [8].

Aygün et al. focused on understanding people's views on vaccines and vaccine types during the period when vaccine development and community vaccination studies were carried out during the COVID-19 pandemic. Researchers collected 928,402 different vaccine-focused tweets to examine Twitter users' attitudes towards vaccination in the US, UK, Canada, Turkey, France, Germany, Spain and Italy. Data sets were prepared in two different languages (English and Turkish), and 4 different directions and 4 different BERT models were used to classify the tweets. Sentiment analysis was conducted on the 6 most widely used COVID-19 vaccines and the results are presented by country. While the success of the method varies between 84% and 88% in terms of F1 Score, the total accuracy value is determined as 87%. This study represents the first attempt to understand community views on the vaccination process [9].

Çelik and Kaplan evaluated the classification success using balanced data in a data set containing 4203 SMS and according to the study results, the highest classification successes were obtained using Logistic Regression with SMOTE (80.1%), Condensed Nearest Neighbor with XGBoost (62.1%) and Random Undersampling Technique with Logistic Regression (73.8%) [10].

Avvaru et al. implemented various versions of LSTM models (LSTM, stacked LSTM, Bi-LSTM, and CNN-LSTM) and BERT and XLNet transformer models on Twitter and Reddit [11]. Özbay provided an effective solution to the problem of aggression detection in Twitter data using the transformer-based CNN model with the Bert model proposed in his study [12].

In recent years, researchers have been applying artificial intelligence techniques to predict diabetes. In this context, a new SMOTE-based deep LSTM system was developed to deal with the class imbalance in the diabetes dataset and its prediction accuracy was measured. In a study where CNN, CNN-LSTM, ConvLSTM, and deep 1D-convolutional neural network (DCNN) techniques were examined and a SMOTE-based deep LSTM method was proposed, it was stated that the proposed model achieved the highest prediction accuracy of 99.64% measured based on the diabetes data set. These results show that, based on classification accuracy, this method outperforms other methods [13].

Bhatti et al. proposed a solution to classify emails into four classes: fraud, suspicious, harassment, and normal. They used the LSTM deep learning approach with stratified sampling to identify email classes. Additionally, sampling methods were used to balance the input dataset. The proposed model achieved a classification accuracy of over 90% by stratified sampling alone and an accuracy of over 95% by applying data balance techniques on the dataset [14].

In another study, a classification was conducted using machine learning methods to classify comments into toxic categories for social media use. The method used in the study is TF-IDF as feature extraction and SVM with Chi-square as feature selection. Additionally, various exploratory scenarios were also carried out to achieve the best performance by applying SVM kernels and preprocessing stages [15].

In their study, Hussein and Ozyurt compared the performances of LSTM, Bi-LSTM and GRU models and the Chi-square feature selection method for sentiment analysis. As a result of experiments conducted on two scaled data sets such as Yelp and US Airways, it has been observed that feature selection methods significantly increase classification accuracy. On the Yelp dataset, the Bi-LSTM model achieved 100% accuracy with Chi-square when using 500 features. In the US Airlines dataset, the GRU-LSTM model achieved 97.9% accuracy with Chi-square when 20 features were used [16].

In another study, CNN and LSTM models were specifically used to classify Spam and non-Spam text messages. The proposed models relied solely on text data and extracted the feature set automatically. 99.44% accuracy was achieved on a reference dataset consisting of 747 Spam and 4,827 non-Spam text messages [17].

In their study, Zhang & Rao presented a method to accurately and quickly perform text classification, which is commonly found in fields such as e-commerce and daily message analysis, with two methods: one-by-one comparison and one-to-one classification. The approach, called “n-BiLSTM,” is used to transform natural language text sentences into similar features with N-gram techniques, and these features are then fed into a bidirectional LSTM. The results of the study are presented for $n = 1, 2, 3$ and when $n = 2$, they achieved the best result with 88.8% [18].

Alfarizi et al.’s aim in their study is to compare the classification method with the LSTM model by adding the word-weighted TF-IDF and LinearSVC model to increase the accuracy in determining sentiment. The dataset used is 18000 divided into 16000 training data along with 2000 test data with 6 emotion classes namely sadness, anger, fear, love, joy and surprise. While the classification accuracy of emotions using the LSTM method was 97.50%, an accuracy value of 89% was obtained using the LinearSVC method [19].

3. Material and Method

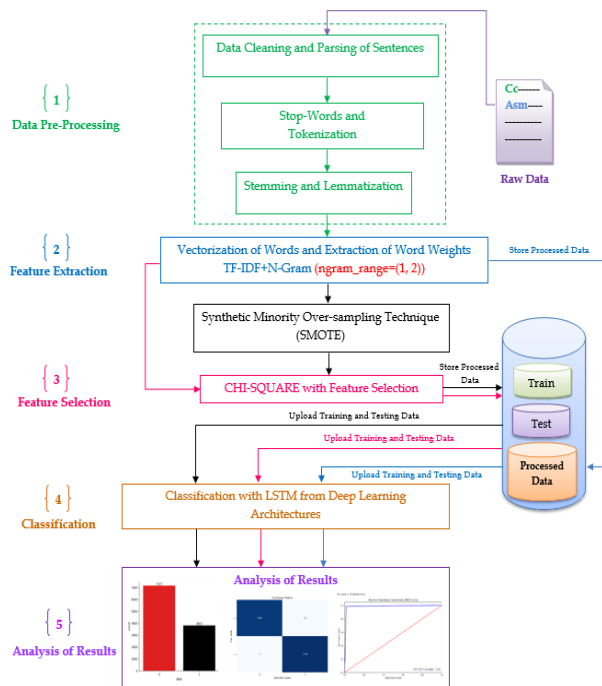


Figure 1. Flow diagram of the proposed methodology

Recently, anti-vaccination against COVID-19 has become a growing source of concern. The strategy of the model and method proposed in this study, which aims to analyze the trends and prevalence of anti-vaccine sentiment by using text data spread on social media platforms such as Twitter, is shown in Figure 1.

3.1. Dataset Construction

Twitter is one of the most popular social media platforms with 353 million active users and more than 500 million tweets are shared every day. Additionally, the Twitter API is allowed to pull public tweets, including tweet text, user information, retweets, and mentions, in JSON format, and a Python library called Twarc is used for this purpose. Specific keywords are used to collect relevant tweets about COVID-19 vaccines, and only English-language tweets are taken into account. Additionally, replies to tweets, retweets, and quoted tweets are ignored. In total, a total of 15,465,687 vaccine-related tweets were collected from December 1, 2020, to July 31, 2021 [8]. In accordance with Twitter's terms of service, the dataset is anonymized, contains only tweet IDs, and is publicly shared with users via the GitHub platform.

A function called `get_tweet_by_id` is defined to retrieve the content of a particular tweet and an associated reply using the Twitter API. By obtaining the tweet ID and response from GitHub, this function uses Twitter's `oEmbed` API to extract the tweet content. The content of this tweet was later removed. Then, tweet contents were retrieved from a specific tweet list by using the `get_tweet_by_id` function in a loop and these contents were added to a DataFrame. Any missing data is then dropped from this data frame. The number of missing or None values was checked and the cleaned data was saved in a CSV file.

A data set was created by creating a code block and extracting English tweet contents and their responses from the tweet ID list. The raw data set consists of 10950 rows and 2 columns after the specified cleaning process. The columns are named "text" and "label". While 7147 of the lines in the text column are in the label '0', 3803 of them are in the label '1'. As seen in Figure 2, in the "label" column of the data set used in the study, those who are not anti-vaccine are labeled as '0' and those who are anti-vaccine are labeled as '1'.

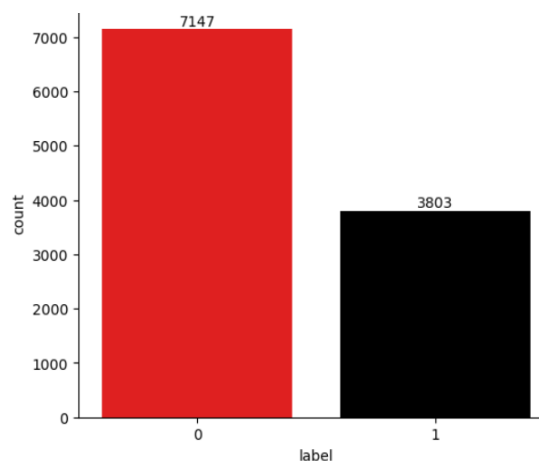


Figure 2. Distribution of the dataset via the label column

3.2. Data Pre-processing

Data preprocessing is an important stage that includes cleaning and editing steps on text data [20]. These steps ensure that text data becomes analyzable, consistent, and meaningful. More detailed explanations of the steps used in the data preprocessing phase are as follows:

3.2.1. Data Cleaning and Parsing of Sentences

Text cleaning involves removing noise (e.g., special characters, numbers, etc.) from the data. Text normalization involves bringing texts into a certain format, such as case conversion.

Conversion to Lowercase: All characters in the text were converted to lowercase, eliminating the distinction between uppercase and lowercase letters. In this way, “COVID” and “covid” are treated as the same word.

Removing Hashtags: Hashtags (#) encountered in these texts taken from the Twitter platform have been removed from the text. Hashtags often contain additional information on the topic and can be distracting in analysis.

Removing URLs: Web addresses (URLs) contained within the text are unnecessary to understand the content of the text and have therefore been removed. Removing URLs helps clean up the text and make it analyzable.

Removing Special Characters: Special characters, markings, or punctuation marks in the text are removed. This step increases the homogeneity of the text and simplifies the analysis process.

Removing Usernames: Removed usernames (@username) in the text. Usernames are unnecessary to understand the content of the text and can be misleading in analysis.

Remove Double Spaces: Double spaces within the text have been replaced with single spaces. This step preserves the order of the text and ensures consistency in subsequent processing.

Removing Numbers and Numbers: Numbers in the text have been removed. Since text analysis generally focuses on textual content, it is desired to reduce the effect of numbers in the text.

Removing Single Letters: Single letters (\b\w\b) that do not make sense on their own have been removed. For example, single letters such as “a” or “I” generally do not change the meaning of the text and can therefore be removed.

Removing Emojis: Emojis in the text were removed by converting them to ASCII characters. This step is implemented considering that emojis may cause undesirable effects in the analysis.

3.2.2. Stop-words and Tokenization

This step involves removing words from the text that do not have meaning or are not necessary for analysis. A stop_words set was used to extract English stop words. Tokenization is used to split the text into pieces or “tokens”. For example, breaking sentences into words. The text is separated into tokens by a simple space-splitting process.

3.2.3. Stemming and Lemmatization

This step involves finding the root of the word. For example, the word “keeping” is reduced to its root as “keep”. Lemmatization was performed using WordNetLemmatizer. By completing these steps, text data becomes ready for analysis and more robust results are obtained. Therefore, raw data turns into processed data.

3.3. Feature Extraction

Text classification is a widely used technique in the field of natural language processing and allows the assignment of a text to a specific category or class. The feature extraction step is very important to carry out this process effectively. Because extracting meaningful features from text data directly affects text classification performance. Frequently used feature extraction techniques include TF-IDF and N-gram models. These methods are word embedding or word vector methods used to represent texts, in other words, to digitize texts.

3.3.1. TF-IDF

TF-IDF is a numerical statistical method that reflects the importance of a term in a document relative to the entire collection of documents. It consists of two main components.

Term Frequency (TF): Measures how often a term occurs in a document. It calculates the number of times a term appears in the document by dividing it by the total number of terms in the document. This indicates the uniqueness of a term in the document. Example: If the term "covid" appears 5 times in a document containing 100 words, the term frequency of the term "covid" will be $5/100 = 0.05$.

Inverse Document Frequency (IDF): Measures the rarity of a term within the entire document collection. It is calculated by taking the logarithm of the ratio of the number of documents in which a term occurs to the total number of documents. This determines the importance of a term in the entire corpus. Example: If there are 1,000,000 documents in the collection and the term "covid" appears in 1000 documents, the inverse document frequency of the term "covid" will be $\log(1,000,000/1,000) = 3$.

After TF and IDF are calculated, the TF-IDF value is obtained. This gives higher weights to terms that occur frequently in the document but are rare in the entire collection.

3.3.2. N-gram

N-grams are sequences of n consecutive elements (words in text processing). It is used to capture the local structure of a text by taking into account the relationship between neighboring words.

Uni-Gram (1-Gram): Single words in the text. For example: "covid", "vaccine", "detected".

Bi-Gram (2-Gram): Two consecutive word pairs. For example: "covid vaccine", "vaccine detected".

Tri-Gram (3-Gram): Three consecutive words. For example: "covid vaccine detected".

N-grams are used to better capture word orders and contexts in text data. It is valuable in tasks such as language modeling, machine translation, and text generation. These techniques are widely used in natural language processing tasks to extract meaningful features from text data and improve the performance of machine learning models. It can be useful to try different N-gram ranges, especially when you want to examine language structure and expression patterns. However, higher N-gram ranges may result in greater dimensionality and thus a larger feature space, which may increase the training time of the model. Therefore, a balanced approach is important when choosing the N-gram range.

In this study, pre-processed text data is converted into a high-dimensional digital representation (vectorization) by applying the TF-IDF method. Here, each dimension represents a unique term or combination of terms. In addition, the range of n-grams used in the study was determined as (1, 2). Here, in addition to uni-grams, consecutive words, i.e. bi-grams, are also used. This means that features containing each term and pairs of consecutive words will be created. These transformed feature vectors can be fed into deep-learning models for tasks such as text classification, clustering, or information retrieval.

3.4. SMOTE

SMOTE is a technique used to address the issue of class imbalance when working with unbalanced datasets. It is used to increase performance, especially in classification problems, when the number of examples of the rare class is low [21]. SMOTE synthetically increases the minority class samples by creating random points among existing data points. This increases the representation of the minority class while helping the model generalize better against that class. Using SMOTE can reduce the tendency of the model to misclassify the minority class due to class imbalance, and ultimately help achieve a more balanced classification model. In the data set used in the study, the number of tweets labeled '0', that is, non-anti-vaccine, is 7147, while the number of tweets labeled '1', that is, anti-vaccination, is 3803. SMOTE was used in the proposed model to

eliminate class imbalance. The number of samples labeled '0' and '1' was equalized, that is, the number of samples labeled '0' became 7147, and the number of samples labeled '1' became 7147. The total number of samples used in the proposed model was 14294.

3.5. Feature Selection

Feature selection, which has an important place among data analysis methods, especially in recent years, helps researchers extract meaningful information from complex data sets. In this study, the use of the Chi-square method for feature selection in detecting COVID-19 anti-vaccination was examined. Chi-square is considered a powerful tool to identify relationships and connections between variables in the data set. This study addresses the effectiveness and applicability of Chi-square in the feature selection process.

3.5.1. Chi-Square Test

Feature selection is a critical step that directly affects the performance of the text classification model. One of the important reasons why feature selection affects text classification is the determination of meaningful features. Texts often contain large and complex bodies of data. Feature selection can help the model identify meaningful features, reducing the impact of redundant or noisy features. This allows the model to work on more focused and effective features [22].

The use of Chi-square as a feature selection method played an important role in the study carried out for COVID-19 anti-vaccine detection. Initially, a hybrid of TF-IDF and N-gram was used. 10000 features were determined with the max_features parameter. In feature selection, the ngram_range parameter was selected as (1, 2). Chi-square method was used to improve the performance of the model and eliminate unnecessary features. According to Equation 1, Chi-square values are calculated to determine the relationship between each feature and the target, and the desired number of features with the highest Chi-square scores are selected.

$$x^2 = \sum \frac{(O_i - E_i)^2}{E_i} \quad (1)$$

here, x^2 represents the Chi-square statistic, O_i represents observed frequencies, E_i represents expected frequencies. Σ shows the sum of terms calculated and summed for all categories. In Equation 1, O_i refers to the observed frequency, that is, the actual frequency in the data, and E_i refers to the expected frequency. Expected frequencies are calculated to be equally distributed across categories if the two variables are independent. The chi-square statistic represents the sum of the squares of the difference between the observed and expected frequencies divided by the expected frequencies. This statistic determines how large the relationship between variables is. A higher Chi-square statistic value indicates a stronger relationship between variables. The Chi-square test is a method used for categorical feature selection and evaluates the significant difference between observed and expected values. This test is used to measure the strength of the relationship between variables and examines the difference between observed and expected frequencies to determine statistical significance [23].

The SelectKBest class was created to select the top 6000 features in the dataset using the chi2 statistic. This helps preserve important features while reducing the training time of the model and reduces the risk of overfitting. This selection process uses a statistical method to find the most significant relationships between features, allowing the model to generalize better. As a result of the analysis made with the Chi-square test, the most decisive $k = 6000$ feature with the highest accuracy was selected. This choice enabled the model to perform better and accurately detect anti-vaccination. These results highlight the effectiveness of Chi-square in the feature selection process and its importance for COVID-19 anti-vaccine detection.

3.6. LSTM Architecture

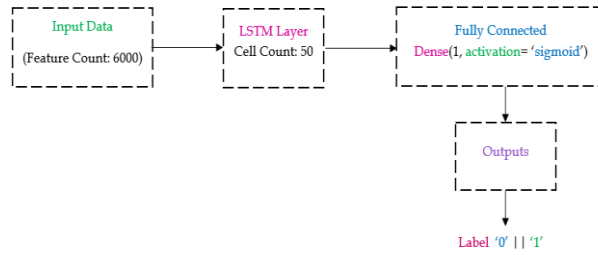


Figure 3. The structure of an LSTM model

In this study, LSTM deep learning architecture was used to classify pro-vaccine or anti-vaccine tweets about COVID-19 [24]. 10000 features were selected using TF-IDF and N-gram in training the model. SMOTE was used to balance the dataset. Then, 6000 features were selected using the Chi-square technique. The resulting balanced data set was classified with the LSTM model. The model evaluated its ability to detect anti-vaccine content by analyzing the textual content of tweets. The results demonstrated the ability of the LSTM model to identify anti-vaccine tweets with high accuracy and efficiency. The structure of an LSTM model is shown in Figure 3. The stages of creating the LSTM model used in the study are as follows:

Creating LSTM Layer: LSTM is used specifically for processing sequential data such as time series data. The LSTM layer is a type of RNN layer but with more advanced memory mechanisms than traditional RNNs. Different classification performances were evaluated as 20, 50, 70, and 100 cells in the LSTM layer. In the proposed model, an LSTM layer consisting of 50 cells is defined.

Creating the Fully Connected (Dense) Layer: Following the LSTM layer, one or more fully connected layers are usually added. This layer receives the outputs of the LSTM layer and is used to produce the desired outputs. In the proposed model, a fully connected layer with a single neuron is added. This neuron has a sigmoid activation function that is often used in binary classification problems. This ensures that the output falls between 0 and 1 and can be interpreted with probability values.

Compiling the Model: The compilation step determines the model's loss function, optimization algorithm, and optional metrics. Binary cross-entropy (binary_crossentropy) is used as the loss function of the model. This is a commonly used loss function for binary classification problems. "Adam" was chosen as the optimization algorithm. Adam is an effective optimization algorithm that accelerates training using the adaptive momentum method. Additionally, the accuracy metric is also monitored during training.

Training the Model: Training the model is performed over a certain number of iterations (epochs) on the data. During training, the epoch value was selected as 5. batch_size, the number of samples to be used in each training step is determined as 32. The study focuses on the classification of COVID-19 anti-vaccine tweets using the LSTM deep learning architecture, making a valuable contribution to solving an important problem in this field. Details and analysis of the results obtained with the feature selection and balancing techniques used will be presented. The training hyperparameters of the LSTM model are given in Table 1.

Table 1. Hyperparameters of the LSTM model

Model	Batch_size	Epochs	LSTM Cell
LSTM	32	5	50

4. Experimental Results and Discussion

4.1. Classification Performance Metrics

The study presents a review of commonly used metrics to evaluate the performance of classification models. Metrics used to evaluate the accuracy of the model in classification problems include accuracy, precision, sensitivity, and F1 score. The use of graphical methods such as the ROC curve is also examined. Complexity matrix-based metrics detail the impact of false positives and false negatives on model performance. Classification performance is evaluated through the metrics included in the complexity matrix shown in Table 2.

Table 2. Two-label confusion matrix

		Predicted Labels	
		Positive	Negative
True Labels	Positive	TP	FP
	Negative	FN	TN

Confusion matrix is a widely used tool to evaluate the performance of classification algorithms [25]. The key terms found in the confusion matrix are:

True Positive (TP): True positive. The number of true positive instances that the model correctly predicted as positive.

True Negative (TN): True negative. The number of true negative instances that the model correctly predicted as negative.

False Positive (FP): False positive. The number of instances in which the model incorrectly predicted a negative instance as positive.

False Negative (FN): False negative. The number of instances in which the model incorrectly predicted a positive instance as negative.

The following metrics were determined to evaluate classification performance using the confusion matrix and are listed below with their descriptions:

Accuracy: It is the ratio of correctly predicted samples to the total number of samples. It is a measure of overall model performance, but may not be sufficient on its own for unbalanced classes or datasets. It is calculated as given in Equation 2.

$$Accuracy = \frac{(TP + TN)}{(TP + TN + FP + FN)} \quad (2)$$

Precision: The ratio of samples predicted to be positive to samples that are actually positive. It is important in situations aiming to reduce false positives (FP). It is calculated as in Equation 3.

$$Precision = \frac{TP}{(TP + FP)} \quad (3)$$

Recall: The ratio of true positive samples to correctly predicted positive samples. It is important in situations aiming to reduce false negatives (FN). It is calculated as in Equation 4.

$$Recall = \frac{TP}{(TP + FN)} \quad (4)$$

F1 score: It is the harmonic mean of precision and sensitivity. It can be used as a substitute for accuracy for unbalanced classes or datasets. It is calculated as in Equation 5.

$$F1\ score = 2 * \frac{(precision * recall)}{(precision + recall)} \quad (5)$$

ROC Curve: Receiver Operating Characteristic Curve and Area Under the Curve (AUC) It is a graphical tool used to evaluate the performance of classification algorithms. AUC refers to the area under the ROC curve, and the closer it is to 1, the better the performance of the model.

4.2. Performance Evaluation

First of all, after the Twitter data set was pre-processed with data cleaning and parsing of sentences, stop-words and tokenization, and stemming and lemmatization, feature extraction was performed with TF-IDF and N-gram methods and then classified using the LSTM deep learning algorithm. The results obtained show that the highest accuracy rate is 97.35%. The confusion matrix obtained at this stage is shown in Figure 4 and the ROC Curve is shown in Figure 5.

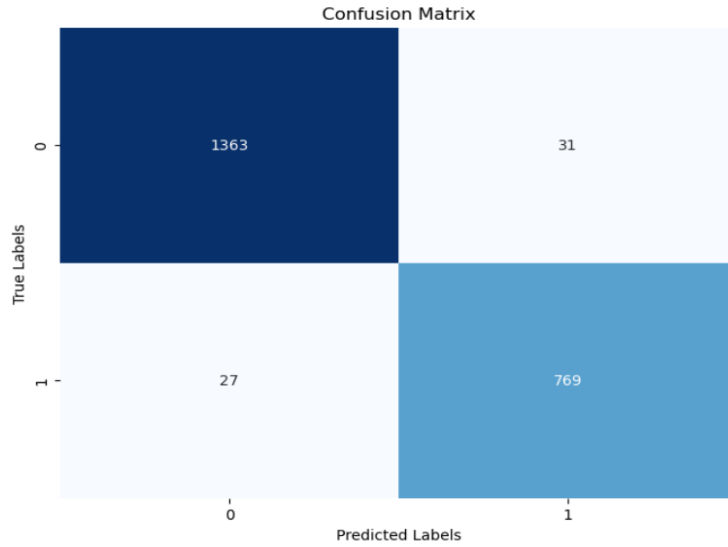


Figure 4. Confusion matrix of LSTM with TF-IDF and N-gram

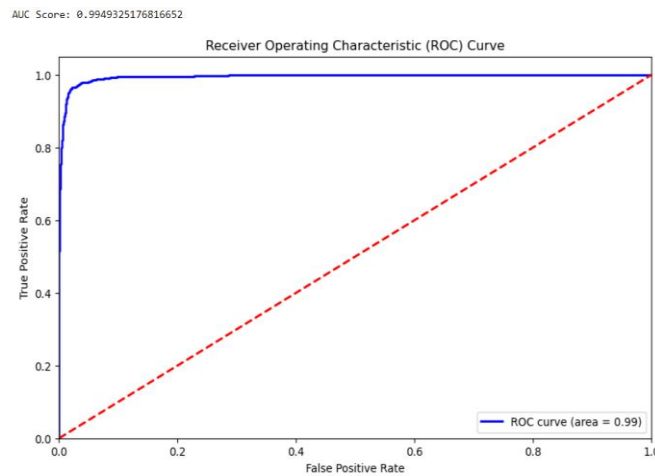


Figure 5. ROC curve of LSTM with TF-IDF and N-gram

In the second stage, feature extraction was made with TF-IDF and N-gram without using SMOTE, and the highest accuracy rate was determined as 98.36% according to the results obtained by performing feature selection with Chi-square. The confusion matrix obtained at the second stage is shown in Figure 6 and the ROC Curve is shown in Figure 7.

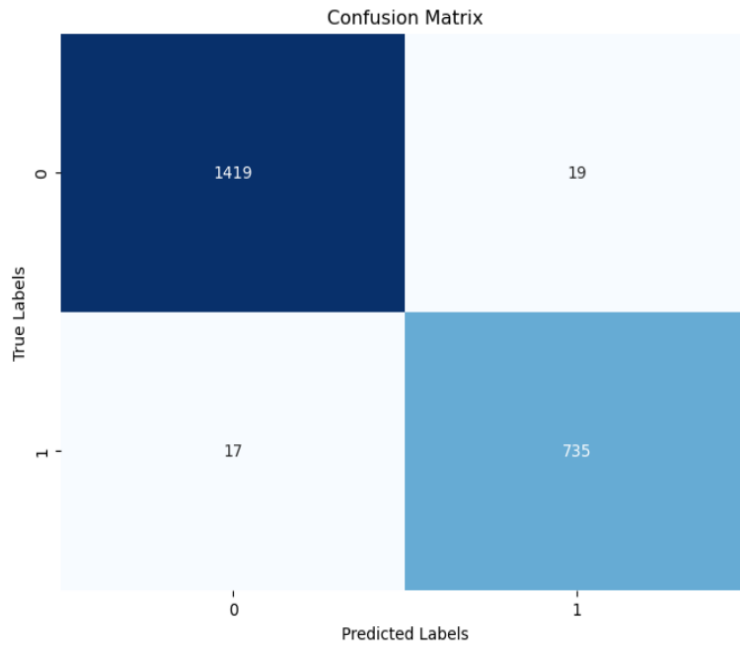


Figure 6. Confusion matrix of LSTM with TF-IDF, N-gram, and Chi-square feature selection

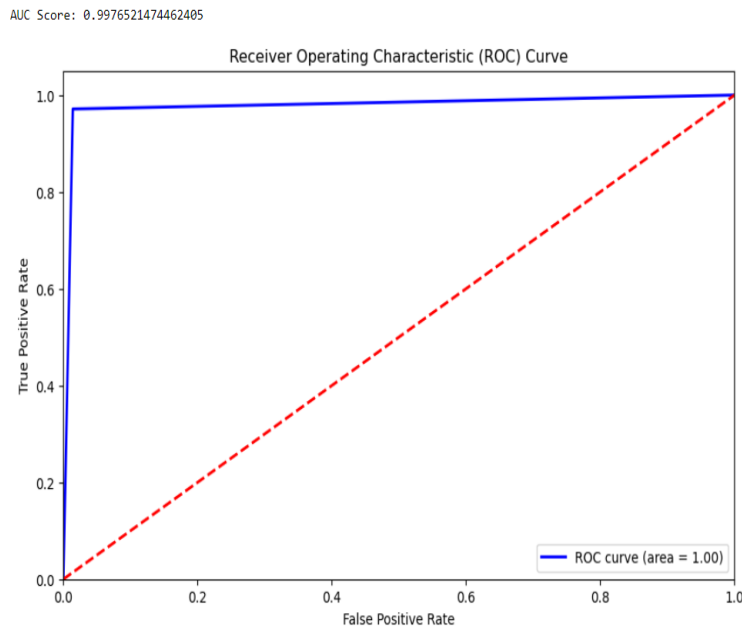


Figure 7. ROC curve of LSTM with TF-IDF, N-gram, and Chi-square feature selection

In the third stage, the data set was balanced using SMOTE, feature extraction was performed with TF-IDF and N-gram, and feature selection was performed with Chi-square, and according to the results obtained, the highest accuracy rate was determined as 99.23%. The confusion matrix obtained at the third stage is shown in Figure 8 and the ROC Curve is shown in Figure 9.

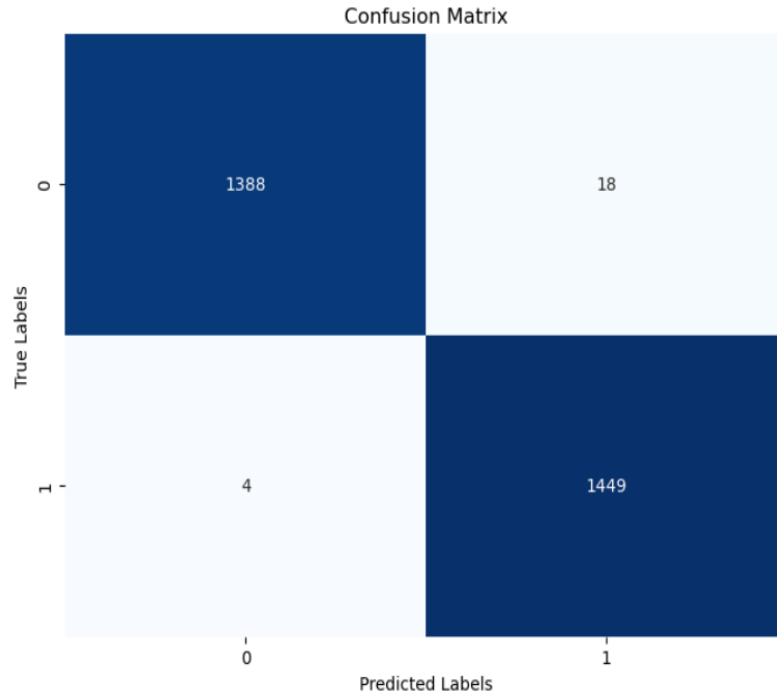


Figure 8. Confusion matrix of LSTM with TF-IDF, N-gram, Chi-square feature selection, and SMOTE

AUC Score: 0.9977120423717613

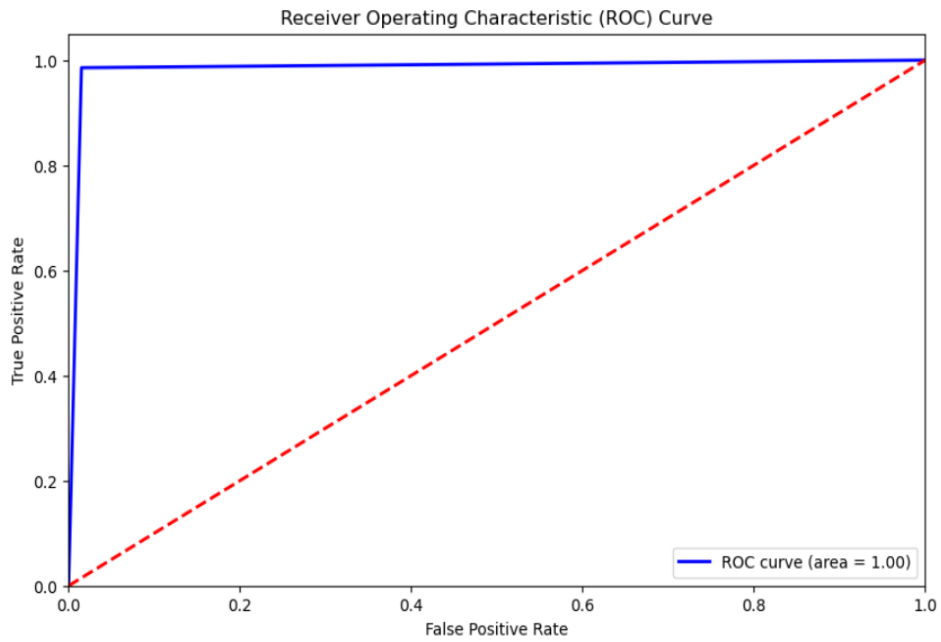


Figure 9. ROC curve of LSTM with TF-IDF, N-gram, Chi-square feature selection, and SMOTE

Table 3. Evaluation of the proposed method through performance metrics

Methods	Feature	Model	Accuracy	Precision	Recall	F1	ROC
TF-IDF + N-gram (1,2)	10000	LSTM	97.35%	97.8%	98.1%	97.9%	99.5%
TF-IDF + N-gram (1,2) + Chi-square	6000	LSTM	98.36%	98.7%	98.8%	98.8%	99.8%
TF-IDF + N-gram (1,2) + Chi-square + SMOTE (Proposed method)	6000	LSTM	99.23%	98.7%	99.7%	99.2%	99.8%

The results in Table 3 summarize a study evaluating the impact of feature selection and extraction on the performance of deep learning-based classification models. Initially, data obtained using a large feature set was processed with complex deep learning architectures such as LSTM. 10000 features derived using TF-IDF + N-Gram (1,2) initially yielded 97.35% accuracy. However, when the Chi-square method was applied to reduce the number of features and reduce the complexity of the model, 98.36% accuracy was achieved. At this point, remarkably, the feature selection and reduction process improved the overall performance of the model. 6000 features determined by chi-square appear to create a less complex model, which increases the accuracy rate. Moreover, 99.23% accuracy, a significant increase in the performance of the model, was observed when the SMOTE method was used to balance class labels in unbalanced datasets. This suggests that SMOTE, in particular, can help underrepresented classes to be better learned by the model, thereby increasing the precision and recall rate of the model. It has been shown that the proposed model achieves higher success in terms of other performance metrics, including Precision, Recall, F1 score, and ROC [26].

These results emphasize that feature selection and balancing methods can significantly affect the performance of deep learning models and that using appropriate methods can increase the reliability of the model. This work can be seen as an important step in the development of deep learning-based classification models, as choosing and balancing the right features can enable the model to generalize better to real-world data.

Table 4 compares the performance of existing SOTA methods and models in the literature for identifying anti-vaccine tweets. The latest methods used to identify anti-vaccine tweets demonstrate varying levels of success. Among these methods, the BERT method stands out, with Hayawi et al. [8] achieving an impressive 98% accuracy measured by the F1 score. Similarly, Kariyapperuma et al. [4] achieved a high accuracy of 97.6% using LSTM. However, the innovative approach developed in this study achieved a result that exceeds the success of existing methods with 99.23% accuracy and 99.21% F1 score. An impressive 99.23% accuracy result was achieved with this model, which is a combination of TF-IDF + N-Gram (1,2) + Chi-square + SMOTE and the deep learning-based LSTM model. In addition to establishing a new reference point in the field of identifying anti-vaccine sentiments, this model also highlights the effectiveness of advanced natural language processing techniques and deep learning architectures to deal with complex social media data.

Table 4. Evaluation of the proposed method through performance metrics

Study	Year	Method	Accuracy / F1
Qorib et al. [7]	2023	TextBlob + TF-IDF + LinearSVC	96.8%
Hayawi et al. [8]	2022	BERT	98% (F1)
Aygün et al. [9]	2021	mBERT-base	86%
Kariyapperuma et al. [4]	2022	LSTM	97.6%
To et al. [5]	2021	BERT	91.6%
Quintana et al. [27]	2022	LSTM	77%
Proposed method	2024	TF-IDF + N-gram + Chi-square + SMOTE	99.23%

Building on observer work by Quintana et al., this study of vaccine discussions on Twitter clearly identifies and visualizes language patterns between antivaxes (anti-vaccine campaigners and vaccine deniers) and other groups. Additionally, using features of Antivaxes' tweets, text classifiers have been developed to identify users using anti-vaccine language. This contributes to improving the health of the epistemic environment and supporting public health initiatives by creating an early warning mechanism [27].

5. Conclusions

In this study, Twitter text data was examined using a deep learning approach to determine COVID-19 anti-vaccination. In the first stage, TF-IDF and N-gram methods were used together to extract meaningful features from the texts. A chi-square statistical test was applied to select the most decisive features among the obtained features. In this way, it is aimed to increase the performance of the model and avoid unnecessary information. SMOTE was used to ensure that the classification model required a balanced training dataset. This technique allowed us to combat the oversampling problem while eliminating data imbalance by increasing the samples

of the minority class with synthetic samples. LSTM deep learning model was used to process text data more effectively and make decisions. This deep learning architecture enabled us to achieve a high accuracy rate by better capturing the hidden relationships between texts. The effectiveness of the model was evaluated through performance metrics. It has been shown that the proposed model can be used successfully in detecting COVID-19 anti-vaccination by achieving a high accuracy rate of 99.23%. Therefore, it shows that deep learning-based approaches can be used effectively to detect COVID-19 anti-vaccination. Using a larger data set and collecting data from different social media platforms in future studies may help increase the generalization ability of the model. Additionally, a comparative analysis of different feature extraction methods and deep learning architectures can be performed to improve the performance of the model. This methodology could potentially be valuable in important applications such as detecting and preventing the spread of anti-vaccine views on social media platforms.

6. Acknowledgement

This study was funded by Firat University (FUBAP) with the scientific research project number MF.23.37.

7. Author Contribution Statement

In this study, Author 1 contributed to the development of the method, obtaining experimental results, and preparation of the paper; Author 2 contributed to the creation of the idea, design and organization.

8. Ethics Committee Approval and Conflict of Interest

“There is no need for an ethics committee approval in the prepared article”

“There is no conflict of interest with any person/institution in the prepared article”

9. List of Abbreviations

COVID-19	Coronavirus Disease-2019
TF-IDF	Term Frequency-Inverse Document Frequency
SVM	Support Vector Machine
LR	Logistic Regression
LSTM	Long Short Term Memory
ANN	Artificial Neural Networks
BERT	Bidirectional Encoder Representations from Transformers
SMOTE	Synthetic Minority Oversampling Technique
AI	Artificial Intelligence
SMS	Short Message Service
CNN	Convolutional Neural Network
API	Application Programming Interface
CSV	Comma Separated Values
ROC	Receiver Operating Characteristic
AUC	Area Under the Curve

10. References



- [1] C. H. van Werkhoven, A. W. Valk, B. Smagge, H. E. de Melker, M. J. Knol, S. J. Hahné and B. de GierEarly, “COVID-19 vaccine effectiveness of XBB. 1.5 vaccine against hospitalisation and admission to intensive care, the Netherlands”, *Eurosurveillance*, 29(1), 2300703, 9 October to 5 December 2023.
- [2] P. Xu, D. A. Broniatowski and M. Dredze, “Twitter social mobility data reveal demographic variations in social distancing practices during the COVID-19 pandemic”, *Scientific reports*, vol. 14, no 1, pp. 1165, 2024.

- [3] M. Umer, Z. Imtiaz, M. Ahmad, M. Nappi, C. Medaglia, G. S. Choi and A. Mehmood, "Impact of convolutional neural network and FastText embedding on text classification", *Multimedia Tools and Applications*, vol. 82, no 4, pp. 5569-5585, 2023.
- [4] K. R. S. N. Kariyapperuma, K. Banujan, P. M. A. K. Wijeratna and B. T. G. S. Kumara, "Classification of covid19 vaccine-related tweets using deep learning", In 2022 International Conference on Data Analytics for Business and Industry (ICDABI), IEEE, pp. 1-5, October, 2022.
- [5] Q. G. To, K. G. To, V. A. N. Huynh, N. T. Nguyen, D. T. Ngo, S. J. Alley and C. Vandelanotte, "Applying machine learning to identify anti-vaccination tweets during the covid-19 pandemic," *International journal of environmental research and public health*, vol. 18, no 8, pp. 4069, 2021.
- [6] A. Mallik and S. Kumar, "Word2Vec and LSTM based deep learning technique for context-free fake news detection", *Multimedia Tools and Applications*, vol. 83, no 1, pp. 919-940, 2024.
- [7] M. Qorib, T. Oladunni, M. Denis, E. Ososanya and P. Cota, "Covid-19 vaccine hesitancy: text mining, sentiment analysis and machine learning on covid-19 vaccination twitter dataset", *Expert Systems with Applications*, vol. 212, pp. 118715, 2023.
- [8] K. Hayawi, S. Shahriar, M. A. Serhani, I. Taleb and S. S. Mathew, "ANTi-Vax: a novel Twitter dataset for covid-19 vaccine misinformation detection", *Public health*, vol. 203, pp. 23-30, 2022.
- [9] I. Aygün, B. Kaya and M. Kaya, "Aspect based twitter sentiment analysis on vaccination and vaccine types in covid-19 pandemic with deep learning", *IEEE Journal of Biomedical and Health Informatics*, vol. 26, no 5, pp. 2360-2369, 2021.
- [10] Ö. Çelik and G. Kaplan, "Yeniden Örnekleme Teknikleri Kullanarak SMS Verisi Üzerinde Metin Sınıflandırma Çalışması", *Erciyes Üniversitesi Fen Bilimleri Enstitüsü Fen Bilimleri Dergisi*, vol. 36, no 3, pp. 433-442, 2020.
- [11] A. Avvaru, S. Vobilisetty and R. Mamidi, "Detecting sarcasm in conversation context using transformer-based models", In *Proceedings of the second workshop on figurative language processing*, pp. 98-103, July, 2020.
- [12] E. Özbay, "Transformör-tabanlı evrişimli sinir ağı modeli kullanarak twitter verisinde saldırganlık tespiti", *Konya Journal of Engineering Sciences*, vol. 10, no 4, pp. 986-1001, 2022.
- [13] S. A. Alex, N. Z. Jhanjhi, M. Humayun, A. O. Ibrahim and A. W. Abulfaraj, "Deep lstm model for diabetes prediction with class balancing by smote", *Electronics*, vol. 11, no 17, pp. 2737, 2022.
- [14] P. Bhatti, Z. Jalil and A. Majeed, "Email Classification using LSTM: A Deep Learning Technique", In 2021 International Conference on Cyber Warfare and Security (ICWS), IEEE, pp. 100-105, November, 2021.
- [15] N. Azzahra, D. Murdiansyah and K. Lhaksana, "Toxic comment classification on social media using support vector machine and chi square feature selection", *International Journal on Information and Communication Technology (IJoICT)*, vol. 7, no 1, pp. 64-76, 2021.
- [16] M. Hussein and F. Özyurt, "A new technique for sentiment analysis system based on deep learning using Chi-Square feature selection methods", *Balkan Journal of Electrical and Computer Engineering*, vol. 9, no 4, pp. 320-326, 2021.
- [17] P. K. Roy, J. P. Singh and S. Banerjee, "Deep learning to filter sms spam. future generation computer systems", vol. 102, pp. 524-533, 2020.
- [18] Y. Zhang and Z. Rao, "n-bilstm: bilstm with n-gram features for text classification", In 2020 IEEE 5th Information Technology and Mechatronics Engineering Conference (ITOEC), IEEE, pp. 1056-1059, June, 2020.
- [19] M. I. Alfarizi, L. Syafaah and M. Lestandy, "Emotional text classification using tf-idf (term frequency-inverse document frequency) and lstm (long short-term memory)", *JUITA: Jurnal Informatika*, vol. 10, no 2, pp. 225-232, 2022.
- [20] F. A. Özbay and B. Alataş, "Çevrimiçi sosyal medyada sahte haber tespiti", *Dicle Üniversitesi Mühendislik Fakültesi Mühendislik Dergisi*, vol. 11, no 1, pp. 91-103, 2020.
- [21] A. Ciran and E. Özbay, "Optimization-based feature selection in deep learning methods for monkeypox skin lesion detection", In 2023 7th International Symposium on Multidisciplinary Studies and Innovative Technologies (ISMSIT), IEEE, pp. 1-6, October, 2023.
- [22] İ. Sel, C. Yeroğlu and D. Hanbay, "Feature selection by using heuristic methods for text classification", In 2019 International Artificial Intelligence and Data Processing Symposium (IDAP) IEEE, pp. 1-6, September, 2019.

- [23] X. Jin, A. Xu, R. Bie and P. Guo, “Machine learning techniques and chi-square feature selection for cancer classification using SAGE gene expression profiles”, In *Data Mining for Biomedical Applications: PAKDD 2006 Workshop, BioDM 2006*, Singapore, Springer Berlin Heidelberg, pp. 106-115, April 9, 2006.
- [24] M. Yildirim, “Detection of COVID-19 fake news in online social networks with the developed CNN-LSTM based hybrid model”. *Review of Computer Engineering Studies*, vol. 9, no. 2, pp. 41-48, 2022.
- [25] Y. Eroglu, M. Yildirim and A. Cinar, “Diagnosis of periventricular leukomalacia in children with artificial intelligence-based models developed using brain magnetic resonance images”, *Signal, Image and Video Processing*, vol. 17, no. 8, pp. 4543-4550, 2023.
- [26] F. B. Demir, M. Baygin, I. Tuncer, P. D. Barua, S. Dogan, T. Tuncer and U. R. Acharya, “MNPDenseNet: automated monkeypox detection using multiple nested patch division and pretrained densenet201,”, *Multimedia Tools and Applications*, pp. 1-23, 2024 .
- [27] I. O. Quintana, M. Cheong, M. Alfano, R. Reimann and C. Klein, “Automated clustering of covid-19 anti-vaccine discourse on twitter,”, *arXiv preprint arXiv:2203.01549*, 2022.



Geliştirilmiş Öğretme-Öğrenme Tabanlı Optimizasyon Algoritmaları Kullanılarak Konsol İstinat Duvarı Tasarımının Optimizasyonu

Bilal TAYFUR¹ , Hakan Alper KAMILOĞLU^{2*} 

^{1,2}Inşaat Mühendisliği Bölümü, Mühendislik Fakültesi, Bayburt Üniversitesi, Bayburt, Türkiye.

¹btayfur@bayburt.edu.tr, ²hkamiloglu@bayburt.edu.tr

Geliş Tarihi: 01.02.2024

Kabul Tarihi: 02.04.2024

Düzeltilme Tarihi: 05.03.2024

doi: <https://doi.org/10.62520/fujece.1430236>

Araştırma Makalesi

Alıntı: B. Tayfur ve Hakan A. Kamiloğlu, "Geliştirilmiş öğretim-öğrenme tabanlı optimizasyon algoritmaları kullanılarak konsol istinat duvarı tasarımının optimizasyonu", Fırat Üni. Deny. ve Hes. Müh. Derg., vol. 3, no 2, pp. 134-150, Haziran 2024.

Öz

Dayanma yapıları, geoteknik mühendisliğinde zemin seviyelerini desteklenmesi, şev göçmelerinin önlenmesi ve tesfiye yüzeylerinin oluşturulması açısından önem arz etmektedirler. Bu yapıların tasarımı, malzeme kullanımını ve maliyeti en aza indirirken iç ve dış stabilite için optimizasyonu içerir. Bu çalışma, betonarme konsol istinat duvarlarının Öğretim-Öğrenme Tabanlı Optimizasyon (TLBO) algoritması ve araçlarla geliştirilmiş bir versiyonu (I-TLBO) kullanılarak optimize edilmesine odaklanmaktadır. Konsol istinat duvarı tasarım süreci iki amaç fonksiyonunu dikkate almaktadır: ağırlığı ve maliyeti en aza indirme. Çalışma, geometrik ve yapısal tasarım değişkenlerini, geoteknik ve yapısal kısıtları ve optimizasyon süreçlerini incelemektedir. Optimizasyon sonuçları, genetik algoritmalar, evrimsel stratejiler ve parçacık sürüsü optimizasyonu gibi literatürdeki diğer algoritmalarla karşılaştırılmıştır. Geliştirilmiş TLBO algoritması, daha düşük tasarım boyutları ve daha düşük maliyetler elde ederek görece daha başarılı sonuçlar vermiştir. Geliştirilmiş TLBO algoritması tasarım kısıtlamalarını sınırlarına yaklaşırken daha verimli çözümler sunmuş, daha uygun maliyetli ve yapısal olarak daha stabil konsol istinat duvarı tasarımları elde edilmesini olanak tanımıştır. Çalışma sonucunda, I-TLBO algoritmasının konsol istinat duvarı tasarımının optimizasyonunda diğer yöntemlere göre daha düşük maliyet ve daha düşük ağırlıkların elde edilmesi bakımından etkin sonuçlar sunduğu görülmüştür.

Anahtar kelimeler: İstinat duvarı tasarımı, Konsol istinat duvarı, Stabilite analizleri, Optimizasyon, Öğretim-öğrenme tabanlı optimizasyon (TLBO)

* Yazışılan yazar



İntihal Kontrol: Evet – Turnitin

Şikayet: fujece@firat.edu.tr

Telif Hakkı ve Lisans: Dergide yayın yapan yazarlar, CC BY-NC 4.0 kapsamında lisanslanan çalışmalarının telif hakkını saklı tutar.



Optimization Of Cantilever Retaining Wall Design Using Improved Teaching-Learning-Based Optimization Algorithms

Bilal TAYFUR¹ , Hakan Alper KAMILOĞLU^{2*} 

^{1,2}Department of Civil Engineering, Engineering Faculty, Bayburt University, Bayburt, Türkiye.

¹btayfur@bayburt.edu.tr, ²hkamiloglu@bayburt.edu.tr

Received: 01.02.2024

Accepted: 02.04.2024

Revision: 05.03.2024

doi: <https://doi.org/10.62520/fujece.1430236>

Research Article

Citation: B. Tayfur and Hakan A. Kamiloglu, "Optimization of cantilever retaining wall design using improved teaching-learning-based optimization algorithms", *Firat Univ. Jour. of Exper. and Comp. Eng.*, vol. 3, no 2, pp. 134-150, June 2024.

Abstract

Retaining structures play a crucial role in geotechnical engineering to support soil levels, prevent slope failure, and create flat surfaces for construction. Designing these structures involves optimizing internal and external stability while minimizing material usage and cost. This study focused on optimizing reinforced concrete cantilever retaining walls using the Teaching-Learning Based Optimization (TLBO) algorithm and an improved version (I-TLBO) with agents. In the context of the study, geometric-structural design variables, geotechnical - structural constraints, and optimization processes were examined. Minimizing weight and minimizing cost of the wall were the objectives considered in the cantilever retaining wall design process. The optimization results were compared with other algorithms in the literature, such as genetic algorithms, evolutionary strategies, and particle swarm optimization. The improved TLBO algorithm demonstrated superior performance, achieved lower design dimensions, and reduced costs. It provided more efficient solutions that pushed design constraints closer to their limits, resulting in a cost-effective and structurally sound cantilever retaining wall design. As a result of the study, the I-TLBO algorithm was found to be more cost and weight-effective than other methods in the optimization of cantilever retaining wall design.

Keywords: Retaining wall design, Cantilever retaining wall, Stability analyses, Optimization; teaching-learning-based optimization (TLBO)

*Corresponding author

1. Introduction

Retaining structures used to support different soil levels, prevent slope failure, or create flat surfaces for construction projects have vital importance in geotechnical engineering. Various forms of the retaining structure, such as gravity walls, cantilever walls, sheet pile walls, gabion walls, or reinforced soil, can be used to support the forces exerted by the retained soil, water pressure, seismic load, or surcharge loads. The major matter in the design of retaining structures is to provide internal stability and external stability requirements cost-effectively. Determination of optimal balance between structural integrity and the use of the material has great significance in the engineering aspects. The essence of optimization applications for this purpose is to find cost-effective solutions, reduce material usage and at the same time provide structural efficiency.

Cantilever retaining walls are a widely used structure type to sustain lateral earth stability and the use of this type of walls has been gradually increased since World War II [1]. Unlike other retaining wall designs, which rely on additional support from braces or tiebacks, a cantilever wall derives its strength from a rigid, vertical stem that extends into the ground. The stem is typically thicker at the base and tapers towards the top, creating a triangular cross-section. The key feature of a cantilever wall is the presence of a horizontal arm or "heel" at its base, which provides a counterbalance against the lateral pressure exerted by the retained material. This arm allows the wall to resist the forces acting on it and maintain stability. Additionally, a shear key subjected to passive earth pressure can be used to increase the stability of the wall.

There are many studies in the literature about the investigation of optimization methods that can be used to design reinforced cantilever retaining walls. Genetic algorithms [2], teaching learning-based algorithm [3], charged system search (CSS) and improved harmony search [4], fuzzy adaptive metaheuristic algorithm [5], big bang–big crunch [6], particle swarm optimization [7], ant colony optimization [8], grey wolf optimization [9], simulated annealing [10], evolutionary algorithms [11,12], multi-objective optimization, firefly algorithm (FA), harmony search algorithm (HS) and improved firefly algorithm-harmony search (IFA-HS) [13] are major methods used in the studies. These optimization methods can be used individually or in combination with each other to solve optimization problems. Although the optimization of retaining walls in terms of weight and cost has been investigated using different algorithms in the literature, there are very few studies investigating the optimization performances of these walls with TLBO and I-TLBO algorithms.

The Teaching-Learning-Based Optimization (TLBO) algorithm is an optimization method that takes its cues from how students collaborate to grow as individuals [14]. TLBO offers advantages such as simplicity in implementation, fewer parameters to tune, population-based exploration, analogy to teacher-student dynamics for better exploration, adaptability to various problems, global exploration, balanced exploration-exploitation, and no need for gradient information [14–16]. In many studies, the TLBO mechanisms have demonstrated excellent results, particularly in terms of convergence. However, it has been observed and seen in studies that the algorithm tends to get stuck in local optima in some problems [17]. To overcome this disadvantage, this study aims to enhance the TLBO algorithm. If the algorithm does not show improvement over a certain number of iterations, except for the best individual, individuals in the population are replaced with randomly generated agents. The studies on optimum design of cantilever retaining walls several soil properties such as different soil characteristics [18], soil heterogeneity [8], permeability [19], particle size [20] were considered using above-mentioned optimization algorithms.

This study intended to examine the performance of TLBO and I-TLBO algorithms for the optimal design of reinforced concrete cantilever retaining walls. The algorithms were coded in C# software considering the weight and cost of the structure was the object function. In this context, a widely used cantilever retaining wall example was used in the optimization process to compare the performance of the TLBO and I-TLBO approaches with other algorithms in the literature.

2. Optimization Process

General outlines of the study were prepared considering [9]. For the optimal design of a reinforced concrete retaining wall, two different objective functions were used in the context of variables and constraints. The first objective function used aims to design the retaining wall in the lightest possible form, independent of cost. The first objective function can be expressed as follows:

$$f_{weight} = W_{st} + W_c \quad (1)$$

W_{st} and W_c represent the total weight of reinforcement and concrete used in the retaining wall, respectively. The second objective function used aims to minimize the total cost based on material weights and can be expressed as follows:

$$f_{cost} = W_{st} C_s + W_c C_c \quad (2)$$

C_s and C_c represent the unit cost of reinforcement and concrete, respectively. The design variables given in Fig.1 were considered for calculating the weight and cost of the wall. Weights of concrete and reinforcement were taken into account in the determination of the cost of the wall. During the optimization phase, constraints were established based on safety factors against sliding, overturning, and bearing capacity parameters.

2.1. Design variables

Seven geometric and three structural design variables seen in Fig.1 were considered in the optimization process of the cantilever retaining wall. In accordance with the geometry of the wall, geometric design factors were selected, and structural design variables were modeled in relation to the critical sections of the wall. The variables X_1 , X_2 , X_3 , X_4 , and X_5 represent the width of the foundation, width of the toe, stem thickness at the bottom, stem thickness at the top, and foundation thickness respectively. Additionally, expressions of the reinforcements of the wall are R_1 : vertical reinforcement area, R_2 : the horizontal reinforcement area of the foundation, and R_3 : the horizontal reinforcement area of the heel per unit length of the wall.

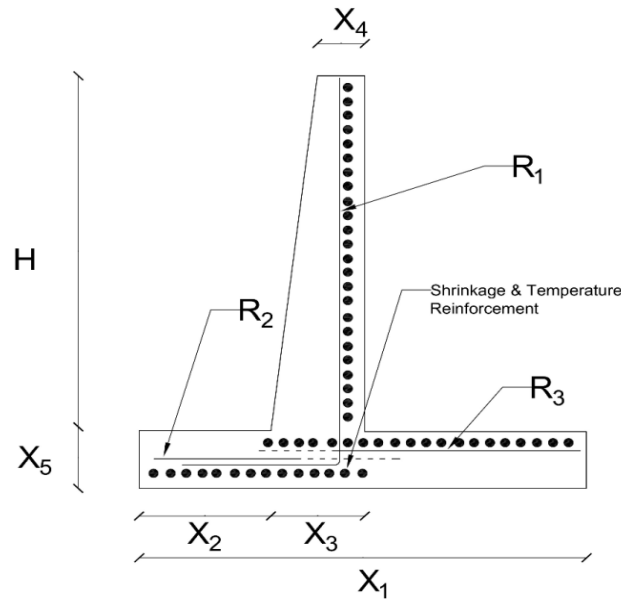


Figure 1. Design variables of the wall considered for the optimization process

The rebar used in the reinforcement design was limited to a range of 3 to 28 units in each direction, with diameters between 10 and 30. All possible cross-sections in this range that exceeded a total cross-sectional area of 127.42 cm² were excluded. In this context, a total of 264 cross-sections were used within the scope of optimization. The reinforcement pool prepared considering the abovementioned method is presented in Table 1.

Table 1. Reinforcement variable pool

Reinforcement index	Number of rebar	Bar size (mm)	Total steel area (cm ²)
1	3	10	2.356
2	4	10	3.141
3	3	12	3.393
4	5	10	3.927
.	.	.	.
.	.	.	.
.	.	.	.
131	14	18	35.626
132	18	16	36.191
133	8	24	36.191
134	24	14	36.945
.	.	.	.
.	.	.	.
.	.	.	.
261	20	28	123.150
262	28	24	126.669
263	18	30	127.234
264	24	26	127.423

2.1.1. Geotechnical modeling

Loads considered in the checks were presented in Fig. 2. In the context of the study following notation was assumed. W_S : weight of the wall, W_B : Weight of the soil block above the heel, Q_{SU} : Surcharge load, P_A : Active earth thrust actin on the soil block above the heel, P_B : Resultant of the base pressure, P_{p1} : Passive earth thrust actin on the foundation, and P_{p2} : Passive earth thrust acting on the stem of the wall. The plain-strain condition was supposed to simplify the problem. Therefore, loads per unit length of the wall were taken into account in the analyses.

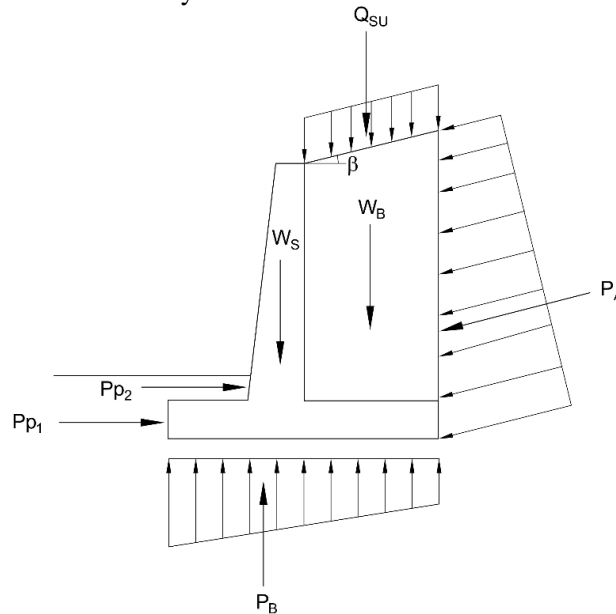


Figure 2. The thrusts considered in the optimization process

Active and passive lateral earth thrusts acting on the wall were calculated with Rankine Theory [21]. Active and passive earth pressure coefficients used for earth thrust calculations were obtained with Eq.(3) and Eq.(4) respectively. In the equations, the backfill inclination angle was represented with β and the internal friction angle of the backfill was represented with ϕ .

$$K_a = \frac{\cos \beta \left(\cos \beta - \sqrt{(\cos \beta)^2 - (\cos \phi)^2} \right)}{\cos \beta + \sqrt{(\cos \beta)^2 - (\cos \phi)^2}} \quad (3)$$

$$K_p = \left[\tan \left(45 + \frac{\phi}{2} \right) \right]^2 \quad (4)$$

Overtuning, sliding, and bearing capacity checks are the major components required to control the external stability of the wall. Safety factors were taken into account in the checks. The safety factor for overturning was determined by dividing the sum of the moments of driving force (ΣMD) by the sum of the moments of resisting force (ΣMR) (Eq.5). The moments about the front face of the toe were considered in the analyses.

$$F_{so} = \frac{\Sigma M_R}{\Sigma M_D} \quad (5)$$

Eq.(6) was used in the sliding checks. F_{SS} representing the safety factor for sliding was determined by dividing the resisting forces (ΣF_R) into driving forces (ΣF_D). Resisting forces and driving forces were determined with Eq.(7), Eq.(8), and Eq.(9). In calculation of the resisting force (Eq.(7)), strength parameters of the base soil (ϕ_{base} , c_{base}) were taken into account. On the other hand, the strength parameters of the backfill soil were considered in the determination of the driving force (Eq.(8)). Passive earth thrusts acting on the foundation and the stem were determined using Eq.(10). The term D_1 is the depth between foundation base and the soil surface that leads to passive earth pressure.

$$F_{ss} = \frac{\Sigma F_R}{\Sigma F_D} \quad (6)$$

$$\Sigma F_R = (\Sigma N) \tan \left(\frac{2}{3} \phi_{base} \right) + \frac{2}{3} B c_{base} + P_p \quad (7)$$

$$\Sigma F_D = P_A \cos \beta \quad (8)$$

$$\Sigma N = W_S + W_B + Q_{SU} + P_{a1y} + P_{a2y} \quad (9)$$

$$P_p = P_{p1} + P_{p2} = \frac{1}{2} \gamma_{fill} D_1^2 K_p + 2c D_1 \sqrt{K_p} \quad (10)$$

The ultimate bearing capacity of the base soil and maximum pressure applied from the foundation was calculated as follows for the bearing capacity check.

$$F_{SB} = \frac{q_u}{q_{max}} \quad (11)$$

Eq.(12) was used to determine the ultimate bearing capacity of the base soil. The Terzaghi ultimate bearing capacity theory [22] suggested for strip foundations was used to determine the q_u value. Due to the backfill, the foundation of the wall is subjected to eccentric load. This leads to a decrease in the ultimate bearing capacity of the base soil and therefore it is required to revise Eq.(12). For that purpose,

Meyerhof's Effective Area Method [23] was applied by reducing foundation width by twice the eccentricity (B-2e).

$$q_u = c_{base} N_c + \gamma_{fill} D_1 N_q + \frac{1}{2} \gamma_{base} N_\gamma (B - 2e) \quad (12)$$

Maximum and minimum pressure exerted from the foundation was calculated with Eq.(13). Eccentricity was calculated with Eq.(14). In the equation overturning moment was represented with M_o , the resisting moment was represented with M_R , and the total axial load was represented with ΣV .

$$q_{\min, \max} = \frac{\Sigma V}{B} \left(1 \pm \frac{6e}{B} \right) \quad (13)$$

$$e = \frac{\Sigma M_R - \Sigma M_o}{\Sigma V} \quad (14)$$

2.1.2. Structural modeling

Shear and moment capacity checks were performed for internal stability. Critical sections of the wall such as the heel, toe, and stem were taken into account in the checks. The study considered the parameters specified in Equation (15), where M_n represents the nominal flexural strength, E_s denotes the reduction factor, and M_d represents the design moment for the critical section, which is determined through the application of factored loads and forces.

$$E_s M_n \geq M_d \quad (15)$$

The strength reduction factor was assumed to be 0.9 considering the ACI 318-05 for tension controlled sections. Equations (16), (17), and (18), where T is the tension force acting on the nodal zone and C is the compression force acting on the nodal zone, were included in the calculation of M_n . Where f_y is the reinforcement's yield strength and is area, f_c is the compression strength of the concrete The stress block's width is denoted by b, its effective depth by d, and its equivalent rectangular stress block's depth by a.

$$M_n = T \left(d - \frac{a}{2} \right) \quad (16)$$

$$T = A_s f_y \quad (17)$$

$$C = 0.85 f_c b a \quad (18)$$

Eq.(21) was derived from Eq.(19) and (20). The equation was used to calculate the depth of the equivalent rectangular stress block (a) where c is the distance from the extreme compression bar to the neutral axis and β_1 is a factor based on f_c .

$$a = \beta_1 c \quad (19)$$

$$A_s f_y = 0.85 f_c b a \quad (20)$$

$$a = \frac{A_s f_y}{0.85 f_c b} \quad (21)$$

The criteria given in Eqs. (22), and (23) were considered in shear capacity design based on ACI 318-05 code.

$$E_s V_n \geq V_d \quad (22)$$

$$V_n = E_s 0.17 \sqrt{f_c} bd \quad (23)$$

Shear and moment strengths of the structure of the stem, toe, and heel were determined separately by taking into account the load factors given in Eqs. (24) and (25) where D, L, and H represent dead load, live load, and earth thrust exerted by earth pressure and groundwater pressure respectively.

$$U = 1.4D + 1.7L + 1.7H \quad (24)$$

$$U = 0.9D + 1.7H \quad (25)$$

The stem's shear and moment strengths were calculated using Equations (26-29). L_h is the foundation slab's heel portion, and cc is the depth of the concrete cover in Equations (28 and 29). The critical section of the toe, d_s , is given in Eq. (29) and is situated at $dt(X_5 - cc)$ distant from the wall.

$$Md_{stem} = 1.7 \left[qK_a \cos \beta \frac{(H_s + H)^2}{2} + K_a \gamma_{fill} \cos \beta \frac{(H_s + H)^3}{6} \right] \quad (26)$$

$$Vd_{stem} = 1.7 \left[qK_a \cos \beta (H_s + H - ds) + K_a \gamma_{fill} \cos \beta \frac{(H_s + H - ds)^2}{2} \right] \quad (27)$$

$$H_s = (L_h) \tan \beta \quad (28)$$

$$ds = X_5 - cc \quad (29)$$

The shear and moment strength calculations for the toe were performed with Eqs. (30) and (31). In the equations D is the depth of soil above the toe. l_{toe} is the length of the toe q_2 , q_{dt} , q_{max} and q_{min} were determined from the pressure distribution emanating from the foundation base. q_2 is the pressure acting on the intersection of stem and toe, and q_{dt} is the soil pressure at the critical section of the toe.

$$Md_{toe} = \left[1.7 \left(\frac{q_2}{6} + \frac{q_{max}}{3} \right) - 0.9 (\gamma_c X_5 + \gamma_{fill} D) \right] t_{toe}^2 \quad (30)$$

$$Vd_{toe} = \left[1.7 \left(\frac{q_{dt} + q_{max}}{2} \right) - 0.9 (\gamma_c X_5 + \gamma_{fill} D) \right] (l_{toe} - dt) \quad (31)$$

The shear and moment strength calculations for the heel were performed with Eqs. (32) and (33). In the equations q_1 was determined from the pressure distribution of the foundation. The pressure on the intersection of the heel and stem was considered as q_1 . W_{bs} is triangular backfill mass above the stem. W_{bsdh} is the backfill mass of the critical section

$$Md_{heel} = \left[\left(\frac{1.7q + 1.4\gamma_c X_5 + 1.4\gamma_{fill} H}{2} \right) + \left(\frac{1.4W_{bs}}{3} \right) + \left(\frac{q_1 + 2q_{min}}{6} \right) \right] L_H^2 \quad (32)$$

$$Vd_{heel} = \left[(1.7q + 1.4\gamma_c X_5 + 1.4\gamma_{fill} H) + 1.4 \left(\frac{W_{bs} + W_{bsdh}}{2} \right) - 0.9 \left(\frac{q_{dh} + q_{min}}{2} \right) \right] (L_h - dh) \quad (33)$$

The minimum area of flexural reinforcement and minimum steel reinforcement ratio were determined with Eqs. (34) and (35) considering the ACI 318–05.

$$A_{s_{\min}} = 0.25 \frac{\sqrt{f_c}}{f_y} bd \quad (34)$$

$$\rho = \frac{As}{bd} \quad (35)$$

The following formulations were used to determine the reinforcement ratio (ρ_b), development length (l_d), and development length of a standard hook (l_{dh}).

$$\rho_b = \left[\frac{0.85 \beta_1 f_c}{f_y} \right] \left[\frac{600}{600 + f_y} \right] \quad (36)$$

$$l_d = \left(\frac{12 f_y \psi_1 \psi_e \lambda}{25 \sqrt{f_c}} \right) d_b \rightarrow d_b \leq 19mm \quad (37)$$

$$l_d = \left(\frac{12 f_y \psi_1 \psi_e \lambda}{20 \sqrt{f_c}} \right) d_b \rightarrow d_b > 19mm \quad (38)$$

$$l_{dh} = \left(\frac{0.24 f_y}{\sqrt{f_c}} \right) d_b \quad (39)$$

3. Constraints

It is necessary to search a limited area for potential optimization problem solutions. The structural and geotechnical design constraints were established, and together these make up the search spaces[9]. In the context of the study, a total of 25 constraints were used in the optimization process. The constraints of the study can be classified into two subcategories: geotechnical constraints and structural constraints.

3.1. Geotechnical constraints

In the geotechnical constraints, factors of safety against slippage, overturning, and bearing capacity were considered. In this section, the constraints are expressed as follows in comparison with the design factors to avoid any collapse in the foundation soil.

$$g(1) = \frac{F_{SO_{design}}}{F_{S_o}} - 1 \leq 0 \quad (40)$$

$$g(2) = \frac{F_{SS_{design}}}{F_{S_s}} - 1 \leq 0 \quad (41)$$

$$g(3) = \frac{F_{SB_{design}}}{F_{S_B}} - 1 \leq 0 \quad (42)$$

3.2. Structural constraints

Components of a retaining wall have to fulfill the necessary requirements for reinforcing, moment, and shear capability. The following constraints were used to sustain internal integrity.

$$g(4) = q_{\min} - 1 \leq 0 \quad (43)$$

$$g(5-8) = \frac{M_d}{M_n} - 1 \leq 0 \quad (44)$$

$$g(9-12) = \frac{V_d}{V_n} - 1 \leq 0 \quad (45)$$

$$g(13-16) = \frac{A_{s_{\min}}}{A_s} - 1 \leq 0 \quad (46)$$

$$g(17-20) = \frac{A_s}{A_{s_{\max}}} - 1 \leq 0 \quad (47)$$

$$g(21) = \frac{X_2 + X_3}{X_1} - 1 \leq 0 \quad (48)$$

$$g(22) = \frac{X_6 + X_7}{X_1} - 1 \leq 0 \quad (49)$$

$$g(23) = \frac{l_{db_{stem}}}{X_5 - cc} - 1 \leq 0 \quad \text{or} \quad g(23) = \frac{l_{dh_{stem}}}{X_5 - cc} - 1 \leq 0 \quad (50)$$

$$g(24) = \frac{l_{db_{toe}}}{X_1 - X_2 - cc} - 1 \leq 0 \quad \text{or} \quad g(24) = \frac{12l_{dh_{toe}}}{X_5 - cc} - 1 \leq 0 \quad (51)$$

$$g(25) = \frac{l_{db_{heel}}}{X_2 + X_3 - cc} - 1 \leq 0 \quad \text{or} \quad g(25) = \frac{l_{dh_{heel}}}{X_5 - cc} - 1 \leq 0 \quad (52)$$

4. Improved Teaching-Learning Based Optimization Algorithm with Agents

The Teaching-Learning-Based Optimization (TLBO) algorithm is an optimization algorithm based on the process of students in a classroom interacting with each other to improve themselves [1, 24]. The algorithm consists of two main phases. In the first phase, the individual with the best objective function value in the population tries to improve other individuals. Individuals that show improvement in terms of the objective function are updated. In the second phase, individuals in the population engage in one-to-one interactions, striving for improvement. At this point, the individuals that show progress are updated to enhance the population. This algorithm has been tested in various optimization problems and has shown highly effective results in the context of structural optimization [2-5]. In many studies, the TLBO mechanisms have demonstrated excellent results, particularly in terms of convergence. The local optimum avoidance mechanisms of population-based algorithms are important for the results obtained. This study aims to enhance the TLBO algorithm, in this respect. When the algorithm gets stuck at the local optimum, it is usually due to the population clustering around a particular solution. Therefore, it is useful to have a mechanism for the algorithm to move out of this clustering area. There are numerous studies developed in this regard [3, 6]. In this study, a local optimum avoidance approach suitable for the problem is developed. Before activating the developed mechanism, the algorithm tries to find out whether it is stuck at the local optimum. This decision is determined as no improvement of the best solution over a predetermined number of generations. For this problem, this number was set to 10 generations. Then the mechanism switches on and replaces all individuals in the population with new individuals whose parameters are randomly determined, except for the best solution. These new individuals injected into the algorithm are identified as agents and the activation of the mechanism is

tracked by the variable "agentcounter". Once the agents have been activated, the variable is reset to zero and the algorithm starts following the course of the algorithm again. The flowchart of this improved version of the TLBO algorithm is shown in Figure 3. The boundary values of the parameters for the optimization process are presented in table x.

Table 2. Boundries of the parameters [7]

Design variable	Lower Bound	Upper Bound
X1	1.3090 m	2.3333 m
X2	0.4363 m	0.7777 m
X3	0.2000 m	0.3333 m
X4	0.2000 m	0.3333 m
X5	0.2722 m	0.3333 m
R1	Index: 1 2.356 cm ²	Index: 264 127.423 cm ²
R2	Index: 1 2.356 cm ²	Index: 264 127.423 cm ²
R3	Index: 1 2.356 cm ²	Index: 264 127.423 cm ²

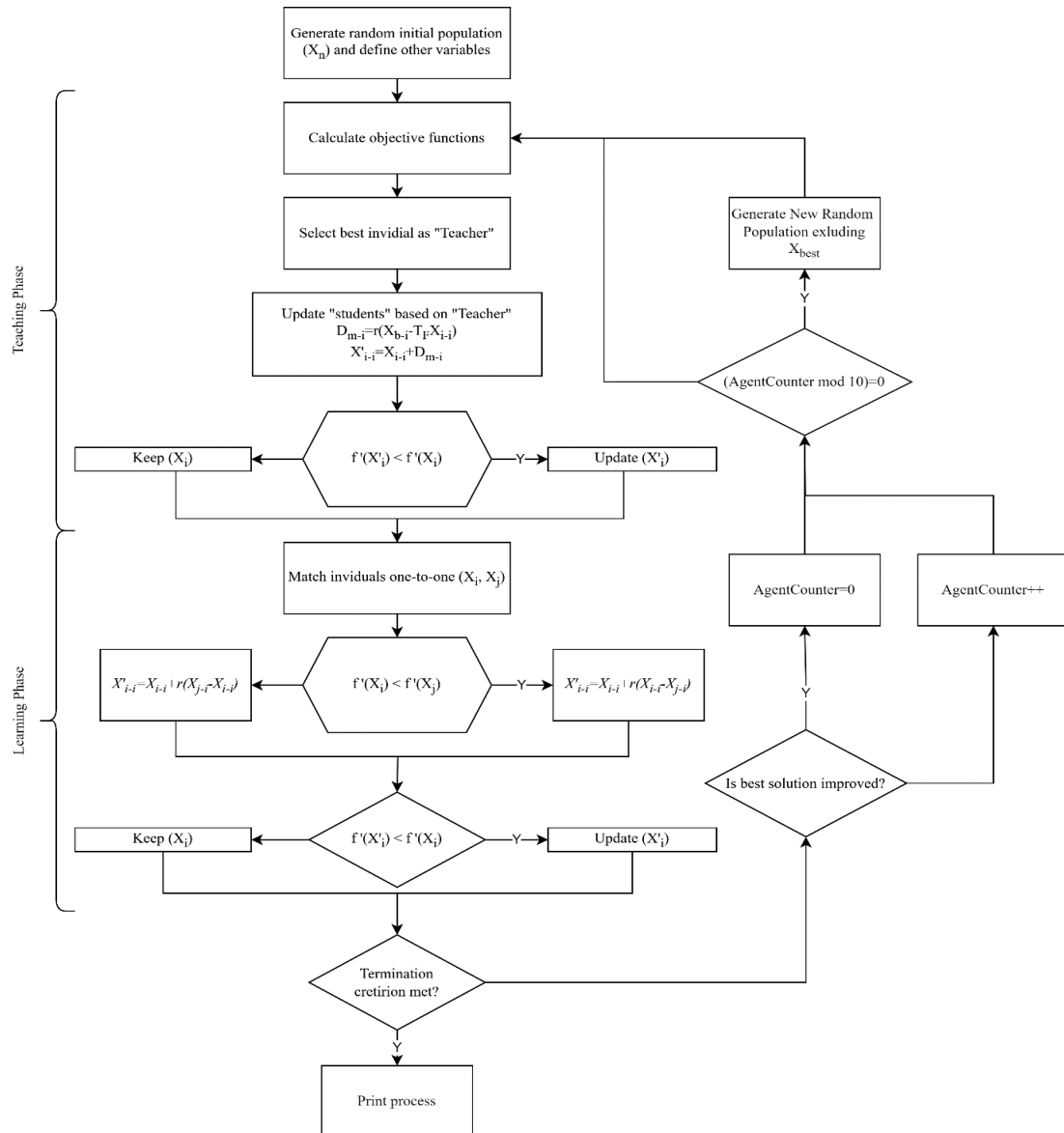


Figure 3. Flowchart of the I-TLBO with agents

A numerical example used by several studies [6, 9, 11, 25] was taken into account to evaluate the efficiency of the suggested algorithms. Table 3 displays the design parameters and wall measurements taken into account in the numerical example. The parameters in the Table 3 represents a case used in the optimizing the cantilever retaining wall. Field or laboratory tests were not performed to obtain the parameters.

Table 3. Parameters considered for the example [9]

Input parameters	Symbol	Value	Unit
Height of stem	H	3	m
Steel reinforcement yield strength	f_y	400	MPa
Compressive strength of concrete	F_c	21	MPa
Concrete cover	cc	7	cm
Shrinkage and temperature reinforcement percentage	ρ_{st}	0.002	-
Surcharge load	Q	20	kPa
Backfill slope	B	10	°
Internal friction angle of base soil	ϕ_{base}	0	°
Internal friction angle of retained soil	ϕ	36	°
Unit weight of retained soil	γ_{fill}	17.5	kN/m ³
Unit weight of base soil	γ_{base}	18.5	kN/m ³
Unit weight of steel	G _s	78.5	kN/m ³
Unit weight of concrete	γ_c	23.5	kN/m ³
Depth of soil in front of the wall	D	0.5	m
Cost of steel	C _s	0.4	\$/kg
Cost of the concrete	C _c	40	\$/kg
The factor of safety for overturning stability	FSO _{design}	1.5	-
The factor of safety for sliding	FSS _{design}	1.5	-
The factor of safety for bearing capacity	FSB _{design}	1.5	-
The base soil's cohesiveness	c _{base}	125	kPa

The performance of TLBO was evaluated by several studies in the literature [26, 27]. In the study, TLBO was separately applied with both the traditional version and the version developed in this study for the two objective functions mentioned. As a result, four different optimization processes were planned. For each process, the stopping criterion of the algorithm was set as not improving the current best solution for 50 iterations. Each process was run five times, and the variable values and outcomes of the best solutions obtained were presented in Table 4.

Table 4. Results of optimization processes.

	Best-Weight		Best-Cost	
	TLBO	I-TLBO	TLBO	I-TLBO
X ₁	1.67	1.60	1.72	1.66
X ₂	0.57	0.59	0.60	0.53
X ₃	0.21	0.21	0.28	0.30
X ₄	0.20	0.20	0.23	0.20
X ₅	0.28	0.28	0.28	0.28
R ₁	78	76	38	76
R ₂	120	33	17	33
R ₃	76	28	17	28
Best	2659.714 (kg)	2627.293 (kg)	74.8866 (\$)	72.0398 (\$)
Mean ± Std.D.	2779.05 ± 53.60	2694.69 ± 24.97	81.35 ± 2.62	75.36 ± 1.11

As can be seen, the improved version of the algorithm has produced better results in terms of both average and best values for both objective functions. The capacity utilization ratios (CUR) values were used to show the extent to which the algorithm is proportionally challenging the constraints to which it is subjected. In this way, it is tried to show how effective the optimization algorithm produces effective results from a different perspective in terms of the problem. The capacity utilization ratios of the

obtained optimal designs in terms of constraints for each combination are presented in Figure 4. As can be seen in Figures 4a and 4b, where the CUR values for the weight-optimized designs are presented, the improved version of TLBO uses limiters with a higher capacity. The corresponding utilization ratios are on average 0.427 for TLBO and 0.459 for I-TLBO. It can be seen from Figs. 4c and 4d, the same is true for the optimization process for the best cost. In this context, the average CUR values are 0.476 for TLBO and 0.484 for I-TLBO. Therefore, it can be argued that for both optimization processes, the improved version of the TLBO algorithm pushes the bounding capacities to a higher extent than the original version.

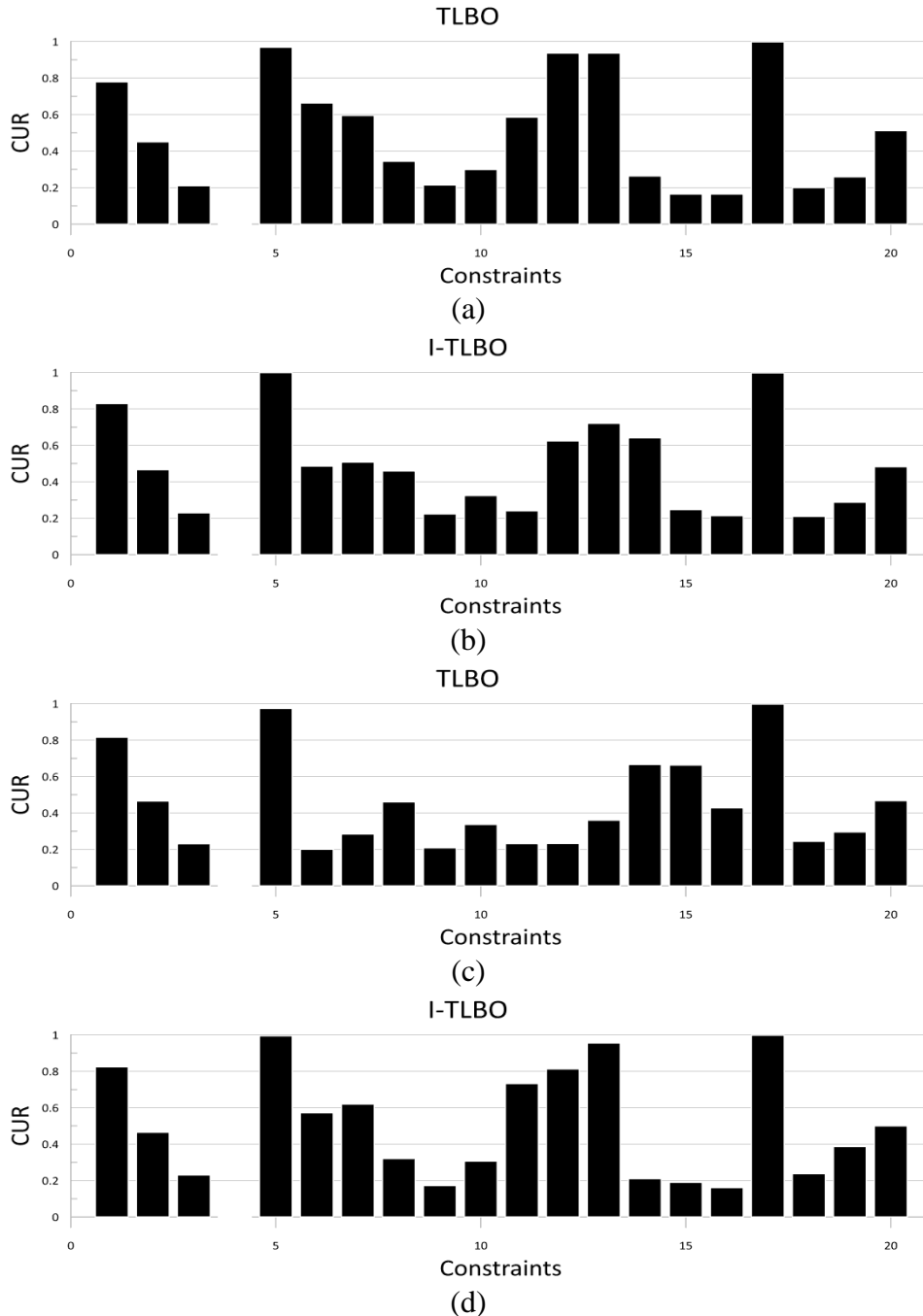


Figure 4. Capacity utilization ratios (CUR) of best solutions (a) TLBO-Best weight, (b) I-TLBO-best weight (c) TLBO-Best cost, (d) I-TLBO-Best cost

It can be observed that the improved TLBO approach brings the constraint capacities closer to their limits compared to the traditional version. Additionally, the convergence curves of the two algorithms used separately for each objective function are provided in Figs. 5 and 6 throughout the process.

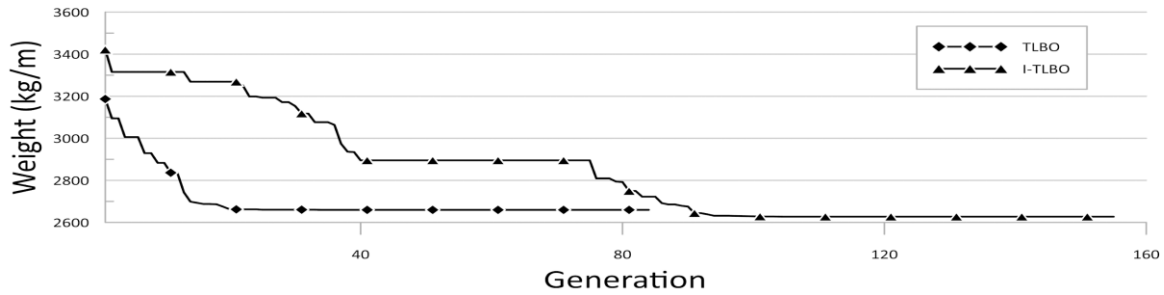


Figure 5. Convergence history for weight optimization

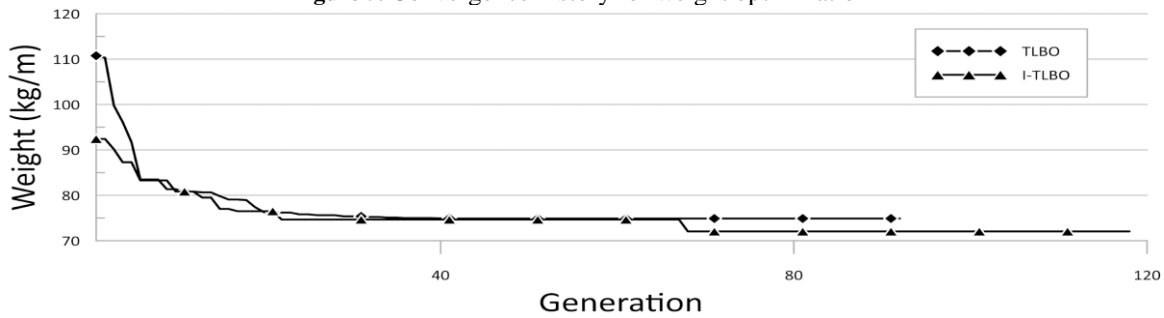


Figure 6. Convergence history for cot optimization

The wall's dimension (X_1 - X_5) and the sections of reinforcements (R_1 - R_3) of the reinforcements used in the wall were considered design variables. The optimum values of the X and the R variables were determined with TLB and I-TLBO algorithms based on minimum weight and minimum cost. In Table 5 and Table 6, the optimum values determined by TLBO and I-TLBO algorithms are compared with other algorithms in the literature. Grey Wolf Optimization (GWO) [9], Search Group Algorithm (SGA) and Backtracking Search Algorithm (BSA) [29], Big Bang–Big Crunch Algorithm (BB-BC) [6], Genetic Algorithm (GA) [11], Differential Evolution (DE), Evolutionary Strategy (ES), Biogeography Based Optimization Algorithm (BBO), Differential Evolution (DE), Evolutionary Strategy (ES), Biogeography Based Optimization Algorithm (BBO), Interior Search Algorithm (ISA) [30], Particle Swarm Optimization (PSO), Accelerated Particle Swarm Optimization (APSO) [28] were evaluated in the comparison. As can be seen from Table 5, TLBO algorithms yielded significantly lower dimensions than the other approaches, especially in X_1 , X_2 , and X_3 dimensions. As a result of the evaluation between TLBO and I-TLBO algorithms, it is seen that the I-TLBO algorithm gives a lower dimension for the X_1 dimension, and the TLBO algorithm gives a lower dimension for the X_2 dimension.

Table 5. Low-weight design variables determined with various optimization approaches

	X_1	X_2	X_3	X_4	X_5	R_1	R_2	R_3
TLBO (This study)	1.67	0.57	0.21	0.20	0.28	78	120	76
I-TLBO (This study)	1.60	0.59	0.21	0.20	0.28	76	33	28
GWO	1.80	0.67	0.21	0.20	0.28	82	15	15
SGA	1.71	0.65	0.20	0.20	0.27	77	23	17
BSA	1.71	0.64	0.20	0.20	0.27	77	14	14
BB-BC	1.74	0.65	0.20	0.20	0.27	77	17	17
ISA	1.84	0.75	0.39	0.20	0.27	34	15	15
DE	1.87	0.62	0.29	0.20	0.27	34	19	16
GA	1.91	0.58	0.27	0.20	0.28	50	21	15
BBO	1.84	0.74	0.27	0.20	0.27	37	14	14
ES	1.84	0.69	0.32	0.22	0.28	26	22	29
APSO	1.84	0.57	0.27	0.20	0.27	40	28	17
PSO	1.84	0.74	0.29	0.20	0.27	33	14	14

The mean and best objective function values for the algorithms are displayed in Table 6. It is seen from the table that TLBO algorithms are among the algorithms that give the lowest weight value. As a result of the comparison between TLBO and I-TLBO algorithms, it is seen that the I-TLBO algorithm provides a lower-weight design.

Table 6. Comparison of low-weight design results (kg/m)

	Best	Mean
TLBO (This study)	2659.714	2779.05 ± 53.60
I-TLBO (This study)	2627.293	2694.69 ± 24.97
GWO	2721.7915	2748.7809
SGA	2584.46	2589.00
BB-BC	2608.38	-
ISA	2665.8027	2677.5681
GA	2744.80	2850.90
DE	2726.50	2851.00
ES	2762.40	2845.00
BBO	2665.80	2677.70
PSO	2665.80	2687.60
APSO	2668.00	2687.60
FA	2666.50	2673.40
CS	2665.80	2665.80

The optimum values of the X and the R variables determined with low-cost design objective function were presented in Table 7. In this section, the cost-based performances of TLBO algorithms were compared with algorithms such as Genetic Algorithm (GA), Differential Evolution (DE), Evolutionary Strategy (ES), and Biogeography Based Optimization (BBO) [28]. From Table 7, it is seen that TLBO algorithms offer lower cross-sections than the other algorithms especially for X₁ and X₂. As a result of the comparison between I-TLBO and TLBO algorithms, it is seen that lower values are obtained with the I-TLBO algorithm.

Table 7. Low-cost design variables determined with various optimization approaches (\$/m)

	X ₁	X ₂	X ₃	X ₄	X ₅	R ₁	R ₂	R ₃
TLBO (This study)	1.720	0.600	0.280	0.230	0.280	38	17	17
I-TLBO (This study)	1.660	0.530	0.300	0.200	0.280	76	33	28
GA	1.91	0.586	0.272	0.201	0.280	40	21	15
DE	1.872	0.616	0.290	0.206	0.271	34	19	16
ES	1.845	0.691	0.320	0.221	0.280	26	22	29
BBO	1.842	0.737	0.277	0.200	0.270	91	36	44

Table 8 presents the final low-cost design objective function values, including the best, mean, and SD values. As shown in the table, the best low-cost design was achieved by the I-TLBO algorithm with the best of \$72.0398/m. When the mean values are considered, it is seen that the I-TLBO algorithm offers the lowest cost design after the BBO algorithm. On a cost basis, the I-TLBO algorithm suggests a significantly lower cost design compared to the TLBO algorithm.

Table 8. Comparison of design cost for the example (\$/m)

	Best	Mean
TLBO (This study)	74.8866	81.35 ± 2.620
I-TLBO (This study)	72.0398	75.36 ± 1.110
GA	77.6300	82.16 ± 1.600
DE	75.4900	82.23 ± 1.673
ES	78.0700	81.71 ± 1.308
BBO	73.0800	73.91 ± 0.827

5. Conclusions

This study intended to optimize the design of reinforced concrete cantilever retaining walls using the Teaching-Learning-Based Optimization (TLBO) algorithm and an improved version of TLBO called I-TLBO. The design objectives were to minimize the weight and the cost of the retaining wall while satisfying various geotechnical and structural constraints. The optimization process involved determining optimal values for design variables related to wall dimensions and reinforcement areas. Key conclusions drawn from the study are as follows:

- The TLBO algorithms, both the traditional version and I-TLBO, outperformed other optimization algorithms in terms of achieving lower weights and costs for the retaining wall design.
- The I-TLBO algorithm provided better results in terms of both mean and best values for both the weight and cost optimization objectives.
- Both TLBO algorithms, especially I-TLBO, brought the constraint capacities closer to their limits compared to the traditional version, indicating improved constraint satisfaction.
- The convergence history of the algorithms showed that I-TLBO converged faster and achieved better solutions compared to the traditional TLBO, highlighting the effectiveness of the introduced improvements.

In summary, the study demonstrated that the I-TLBO algorithm, an improved version of the TLBO algorithm, is highly effective for optimizing the design of reinforced concrete cantilever retaining walls. It consistently provided better results in terms of both weight and cost optimization compared to other algorithms considered in the study. While the study shows promise for I-TLBO, it would be beneficial to compare its performance with other well-established optimization algorithms for retaining wall design problems. This would provide a broader perspective on its effectiveness.

6. Credit Authorship Contribution Statement

Bilal Tayfur: Investigation, Conceptualization, Data analysis, Validation; Hakan Alper Kamiloğlu: Methodology, Investigation, Writing, Review and editing.

7. Ethics Committee Approval and Conflict of Interest

The authors declare that they have no known competing financial interests or personal relationships that could have appeared to influence the work reported in this paper.

8. References

- [1] A. Scotto di Santolo, and A. Evangelista, "Dynamic active earth pressure on cantilever retaining walls", *Comput. Geotech.* vol. 38, pp. 1041–1051, 2011.
- [2] A. Kaveh, M. Kalateh-Ahani and M. Fahimi-Farzam, "Constructability optimal design of reinforced concrete retaining walls using a multi-objective genetic algorithm." *Struct. Eng. Mech.*, vol. 47, pp. 227–245, 2013.
- [3] R. Temur and G. Bekdas, "Teaching learning-based optimization for design of cantilever retaining walls." *Struct. Eng. Mech.* vol. 57, pp. 763–783, 2016.
- [4] A. Kaveh and A.F. Behnam, "Charged system search algorithm for the optimum cost design of reinforced concrete cantilever retaining walls." *Arab. J. Sci. Eng.* vol. 38, pp. 563–570, 2013.
- [5] F. Keivanian, R. Chiong, A.R. Kashani, and A.H. Gandomi, "A fuzzy adaptive metaheuristic algorithm for identifying sustainable, economical, lightweight, and earthquake-resistant reinforced concrete cantilever retaining walls." *ArXiv. Prepr. ArXiv.* 2302.00198.
- [6] C.V. Camp, and A. Akin, "Design of retaining walls using big bang–big crunch optimization." *J. Struct. Eng.* Vol.138, pp.438–448.
- [7] S. Srivastava, S. Pandey, and R. Kumar, "Optimization of reinforced concrete cantilever retaining wall using particle swarm optimization." *IOP Conf Ser Mater Sci Eng* vol. 1225:012042, 2022.

- [8] C. Xu, B. Gordan, M. Koopialipoor, D. J. Armaghani, M.M. Tahir, and X. Zhang, "Improving performance of retaining walls under dynamic conditions developing an optimized ANN based on ant colony optimization technique." *IEEE Access*, Vol. 7, 94692–700, 2019.
- [9] E.N. Kalemci, S.B. İkizler, T. Dede and Z. Angın, "Design of reinforced concrete cantilever retaining wall using Grey wolf optimization algorithm" *Structures*, vol. 23, pp. 245–253, 2020.
- [10] B. Ceranic, C. Fryer and R.W. Baines, "An application of simulated annealing to the optimum design of reinforced concrete retaining structures." *Comput. Struct.* vol. 79, pp.1569–1581, 2001.
- [11] A.H. Gandomi, A.R. Kashani, D.A. Roke and M. Mousavi, "Optimization of retaining wall design using evolutionary algorithms." *Struct. Multidiscip. Optim.* vol. 55, pp. 809–825, 2017.
- [12] A.H. Gandomi, and A.R. Kashan, "Automating pseudo-static analysis of concrete cantilever retaining wall using evolutionary algorithms." *Measurement*, vol. 115, pp. 104–124.
- [13] R. Sheikholeslami, B.G. Khalili, A. Sadollah and J. Kim, "Optimization of reinforced concrete retaining walls via hybrid firefly algorithm with upper bound strategy." *KSCE J. Civ. Eng.* vol. 20, pp. 2428–2438, 2016.
- [14] R.V. Rao, V.J. Savsani, and D.P. Vakharia, "Teaching-learning-based optimization: A novel method for constrained mechanical design optimization problems." *CAD Comput. Aided. Des.* vol. 43, pp. 303–315, 2011.
- [15] R.V. Rao, V.J. Savsani, and D.P. Vakharia, "Teaching-learning-based optimization: an optimization method for continuous non-linear large scale problems." *Inf. Sci. (Ny)*. vol.183, pp.1–15.
- [16] F. Zou, L. Wang, X. Hei, D. Chen and D. Yang, "Teaching-learning-based optimization with dynamic group strategy for global optimization." *Inf. Sci. (Ny)* vol. 273, pp.112–131.
- [17] M. Črepinšek, S.H. Liu, and L. Mernik, "A note on teaching-learning-based optimization algorithm." *Inf. Sci. (Ny)*, vol.212, pp. 79–93, 2012.
- [18] E. Uray, and S. Çarbaş, "Dynamic loads and different soil characteristics examination on optimum design of cantilever retaining walls utilizing Harmony Search Algorithm." *I. Int. J. Eng. Appl. Sci.*, vol.213, pp. 140-154, 2021.
- [19] N.H. Ri, Y.S. Ri, Y.A. Kim Z. Ma, and Y. Liu and S. Çarbaş, "Stability analysis and size optimization of retaining walls on unsaturated soil." *Soil Mech. Found. Eng.*, vol.57, pp. 191-199, 2020.
- [20] G. Bath, J. Dhillon and B. Walia, "Optimization of geometric design of retaining wall by Differential Evolution Technique" *Int. J. Comput. Eng. Res.*, vol.8, pp. 191-199, 2018.
- [21] W.J.M. Rankine. "On the stability of loose earth." *Philos Trans R Soc London* 1857;147:928.
- [22] K. Terzaghi, *Theoretical Soil Mechanics*. New York: Wiley; 1943.
- [23] G.G. Meyerhof. *The Bearing Capacity of Foundations Under Eccentric and Inclined Loads*. 3rd ICSMFE, Zürich: 1953, p. 440–5.
- [24] V. Toğan, "Design of planar steel frames using Teaching-Learning Based Optimization." *Eng. Struct.* vol. 34, pp. 225–232, 2012.
- [25] R.V. Rao and V. Patel, "An improved teaching-learning-based optimization algorithm for solving unconstrained optimization problems." *Sci. Iran.* vol. 20, pp. 710–720.
- [26] M. Artar, and S. Carbas, "Discrete sizing design of steel truss bridges through teaching-learning-based and biogeography-based optimization algorithms involving dynamic constraints." *Structures*, vol. 34 pp. 3533–3547, 2021.
- [27] S.O. Degertekin and M.S. Hayalioglu, "Sizing truss structures using teaching-learning-based optimization." *Comput. Struct.* vol. 119, p.p. 177–188, 2013.
- [28] S.O. Degertekin and M.S. Hayalioglu, "Sizing truss structures using teaching-learning-based optimization." *Comput. Struct.* vol. 119, p.p. 177–188, 2013.
- [29] Lopez R, "Optimum project of cantilever retaining wall using search group algorithm and backtracking search algorithm." *Rev. Int. Métodos. Numéricos. Para. Cálculoy. Diseño. En. Ing.* 2017.
- [30] A.H. Gandomi, A.R. Kashani, and F. Zeighami, "Retaining wall optimization using interior search algorithm with different bound constraint handling." *Int. J. Numer. Anal. Methods. Geomech.* vol. 41, pp. 1304–1331, 2017.



Çelik Taban Plaka ile Manşonlu Ankraj Çubuğu Bağlantılarının Performans Değerlendirmesi

Muhammed ATAR^{1*} , Erkut SAYIN² 

^{1,2}İnşaat Mühendisliği Bölümü, Mühendislik Fakültesi, Fırat Üniversitesi, 23119 Elazığ, Türkiye.

¹matar@firat.edu.tr, ²esayin@firat.edu.tr

Geliş Tarihi: 12.07.2023

Kabul Tarihi: 18.04.2024

Düzeltilme Tarihi: 28.12.2023

doi: <https://doi.org/10.62520/fujece.1465442>

Araştırma Makalesi

Alıntı: M. Atar, E. Sayın, “Çelik taban plaka ile manşonlu ankraj çubuğu bağlantılarının performans değerlendirme”, Fırat Üni. Deny. ve Hes. Müh. Derg., vol. 3, no 2, pp. 151-159, Haziran 2024.

Öz

Bu araştırma, çevrimsel yükleme altında çelik ankraj ile açıkta kalan taban plakası bağlantılarının performansına odaklanan bir çalışmanın sonuçlarını sunmaktadır. Çalışma, kolon-ankraj bağlantılarının sünekliğini artırmayı amaçlayan yeni bir methodu tanıtmaktadır. Taban plakası ile ankraj çubuğu rondelası arasında belirli bir geometriye sahip bir çelik pul dahil edilerek, bağlantıdaki yük yolu kesintiye uğrar ve bu da daha sünek bir davranış elde edilmesini sağlar. Araştırma, yeni yöntem metodunu tanıtmak amaçlı, farklı pul şekillerine sahip açıkta kalan taban plakası bağlantılarını incelemek için doğrulanmış ve sonuçları karşılaştırılmış bir sonlu eleman (FE) modeli kullanır. Bu çalışmada açıklanan yenilikçi yaklaşım, bağlantıların kapasitelerine ek olarak bağlantıların dönme kapasitesini önemli ölçüde geliştirme potansiyeline sahiptir.

Anahtar kelimeler: Çevrimsel yükleme, Taban plakası bağlantısı, Süneklik, Güçlendirme, Dönme kapasitesi

*Yazışılan Yazar

İntihal Kontrol: Evet – Turnitin

Şikayet: fujece@firat.edu.tr

Telif Hakkı ve Lisans: Dergide yayın yapan yazarlar, CC BY-NC 4.0 kapsamında lisanslanan çalışmalarının telif hakkını saklı tutar.



Performance Assessment of Base Plate Connections with Anchor Rod Sleeves

Muhammed ATAR^{1*} , Erkut SAYIN² 

^{1,2}Civil Engineering Department, Engineering Faculty, Firat University, 23119 Elazig, Türkiye.

¹matar@firat.edu.tr, ²esayin@firat.edu.tr

Received: 12.07.2023

Accepted: 18.04.2024

Revision: 28.12.2023

doi: <https://doi.org/10.62520/fujece.1465442>

Research Article

Citation: M. Atar, E. Sayın, "Performance assessment of base plate connections with anchor rod sleeve", Firat Univ. Jour. of Exper. and Comp. Eng, vol. 3, no 2, pp. 151-159, June 2024.

Abstract

This research presents findings from a study focused on evaluating the performance of exposed base plate connections featuring anchor rods under cyclic loading conditions. The study introduces an innovative sleeve system approach designed to enhance the ductility of column base connections. The inclusion of a steel sleeve with defined geometric characteristics between the base plate and the anchor rod washer modifies the load path within the connection, resulting in a more ductile response. The study utilizes a validated finite element (FE) model to analyze exposed base plate connections featuring different sleeve shapes, illustrating the concept behind this novel method. The innovative approach discussed in this research has the potential to significantly increase the rotational capacity of connections without compromising their inherent strength.

Keywords: Cyclic loading, Base plate connection, Ductility, Retrofitting, Rotational capacity

*Corresponding author

Plagiarism Checks: Yes – Turnitin

Complaints: fujece@firat.edu.tr

Copyright & License: Authors publishing with the journal retain the copyright to their work licensed under the CC BY-NC 4.0

1. Introduction

Exposed base plate connections are widely employed for transmitting axial stresses, shear, and moments from the steel structure to the foundation. The overall structural performance during earthquakes is heavily influenced by the rotational capacity and energy dissipation capabilities of these base plate connections. As a result, extensive research has been conducted on exposed base plate connections to enhance their performance characteristics [1-10].

The ductile anchor approach, as recommended by several studies [6, 8, 11, 12, 13], has been suggested to improve the rotational capacity of base connections. Various tests, including tension tests on individual anchor rods [10] and combined shear and tension tests [11], have been carried out to evaluate the impact of elongation length on deformation capacity. The force generated in the anchor rod is affected by both the bearing between the anchor and grout and exposed length, which significantly impact the overall strength of the connection. Additionally, Shaheen et al. [14] introduced a novel sleeve system applied to exposed base plate connection aimed at improving the rotational capacity, which was investigated through detailed numerical analysis. The analyses released that the proposed system noticeably increases the rotational connection capacity under monotonic loading conditions. Additionally, it is important to highlight that the research in the previous study was conducted under monotonic loading conditions [14]. This may not directly apply to connections exposed to dynamic forces, such as seismic events, without additional research.

This study introduces a novel sleeve system with the goal of enhancing deformation capacity of exposed base plate connections subjected to cyclic loading. This suggested approach not only improves the effectiveness of newly installed base plate connections but also serves as a cost-effective retrofitting device for existing connections. In the case of retrofitting phenomena, if the rod falls short in length to fit the sleeve between the washer and the base plate, it can be elongated through the use of a coupling nut or through welding for the retrofitting purpose. The focus of the research is primarily on exposed base plate connections with thick plates, where failure is predominantly influenced by the anchor rod. To carry out the parametric analysis, a finite element (FE) model is employed, which has been validated through experimental testing.

2. System Description

The proposed sleeve system is illustrated in Figure 1, where it is positioned between the base plate and the washer of the anchor rod in the exposed base plate connection. The sleeve system can be identified by its characteristics such as thickness, length and wall curvature, which is incorporated to prevent immediate buckling of the wall and lead to bending failure. The curvature of the sleeve wall is determined by the amplitude and waveform of the sleeve. Although several waveform configurations may define the sleeve design, the objective is to achieve optimal structural performance with minimal manufacturing costs. This study specifically focuses on a sleeve design with positive Gaussian curvature, as negative Gaussian curvatures may necessitate a non-standard washer due to the substantial forces resulting from the bearing between the sleeve and the washer.

To ensure increased ductility, it is essential for the sleeve to undergo bending deformation before any other components of the connection fail. For this reason, the capacity of the sleeve must be less than the force applied to the anchor rod at the point of failure. This ensures that the sleeve absorbs a significant portion of the forces and allows for controlled deformation, promoting a more ductile behaviour of the overall base plate connection

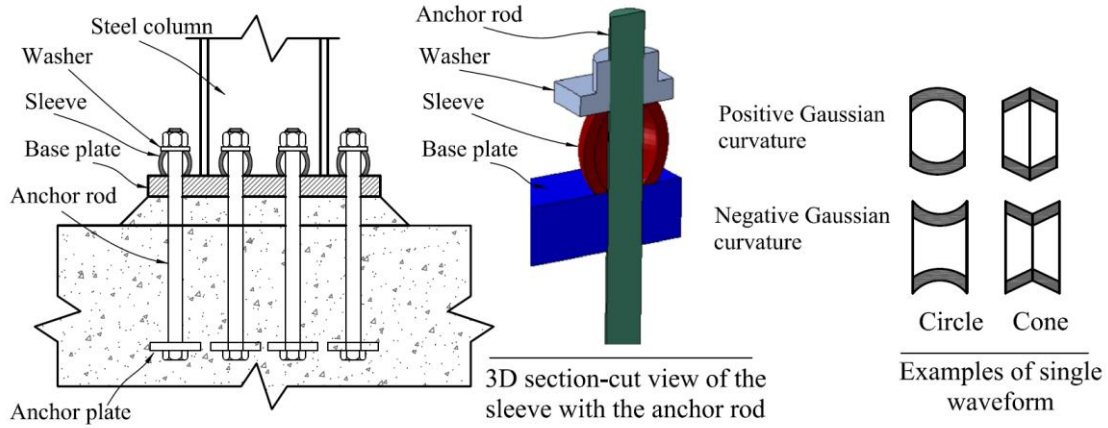


Figure 1. Base plate connection with sleeve application [13]

3. Finite Element Model Development

The column base connection depicted in Figure 2 was modelled using 3D FE implicit solver analysis in ABAQUS/CAE [15]. The accuracy of the FE model was verified by comparing it with the experimental test (#M2) conducted by Gomez et al. [16]. To simplify the modelling process, only half of the test specimen was simulated due to its symmetric geometry and boundary conditions. The symmetry axis was defined to run through the centre of the column's web as detailed in Figure 2.

The column and base plate were represented using shell elements (S4R), while the grout and the upper portion of the anchor rods were modelled using solid elements (C3D8R). To reduce computational costs, the portion of the anchor rod beneath the lower surface of the grout was modelled using beam elements (B31), and a coupling constraint was assigned between the two parts of the anchor rod. It is important to note that the concrete pedestal and foundation were not included in the model. However, lateral restraints were applied to the anchor rod using beam elements, and the bottom surface of the concrete grout was restrained in both the vertical and lateral directions to simulate the effects of the overall connection system.

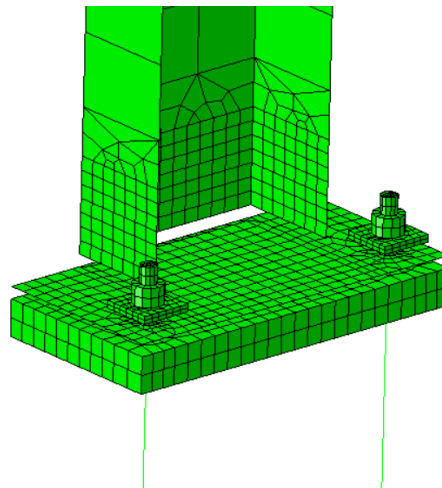


Figure 2. Exposed base plate FE modelling presentation

In the FE model of the connection part, surface-to-surface interactions were incorporated between various components. All the surface interactions (anchor rod - base plate, bottom surface of the base plate - top surface of the concrete grout, washer - base plate) included a coefficient of friction of 0.2

[14]. For certain components, such as anchor rod-nut, and nut-washer, monolithic surface interactions were employed. This means that separation between these components was not allowed during the analysis, assuming a rigid connection. Similarly, since the welds did not experience any crack deformations during the test, a monolithic surface was considered for the surface interacted between the base plate and column.

A bilinear von Mises yield criterion with isotropic hardening was utilized to model the material behaviour in the FE model of connection. The material properties were determined based on the findings of Gomez et al. [3]. For the anchor rod, the yield stress (f_y) was set to 785 MPa, and the ultimate stress (f_u) was set to 1010 MPa. Regarding the base plate, the yield stress (f_y) was defined as 278 MPa, while the ultimate stress (f_u) was set to 473 MPa. The constitutive model employed for the concrete material was assumed to be elastic-perfectly-plastic, since a compressive strength of 25 MPa was entered to the concrete material.

4. FE Model Validation

In this subsection, the experimental performance of an exposed base plate connection was validated through a 3D FE modelling simulation analysis. The model was subjected to lateral loading using displacement control with cyclic drift, following the methodology described in reference [3]. The moment-rotation results obtained from the FE analysis were compared to the experimental test results, and a strong agreement between the two was observed, as shown in Figure 3. This agreement indicates that the FE model accurately presents the elastic and plastic behaviour of the reference model connection. Furthermore, it is noteworthy that the tested connection had a capacity of 120 kN.m, while the FE model predicted a capacity of 118 kN.m. The alignment between the experimental and FE model capacities illustrates a high level of accuracy in predicting the performance of the connection.

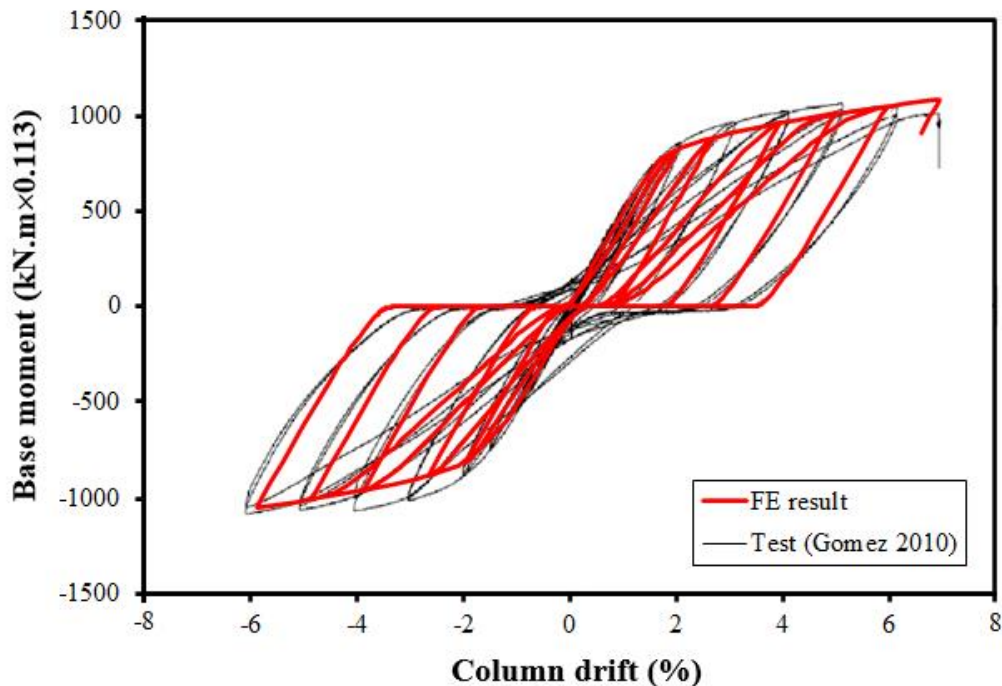


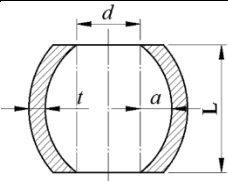
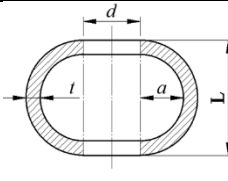

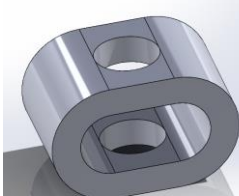
Figure 3. Experimental and numerical results comparison

5. Parametric Study

The behaviour of the proposed connection model under cyclic loading was investigated by conducting a numerical analysis on the validated FE model. The focus was on two types of sleeves: circular waveform (CW) and U-shape (US), both made of steel grade S355, as outlined in Table 1 and Figure 4.

For the CW and US sleeve types, the plastic amplitude (PA) was determined by incrementally increasing the amplitude value by 1.0 mm until the sleeve reaches its maximum capacity, resulting in crushing phenomena occurring before failure of other components. The analysis of the results was based on the geometric characteristics of each sleeve, including variations in length (L), amplitude (a), and thickness (t). By contrasting the obtained results for the connection with and without sleeves, the study aimed to determine the impact of the sleeve device on the structural performance.

Table 1. Sleeve waveform configurations and geometric parameters

	Circular	U-shaped
Geometric parameters		
3D view		

US / CW: The wave form of the sleeve.

L: The sleeve length.

t: The sleeve thickness in mm.

a: The amplitude value in mm.

Figure 4. Specimen identification

5.1. Cyclic behaviour and failure modes of Circular waveform (CW) sleeves in exposed base plate connections

The distribution of plastic strain and connection performance for CW sleeve connections are shown in Figure 5. With a 7 mm amplitude, the sleeve reached its load-bearing capacity at 7% drift before the bolt reached its limit, causing a severe plastic deformation that was followed by total crushing of the sleeve at 10% drift (see Figure 5). A significant force created in the anchor rods once the sleeve got jammed in between the end plate and the washer. It should be noted that the connection eventually failed because of to the anchor rod, showing that the sleeve did not change the failure mode, even though it postponed it to a higher drift.

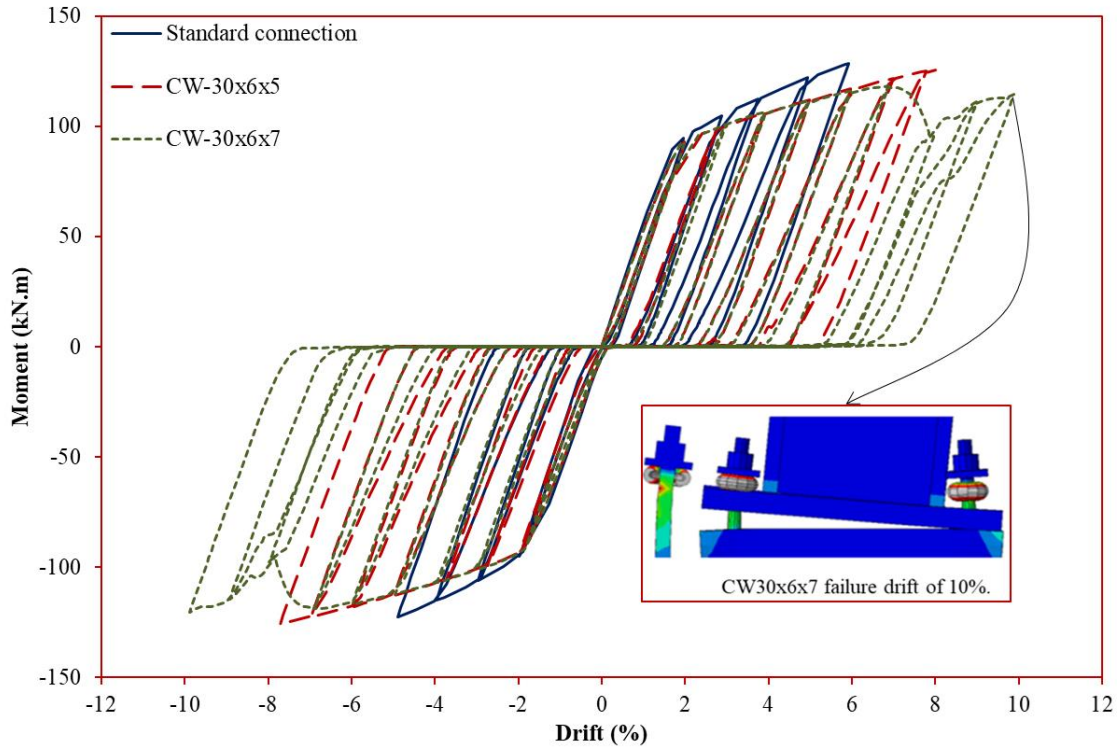


Figure 5. Moment-drift response and deformed shape for the base plate connection with the CW sleeves of length 30 mm

The initial stiffness of the proposed sleeve system is nearly identical to that of the standard configuration for all amplitude values. However, the drift capacity varies depending on the amplitude value, resulting in different levels of drift. When an amplitude value of 5 mm was adopted, the drift ratio enhanced by approximately 50% compared to the standard connection. Examination of the deformed configuration of the connections at their maximum capacity indicated that sleeves with a 5 mm amplitude exhibited greater capacity than the bolts, leading to bolt failure occurring before complete sleeve failure (see Figure 5). The improvement in drift can be attributed to the limited deformation observed in the sleeve before the failure of the anchor rod.

The plastic amplitude (PA) at which the sleeve's capacity is marginally lower than that of the bolt, resulting in complete crushing of the sleeve before bolt failure, was established at 7 mm. When the PA was adopted, the drift ratio for the sleeved connection was approximately 73% higher compared to the connection without the use of a sleeve. The moment for PA initially decreases once the sleeve reaches its full capacity at around a 7% drift (see Figure 5 for model CW-30x6x7). Following the complete crushing of the sleeve, which jammed between the base plate and the washer, the moment increases as the drift continues until bolt failure is observed.

5.2. Cyclic behaviour and failure modes of U-shape waveform (US) in exposed base plate connection

The U-shape sleeves designed with a length of 40 mm and varying thicknesses are influenced by the amplitude values in terms of their performance. Figure 6 presents an analysis of sleeves with a U-shape regarding the distribution of plastic strain and the moment-drift behaviour. In the case of model US-40x9x11, the sleeve was crushed prior to the failure of the bolt due to the lower capacity of the sleeve compared to the bolt. It is worth noting that increment in the thickness of the sleeve leads to a higher capacity than that of the bolt. Consequently, the bolt fails prior to the sleeve which should experience a high level of plastic deformation to observe more ductile behaviour. Moreover, sleeve types with larger

wall thicknesses, such as US-40x11x9, did not exhibit substantial plastic deformation before the bolt failure.

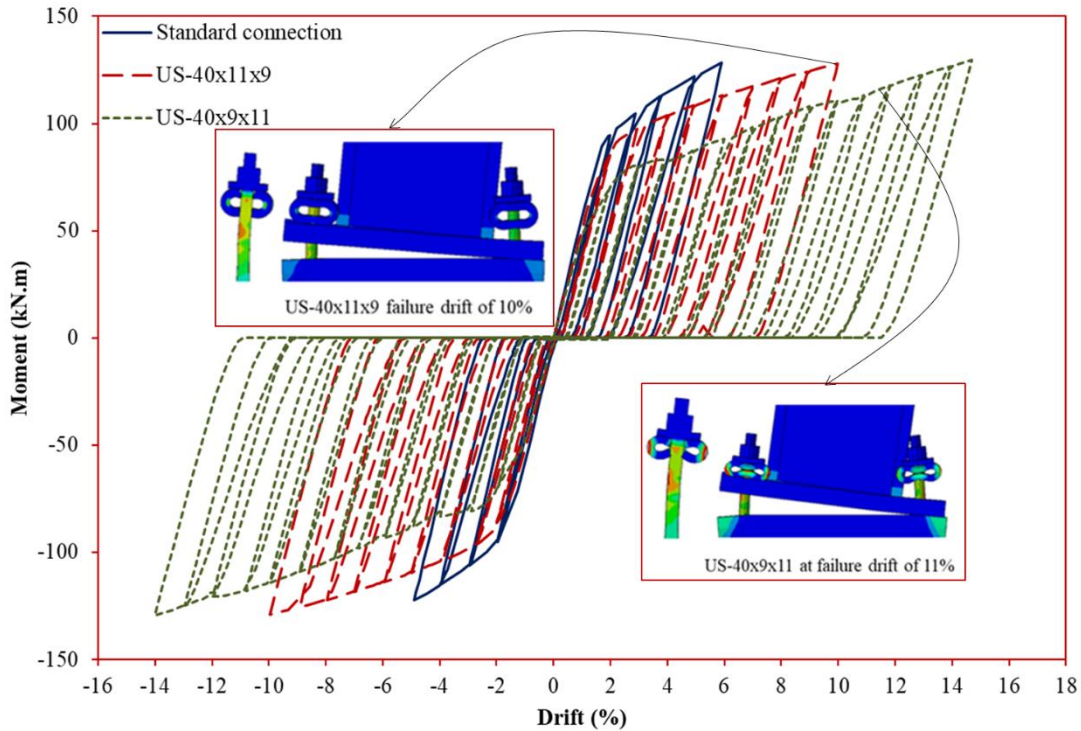


Figure 6. Moment-drift response and deformed shape for the base plate connection with the U-shape sleeves of length 40 mm

Although the proposed sleeve system exhibits a similar initial stiffness as the standard configuration for all amplitude values, it has been observed that the column drift is higher in connections utilizing the sleeves compared to the standard connection.

The drift capacity is dependent on the chosen amplitude value, with different amplitudes yielding different levels of drift. Specifically, when amplitude values of 11 mm were employed, there was a significant increase in the drift ratio, approximately 183% higher than that of the standard connection. Upon examining the connection model at their maximum capacity, it was discovered that the US-40x9x11 sleeve type had a lower capacity than the bolt, resulting in the complete crushing of the sleeve before the bolt failure as depicted in Figure 6. It is worth noting that the full crushing of the US-40x11x9 sleeve model was not observed, as the capacity of the proposed sleeve system exceeded the bolt capacity.

6. Conclusion

The main focus of this paper is to assess a recently developed sleeve system designed for column-base connections subjected to cyclic loading. The study involves modelling and validation of a finite element model through reference model (experimental tests). The study expanded with parametric study to examine different types of sleeve with distinct geometries: circular (CW) and U-shaped (US) waveforms. The objective is to compare the performance of the proposed system with that of a standard connection in terms of ductility and rotational capacity.

The results of the study indicate that the proposed sleeve system exhibits higher resistance and improved rotational capacity compared to the standard connection. This suggests that the performance of steel column base connections can be enhanced through the implementation of the sleeve system. Both the

CW and US geometries of the sleeve system demonstrate effectiveness in improving connection performance.

7. Author Contribution Statement

In the study, Author 1 contributed to forming the idea, making the design and literature review, modelling and validation, reviewing and examination of the results; Author 2 contributed to conceptualization, reviewing and checking the spelling and checking the article in terms of content.

8. Ethics Committee Approval and Statement of Conflict of Interest

“There is no need for an ethics committee approval in the prepared article”






“There is no conflict of interest with any person/institution in the prepared article”

9. References

- [1] S. Kishiki, X. Yang, T. Ishida, N. Tatsumi, and S. Yamada, “Experimental study of concrete breakout failure mechanism in an exposed column base with a foundation beam” *Eng. Struct.*, vol. 243, Sep. 2021.
- [2] X. Yang and S. Kishiki, “Evaluation of ultimate strength of exposed column bases considering the bearing stress of foundation concrete” *Eng. Struct.*, vol. 268, no. July, p. 114712, 2022.
- [3] I. Gomez, A. Kanvinde, and G. G. Deierlein, “Exposed column base connections subjected to axial compression and flexure” AISC Final Report. Chicago., 2010.
- [4] C. A. Trautner, T. Hutchinson, P. R. Grosser, and J. F. Silva, “Effects of detailing on the cyclic behavior of steel baseplate connections designed to promote anchor yielding” *J. Struct. Eng.*, vol. 142, no. 2, Feb. 2016.
- [5] K. Tsavdaridis, M. Shaheen, C. B.- Structures, and undefined 2016, “Analytical approach of anchor rod stiffness and steel base plate calculation under tension” Elsevier.
- [6] M. A. Shaheen, K. D. Tsavdaridis, and E. Salem, “Effect of grout properties on shear strength of column base connections: FEA and analytical approach” *Eng. Struct.*, vol. 152, pp. 307–319, 2017.
- [7] T. Falborski, P. Torres-Rodas, F. Zareian, and A. Kanvinde, “Effect of base-connection strength and ductility on the seismic performance of steel moment-resisting frames” *J. Struct. Eng.*, vol. 146, no. 5, May 2020.
- [8] C. A. Trautner, T. Hutchinson, P. R. Grosser, and J. F. Silva, “Investigation of steel column–baseplate connection details incorporating ductile anchors” *J. Struct. Eng.*, vol. 143, no. 8, Aug. 2017.
- [9] A. Hassan, B. Song, C. G.-J. of S., and undefined 2022, “Seismic performance of exposed column–base plate connections with ductile anchor rods” *ascelibrary.org*.
- [10] C. Trautner, T. Hutchinson, M. Copellini, P. Grosser, R. Bachman, and J. Silva, “Developing ductility using concrete anchorage” *ACI Struct. J.*, vol. 114, no. 1, pp. 101–112, Jan. 2017.
- [11] J. E. Parks, C. P. Pantelides, L. Ibarra, and D. H. Sanders, “Stretch length anchor bolts under combined tension and shear” *ACI Struct. J.*, vol. 115, no. 5, pp. 1317–1328, Sep. 2019.
- [12] M. Wang, C. Zhang, Y. Sun, and K. Dong, “Seismic performance of steel frame with replaceable low yield point steel connection components and the effect of structural fuses” *J. Build. Eng.*, 2022.
- [13] M. Wang and P. Bi, “Study on seismic behavior and design method of dissipative bolted joint for steel frame with replaceable low yield point steel connected components” *Constr. Build. Mater.*, 2019.
- [14] M. A. Shaheen, K. D. Tsavdaridis, F. P. V. Ferreira, and L. S. Cunningham, “Rotational capacity of exposed base plate connections with various configurations of anchor rod sleeves” *J. Constr. Steel Res.*, vol. 201, no. August 2022, p. 107754, 2023.
- [15] U. 2019. ABAQUS. Abaqus 6.19. Dassault Systèmes Simulia Corp, Provid RI, “No Title”
- [16] I. R. Gomez, “Behavior and design of column base connections” University of California, Davis, 2010.



Vision Based Transformer Tekniği İle İnsan Konuşmasından Nörolojik Bozuklukların Sınıflandırılması

Emel SOYLU^{1*} , Sema GÜL² , Kübra ASLAN KOCA³ , Muammer TÜRKÖĞLU⁴ ,
Murat TERZİ⁵ 

¹Yazılım Mühendisliği Bölümü, Mühendislik Fakültesi, Samsun Üniversitesi, Samsun, Türkiye.

²Lisansüstü Enstitüsü, Nörobilim Bölümü, Ondokuz Mayıs Üniversitesi, Samsun, Türkiye.

³Yazılım Mühendisliği Bölümü, Mühendislik Fakültesi, Samsun Üniversitesi, Samsun, Türkiye.

⁴Nöroloji Bölümü, Tıp Fakültesi, Ondokuz Mayıs Üniversitesi, Samsun, Türkiye.

¹emel.soylu@samsun.edu.tr, ²sema.gul@omu.edu.tr, ³kubraslantr@gmail.com,

⁴muammer.turkoglu@samsun.edu.tr, ⁵mterzi@omu.edu.tr

Geliş Tarihi: 17.03.2024

Kabul Tarihi: 25.04.2024

Düzeltilme Tarihi: 30.03.2024

doi: <https://doi.org/10.62520/fujece.1454309>

Araştırma Makalesi

Alıntı: E. Soylu, S. Gül, K. A. Koca, M. Türkoğlu ve M. Terzi, "Vision based transformer tekniği ile insan konuşmasından nörolojik bozuklukların sınıflandırılması", Fırat Üni. Deny. ve Hes. Müh. Derg., vol. 3, no 2, pp. 160-174, Haziran 2024.

Öz

Bu çalışmada, Parkinson hastalığı, Multipl Skleroz (MS), sağlıklı bireyler ve diğer kategoriler gibi farklı sağlık kategorilerinin insan konuşmasından yüksek doğrulukta sınıflandırılması için transformatör tabanlı sinir ağı yaklaşımını sunuyoruz. Bu yaklaşım, insan konuşmasının spektrogramlara dönüştürülmesinde yatmaktadır ve daha sonra bu spektrogramlar görsel görüntülere dönüştürülmektedir. Bu dönüşüm süreci, ağımızın çeşitli sağlık koşullarını belirten karmaşık ses desenlerini ve ince nüansları yakalamasını sağlar. Yaklaşımımızın deneysel doğrulaması, Parkinson hastalığı, MS, sağlıklı bireyler ve diğer kategoriler arasında yüksek performanslı sonuçlar vermiştir. Bu başarı, spektrogram analizi ve vision based transformer tekniği birleşimine dayanan yenilikçi, invaziv olmayan bir tanı aracı sunarak potansiyel klinik uygulamalar için kapıları açmaktadır.

Anahtar kelimeler: Nörolojik bozukluk sınıflandırması, Transformatör tabanlı sinir ağı, Ses sınıflandırması

*Yazışılan yazar

İntihal Kontrol: Evet – Turnitin

Şikayet: fujece@firat.edu.tr

Telif Hakkı ve Lisans: Dergide yayın yapan yazarlar, CC BY-NC 4.0 kapsamında lisanslanan çalışmalarının telif hakkını saklı tutar.



Vision Transformer Based Classification of Neurological Disorders from Human Speech

Emel SOYLU^{1*} , Sema GÜL² , Kübra ASLAN KOCA³ , Muammer TÜRKOĞLU⁴ ,
Murat TERZİ⁵ 

^{1,4} Department of Software Engineering, Faculty of Engineering, Samsun University, Samsun, Türkiye.

² Graduate Institute, Department of Neuroscience, Ondokuz Mayıs University, Samsun, Türkiye.

³ Department of Software Engineering, Faculty of Engineering, Samsun University, Samsun, Türkiye.

⁵ Department of Neurology, Faculty of Medicine, Ondokuz Mayıs University, Samsun, Türkiye.

¹emel.soylu@samsun.edu.tr, ²sema.gul@omu.edu.tr, ³kubraslantr@gmail.com,

⁴muammer.turkoglu@samsun.edu.tr, ⁵mterzi@omu.edu.tr

Received: 17.03.2024

Accepted: 25.04.2024

Revision: 30.03.2024

doi: <https://doi.org/10.62520/fujece.1454309>

Research Article

Citation: E. Soyly, S. Gül, K. A. Koca, M. Türkoğlu ve M. Terzi, "Vision transformer based classification of neurological disorders from human speech", *Firat Univ. Jour. of Exper. and Comp. Eng.*, vol. 3, no 2, pp. 160-174, June 2024.

Abstract

In this study, we introduce a transformative approach to achieve high-accuracy classification of distinct health categories, including Parkinson's disease, Multiple Sclerosis (MS), healthy individuals, and other categories, utilizing a transformer-based neural network. The cornerstone of this approach lies in the innovative conversion of human speech into spectrograms, which are subsequently transformed into visual images. This transformation process enables our network to capture intricate vocal patterns and subtle nuances that are indicative of various health conditions. The experimental validation of our approach underscores its remarkable performance, achieving exceptional accuracy in differentiating Parkinson's disease, MS, healthy subjects, and other categories. This breakthrough opens doors to potential clinical applications, offering an innovative, non-invasive diagnostic tool that rests on the fusion of spectrogram analysis and transformer-based models.

Keywords: Neurological disorder classification, Vision transformer, Audio classification

*Corresponding author

1. Introduction

Sound is one of the components that make up human perception in nature. The direction, intensity, and duration of sound play a major role in our understanding and interpretation of environmental events. Differences in sounds allow us to distinguish events. Sounds are generally composed of harmonic signals. The signal emitted in the air is received by the human ear, passed through certain neural processes in the brain, reaches the relevant auditory centers, and is interpreted [1]. Artificial intelligence techniques are used in sound analysis processes with the imitation of this mechanism.

Voice analysis of people is the subject of many fields of study. Speech signals are used as input sources in human-computer interaction to develop various applications such as automatic speech recognition, speech emotion recognition, gender and age recognition [2-4].

The human larynx functions in roles such as speaking, breathing, swallowing, coughing and has a complex functional structure. The coordination of these roles is very sensitive to being affected in individuals with neurological diseases. Sound problems arise because the larynx mechanism cannot meet the demand for sound due to functional or structural reasons. There are many factors that will affect the sound production mechanism. Speech habits, health problems, chronic diseases, habits, neurological disorders can be given as examples of factors that cause voice problems. In this study, neurological disease classification is made by voice analysis of patients diagnosed with neurological disease.

In the diagnosis of neurological diseases, the patient's history and physical examination usually come to the fore. Voice-related changes can often be overlooked [5]. Even if the patient does not have a complaint about the voice that can be expressed directly, the evaluation of the voice during the anamnesis or examination can make a significant contribution to the diagnosis of individuals with neurological diseases. With the effect of functions such as articulation and phonation during the speech, hypophonic, dysarthric, and ataxic sounds can contribute to the diagnosis. While hypophonic speech may suggest basal ganglia involvement with accompanying bradymia, it may suggest the involvement of the pyramidal pathway in a patient with first and second motor neuron findings. Dysarthric speech pattern suggests cerebellar involvement together with other threshold examination findings. A muffled speech pattern can be seen in motor neuron diseases, and speech problems up to motor or global aphasia can be seen in patients with cerebral cortical involvement. All these voice changes, together with the affected neurological system and other findings, provide important information about the diagnosis.

In the literature, there are studies based on computer-based processing of patients' voice data and early detection and diagnosis of diseases in health sciences. Abnormal condition detection by processing breath sound [4], [6], heart sound [7-12], knee joint sound processing for non-invasive diagnosis and monitoring of joint disorders such as osteoarthritis and chondromalacia [13], COVID-19 detection from cough, sound, breath sound, Alzheimer's detection from the speech process [14], Parkinson's detection [15] can be given as examples of sound processing studies in the health field [16-23].

The frequency spectrum of an audio signal can be expressed visually in the form of a spectrogram. The spectrogram can be constructed using an optical spectrometer, bank of band-pass filters, Fourier transform, or wavelet transform methods. Spectral representations are involved in classification or regression neural networks.

There are examples in the literature on converting audio signals to spectrograms and classifying them with artificial intelligence techniques. COVID-19 detection with lung breath sound [24], seizure detection from electroencephalography (EEG) signals [25], recognition of surrounding sounds, bird sound recognition [26], and emotion detection from community voice [27] are some examples of such studies.

The application of deep learning models for voice recognition in predicting vocal fold diseases related to neurological disorders has shown promise [28]. By leveraging spectrogram-based techniques, researchers have been able to develop AI tools for predicting vocal cord pathology in primary care settings, emphasizing the importance of spectrogram analysis in diagnosing voice-related issues [29]. The analysis of voice

spectrograms plays a significant role in detecting, monitoring, and classifying neurological diseases based on voice characteristics. By utilizing advanced technologies like convolutional neural networks (CNN) and deep learning models, researchers are making strides in leveraging spectrogram data to improve the diagnosis and management of neurological conditions through voice analysis.

Transformer networks, initially designed for natural language processing (NLP), have found groundbreaking applications in various domains, including image classification. In image classification tasks, the primary objective is to categorize input images into predefined classes or labels [30]. Traditionally, CNNs have been the dominant choice for image classification due to their ability to capture spatial hierarchies within images. However, transformer networks have introduced a paradigm shift by leveraging attention mechanisms to process images in a non-sequential manner, making them highly effective in capturing global dependencies and relationships within image data [31-35].

Transformers find versatile applications in health data utilization. These applications span disease diagnosis by analyzing symptoms and medical histories, medical image processing such as segmentation and detection, drug discovery via genetic and molecular analysis, medical text processing for reports and records, biomedical natural language understanding, and health record management. Transformers offer a flexible framework for handling health data, showing great promise across various healthcare domains [36-39].

In the scope of this research, we employed transformer models to classify human voices, a task that sets the foundation for our investigation. Employing our proprietary dataset, we sourced audio recordings from both healthy individuals and those affected by conditions like Multiple Sclerosis and Parkinson's, introducing a distinctive dimension to our work. The collection process involved individuals with diagnosed conditions, underscoring our unique methodology. This unconventional approach significantly contributed to the ingenuity of our study, and because of this innovative dataset creation, we achieved remarkable levels of accuracy.

The upcoming sections of the paper encompass various aspects, including a review of related works, an in-depth exploration of the employed methodology, a detailed presentation of the dataset used, and an insightful discussion.

2. Relevant Work

In the literature, there are computer-based auxiliary studies for the detection of neurological diseases. In Table 1, the type of neurological disease, data types used in the diagnosis, method, and study years are given. This table provides information about various neurological disorders, the type of data used for diagnosis, the number of samples, diagnosis methods (such as Artificial Intelligence, Support Vector Machine, etc.), accuracy percentages, publication years, and references for each study. The disorders covered include Multiple Sclerosis (MS), Alzheimer's, and Parkinson's disease, along with the specific data types and methods used for diagnosis. As evident from the table, successful classification outcomes are achieved by training the language datasets obtained through speech features using artificial intelligence techniques.

The existing literature has bolstered our belief in the feasibility of classifying neurological diseases based on sound data. Contemporary literature explores the transformation of sound data into spectrograms and subsequent classification through deep learning techniques, although typically focusing on individual diseases. In contrast, our proposed study seeks to discern both MS and Parkinson's diseases from a dataset encompassing 12 patient categories (MS, Amyotrophic Lateral Sclerosis (ALS), Spinocerebellar Ataxia (SCA), Alzheimer's, Epilepsy, Parkinson's, Myasthenia Graves, Myelitis, Motor Aphasia, Psychological, Fiedreich Ataxia, Language Problem) and healthy individuals. A distinguishing feature of this study is the dataset's diverse range of disease types, setting it apart from prior research. We employ a larger patient cohort and solely utilize voice recordings for classification purposes. The utilization of everyday mobile phones for voice recording, as opposed to specialized devices, makes our approach practical, cost-effective, and distinct from prior dataset creation methodologies.

Table 1. Relevant work

Neurological Disorder	Data type to use in the diagnosis	Number of samples	Diagnosis method	Accuracy (%)	Year of Publication	Reference
MS	Conversation, demographics	65 patients, 66 healthy individuals	Artificial Intelligence	82	2022	[40]
MS	brain magnetic resonance images	168 lesion images obtained from 3 patients	Support Vector Machine	81.5	2010	[41]
Alzheimer	Speech Features	2033 audio recordings collected from 99 patients	Machine Learning	78.7	2019	[42]
Alzheimer	Speech Features	80 healthy, 13 early diagnoses, 5 patients	LDA classifier	85.7	2016	[43]
MS	surface electromyography (sEMG) signals	450-sentence speech collected from 3 sick individuals	CNN	81	2020	[44]
Parkinson	Pc-Gita (Vowel monologues, sentences, words, read text)	50 healthy, 50 Parkinson individuals	CNN	98.3	2020	[45]
Alzheimer	Speech Features	254 Alzheimer's and 250 Healthy individuals	Machine Learning	89.4	2020	[46]
Parkinson	Speech Features	91 subjects, 43 suffering from PD with each person on an average giving 5-6 different samples	CNN	89.15	2019	[47]
Parkinson, ALS	Speech Features	60 ALS, 60 Parkinson, 60 Healthy individuals	CNN	87	2020	[48]
Parkinson	Speech Features	120 speech samples from 20 Healthy, 28 Parkinson individuals	Generative Adversarial Network	90.5	2020	[49]
Parkinson	Speech Features	181 speakers, 1797 recordings from 3 different languages	Vision Transformer	78	2021	[50]
Parkinson	Gait	64468 gait data	Transformer	97.4	2022	[51]
Parkinson	Drawing	315 Healthy, 279 Parkinson sample	CNN	95.29	2023	[52]
MS, Parkinson	Speech Features	204 MS, 172 Parkinson, 212 Other, 94Healthy individuals	Vision Transformer	93.14	-	Our proposed research

3. Method

For many years the key point in audio analysis has been feature design and selection. In feature extraction, higher-order statistics of spectral center and spectral shape, zero crossing statistics, harmonics, fundamental frequency, and temporal explanations were used [53]. Today, feature extraction is done by deep networks. In this method, networks produce successful results when enough samples are used. The Fourier transform enables the representation of signals from the time domain into the frequency domain. This concept was introduced by Jean Baptiste Joseph Fourier, a French mathematician and physicist. Utilizing the Fourier Transform, the original time-based signal can be deconstructed into sinusoidal components, each possessing an amplitude, phase, and frequency. A waveform that appears complex in the time domain translates to a vertical line within the frequency domain. This concise depiction in the frequency domain serves to highlight essential frequencies. The Fourier Transform effectively dissects intricate time-based signals into distinct

frequency constituents, simplifying comprehension. The transition from the frequency domain back to the time domain preserves all data, ensuring fidelity. Given that audio signals are dynamic and not static, their characteristics fluctuate over time. Consequently, attempting a single Fourier transform across an entire 5-minute lecture's speech would be impractical. Such an approach would yield indistinct data for analysis. Alternatively, the Fourier transform is applied to successive signal frames, introducing the concept of Short-Time Fourier Transform (STFT). This approach better accommodates the variable nature of audio signals and enhances the extraction of meaningful features for analysis. The human perception of sound intensity follows a logarithmic scale, emphasizing the significance of logarithmic amplitude. Calculating the logarithmic value can be achieved using the Librosa library. Librosa, a Python package tailored for music and audio analysis, encompasses essential components to construct information retrieval systems employed in audio analysis [54-56].

Utilizing spectrograms, which visually represent sound signals, and employing deep learning for classification purposes is crucial due to several reasons. Firstly, spectrograms enable the capture of complex patterns within audio data, facilitating comprehensive analysis. Secondly, by treating sound as images, deep learning models can extract relevant features using image processing techniques, enhancing classification accuracy. Additionally, spectrogram-based representations offer interpretable features, aiding in understanding the acoustic properties associated with different health conditions. Lastly, leveraging deep learning architectures designed for image classification tasks ensures compatibility and efficiency in health category classification. Overall, combining spectrograms and deep learning techniques presents a powerful approach for sound-based classification in healthcare, advancing diagnostic capabilities and patient care.

In this study, voice data from different neurological patients and healthy individuals were evaluated. Individuals are told a sample sentence and recorded. The collected data were labelled by the specialist physician. Diagnosis of diseases and affected neurological systems were recorded after neurological evaluation.

The dataset was created by eliminating the misleading ones in the obtained data. It is aimed to collect enough data to enable machine learning for each disease category. The steps of the method used in this study can be summarized as follows. The block diagram of the proposed system is given in Figure 1.

- Data collecting
- Data labelling
- Data elimination
- Extraction of spectrograms of audio signals
- Classification with vision transformer (ViT)

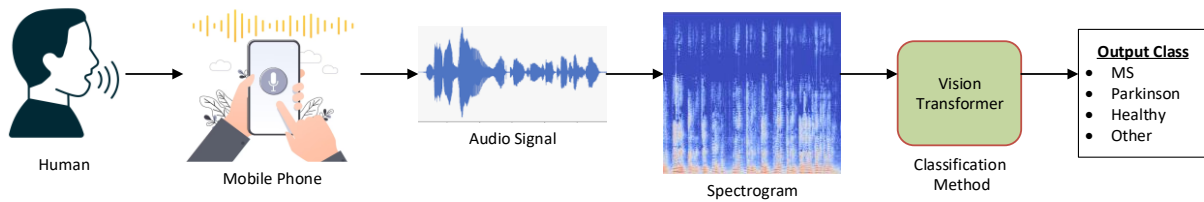


Figure 1. Patient voice classification block diagram

In the Colab environment, librosa library was used for the conversion of sound files to spectrograms, tensorflow library for convolutional neural network models, matplotlib library for graphical drawings, cv2 library for image cropping and resizing.

3.1. Dataset Description

The dataset used in this study was obtained by having patients diagnosed with MS, Parkinson and other neurological diseases (ALS, SCA, Alzheimer's, Epilepsy, Parkinson, Myasthenia Graves, Myelitis, Motor Aphasia, Psychological, Fiedreich Ataxia, Language Problem) and healthy individuals say a common sentence in Turkish. In the dataset, there were .wav audio files of 204 individuals with MS, 172 with Parkinson's, 212 with other neurological diseases, and 94 healthy individuals. The study group consisted of individuals between the ages of 18 and 65 who had been diagnosed with a neurological disease.

The dataset meticulously obtained and employed in this study deserves commendation for its unprecedented contribution to the field of healthcare and software development. It stands as a testament to the pioneering spirit of multidisciplinary research, bridging the realms of medicine and technology. This unique dataset, drawn from real patients and healthy individuals, represents a valuable resource that has paved the way for innovative and groundbreaking advancements. Its richness, authenticity, and comprehensiveness serve as the cornerstone of our transformative approach, allowing us to harness the power of artificial intelligence and machine learning for the early diagnosis and differentiation of neurological diseases. In Figure 2, the process of obtaining the spectrogram graph from the audio file and cutting the image is shown visually, respectively. By applying this process to each sound file, spectrogram images are obtained. The details of the dataset are given in Table 2. 85% of these images are used to create a classification model and 15% is used to test the accuracy of the model. The training and test data in the dataset are randomly determined.

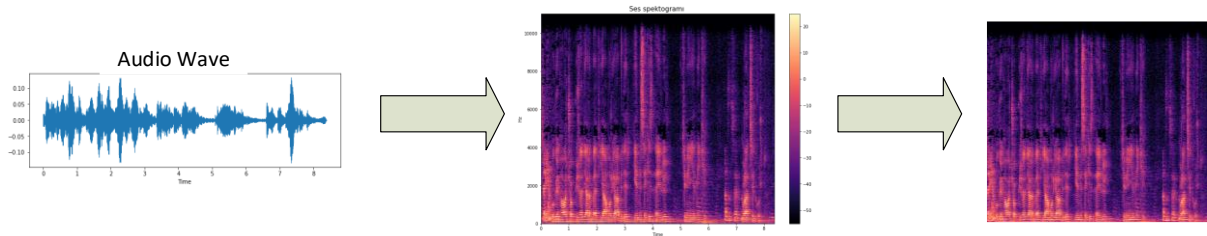


Figure 2. Process of obtaining spectrogram from audio file

Table 2. Details of the dataset

Class	Number of samples	Train data	Test Data
Healthy	94	80	14
MS	204	174	30
Parkinson	172	146	26
Other	212	180	32
Total	682	580	102

Google Colaboratory, shortly Colab, was used for image classification with dataset editing and transfer-based deep learning technique. Colab is a product offered by Google Research. It is particularly suitable for machine learning, data analysis, and education. With Colab, people can write and execute Python code through the browser.

3.2.Transformers

Unlike CNNs that process images pixel by pixel, transformer networks divide images into N patches fixed-size patches. This process is called linear embedding of patches (Elin). Each image patch x_i is linearly embedded into a lower-dimensional space using the Elin operation enabling the network to capture essential features given in Eq.1.

$$z_i = Elin(x_i) \tag{1}$$

Transformer networks, originally developed for sequence data, don't inherently possess spatial information. To address this, positional encodings are introduced, allowing the model to understand the relative positions of patches. To incorporate positional information, positional encodings are added to the token embeddings as given in Eq.2.

$$z_{i_pos} = z_i + Epos(i) \quad (2)$$

The self-attention mechanism is a key component of transformers. It allows each patch to attend to all other patches, capturing long-range relationships and enabling the model to recognize complex patterns. The self-attention mechanism calculates attention scores and output embeddings for each pair of tokens (i, j) as given in Eq.3.

$$Attention(z_{i_pos}, z_{j_pos}) = Softmax\left(\frac{(z_{i_pos} \cdot z_{j_pos})^T}{\sqrt{d_k}}\right) \cdot z_{j_pos} \quad (3)$$

The transformer encoder processes the embedded patches along with positional encodings. Multiple layers of encoders capture hierarchical features and generate context-aware representations. Multi-Head Self-Attention combines multiple attention heads to capture different relationships. The equation of this process is given in Eq.4. Each Head_k operates similarly to the self-attention mechanism but with different learned weight matrices. Each Head_k operates similarly to the self-attention mechanism but with different learned weight matrices.

$$MultiHead(z_{i_pos}) = Concat(Head_1(z_{i_pos}), \dots, Head_h(z_{i_pos})) \cdot W_o \quad (4)$$

The Transformer Encoder processes the output of the multi-head self-attention and combines it with the original input. The equation of this process is given in Eq.5. LayerNorm performs layer normalization, and the output is added to the original token embedding.

$$Output_i = LayerNorm(MultiHead(z_{i_pos}) + z_{i_pos}) \quad (5)$$

Once the patch representations are processed, a global classification token is added. This token aggregates information from all patches and contributes to the final classification decision. The aggregation function combines all the token embeddings into a single global token as given in Eq. 6.

$$Global_Token = Aggregation(z_{1_pos}, \dots, z_{N_pos}) \quad (6)$$

The global token's representation is fed into the classification layer, which maps it to the respective classes as given in Eq. 7. Here, W_cls represents the weight matrix for the classification layer

$$Class_Logits = Global_Token \cdot W_{cls} \quad (7)$$

The softmax activation function is applied to the class logits to obtain class probabilities as given in Eq. 8. We chose to use the softmax activation function to obtain class probabilities because softmax ensures that the output probabilities sum up to 1, which is desirable for interpreting the output as probabilities of different classes. Additionally, softmax normalizes the logits, making them more interpretable and suitable for multi-class classification tasks. Softmax is more suitable for obtaining class probabilities at the output layer.

$$Class_Probabilities = Softmax(Class_Logits) \quad (8)$$

The model is trained using labelled image data and a loss function. Commonly used loss functions include categorical cross-entropy. After training, the model's accuracy is evaluated on unseen test data. Transformer networks' success in image classification highlights their adaptability to diverse data types and tasks beyond

NLP. They have demonstrated state-of-the-art performance on various benchmark datasets and have contributed to pushing the boundaries of image understanding. The architecture of model is given in Figure 3. The illustration is inspired from [57].

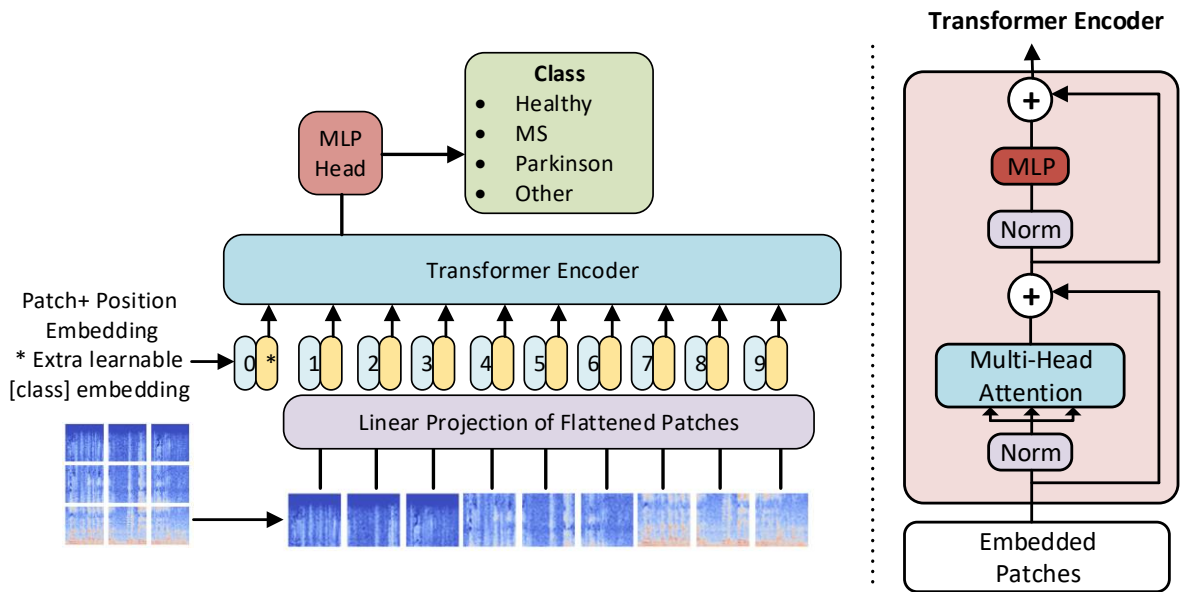


Figure 3. Model overview

In our research, we conducted a retraining process on Google's 'vit-base-patch16-224-in21k' model. The ViT-Base model comprises 12 layers with a hidden size of 768, an MLP size of 3072, and incorporates 12 attention heads, totaling 86 million parameters [57]. Utilizing the Adam optimizer and setting a learning rate of 1e-6, along with adjusting hyperparameters after 100 epochs, we managed to decrease the training loss to 0.05. The epoch count was decided after numerous iterations, reaching the desired error level as the determining factor. The training progress outcomes are depicted in Figure 4.

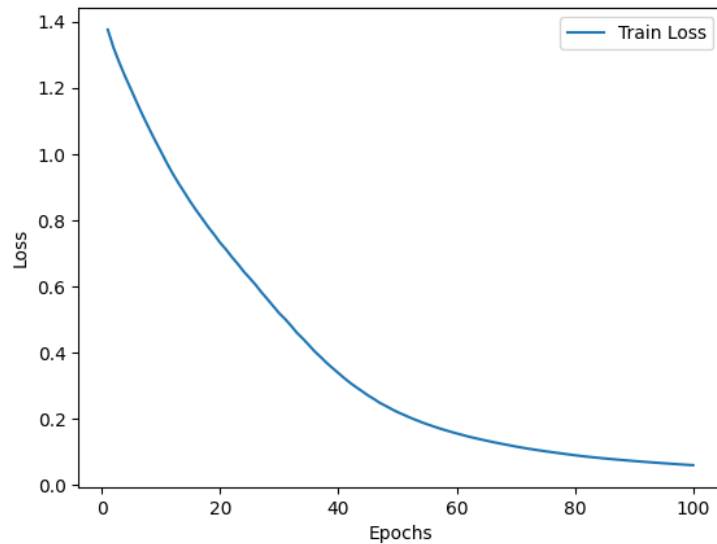


Figure 4. Train loss curve

4. Results

In this study, a dataset was created from the recorded data by having 682 individuals with neurological diseases say an example sentence. By transforming the audio data in the created dataset into spectrogram images, the classification of neurological diseases is provided by vision transformer-based learning. The confusion matrix of experiments is given in Figure 5. As a result of experiments with test data, an 92.15% success rate was obtained.

Class	Healthy	MS	Parkinson	Other
Healthy	14	0	0	0
MS	0	25	3	2
Parkinson	0	0	26	0
Other	0	0	3	29

Figure 5. Confusion Matrix

Table 3 contains various metrics used to evaluate the performance of a classification model. n truth (True Count) is the number of actual data points for each class. n classified (Classified Count) is the number of data points correctly classified by the model for each class. Accuracy measures the ratio of correct predictions made by the model to the total number of data points. This metric assesses the overall performance of the model. Precision indicates the proportion of positive predictions that are true positives. It measures how accurate the model's positive predictions are for a class. Recall measures how many of the true positive examples were correctly predicted. It assesses the model's ability to capture true positives. For instance, the recall for the "Parkinson" class is 94%, indicating that most of the true positives for this class were correctly predicted. The F1 score is a metric that balances precision and recall. Ideally, you want to achieve a high F1 score with both high precision and recall. As can be seen from the table, "Healthy" and "Parkinson" classes have high accuracy and F1 scores. Out of 102 test inputs, 94 were correctly predicted, resulting in an overall accuracy of 92.15%.

Table 3. Results for ViT

		Truth data				Classification overall	F1 Score
		Healthy	MS	Parkinson	Other		
Classifier results	Healthy	14	0	0	0	14	100%
	MS	0	25	3	2	30	83%
	Parkinson	0	0	26	0	26	100%
	Other	0	0	3	29	32	91%
	Truth overall	14	25	32	31	102	
	Recall	100%	100%	81.25%	93.55%		
Overall accuracy	92.15%						

We also conducted testing on the dataset using various other architectures, resulting in the outcomes presented in Table 3. DenseNet121 achieved an accuracy of 67.91%. DenseNet201 achieved an accuracy of 64.93%. Xception achieved an accuracy of 73.88%. InceptionV3 achieved an accuracy of 72%. MobileNet achieved an accuracy of 73.13%. EfficientNetB0 achieved an accuracy of 80.6%. EfficientNetB0 architecture showed strong performance with an accuracy of 80.6%. EfficientNetV2B3 achieved an accuracy

of 76.87%. Vision Transformer achieved an accuracy of 92.15%. The Vision Transformer architecture performed exceptionally well with an accuracy of 92.15%. This indicates that it correctly classified a vast majority of the test data, demonstrating its effectiveness for the task.

Table 4. Accuracy results for other deep learning techniques

Architecture	Accuracy
DenseNet121	67.91 %
DenseNet201	64.93 %
Xception	73.88 %
InceptionV3	72 %
MobileNet	73.13 %
EfficientNetB0	80.6 %
EfficientNetV2B3	76.87 %
Vision Transformer	92.15%

5. Discussion

In recent years, the intersection of artificial intelligence and healthcare has opened up exciting possibilities for the early detection and diagnosis of various medical conditions. One particularly promising area of research is the classification of neurological diseases through the analysis of audio data. This innovative approach holds immense potential in revolutionizing the field of healthcare, especially in the realm of neurological disorders.

Neurological diseases encompass a wide range of disorders, including but not limited to Parkinson's disease, Multiple Sclerosis (MS), Alzheimer's disease, and more. Early detection and accurate diagnosis of these conditions are pivotal for improving patient outcomes and enhancing the quality of life for individuals affected by these diseases. Audio-based neurological disease classification plays a crucial role in achieving early detection. By analyzing the unique vocal patterns and speech characteristics of patients, machine learning models can identify subtle deviations that might indicate the presence of neurological disorders. This non-invasive approach can significantly reduce the time between symptom onset and diagnosis, enabling timely medical intervention and treatment.

One of the most compelling aspects of audio-based classification is its potential to democratize healthcare. Access to specialized medical facilities and experts can be limited in many regions, particularly in rural or underserved areas. Audio-based diagnostic tools can be easily distributed and utilized remotely, bridging the gap between patients and healthcare resources. Patients can record their speech and vocal samples in the comfort of their homes, making it easier to monitor their health and share data with healthcare providers. This accessibility not only reduces the burden on healthcare systems but also empowers individuals to take a more active role in managing their health. Audio-based neurological disease classification offers an objective and quantitative approach to diagnosis. Traditional diagnostic methods may rely on subjective assessments or a series of clinical tests, which can be prone to human error or bias. In contrast, machine learning models process audio data with consistency, providing reliable and reproducible results.

These models can analyze a multitude of features within speech data, detecting subtle changes that may escape human observation. As a result, healthcare professionals can make more informed decisions, leading to improved patient care. The field of audio-based neurological disease classification is still evolving, presenting exciting opportunities for further research and innovation. The development of advanced machine learning algorithms and the integration of state-of-the-art technologies, such as Vision Transformers, promise even greater accuracy and specificity in disease classification.

Additionally, collaborative efforts between researchers, clinicians, and technology experts are crucial for advancing this field. As we continue to refine and expand our understanding of neurological disease markers in audio data, we pave the way for novel diagnostic tools that can benefit millions of individuals worldwide.

6. Conclusions

In this study, we propose a transformative approach that aims to achieve highly accurate classification within different health categories, including Parkinson's disease, Multiple Sclerosis (MS), healthy individuals, and other categories. We utilize a transformer-based neural network as the basis of our approach. The most important innovation lies in the conversion of human speech into spectrograms, which are then converted into visual images. This transformation process allows our neural network to capture complex sound patterns and subtle nuances that indicate various health conditions. Experimental validation of our approach yields impressive results. It demonstrates exceptional accuracy in distinguishing between Parkinson's disease, MS, healthy subjects, and other categories. This breakthrough offers an innovative and non-invasive diagnostic tool that combines spectrogram analysis with transformer-based models, offering promising prospects for potential clinical applications.

We also conducted comparative experiments with various other deep learning architectures. These experiments demonstrate the superiority of ViT in achieving an accuracy of 92.15%, outperforming other architectures in correctly classifying health categories. We are currently continuing data collection and actively working to broaden the range of classes while striving to attain higher levels of accuracy in our forthcoming research endeavors.

Our research marks a promising step towards leveraging advanced machine learning techniques, specifically Vision Transformers, for effective health category classification based on sound patterns. These results have significant potential to improve diagnostic capabilities and contribute to non-invasive medical evaluations. Our research presents a non-invasive diagnostic tool capable of significantly enhancing the accuracy and efficiency of clinical diagnoses, particularly for conditions like Parkinson's disease and Multiple Sclerosis. By effectively classifying health categories based on sound patterns, healthcare professionals are empowered to make more informed decisions regarding patient care and treatment plans. Moreover, our method opens new horizons in remote monitoring and telemedicine applications. The ability to convert human speech into spectrograms and analyze them using transformer-based neural networks enables the development of smartphone apps or similar devices for recording and remotely analyzing speech patterns. This innovation can revolutionize healthcare delivery by facilitating timely assessments of patients' health statuses without the need for in-person visits. Additionally, our approach holds promise for early detection and prevention efforts. By capturing subtle nuances in sound patterns associated with various health conditions, it has the potential to identify early signs of Parkinson's disease, Multiple Sclerosis, and other ailments. Such early detection can prompt timely interventions, ultimately leading to improved patient outcomes and reduced healthcare burdens. Our research serves as a catalyst for further advancements in machine learning techniques within healthcare. It lays the groundwork for future studies to expand the range of classes beyond Parkinson's disease and Multiple Sclerosis, and to enhance the accuracy of classification algorithms. Through continued research and development, our approach stands to revolutionize healthcare practices, offering innovative solutions to pressing medical challenges.

7. Acknowledgement

This study attracted great attention at the 58th National Neurology Congress in Turkey and was awarded the second prize in the oral presentation category.

8. Author Contribution Statement

In the study, Murat Terzi, Emel Soylu, Sema Gül contributed to the creation of the idea, design, and literature review; Emel Soylu, Kübra Arslan Koca, Muammer Türkoğlu contributed to the analysis of the results, the provision of materials, and the review of the results.

9. Ethics Committee Approval and Conflict of Interest

The study protocol for this dataset was approved by the Ondokuz Mayıs University Clinical Research Ethics Committee (2022-545/2023). Written informed consent form was obtained from the address in the working environment and patient contents were extracted to ensure anonymity.

10. References

- [1] B. Karasulu, “Çoklu ortam sistemleri için siber güvenlik kapsamında derin öğrenme kullanarak ses sahne ve olaylarının tespiti,” *Acta INFOLOGICA*, vol. 3, no. 2, pp. 60–82, 2019.
- [2] A. Tursunov, J. Y. Choeh, and S. Kwon, “Age and gender recognition using a convolutional neural network with a specially designed multi-attention module through speech spectrograms,” *Sensors*, vol. 21, no. 17, p. 5892, 2021.
- [3] M. Vacher, J.-F. Serignat, and S. Chaillol, “Sound classification in a smart room environment: an approach using GMM and HMM methods,” in *The 4th IEEE Conference on Speech Technology and Human-Computer Dialogue (SpeD 2007)*, Publishing House of the Romanian Academy (Bucharest), 2007, vol. 1, pp. 135–146.
- [4] J. Acharya and A. Basu, “Deep neural network for respiratory sound classification in wearable devices enabled by patient specific model tuning,” *IEEE Trans. Biomed. Circuits Syst.*, vol. 14, no. 3, pp. 535–544, 2020.
- [5] G. Woodson, “Management of neurologic disorders of the larynx,” *Ann. Otol. Rhinol. & Laryngol.*, vol. 117, no. 5, pp. 317–326, 2008.
- [6] A. Abushakra and M. Faezipour, “Acoustic signal classification of breathing movements to virtually aid breath regulation,” *IEEE J. Biomed. Heal. informatics*, vol. 17, no. 2, pp. 493–500, 2013.
- [7] E. Soares, P. Angelov, and X. Gu, “Autonomous learning multiple-model zero-order classifier for heart sound classification,” *Appl. Soft Comput.*, vol. 94, p. 106449, 2020.
- [8] Z. Dokur and T. Ölmez, “Heart sound classification using wavelet transform and incremental self-organizing map,” *Digit. Signal Process.*, vol. 18, no. 6, pp. 951–959, 2008.
- [9] M. Tschannen, T. Kramer, G. Marti, M. Heinzmann, and T. Wiatowski, “Heart sound classification using deep structured features,” in *2016 Computing in Cardiology Conference (CinC)*, 2016, pp. 565–568.
- [10] P. Langley and A. Murray, “Heart sound classification from unsegmented phonocardiograms,” *Physiol. Meas.*, vol. 38, no. 8, p. 1658, 2017.
- [11] Z. Ren, N. Cummins, V. Pandit, J. Han, K. Qian, and B. Schuller, “Learning image-based representations for heart sound classification,” in *Proceedings of the 2018 international conference on digital health*, 2018, pp. 143–147.
- [12] M. Deng, T. Meng, J. Cao, S. Wang, J. Zhang, and H. Fan, “Heart sound classification based on improved MFCC features and convolutional recurrent neural networks,” *Neural Networks*, vol. 130, pp. 22–32, 2020.
- [13] K. S. Kim, J. H. Seo, J. U. Kang, and C. G. Song, “An enhanced algorithm for knee joint sound classification using feature extraction based on time-frequency analysis,” *Comput. Methods Programs Biomed.*, vol. 94, no. 2, pp. 198–206, 2009.
- [14] I. Vigo, L. Coelho, and S. Reis, “Speech-and language-based classification of alzheimer’s disease: a systematic review,” *Bioengineering*, vol. 9, no. 1, p. 27, 2022.
- [15] J. Rusz et al., “Speech biomarkers in rapid eye movement sleep behavior disorder and parkinson disease,” *Ann. Neurol.*, vol. 90, no. 1, pp. 62–75, 2021.
- [16] K. K. Lella and A. Pja, “Automatic diagnosis of covid-19 disease using deep convolutional neural network with multi-feature channel from respiratory sound data: cough, voice, and breath,” *Alexandria Eng. J.*, vol. 61, no. 2, pp. 1319–1334, 2022.
- [17] M. Faezipour and A. Abuzneid, “Smartphone-based self-testing of covid-19 using breathing sounds,” *Telemed. e-Health*, vol. 26, no. 10, pp. 1202–1205, 2020.
- [18] N. Melek Manshour, “Identifying covid-19 by using spectral analysis of cough recordings: a distinctive classification study,” *Cogn. Neurodyn.*, vol. 16, no. 1, pp. 239–253, 2022.

- [19] N. Sharma et al., “Coswara—a database of breathing, cough, and voice sounds for covid-19 diagnosis,” arXiv Prepr. arXiv2005.10548, 2020.
- [20] A. Tena, F. Clarià, and F. Solsona, “Automated detection of covid-19 cough,” *Biomed. Signal Process. Control*, vol. 71, p. 103175, 2022.
- [21] L. Kranthi Kumar and P. J. A. Alphonse, “COVID-19 disease diagnosis with light-weight CNN using modified MFCC and enhanced GFCC from human respiratory sounds,” *Eur. Phys. J. Spec. Top.*, pp. 1–18, 2022.
- [22] M. Kuluozturk et al., “DKPNet41: directed knight pattern network-based cough sound classification model for automatic disease diagnosis,” *Med. Eng. & Phys.*, p. 103870, 2022.
- [23] T. Nguyen and F. Pernkopf, “Lung sound classification using co-tuning and stochastic normalization,” *IEEE Trans. Biomed. Eng.*, 2022.
- [24] T. Tuncer, E. Akbal, E. Aydemir, S. B. Belhaouari, and S. Dogan, “A novel local feature generation technique based sound classification method for covid-19 detection using lung breathing sound,” *Eur. J. Tech.*, vol. 11, no. 2, pp. 165–174, 2021.
- [25] G. C. Jana, R. Sharma, and A. Agrawal, “A 1D-CNN-spectrogram based approach for seizure detection from EEG signal,” *Procedia Comput. Sci.*, vol. 167, pp. 403–412, 2020.
- [26] J. Xie, K. Hu, M. Zhu, J. Yu, and Q. Zhu, “Investigation of different CNN-based models for improved bird sound classification,” *IEEE Access*, vol. 7, pp. 175353–175361, 2019.
- [27] V. Franzoni, G. Biondi, and A. Milani, “Crowd emotional sounds: spectrogram-based analysis using convolutional neural network,” in *SAT@ SMC*, pp. 32–36, 2019.
- [28] H. Hu et al., “Deep learning application for vocal fold disease prediction through voice recognition: preliminary development study,” *J. Med. Internet Res.*, 2021.
- [29] E. C. Compton et al., “Developing an artificial intelligence tool to predict vocal cord pathology in primary care settings,” *Laryngoscope*, 2022.
- [30] A. Vaswani et al., “Attention is all you need,” *Adv. Neural Inf. Process. Syst.*, vol. 30, 2017.
- [31] S. Khan, M. Naseer, M. Hayat, S. W. Zamir, F. S. Khan, and M. Shah, “Transformers in vision: A survey,” *ACM Comput. Surv.*, vol. 54, no. 10s, pp. 1–41, 2022.
- [32] S. Bhojanapalli, A. Chakrabarti, D. Glasner, D. Li, T. Unterthiner, and A. Veit, “Understanding robustness of transformers for image classification,” in *Proceedings of the IEEE/CVF international conference on computer vision*, 2021, pp. 10231–10241.
- [33] K. S. Kalyan, A. Rajasekharan, and S. Sangeetha, “Ammus: A survey of transformer-based pretrained models in natural language processing,” arXiv Prepr. arXiv2108.05542, 2021.
- [34] J. Beal, E. Kim, E. Tzeng, D. H. Park, A. Zhai, and D. Kislyuk, “Toward transformer-based object detection,” arXiv Prepr. arXiv2012.09958, 2020.
- [35] Z. Shao et al., “Transmil: Transformer based correlated multiple instance learning for whole slide image classification,” *Adv. Neural Inf. Process. Syst.*, vol. 34, pp. 2136–2147, 2021.
- [36] F. Shamshad et al., “Transformers in medical imaging: a survey,” *Med. Image Anal.*, p. 102802, 2023.
- [37] A. Hatamizadeh et al., “Unetr: Transformers for 3d medical image segmentation,” in *Proceedings of the IEEE/CVF winter conference on applications of computer vision*, 2022, pp. 574–584.
- [38] Z. Liu, Q. Lv, Z. Yang, Y. Li, C. H. Lee, and L. Shen, “Recent progress in transformer-based medical image analysis,” *Comput. Biol. Med.*, p. 107268, 2023.
- [39] Z. Liu and L. Shen, “Medical image analysis based on transformer: A review,” arXiv Prepr. arXiv2208.06643, 2022.
- [40] E. Svoboda, T. Boril, J. Ruzs, T. Tykalova, D. Horakova, C. Guttman, K. B. Blagoev, H. Hatabu and V. Valtchinov, “Assessing clinical utility of Machine Learning and Artificial Intelligence approaches to analyze speech recordings in Multiple Sclerosis: A Pilot Study,” arXiv Prepr. arXiv2109.09844, 2021.
- [41] D. Yamamoto et al., “Computer-aided detection of multiple sclerosis lesions in brain magnetic resonance images: False positive reduction scheme consisted of rule-based, level set method, and support vector machine,” *Comput. Med. Imaging Graph.*, vol. 34, no. 5, pp. 404–413, 2010.
- [42] F. Haider, S. De La Fuente, and S. Luz, “An assessment of paralinguistic acoustic features for detection of Alzheimer’s dementia in spontaneous speech,” *IEEE J. Sel. Top. Signal Process.*, vol. 14, no. 2, pp. 272–281, 2019.
- [43] J. Weiner, C. Herff, and T. Schultz, “Speech-based detection of alzheimer’s disease in

- conversational german.,” in *Interspeech*, 2016, pp. 1938–1942.
- [44] A. Kapur, U. Sarawgi, E. Wadkins, M. Wu, N. Hollenstein, and P. Maes, “Non-invasive silent speech recognition in multiple sclerosis with dysphonia,” *Proc. Mach. Learn. Heal. NeurIPS Work.*, pp. 25–38, 2020.
- [45] L. Zahid et al., “A spectrogram-based deep feature assisted computer-aided diagnostic system for Parkinson’s disease,” *IEEE Access*, vol. 8, pp. 35482–35495, 2020.
- [46] L. Liu, S. Zhao, H. Chen, and A. Wang, “A new machine learning method for identifying Alzheimer’s disease,” *Simul. Model. Pract. Theory*, vol. 99, p. 102023, 2020.
- [47] A. Johri, A. Tripathi, and others, “Parkinson disease detection using deep neural networks,” in *2019 Twelfth international conference on contemporary computing (IC3)*, 2019, pp. 1–4.
- [48] B. N. Suhas et al., “Speech task based automatic classification of ALS and Parkinson’s Disease and their severity using log Mel spectrograms,” in *2020 international conference on signal processing and communications (SPCOM)*, 2020, pp. 1–5.
- [49] Z.-J. Xu, R.-F. Wang, J. Wang, and D.-H. Yu, “Parkinson’s disease detection based on spectrogram-deep convolutional generative adversarial network sample augmentation,” *IEEE Access*, vol. 8, pp. 206888–206900, 2020.
- [50] D. Hemmerling et al., “Vision transformer for parkinson’s disease classification using multilingual sustained vowel recordings.”
- [51] H.-J. Sun and Z.-G. Zhang, “Transformer-based severity detection of parkinson’s symptoms from gait,” in *2022 15th International Congress on Image and Signal Processing, BioMedical Engineering and Informatics (CISP-BMEI)*, 2022, pp. 1–5.
- [52] S. M. Abdullah et al., “Deep transfer learning based parkinson’s disease detection using optimized feature selection,” *IEEE Access*, vol. 11, pp. 3511–3524, 2023.
- [53] L. Wyse, “Audio spectrogram representations for processing with convolutional neural networks,” vol. 1, no. 1, pp. 37–41, 2017.
- [54] F. Ye and J. Yang, “A deep neural network model for speaker identification,” *Appl. Sci.*, vol. 11, no. 8, p. 3603, 2021.
- [55] “Stft.” [Online]. Available: <https://musicinformationretrieval.com/stft.html>.
- [56] B. Li, “On identity authentication technology of distance education system based on voiceprint recognition,” in *Proceedings of the 30th Chinese Control Conference*, 2011, pp. 5718–5721.
- [57] A. Dosovitskiy et al., “An image is worth 16x16 words: transformers for image recognition at scale. arxiv 2020,” *arXiv Prepr. arXiv2010.11929*, 2010.



Çift Yakıtlı Dizel Bir Motorda BD35 (Biyodizel/Dizel Karışımı) ve Propanol Kullanımının Yanma Karakteristiklerine Etkisinin İncelenmesi

Mutlu OKCU^{1*} , Müjdat FIRAT² , Yasin VAROL³ 

¹Elektrik-Elektronik Mühendisliği Bölümü, Mühendislik Fakültesi, Ardahan Üniversitesi, Türkiye.

^{2,3}Otomotiv Mühendisliği Bölümü, Teknoloji Fakültesi, Fırat Üniversitesi, Elâzığ, Türkiye.

¹mutluokcu@gmail.com, ²mujdatfirat@gmail.com, ³yvarol@gmail.com

Geliş Tarihi: 31.03.2023

Kabul Tarihi: 21.04.2024

Düzeltilme Tarihi: 16.08.2023

doi: <https://doi.org/10.62520/fujece.1464185>

Araştırma Makalesi

Alıntı: M. Okçu, M. Fırat, Y. Vrol, "Çift yakıtlı dizel bir motorda bd35 (biyodizel/dizel karışımı) ve propanol kullanımının yanma karakteristiklerine etkisinin incelenmesi", Fırat Üni. Deny. ve Hes. Müh. Derg., vol. 3, no 2, pp. 175-184, Haziran 2024.

Öz

Bu çalışma, reaktivite kontrollü sıkıştırma ateşleme modunda çalışacak şekilde modifiye edilmiş dizel bir motorda düşük reaktiviteli yakıt olarak propanol ve yüksek reaktiviteli yakıt olarak BD35 yakıtlarının kullanımının motorun yanma karakteristiklerindeki değişimini incelemektedir. Araştırmada, %35 biyodizel ve %65 petrol kökenli dizel karışımından oluşan BD35 yakıtı, yüksek reaktiviteli yakıt olarak doğrudan silindire püskürtülürken, reaktivite kontrollü sıkıştırma ateşleme için düşük reaktiviteli yakıt olarak propanol düşük basınçta emme kanalına püskürtülmüştür. Deneylerde propanol %0, %15, %30 ve %45 olmak üzere dört farklı ön karışım oranında kullanılmıştır. Deneyler %60 motor yükü ve 2400 (d/d) sabit motor hız şartları altında gerçekleştirilmiştir. Elde edilen verilere göre, karışım oranının artmasıyla birlikte silindir içi maksimum basınç değerinin arttığı ve özellikle %45 karışım oranı kullanımında önemli bir artış meydana geldiği tespit edilmiştir. Reaktivite kontrollü sıkıştırma ateşleme konsepti altında test motorunda propanolun düşük reaktiviteli yakıt olarak kullanılmasının ortalama indike basınç değerinde azalmaya neden olduğu gözlemlenmiş olmasına rağmen, karışım oranının artmasıyla birlikte ortalama indike basınçtaki azalma hızının yavaşladığı belirlenmiştir. Son olarak, karışım oranının artmasıyla birlikte silindir içi sıcaklığın önemli ölçüde azaldığı belirlenmiştir. Tüm bulgular analiz edildiğinde, reaktivite kontrollü sıkıştırma ateşleme modunda çalışacak şekilde modifiye edilmiş dizel motorlarda düşük reaktiviteli yakıt olarak propanol ve yüksek reaktiviteli yakıt olarak BD35 kullanımının yüksek yükte motor performansı üzerindeki etkilerini anlamak adına önemli bir yol göstermiştir.

Anahtar Kelimeler: RCCI, Biyodizel, Propanol, Yanma, BD35

*Yazışılan Yazar

İntihal Kontrol: Evet – Turnitin

Şikayet: fujece@firat.edu.tr

Telif Hakkı ve Lisans: Dergide yayın yapan yazarlar, CC BY-NC 4.0 kapsamında lisanslanan çalışmalarının telif hakkını saklı tutar



Investigation of The Effects of BD35 (Biodiesel/Diesel Blend) and Propanol Usage in Combustion Characteristics in A Dual Fuel Diesel Engine

Mutlu OKCU^{1*} , Müjdat FIRAT² , Yasin VAROL³ 

¹Department of Electrical Electronics Engineering, Faculty of Engineering, Ardahan University, Ardahan, Türkiye.

^{2,3}Department of Automotive Engineering, Faculty of Technology, Firat University, Elazığ, Türkiye.

¹mutluokcu@gmail.com, ²mujdatfirat@gmail.com, ³yvarol@gmail.com

Received: 31.03.2023

Accepted: 21.04.2024

Revision: 16.08.2023

doi: <https://doi.org/10.62520/fujece.1464185>

Research Article

Citation: M. Okcu, M. Firat, Y. Vrol, "Investigation of the effects of bd35 (biodiesel/diesel blend) and propanol usage on combustion characteristics in a dual fuel diesel engine", Firat Univ. Jour. of Exper. and Comp. Eng., vol. 3, no 2, pp. 175-184, June 2024.

Abstract

This study investigates the changes in the combustion characteristics of a diesel engine modified to operate in reactivity controlled compression ignition mode using propanol as low reactivity fuel and BD35 as high reactivity fuel. In the study, BD35 fuel, a blend of 35% biodiesel and 65% petroleum-derived diesel, was sprayed directly into the cylinder as a high reactivity fuel, while propanol was sprayed into the intake manifold at low pressure as a low reactivity fuel for reactivity controlled compression ignition. Four different low reactivity fuel premixed ratios of 0%, 15%, 30% and 45% propanol were used in the experiments. The experiments were carried out under 60% engine load and 2400 (rpm) constant engine speed conditions. According to the data obtained, it was found that the maximum in-cylinder pressure value increased with the increase in the premixed ratio and a significant increase occurred especially when 45% premixed ratio was used. Although the use of propanol as low reactivity fuel in the test engine under the reactivity controlled compression ignition concept was observed to cause a decrease in the indicated mean effective pressure, the rate of decrease in the indicated mean effective pressure was found to slow down as the premixed ratio increased. Finally, it was found that the in-cylinder gas temperature decreased significantly with increasing the propanol premixed ratio. When all the findings are analyzed, it has shown an important way to understand the effects of propanol as low reactivity fuel and BD35 as high reactivity fuel on engine performance at high load in diesel engines modified to operate in reactivity controlled compression ignition mode.

Keywords: RCCI, Biodiesel, Propanol, Combustion, BD35

*Corresponding author

1. Introduction

In a wide range of operations, including energy generation via generators and transportation operations such as land, sea, and rail travel, diesel engines are used as a power source. A major disadvantage of diesel engines is that they produce high amounts of pollutants such as NO_x and soot, which are harmful to the environment and human health. Therefore, many studies are carried out by researchers and engine manufacturers to reduce these pollutant emissions from diesel engines. Although there are different studies to reduce these emissions, today researchers mostly focus on in-cylinder combustion strategies and alternative fuel applications due to the problems of exhaust systems such as high cost, maintenance and fuel consumption [1]. In studies on diesel engines in the literature, low-temperature in-cylinder (LTC) combustion techniques were designated as RCCI (Reactivity Controlled Compression Ignition), PCCI (Premixed Charge Compression Ignition), and HCCI (Homogeneous Charge Compression Ignition) [2-4]. HCCI is based on the self-ignition of a homogeneous mixture by compression [5]. According to Demirci and Çınar, [6] utilizing premixed CNG in an HCCI-DI engine reduced CO and soot emissions by 90% as compared to using diesel fuel, but dramatically increased unburned HC and NO_x emissions. Due to these drawbacks of HCCI mode, researchers have begun to look into PCCI mode, which functions similarly to HCCI and traditional diesel burning. In this concept, NO_x and soot emissions are reduced due to low flame temperatures and less rich fuel mixture areas in the combustion chamber [7, 8]. To overcome some of the disadvantages of the HCCI and PCCI concepts, the RCCI concept has become more popular in recent years [9].

By using at least two fuels with different reactivity in RCCI, it is aimed to better control the combustion phases while maintaining low soot and NO_x emissions and high thermal efficiency. Low cetane or low reactivity fuel in RCCI is often injected into the engine through a port during the intake stroke, whereas high cetane or high reactivity fuel is injected directly into the cylinder during the compression stroke. The RCCI concept is claimed to work in a larger load range with extremely low NO_x and soot emissions, an acceptable pressure increase rate, and high indicated efficiency, according to previous studies [9-11]. According to Li et al. [12], RCCI provides better fuel efficiency, a lower ringing index, lower emission values, and more stable operation across a larger load and speed range than HCCI due to its optimum premixed ratio. Curran et al. [13] stated that the RCCI concept significantly reduced NO_x emissions while increasing HC and CO emissions. It also increased thermal efficiency by 7% when compared to traditional diesel combustion. In their study [14], Uyumaz and Solmaz examined the RCCI concept. In this study, they emphasized that RCCI caused high unburned HC and CO emissions and very high maximum pressure rise rates at low engine loads. They also noted that other challenges needed to be resolved, such as in-cylinder maximum pressure peaks at high loads. Due to these challenges, researchers believe that the RCCI concept still has some problems to be solved and they are continuing their work in this field.

Alternative fuels are widely utilized in internal combustion engines to lower the amount of petroleum-based fuels and the pollution-causing exhaust emissions that result from their combustion. In this context, the most researched alternative fuels used in diesel engines are biofuels such as biodiesel and bio alcohols [15]. Biodiesel has important features such as being renewable, having properties close to petroleum diesel, and creating low pollutants. Despite these advantages, high viscosity, poor low flow characteristics, and high NO_x emissions may be demonstrated as some problems that still need to be solved [16]. In the literature, it was been seen that alcohols such as butanol and propanol, which have better fuel characteristics, were suitable for use in internal combustion engines [17]. As mentioned in the previous section, RCCI can achieve a wider load range thanks to fuel and injection management among low-temperature combustion strategies. However, RCCI still has difficulties with high unburned HC and CO emissions under low load conditions, as well as pressure increase rates and maximum pressure values at high loads [18-20]. Also, Imtenan et al. reported that HC and CO emissions can be reduced by using biodiesel [21]. Because of its high viscosity and low calorific value, biodiesel is often employed in diesel engines by blending it with petroleum-based fuel. Certain mixing ratios are chosen in practice, although several alternative mixing ratios ranging from 0% to 100% have been investigated in experimental investigations. The most common and well-liked biodiesel fuel mixes in the US are BD20 and BD35, although a 7% biodiesel blend is commonly utilized in Europe. Additionally, it has been said that some diesel vehicles may run on a blend of 30% biodiesel (BD30) [22], [23].

Taking into account all of these data, biodiesel (BD35, or 35% biodiesel and 65% petroleum diesel by volume) was selected as the high reactivity fuel (HRF), and alcohol-based propanol as the low reactivity fuel (LRF) in this investigation. It is anticipated that employing both BD35 and propanol in the RCCI concept diesel engine will provide benefits such as high cetane numbers and oxygen content, besides negating some drawbacks such as high viscosities and poor heating values. Due to these effects, it is aimed to lower HC and CO emissions, which are the main drawbacks of the RCCI concept.

2. Materials and Method

In the engine laboratory of the Frat University Technology Faculty's Automotive Engineering Department, experiments were conducted. A single-cylinder, four-stroke diesel engine with common rail direct injection (CRDI) that had been adapted to run in the RCCI concept was used for the tests. Table 1 lists the specifications of the engine used in the experiment. In this research, a port fuel injection system was used to inject propanol into the intake channel at 0.5 MPa pressure to ensure the RCCI concept. LRF was injected into the port after the opening of the intake valve at the intake stroke (25° CA aTDC), while HRF was injected directly into the cylinder via the CRDI at the compression stroke (21° CA bTDC). The fuel management mechanism on the control panel was used to determine how much fuel was used. Fuel consumption was calculated with the help of a volumetric scaled fuel tank and verified with precision balances. The volumetric fuel consumption of the engine was determined during the experiments, and it was determined based on the time. BD35, which is used as HRF, was obtained by mixing petroleum-based commercial diesel fuel and commercial biodiesel fuels at 65% and 35% volumetric ratios. The propanol used as LRF was 99.5% pure and was obtained from a commercial company.

Table 1. Technical specifications of the engine

Parameters	Value
Engine type	1 cylinder and 4 stroke
Cylinder Bore x Stroke	86 mm x 70 mm
Cylinder volume	406 cm ³
Compression ratio	18.1
Maximum torque	25.7 Nm @ 2400 rpm
HRF injection type	Common-Rail Direct Injection (CRDI)
HRF injection pressure and time	300 bar @21 °CA (bTDC)
Intake valve open and close (IVO and IVC)	9°CA (bTDC)-93°CA (bTDC)
Exhaust valve open and close (EVO and EVC)	145°CA (aTDC) / 2°CA (aTDC)
E _{total} (J/cycle)	590@60% load

The engine was connected to an electric dynamometer with the Gensan GSA 271 S/4 type to carry out the loading. The tests were conducted under load conditions of 60% of the highest power of the engine and at a stable engine speed of 2400 rpm. The load amount was determined using a Zemic L6W load cell. Figure 1 depicts the overall perspective of the experimental apparatus.

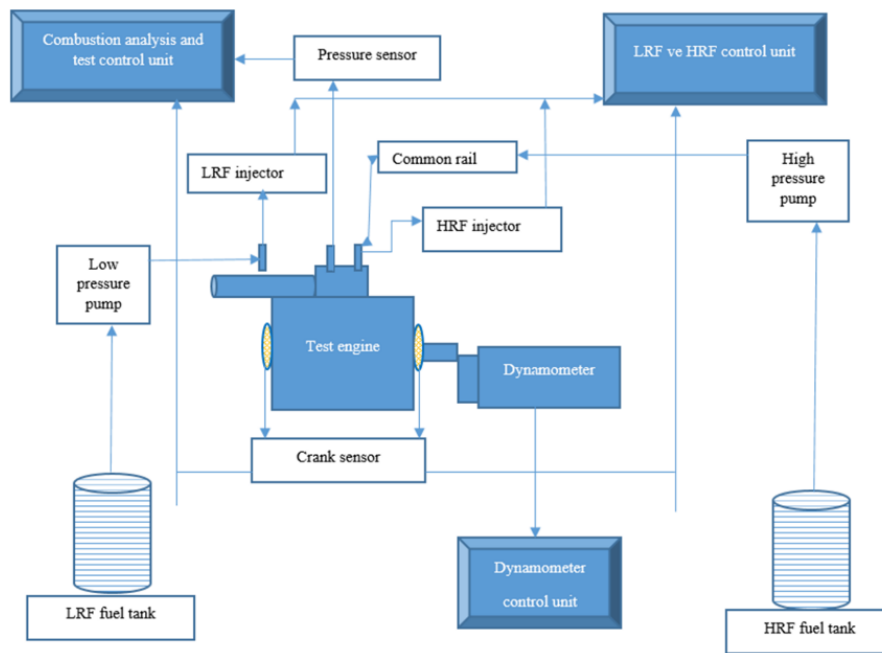


Figure 1. Schematic view of the experimental setup

An Optrand sensor and a Kübler encoder were used as pressure sensors. FebriS was used to examine the data after it was transferred to a data collecting card. For every operating position, the in-cylinder gas pressure was averaged over an average of 200 cycles. The program used the in-cylinder pressure and volume measurements along with the first law of thermodynamics to compute the heat release rate. The knock intensity was determined by the second derivative method. According to the total amount of energy consumed by the conventional diesel engine at 60% load, the amount of energy at 60% engine load in the case of RCCI was calculated for this study. Additionally, the low reactivity fuel premixed ratio (R_p) for the engine's total energy input each cycle was calculated. The R_p (premixed ratio) was determined from the consistent amount of energy provided to the conventional diesel engine per cycle. For this, the product of mass flow rate and lower calorific value of LRF is divided by the sum of the product of mass flow rate and lower calorific value of low and high reactivity fuels. R_p value was determined as 0%, 15%, 30%, and 45%. For instance, it was founded that using high reactivity fuel (BD35) at 60% engine load provided the engine with a total energy of 590 J/cycle. 15% of the 590 J/cycle total energy delivered to the engine in the conventional diesel mode for 15% R_p at this load is delivered to the engine using low reactivity fuel (propanol), and the remaining 85% is delivered to the engine using high reactivity fuel, as previously described. In this case, the experiment was carried out with a premixed ratio of 15% at 60% engine load. This method was used to determine all premixed ratios (R_p).

3. Results and Discussions

Figure 2 illustrates how changes in the LRF premixed ratio affect the in-cylinder pressure and heat release rate (HRR) for both conventional diesel engines (BD35) and RCCI (R_p 15%, 30%, and 45%) at 60% engine load. Examining the data, it was found that, in comparison to BD35, the rise in R_p raised the pressure and HRR. Increasing the R_p up to 45% gradually increased both the pressure and the HRR and the peak values were formed at this R_p . In addition, the increase in the R_p extended the ignition delay and the peak value of the pressure and HRR gradually moved away from the TDC in parallel with the increase in the R_p . Propanol's characteristics, including its low viscosity, high oxygen concentration, and high octane number, were very effective in beginning combustion reactions. Due to the high octane number of propanol and the increasing R_p , the ignition delay was prolonged in all experiments [24]. As a result, there was an effect that increased the pressure velocity and HRR values. In summary, it was determined that the use of propanol as LRF increased the in-cylinder pressure and HRR rate, and the greatest increase occurred with the use of 45% R_p .

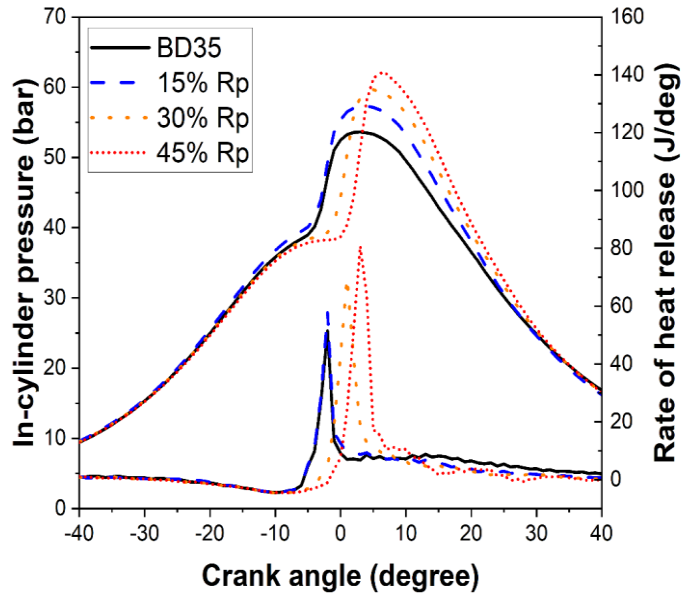


Figure 2. Variation of in-cylinder pressure and heat release rate (HRR) depending on the Rp

The effects of LRF premixed ratio change on indicated mean effective pressure (IMEP) at 60% engine load for conventional diesel engines (BD35) and RCCI (Rp 15%, 30%, and 45%) are shown in Figure 3. According to the data, when the RCCI method was used, the IMEP decreased and the greatest decrease in the IMEP was realized with the 15% premixed ratio. Although IMEP increased again as the premixed ratio increased, the decrease in IMEP continued compared to HRF. As it is known, IMEP directly or indirectly affects many different parameters such as combustion reaction efficiency, in-cylinder pressure, air/fuel ratio and ignition delay. In addition, IMEP is a parameter that is directly related to the amount of energy and pressure in the cylinder and the crank angle at which this energy and pressure of the cylinder occur. The formation of the maximum in-cylinder pressure value at an angle close to the TDC is decisive in the increase or decrease of IMEP. In previous sections, it was stated that the ignition delay rises depending on the increase in the premixed ratio. Although the pressure peak value in the cylinder increased, the crank angle at which this value occurred gradually moved away from the TDC. At the end of this change, negative work increased while positive work decreased with the use of LRF. It is thought that IMEP decreases due to this decrease in positive work. Considering all the data, in the experiments where the Rp was 15%, the maximum decrease in IMEP was realized by approximately 13%.

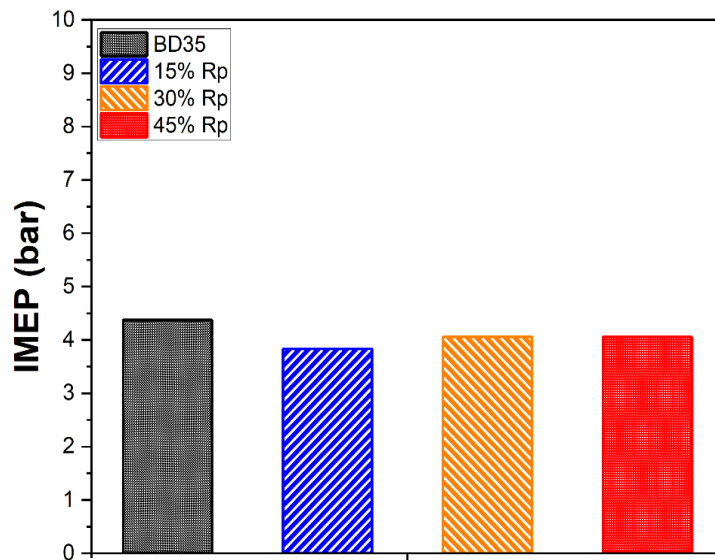


Figure 3. Variation of IMEP depending on the Rp

The impact of a premixed ratio on the maximum pressure increase and knock intensity in an engine using the RCCI concept is seen in Figure 4. When the data were examined, it was determined that the maximum pressure rise increased as the premixed ratio increased. As the premixed ratio increased up to 45%, the pressure rise rate reached its highest level. This change in pressure is due to the prolongation of the ignition delay (result from the premixed ratio), accordingly, the homogeneity level of the charge in the cylinder and the local reactive regions in the cylinder. In addition, with the increase of the premixed ratio, it was observed that the homogeneity of the charge in the cylinder decreased, the number of local reactive zones increased, and the ignition delay was prolonged. Taking these factors into account, at high premixed ratios, the combustion reactions become uncontrollable, and at very short crank angles, the pressure change achieves its maximum value. According to the graphs, a parameter directly affected by the change in the maximum pressure rise value is the engine knock intensity. The effects similar to the change in pressure are also in the values of the knock intensity. It was observed that the knock density reached the maximum level with the use of the premixed ratio of 45%. When all these data were evaluated, it was determined that the increase in the R_p , which caused the maximum pressure to occur, also brought the knock density to the maximum level.

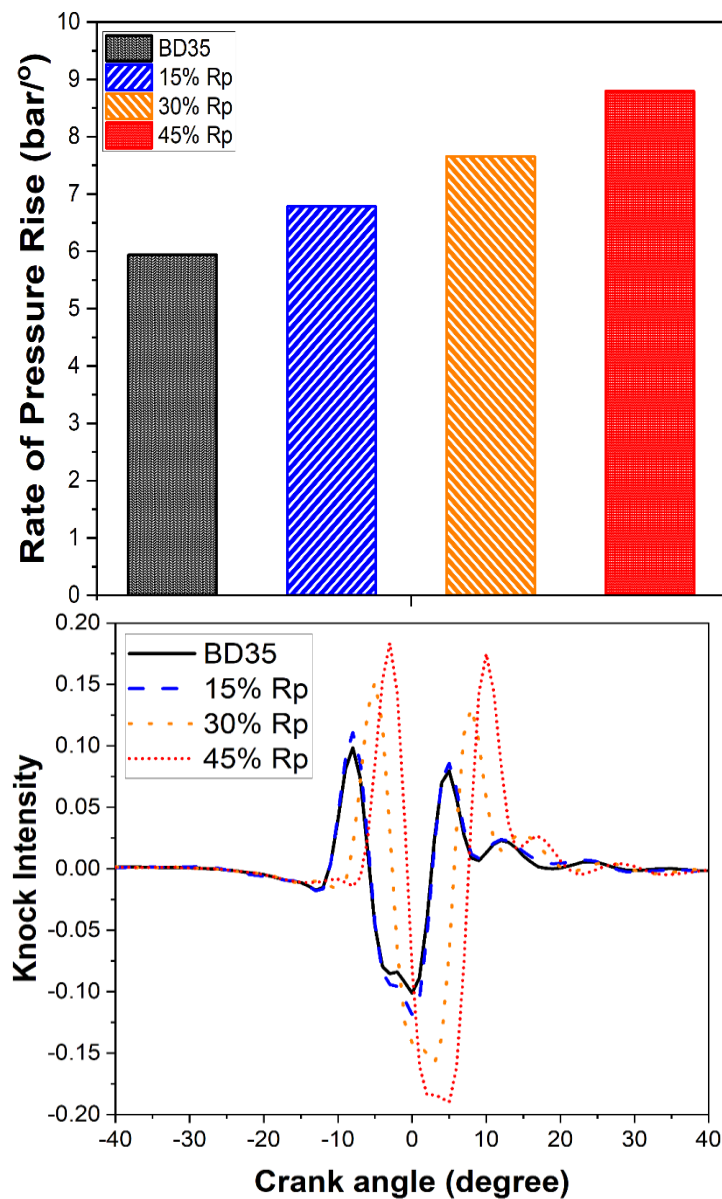


Figure 4. Variation of Rate of Pressure Rise (PRR) and knock density depending on the R_p and CA.

The effect of premixed ratio on cylinder temperature in an engine using the RCCI concept is seen in Figure 5. The results showed that the in-cylinder temperature dropped as R_p increased until the combustion

processes started. As the premixed ratio increased, the effect's intensity increased and the temperature value dropped even more. After the start of combustion reactions, the temperature value suddenly increased at very short crank angles but remained below the temperature peak value according to BD35. Propanol used as LRF is an alcohol with a high heat of vaporization, oxygen content and high octane number. While the high oxygen content of propanol causes the ignition process to be shortened, the ignition delay wants to be prolonged due to its high octane content. This situation caused instability in the temperature change at 30% Rp. In this context, as the premixed ratio increased, the heat of evaporation increased and therefore cold zones were formed in the cylinder. Combustion reactions that started under these conditions caused sudden temperature changes in the cylinder and caused the reactions to be completed at a lower temperature than HRF. Despite the combustion reactions that start and continue at a lower temperature, it is thought that there is not a great decrease in combustion performance since propanol contains higher oxygen and hydrogen compared to BD35. This situation is also seen in the IMEP graph given in Figure 3. This decrease in temperature is thought to be due to the high heat of evaporation of the LRF used.

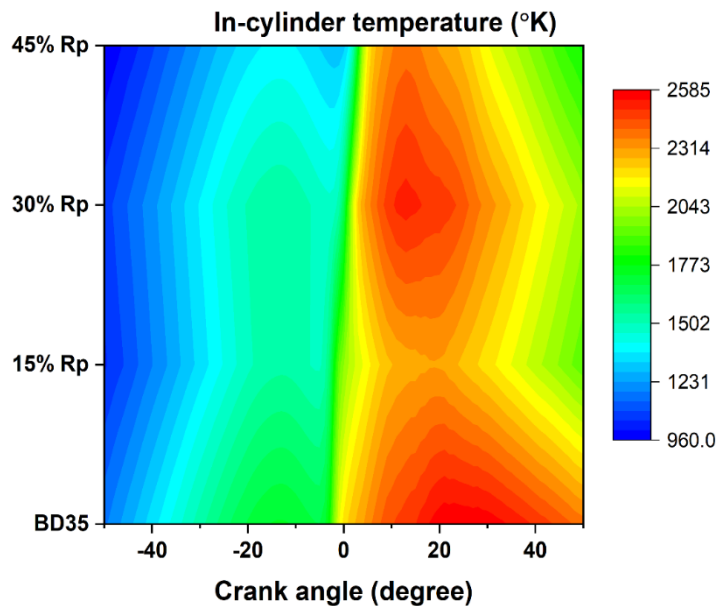


Figure 5. Variation of in-cylinder temperature depending on the Rp and CA.

4. Conclusions

The study investigated the effects of applying the RCCI concept to a single cylinder diesel engine fueled with BD35 and propanol. The results obtained in the above section are presented in detail. Some of the highlights of the study are highlighted below:

- The use of propanol as LRF increased the in-cylinder pressure and heat release rate. The largest increase in pressure was realized by approximately 16% with the use of 45% Rp.
- In the RCCI concept engine, IMEP decreased as Rp increased. The greatest reduction in IMEP was 13% when using a 15% Rp. However, as the Rp increased, this decrease rate decreased and the reduction rate in IMEP was realized as 7% at 45% Rp.
- Knock intensity increased with increasing LRF premixed ratio.
- The increase in Rp had a decreasing effect on the in-cylinder temperature. In the experiment using LRF, although the peak in-cylinder temperature increased abruptly during the rest of the combustion process, it was still a small increase compared to the use of BD35.

As a result, it has been observed that the in-cylinder temperature decreases with the RCCI concept applied to the conventional diesel engine with BD35 fuel. The greater oxygen content in the structure of the low-reactivity fuel compared to the high-reactivity fuel resulted in high pressure and heat release rates during the combustion reactions despite this drop.

5. Acknowledgment

This study was performed under the framework of a project numbered 118M650, financed by the Turkey Scientific and Technological Research Council (TUBITAK).

6. Author Contribution Statement

Mutlu Okcu: Investigation, Validation, Visualization, Writing – original draft, Writing – review & editing. Müjdat Firat: Conceptualization, Investigation, Methodology, Writing – original draft, Writing – review & editing, Project administration, Funding acquisition. Yasin Varol: Conceptualization, Methodology, Writing – original draft, Writing – review & editing, Supervision, Funding acquisition.

7. Ethics Committee Approval and Statement of Conflict of Interest

There is no conflict of interest with any person/institution in the prepared article.

8. References

- [1] M. Lapuerta, J. J. Hernandez, and F. Oliva, “Strategies for active diesel particulate filter regeneration based on late injection and exhaust recirculation with different fuels”, *Int. J. Engine Res.*, vol. 15, no. 2, pp. 209–221, Feb. 2014.
- [2] M. Krishnamoorthi, R. Malayalamurthi, Z. He, and S. Kandasamy, “A review on low temperature combustion engines: performance, combustion and emission characteristics”, *Renew. Sustain. Energy Rev.*, vol. 116, p. 109404, 2019.
- [3] M. Gwalwanshi, M. K. Chauhan, and R. Kumar, “A review of low temperature combustion techniques and the evolution of combustion strategies”, in *Emerging Trends in Mechanical and Industrial Engineering*, X. Li, M. M. Rashidi, R. S. Lather, and R. Raman, Eds., in *Lecture Notes in Mechanical Engineering*, Singapore: Springer Nature Singapore, 2023, pp. 75–83.
- [4] W. Zhao et al., “Towards a comprehensive understanding of mode transition between biodiesel-biobutanol dual-fuel ICCI low temperature combustion and conventional CI combustion–Part I: Characteristics from medium to high load”, *Energy*, vol. 246, p. 123414, 2022.
- [5] A. F. Dönmez, “Analysis of a homogeneous charge compression ignition engine (HCCI) by using a single zone modelling method”, M.Sc. Thesis, Sakarya University, Institute of science, 2010.
- [6] O. K. Demirci and C. Çinar, “The investigation of the effects of using natural gas on the performance and exhaust emissions in an HCCI-DI engine”, *Gazi Univ. J. Sci. Part C Des. Technol.*, vol. 7, no. 2, pp. 317–330, Jun. 2019, doi: 10.29109/gujsc.521668.
- [7] V. Manente, P. Tunestal, and B. Johansson, “Effects of ethanol and different type of gasoline fuels on partially premixed combustion from low to high load”, *SAE Tech. Pap.*, vol. 2010-01-0871, 2010.
- [8] S. Srihari and S. Thirumalini, “Investigation on reduction of emission in PCCI-DI engine with biofuel blends”, *Renew. Energy*, vol. 114, pp. 1232–1237, Dec. 2017.
- [9] S. L. Kokjohn, R. M. Hanson, D. A. Splitter, and R. D. Reitz, “Fuel reactivity controlled compression ignition (RCCI): a pathway to controlled high-efficiency clean combustion”, *Int. J. Engine Res.*, vol. 12, no. 3, pp. 209–226, Jun. 2011.
- [10] J. Li, W. Yang, and D. Zhou, “Review on the management of RCCI engines”, *Renew. Sustain. Energy Rev.*, vol. 69, pp. 65–79, Mar. 2017, doi: 10.1016/j.rser.2016.11.159.
- [11] S. L. Kokjohn and R. D. Reitz, “Reactivity controlled compression ignition and conventional diesel combustion: a comparison of methods to meet light-duty NOx and fuel economy targets”, *Int. J. Engine Res.*, vol. 14, no. 5, pp. 452–468, Oct. 2013.
- [12] Y. Li, M. Jia, Y. Chang, M. Xie, and R. D. Reitz, “Towards a comprehensive understanding of the influence of fuel properties on the combustion characteristics of a RCCI (reactivity controlled compression ignition) engine”, *Energy*, vol. 99, pp. 69–82, 2016.

- [13] S. J. Curran, R. M. Hanson, and R. M. Wagner, "Reactivity controlled compression ignition combustion on a multi-cylinder light-duty diesel engine", *Int. J. Engine Res.*, vol. 13, no. 3, pp. 216–225, Jun. 2012.
- [14] A. Uyumaz and H. Solmaz, "Experimental investigation of the effects of lambda and injection timing on combustion and performance characteristics in a RCCI Engine", *Gazi Univ. J. Sci. Part C Des. Technol.*, vol. 4, no. 4, pp. 299–308, 2016.
- [15] A. Turkcan, "Effects of high bioethanol proportion in the biodiesel-diesel blends in a CRDI engine", *Fuel*, vol. 223, pp. 53–62, 2018.
- [16] F. Aydın and H. Ögüt, "Effects of using ethanol-biodiesel-diesel fuel in single cylinder diesel engine to engine performance and emissions", *Renew. Energy*, vol. 103, pp. 688–694, 2017.
- [17] M. Lapuerta, J. Sánchez-Valdepeñas, J. Barba, D. Fernández-Rodríguez, J. P. Andrés, and T. García, "Analysis of soot from the use of butanol blends in a euro 6 diesel engine", *Energy Fuels*, vol. 33, no. 3, pp. 2265–2277, Mar. 2019.
- [18] J. Benajes, A. García, J. Monsalve-Serrano, and R. L. Sari, "Fuel consumption and engine-out emissions estimations of a light-duty engine running in dual-mode RCCI/CDC with different fuels and driving cycles", *Energy*, vol. 157, pp. 19–30, 2018.
- [19] M. Firat, Ş. Altun, M. Okcu, and Y. Varol, "Comparison of ethanol/diesel fuel dual direct injection (DI2) strategy with reactivity controlled compression ignition (RCCI) in a diesel research engine", *Energy*, vol. 255, p. 124556, 2022.
- [20] M. Elkelawy, E. A. El Shenawy, S. A. Mohamed, M. M. Elarabi, and H. Alm-Eldin Bastawissi, "Impacts of EGR on RCCI engines management: a comprehensive review", *Energy Convers. Manag.* X, vol. 14, p. 100216, May 2022.
- [21] S. Imtenan et al., "Impact of low temperature combustion attaining strategies on diesel engine emissions for diesel and biodiesels: a review", *Energy Convers. Manag.*, vol. 80, pp. 329–356, 2014.
- [22] W. G. Wang, D. W. Lyons, N. N. Clark, M. Gautam, and P. M. Norton, "Emissions from nine heavy trucks fueled by diesel and biodiesel blend without engine modification", *Environ. Sci. Technol.*, vol. 34, no. 6, pp. 933–939, Mar. 2000.
- [23] B. Kampman, A. Van Grinsven, H. Croezen, R. Verbeek, P. Van Mensch, and A. Patuleia, "Bringing biofuels on the market. options to increase EU biofuels volumes beyond the current blending limits", 2013.
- [24] M. Firat, Ş. Altun, M. Okcu, and Y. Varol, "Experimental investigation on combustion and emission characteristics of reactivity controlled compression ignition engine powered with iso-propanol/biodiesel blends", *Propuls. Power Res.*, vol. 11, no. 2, pp. 224–239, 2022.



Isı Emicilerin Geometrik Parametrelerinin ve Akışkan Özelliklerinin Soğutma Üzerindeki Etkisinin RSM Yöntemi İle İncelenmesi

Taha Tuna GÖKSU^{1*}

¹Makine Mühendisliği, Mühendislik Fakültesi, Adıyaman Üniversitesi, Adıyaman, Türkiye.
tgoksu@adiyaman.edu.tr

Geliş Tarihi: 15.03.2024
Kabul Tarihi: 13.05.2024

Düzeltilme Tarihi: 22.04.2023

doi: <https://doi.org/10.62520/fujece.1453248>
Araştırma Makalesi

Alıntı: T. T. Göksu, "Isı emicilerin geometrik parametrelerinin ve akışkan özelliklerinin soğutma üzerindeki etkisinin RSM yöntemi ile incelenmesi", Fırat Üni. Deny. ve Hes. Müh. Derg., vol. 3, no 2, pp. 185-203, Haziran 2024.

Öz

Bu çalışma, blok tiplerinde ve çeşitli akışkanlar kullanılarak tasarlanan ısı alıcıları üzerinde yanıt yüzey yöntemi (RSM) etkisini araştırmaktadır. RSM yöntemi, su, mono-nanoakışkanlar ve hibrit nanoakışkanlar kullanılarak hem dikey hem de yatay yönlerde yerleştirilen blok tipinde tasarlanan ısı emicilerinden elde edilen verilere uygulanmıştır. Veriler beş farklı basınç sınır koşulu altında toplanmış ve 144 veri setine uygulanmıştır. Tasarım parametrelerini analiz etmek ve yedi farklı parametre için denklemler türetmek için Box-Behnken yöntemi kullanılmıştır: yoğunluk, viskozite, özgül ısı, termal iletkenlik, blok kalınlığı, blok mesafeleri ve giriş basıncı sınır koşulları kullanılan parametrelerdir. Denklemler ortalama CPU sıcaklığını, termal direnci ve Performans Değerlendirme Kriterlerini (PEC) belirlemek için kullanılmıştır. Sonuçlar, yatay düzenlemelerde termal direnç (R_{th}), CPU ortalama sıcaklık (T_m) ve Performans Değerlendirme Kriteri (PEC) için R^2 değerlerinin sırasıyla %99.21, %99.21 ve %99.37 olduğunu göstermektedir. Dikey olarak tasarlanan geometrilerdeki R^2 değerleri %97.66, %97.66 ve %98.45 olup FLUENT'ten elde edilen sonuçlar ile ANOVA istatistiksel sonuçları arasında güçlü bir korelasyon olduğunu göstermektedir. Her bir değişkenin doğrusal, kare ve kübik etkileri her bir çözümü önemli ölçüde etkilemiştir. Çalışma, RSM yönteminin, yatay düzenlemelerde daha yüksek R^2 değerleri ve bloklar arasında daha yüksek mesafe ile ısı alıcıları üzerinde önemli bir etkiye sahip olduğu sonucuna varılmıştır. Bir diğer önemli sonuç ise blok kalınlığının artmasının da R_{th} ve T_m üzerinde önemli bir etkiye sahip olduğunu göstermiş, soğutma kapasitesini de artırırken sıcaklık dağılımını homojenleştirdiği görülmüştür.

Anahtar kelimeler: Isı emicisi, RSM, Mono-hibrit nano akışkan, PEC

*Yazışılan yazar

İntihal Kontrol: Evet – Turnitin
Şikayet: fujece@firat.edu.tr

Telif Hakkı ve Lisans: Dergide yayın yapan yazarlar, CC BY-NC 4.0 kapsamında lisanslanan çalışmalarının telif hakkını saklı tutar



Investigation of The Effect of Geometrical Parameters And Fluid Properties of Heat Sinks on Cooling By RSM Method

Taha Tuna GÖKSU^{1*}

¹Mechanical Engineering Department, Engineering Faculty, Adiyaman University, Adiyaman, Türkiye.
¹tgoksu@adiyaman.edu.tr

Received: 15.03.2024
Accepted: 13.05.2024

Revision: 22.04.2024

doi: <https://doi.org/10.62520/fujece.1453248>
Research Article

Citation: T. T. Göksu, "Investigation of the effect of geometrical parameters and fluid properties of heat sinks on cooling by RSM method", *Firat Univ. Jour. of Exper. and Comp. Eng.*, vol. 3, no 2, pp. 185-203, June 2024.

Abstract

This study investigated the effect of the response surface method (RSM) on heat sinks designed in block types and using various fluids. The RSM method was applied to the data obtained from heat sinks designed in block type placed in both vertical and horizontal directions using water, mono, nanofluids, and hybrid nanofluids. The data were collected under five different pressure boundary conditions and applied to 144 data sets. The Box-Behnken method was used to analyze the design parameters and derive equations for seven different parameters: density, viscosity, specific heat, thermal conductivity, block thickness, block distances, and inlet pressure boundary conditions. The equations were used to determine the average CPU temperature, thermal resistance, and Performance Evaluation Criteria (PEC). The findings show that the R^2 values for thermal resistance (R_{th}), average CPU temperature (T_m), and performance evaluation criteria (PEC) for flat arrangements are 99.21%, 99.21%, and 99.37%, respectively. The R^2 values for the vertically designed geometries are 97.66%, 97.66%, and 98.45%, indicating a strong correlation between the results obtained from FLUENT and the ANOVA statistical results. The linear, square, and cubic effects of each variable had a significant impact on each solution. The study concluded that the RSM method has a significant effect on heat sinks with higher R^2 values in horizontal arrangements and a higher distance between blocks. Another important result showed that increasing the block thickness also has a significant effect on R_{th} and T_m , homogenizing the temperature distribution while increasing the cooling capacity.

Keywords: Heat sink, RSM, Mono-hybrid nanofluid, PEC

*Corresponding author

1. Introduction

Electrical equipment that experiences thermal issues must be cooled passively using cost-effective and efficient thermal conductors, such as pin or plate fin heat sinks [1–6]. Researchers Chiu et al. [7,8] investigated the cooling efficiency of circular pin-type heat. Size, shape, amount, arrangement, location, and kind of coolant are some of the many factors that significantly impact a heat sink's effectiveness. Researchers have studied the cooling capacity of heat sinks with many fins using numerical analysis. Results from CFD (Computational Fluid Dynamics) models demonstrate that double-stack configurations dissipate heat more effectively than single-stack designs. The rib cavity, which is the investigation of the effect of the gap between the pin-type designed geometries, has shown to be an incredibly effective tool for creating innovative designs. It is critical to modify the width of the aluminum band and the placement of the connections, and perforated structures improve heat transfer in heat sinks. A lower thermal resistance and a higher Nusselt number are seen in mini-channel heat sinks (Nu). According to their findings, cooling efficiency is improved when phase-change materials and synthetic jets are used [9–23]. Nanofluids are being used more and more to improve heat transfer in different heat sink setups because of their excellent thermal conductivity and density. Kavitha et al.'s computational research [24] showed that using an Al_2O_3 /water nanofluid significantly enhanced heat transfer for a fin-type heat sink by 68%. The idea of utilizing nanoparticles in coolant was first put forth by Choi [25]. To enhance heat control in electronic applications, Choi and Eastman [26] used nanofluids. The experiment looked at how the Al_2O_3 - H_2O nanofluids moved and how they transferred heat in silicon-based trapezoidal microchannels. The experiment looked at how the Al_2O_3 - H_2O nanofluids moved and how they transferred heat in silicon-based trapezoidal microchannels. When compared to pure water, the results showed that there was a small increase in pressure drop and flow friction. The Nusselt number exhibited a positive correlation with the concentration of particles, the Reynolds number, and the Prandtl number. The study also investigated nanoparticle clustering and settling in small channels, revealing uncertain heat transport during boiling. The spider web-inspired baseplate design enhanced the CPU's temperature regulation and thermal efficiency [27,28]. The fins were filled with a graphene/water nanofluid. The cooling performance of a mini-channel heat sink with a wavy pattern was examined using supercritical CO_2 . Using an input temperature as low as 305 K, the study found that the heat transfer coefficient increased by an astounding 8.58 times [29]. A combination of wavy and square fins on an inclined cooler box with magnetized-radiative nanofluid shows a considerable increase in performance [30,31]. Maximum Nusselt number increases of 23.1 percent, 16.5 percent, and 8 percent were achieved using square, triangular, and circular finned fins that were cooled with nanofluid, respectively [32]. When nanofluids are added to the Eulerian-Lagrangian method, the heat transfer coefficient of a micro pin-fin heat sink is enhanced by sixteen percent [33,34].

Nanofluids comprising Al_2O_3 /water and MgO /water were determined to be more efficient than TiO_2 /water and Al_2O_3 /water in a rectangular microchannel heat sink, according to a research [35]. Ozbalcı et al. [36] found that a cost-effective and energy-efficient method of cooling electronic devices is to combine nanofluids with metal foam. On the topic of solar panel cooling, Karaaslan and Menlik looked into the effects mono and hybrid nanofluids [37]. With volume concentrations of 0.5% and 1%, In their study, Ho et al. [38] investigated the effect of various types of nanofluids on a micro-channel heat sink. They found a significant increase in the heat transfer coefficient of 14.43%. In a research conducted by Sriharan et al. [39], the convective heat transfer coefficient was shown to rise by 40%, 28%, and 22% when using nanofluids Al_2O_3 , MgO , and CuO in a hexagonal tube heat sink, respectively. The use of nanofluids to the cooling of heat sinks has been the subject of several investigations. The results demonstrate that, in comparison to more traditional cooling fluids, they possess superior thermal characteristics. Their unique features also contribute to their enhanced heat transfer efficiency, reduced pressure drop, and higher thermal conductivity. Their capacity for practical implementation in various other industries is unquestionable, although encountering certain challenges [40–46,46–48].

Leading researchers, though not frequently, use RSM in the geometrical design of heat sinks. Zhou et al. [49] utilized the RSM method to analyze heat sinks with wavy structures, revealing a 2.8-fold increase in heat transfer compared to straight ducts. Some researchers [50] have used the RSM approach in combination with nanofluid and show several parallels with the presented work, despite the difference in geometrical design. The use of RSM and an artificial neural network to design a micro-channel heat sink

demonstrated that the pareto-optimal design point has better hydraulic and thermal performance than the predefined design [51]. The study [52] focuses on optimizing the design of a heatsink manifold microchannel utilizing MWCNT/water-nanofluid to achieve minimal pressure drop and thermal resistance. The ideal design locations are established through the analysis of the flow field and heat transfer, exhibiting a strong correlation between model predictions and simulation results.

The objective of this study is to examine the impact of RSM on heat sinks that are designed in block types and use various fluids. Several impactful research have employed the RSM method to successfully achieve geometric optimization. The RSM approach is employed to identify the optimal scenario that considers both the geometric impact and the influence of the cooling fluid on the heat sink. The RSM method was applied to data obtained from both vertical and horizontal orientations with different thicknesses (ranging from 0.3–0.6 mm) and gap distances (1–1.5 mm). The fluids used were water, mono-nanofluids (2% volume concentration of CuO/water), and hybrid nanofluids (1% CuO + 1% Fe/water). The data were collected under four different pressure boundary conditions (689, 1370, 2040, and 2750 Pa), resulting in a total of 144 data points. The paper presents a unique value due to the large number of parameters analyzed and the use of the RSM method.

2. Geometry and Boundary Condition

This research investigates eight different heat sink designs in detail using the FLUENT software, all operating under the same boundary conditions. The investigated heat sink designs include a range of thickness (a) values between 0.3 and 0.6 mm, block spacing (s) values between 1 and 1.5 mm, and their matching configurations aligned vertically with the fluid flow. In their experiments, Chiu et al. [7] used a boundary condition of 300 kW/m^2 of heat flux going to the base ($10 \times 10 \text{ mm}^2$) of the heat sink, with a temperature of 300 K at the start. Figures 1 and 2 depict the dimensions of the heat sink, which are 4 mm in height, 2.5 mm in block height, and 1.5 mm above the foundation [7]. Table 1 describes the geometric arrangements used in Figure 1. These arrangements are named based on the thickness of the blocks and the distance between them in the vertical and horizontal orientations.

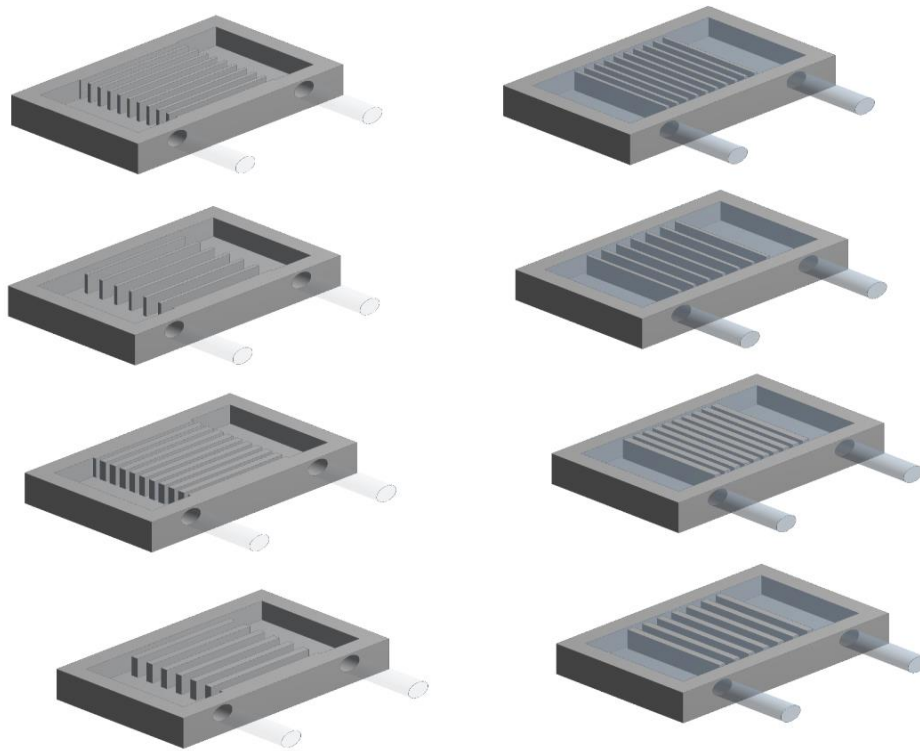


Figure 1. Schematic of heat sinks

Table 1. Named studied heat sinks

Name	Thickness (mm)	Distance (mm)	Orientation
a	0.3	1	Horizontal
b	0.3	1.5	
c	0.6	1	
d	0.6	1.5	
e	0.3	1	Vertical
f	0.3	1.5	
g	0.6	1	
h	0.6	1.5	

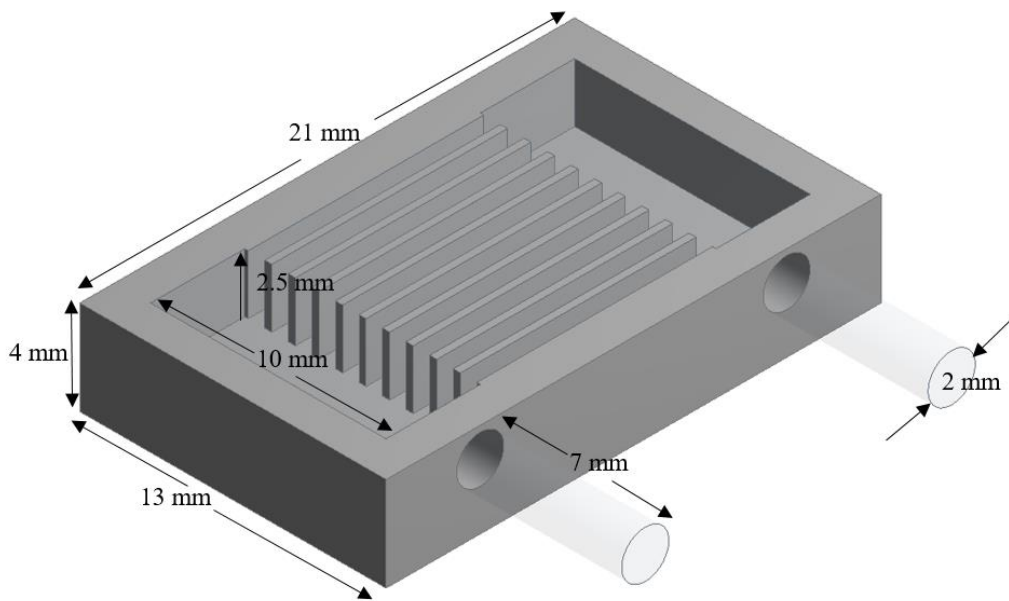


Figure 2. Parametric details of geometry

3. Numerical Analysis

This section will describe the method used to obtain the data presented in the previous paper [53] The cooling performance of the heat sink was investigated using the FLUENT program. The $k-\varepsilon$ turbulence model and SIMPLE solution method were employed.

The boundary conditions used in this investigation were inlet temperature, pressure, and constant heat flow. A steady heat flux of 300 kW/m^2 , input temperatures of 300 K, pressures of 689, 1370, 2040, 2750, 3450, and 4150 Pa were the precise boundary conditions that were established. A prior study [53] set boundary conditions at 689, 1370, 2040, and 2750 Pa, and collected data accordingly. However, for the Box-Behnken Design in RSM, a minimum of 62 data points is required for 7 distinct input variables. To meet this requirement, fresh data points were collected at pressures of 3450 and 4150 Pa. A total of 72 data sets were analyzed using RSM. Furthermore, every wall of the heat sink was subjected to an adiabatic boundary condition.

Effective thermal resistance is the most important metric for evaluating heat sink performance and cooling efficacy (R_{th}). A lower score indicates that the system is more efficient. Equations 1 and 2 demonstrate the computation of R_{th} and the heat transfer coefficient [54]. Equation 3 defines the Reynolds number, and

Equation 4 computes the friction factor. Equation 5 shows the metric for evaluating performance (PEC). Equation 5 uses the pin structure with a circular cross-section to get the value of parameter a [55].

$$R_{th} = \frac{T_{CPU,m} - T_{in}}{q''} \quad (1)$$

$$h = \frac{q''}{T_{CPU,m} - T_{bf_{th}}} \quad (2)$$

$$Re = \frac{\rho \cdot V \cdot D_h}{\mu}, \quad (3)$$

$$f = \frac{2 \cdot \Delta P \cdot D_h}{\rho \cdot L \cdot V^2}, \quad (4)$$

$$PEC = \frac{h_a/h_0}{(f_a/f_0)^{1/3}}. \quad (5)$$

In this context, the letters 'a' and '0' denote the given geometrical shapes names and experimental research geometry [7] relative to circular geometry, respectively. A better grasp of the working fluid's properties as they relate to flow and heat transmission is the primary goal of this research, which aims to maximize efficiency in thermal systems. The process incorporates nanoparticles of iron (Fe) and copper oxide (CuO) into water, which serves as the base fluid. Because the behavior of hybrid nanofluids is best approximated at lower nanoparticle concentrations, a 2% concentration was determined to be optimal for this study [56]. The previous study [53] provided calculations for the thermophysical properties of mono and hybrid nanofluids.

4. Response Surface Method

Predictive model contrary to conventional optimization methods that overlook communication characteristics and responses, the RSM technique can effectively respond to this interaction, resulting in a reduced number of experiments required for the current work and facilitating more efficient numerical and practical processes. Mostly used in practical applications, the RSM has recently shown its usefulness in computational investigations. It is considered a distinctive method due to its notable benefits, such as expediting the computational process and forecasting nonlinear optimal formulas. This approach demonstrates the correlation between the design aspect and the replies. Response Surface Methodology (RSM) employed the Box-Behnken method. Seven design parameters (density, viscosity, specific heat, thermal conductivity, block thickness, void distances, and inlet pressure boundary conditions) were used to determine the relationship between the three responses R_{th} , T_m , and PEC.

5. Result and Discussions

The Response Surface Method (RSM) was used in this study to analyze the data obtained from using different fluids (nano-fluid and hybrid nano-fluid) in CPU cooling. The block type and eight different geometrical structures ($a = 0.3-0.6$ mm, $s = 1-1.5$ mm, vertical and horizontal orientation) were designed and validated with an experimental study [7], as shown in Figure 3. Based on the results obtained, the maximum deviation for R_{th} is below 4.7%, indicating a highly efficient analysis. The

volumetric flow rate showed a maximum deviation of 6.42% between the experimental [7] and numerical studies. In the previous study, four distinct pressures of 689, 1370, 2040, and 2750 Pa were examined. In this study, a minimum of 62 data sets are required for Box-Behnken analysis, considering 7 different parameters. Consequently, new findings were obtained for pressures of 3450 and 4150 Pa in each case. Figures 4, 5, and 6 display all the respective results obtained. The section will be divided into two parts. The first part includes the RSM analysis of the data for different fluids designed in horizontal arrangements, while the second part examines the data for vertical arrangements. The figures clearly show that both R_{th} , T_m , and PEC values increase with increasing inlet pressure boundary conditions. Of course, this is a positive situation for R_{th} and T_m , while the same cannot be said for PEC. For this reason, RSM was performed, and its effect is seen in the equations below. It was seen that the minimum R_{th} was obtained as 0.2563 when mono nanofluid was used, and $a=0.6$ $s=1$ mm. Chiu et al. [7,8] found the minimum thermal resistance in pin-type geometries to be 0.258 at $P = 5000$ Pa in their study, but the presented study found this value to be $R_{th} = 0.256$ at 4150 Pa, making it a significant contribution to the literature. The reason for its importance is that the mentioned studies are both experimental studies and studies used in verification. It is also seen from Figure 5 that the same geometry provides a more uniform temperature distribution. The maximum PEC of 1.04 was obtained when hybrid nanofluid was used, followed by mono nanofluid with 1.03.

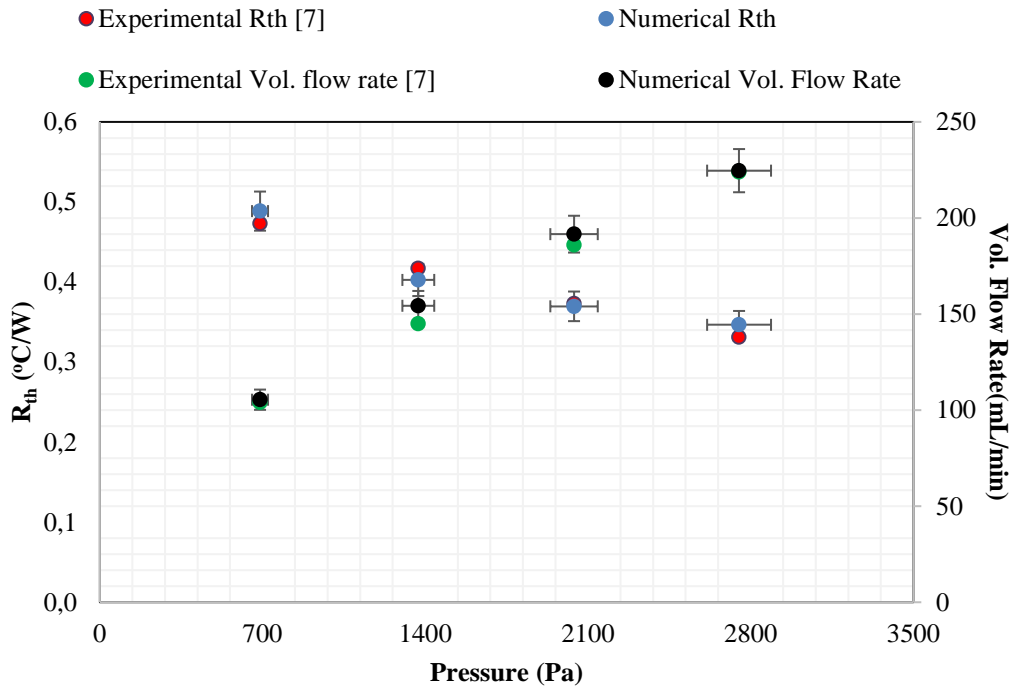
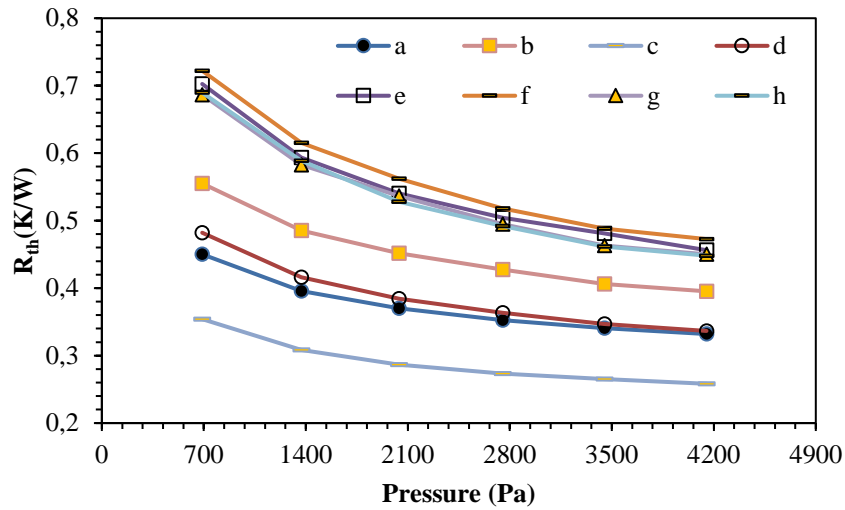
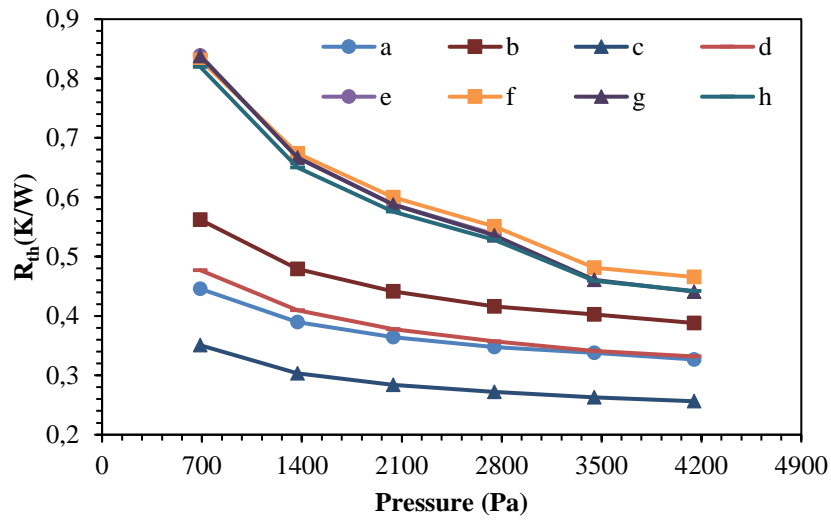


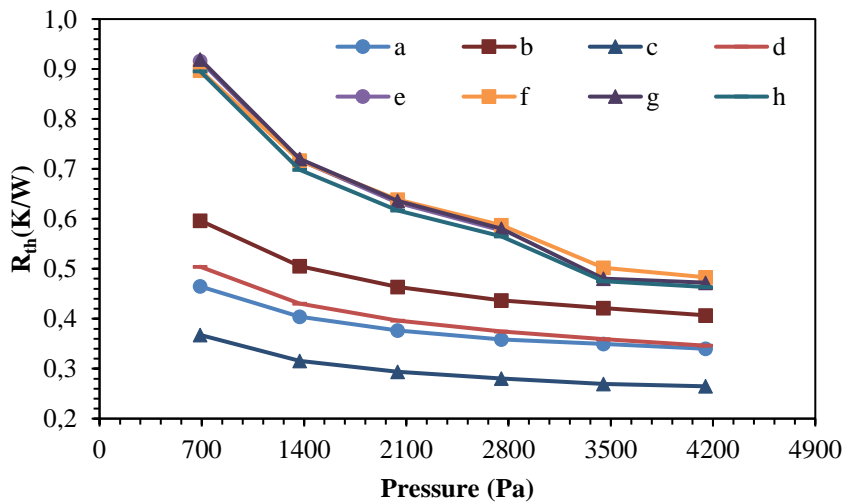
Figure 3. Validation results



(a)

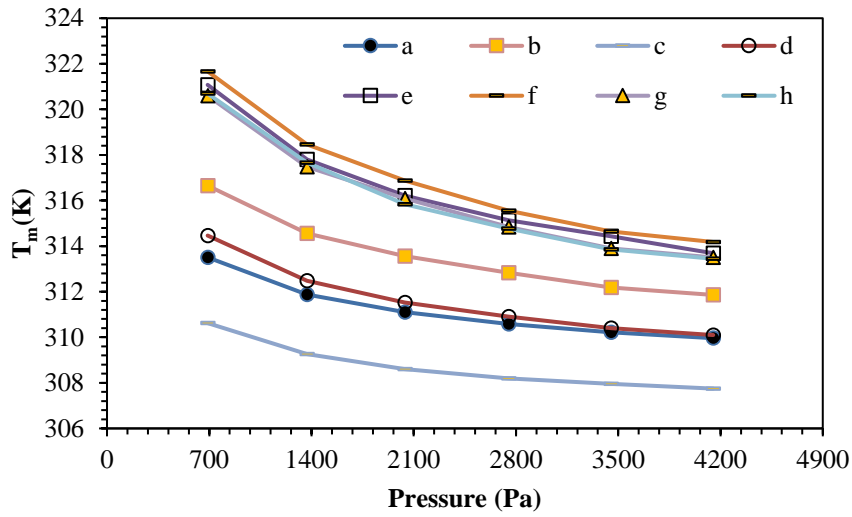


(b)

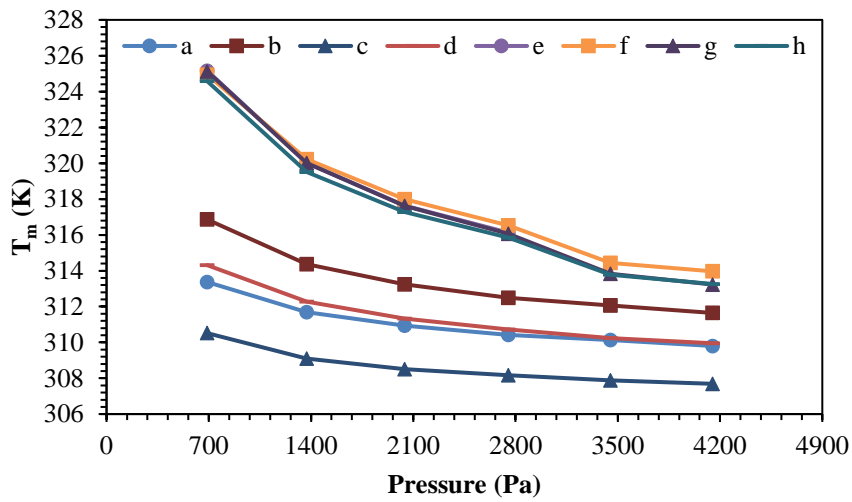


(c)

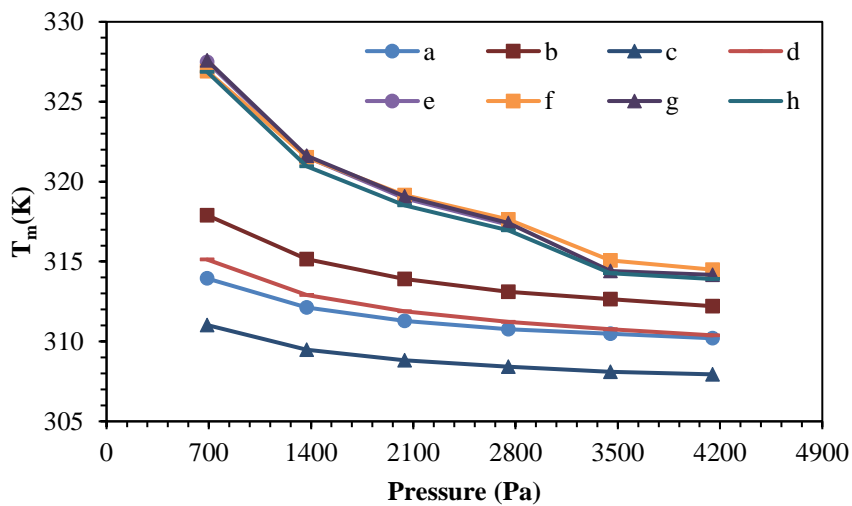
Figure 4. R_{th} Results of (a) water (b) mono (c) hybrid nanofluids



(a)

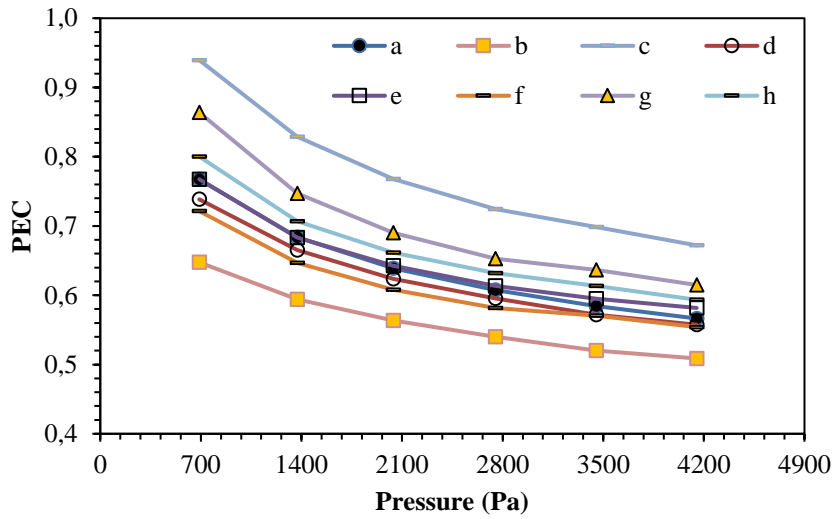


(b)

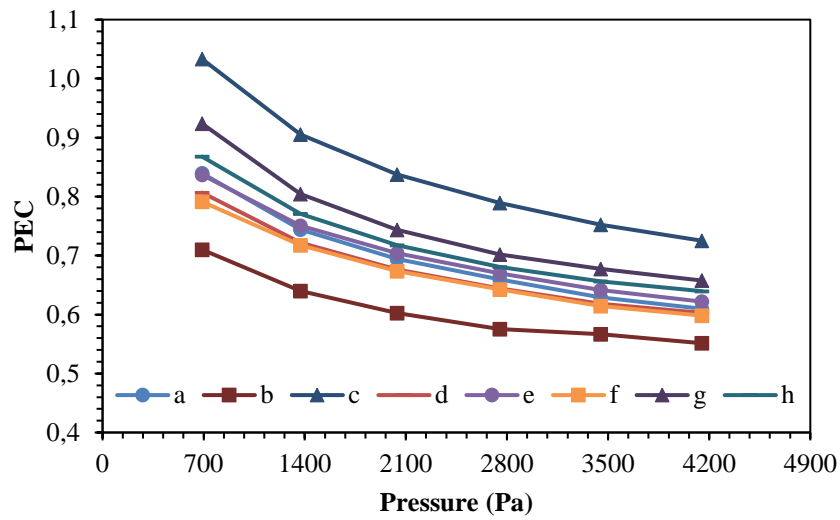


(c)

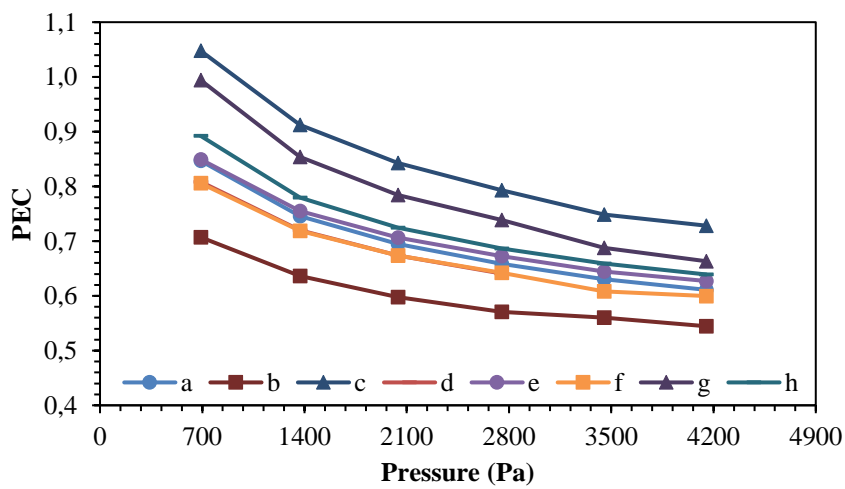
Figure 5. T_m Results of (a) water (b) mono (c) hybrid nanofluids



(a)



(b)



(c)

Figure 6. PEC Results of (a) water (b) mono (c) hybrid nanofluids

5.1. Findings from horizontally oriented geometries

This section presents the ANOVA findings and regression equations based on the data of heat sinks arranged vertically using the Box-Behnken technique. Equations 6, 7, and 8 provide the RSM-derived equations for the results obtained from the aforementioned graphs. The Box-Behnken method is employed to analyze the design parameters and derive equations for a case involving seven different parameters: density, viscosity, specific heat, thermal conductivity, block thickness, block distances, and inlet pressure boundary conditions. The obtained equations are used to determine the average CPU temperature, thermal resistance, and Performance Evaluation Criteria (PEC). The R² value indicates the effectiveness of the obtained equations. The equations derived from the results of R_{th}, T_m, and PEC parameters in horizontal arrangements have R² values of 99.21%, 99.21%, and 99.37%, respectively. These results indicate that the equations and the numerical results obtained through the FLUENT program are reliable. The ANOVA statistical results are presented in Tables 2, 3, and 4 for R_{th}, T_m, and PEC. These tables demonstrate that the F statistical values of the model were significantly high for each response, and the p-value is generally less than 0.001, showing a strong match between each answer and the related model equations. Typically, p-values below 0.001 suggest that the model is statistically significant with a 99% confidence level. The tables clearly indicate that the linear, square, and cubic effects of each variable have a substantial impact on each answer. This is evident from the probability values of each effect, all of which are below 0.05.

$$R_{th} = 0.371 + 0.000011 \rho + 18.8 \mu - 0.367 a + 0.1052 s - 0.000049 P_{inlet} - 0.000014 \rho^*a + (6) \\ 0.000031 \rho^*s - 42.8 \mu^*a + 65.3 \mu^*s - 0.00937 \mu^*P_{inlet} + 0.1009 a^*s + 0.000021 a^*P_{inlet} - \\ 0.000029 s^*P_{inlet}$$

$$T_m = 311.12 + 0.00032 \rho + 564 \mu - 11.02 a + 3.16 s - 0.001461 P_{inlet} - 0.00041 \rho^*a + 0.00092 \rho^*s - (7) \\ 1283 \mu^*a + 1960 \mu^*s - 0.281 \mu^*P_{inlet} + 3.028 a^*s + 0.000638 a^*P_{inlet} - 0.000866 s^*P_{inlet}$$

$$PEC = -0.05 + 0.000832\rho + 23.1\mu + 0.693 a+0.179 s-0.000096 P_{inlet} + 0.000348 \rho^*a - (8) \\ 0.000263 \rho^*s+17\mu^*a - 37.5 \mu^*s - 0.00328 \mu^*P_{inlet} - 0.4790 a^*s - \\ 0.000056a^*P_{inlet}+ 0.000046s^*P_{inlet}$$

Table 2. ANOVA results of R_{th}

Source	DF	Adj. SS	Adj. MS	F-Value	P-Value
Model	15	0.408581	0.027239	466.20	0.000
Linear	5	0.344179	0.068836	1178.14	0.000
ρ	1	0.000036	0.000036	0.61	0.439
μ	1	0.003143	0.003143	53.79	0.000
a	1	0.089761	0.089761	1536.28	0.000
s	1	0.132372	0.132372	2265.58	0.000
Pinlet	1	0.118461	0.118461	2027.48	0.000
Square	1	0.016635	0.016635	284.72	0.000
Pinlet*Pinlet	1	0.016635	0.016635	284.72	0.000
2-Way Interaction	9	0.007855	0.000873	14.94	0.000
ρ*a	1	0.000001	0.000001	0.01	0.903
ρ*s	1	0.000012	0.000012	0.20	0.653
ρ*Pinlet	1	0.000042	0.000042	0.72	0.399
μ*a	1	0.000038	0.000038	0.64	0.425
μ*s	1	0.000244	0.000244	4.18	0.046
μ*Pinlet	1	0.000113	0.000113	1.93	0.170
a*s	1	0.001032	0.001032	17.66	0.000
a*Pinlet	1	0.001026	0.001026	17.56	0.000
s*Pinlet	1	0.005251	0.005251	89.87	0.000
Error	56	0.003272	0.000058		
Total	71	0.411853			

Table 3. ANOVA results of T_m

Source	DF	Adj. SS	Adj. MS	F-Value	P-Value
Model	15	367.723	24.515	466.20	0.000
Linear	5	309.762	61.952	1178.14	0.000
ρ	1	0.032	0.032	0.61	0.439
μ	1	2.828	2.828	53.79	0.000
a	1	80.785	80.785	1536.28	0.000
s	1	119.135	119.135	2265.58	0.000
Pinlet	1	106.615	106.615	2027.48	0.000
Square	1	14.972	14.972	284.72	0.000
Pinlet*Pinlet	1	14.972	14.972	284.72	0.000
2-Way Interaction	9	7.069	0.785	14.94	0.000
ρ *a	1	0.001	0.001	0.01	0.903
ρ *s	1	0.011	0.011	0.20	0.653
ρ *Pinlet	1	0.038	0.038	0.72	0.399
μ *a	1	0.034	0.034	0.64	0.425
μ *s	1	0.220	0.220	4.18	0.046
μ *Pinlet	1	0.101	0.101	1.93	0.170
a*s	1	0.929	0.929	17.66	0.000
a*Pinlet	1	0.923	0.923	17.56	0.000
s*Pinlet	1	4.726	4.726	89.87	0.000
Error	56	2.945	0.053		
Total	71	370.668			

Table 4. ANOVA results of PEC

Source	DF	Adj. SS	Adj. MS	F-Value	P-Value
Model	15	0.958494	0.063900	590.10	0.000
Linear	5	0.767034	0.153407	1416.69	0.000
ρ	1	0.047884	0.047884	442.21	0.000
μ	1	0.000530	0.000530	4.89	0.031
a	1	0.171594	0.171594	1584.64	0.000
s	1	0.237078	0.237078	2189.39	0.000
Pinlet	1	0.310144	0.310144	2864.14	0.000
Square	1	0.031428	0.031428	290.23	0.000
Pinlet*Pinlet	1	0.031428	0.031428	290.23	0.000
2-Way Interaction	9	0.047179	0.005242	48.41	0.000
ρ *a	1	0.000551	0.000551	5.09	0.028
ρ *s	1	0.000876	0.000876	8.09	0.006
ρ *Pinlet	1	0.001454	0.001454	13.42	0.001
μ *a	1	0.000006	0.000006	0.06	0.815
μ *s	1	0.000081	0.000081	0.74	0.392
μ *Pinlet	1	0.000014	0.000014	0.13	0.722
a*s	1	0.023227	0.023227	214.49	0.000
a*Pinlet	1	0.007195	0.007195	66.44	0.000
s*Pinlet	1	0.013341	0.013341	123.20	0.000
Error	56	0.006064	0.000108		
Total	71	0.964558			

5.2. Findings from vertically oriented geometries

This section presents the ANOVA findings and regression equations based on the data of heat sinks arranged horizontally using the Box-Behnken technique. Equations 9, 10, and 11 provide the equations generated from the RSM for the findings seen in the previous graphics. The equations resulting from the analysis of R_{th} , T_m , and PEC parameters in horizontal configurations exhibit R^2 values of, 97.66%,

97.66%, and 98.45%, respectively. The R² results demonstrate parallelism with the values obtained in the horizontal arrangement and exceed a high threshold of 99%, indicating a strong correlation between the results obtained from FLUENT. The ANOVA statistical results are presented in Tables 5, 6, and 7. The tables reveal that the F statistical values of the model were considerably high for each response, with p-values typically below 0.001, indicating a good correlation between each answer and the corresponding model equations. A p-value < 0.001 indicates statistical significance at a 99% confidence level. The tables clearly show that the linear, square, and cubic impacts of each variable significantly influence each solution. The probability values of many effects are less than 0.05, indicating a clear trend.

$$R_{th} = -1.310 + 0.001698 \rho + 348 \mu + 0.048 a + 0.397 s + 0.000256 P_{inlet} + 0.000160 \rho * a - 0.000234 \rho * s - 49 \mu * a - 80.8 \mu * s - 0.0480 \mu * P_{inlet} - 0.1495 a * s - 0.000015 a * P_{inlet} + 0.000000 s * P_{inlet} \quad (9)$$

$$T_m = 260.70 + 0.05093 \rho + 10446 \mu + 1.4 a + 11.90 s + 0.00768 P_{inlet} + 0.000001 P_{inlet} * P_{inlet} + 0.0048 \rho * a - 0.00701 \rho * s - 0.000012 \rho * P_{inlet} - 1463 \mu * a - 2425 \mu * s - 1.441 \mu * P_{inlet} - 4.49 a * s - 0.000461 a * P_{inlet} + 0.000013 s * P_{inlet} \quad (10)$$

$$PEC = -0,154 + 0,000835 \rho + 154,1 \mu + 0,191 a + 0,109 s - 0,000017 P_{inlet} + 0,000003 \rho * a - 0,000064 \rho * s + 184,2 \mu * a - 125,6 \mu * s - 0,0272 \mu * P_{inlet} - 0,0563 a * s - 0,000053 a * P_{inlet} + 0,000017 s * P_{inlet} \quad (11)$$

Table 5. ANOVA results of R_{th}

Source	DF	Adj. SS	Adj. MS	F-Value	P-Value
Model	15	1.22112	0.081408	158.84	0.000
Linear	5	0.87168	0.174335	340.15	0.000
ρ	1	0.05420	0.054195	105.74	0.000
μ	1	0.01104	0.011037	21.53	0.000
a	1	0.00481	0.004812	9.39	0.003
s	1	0.00001	0.000006	0.01	0.912
Pinlet	1	0.79192	0.791920	1545.15	0.000
Square	1	0.07331	0.073314	143.05	0.000
Pinlet*Pinlet	1	0.07331	0.073314	143.05	0.000
2-Way Interaction	9	0.06422	0.007136	13.92	0.000
ρ*a	1	0.00012	0.000117	0.23	0.635
ρ*s	1	0.00069	0.000693	1.35	0.250
ρ*Pinlet	1	0.04496	0.044963	87.73	0.000
μ*a	1	0.00005	0.000050	0.10	0.757
μ*s	1	0.00038	0.000379	0.74	0.393
μ*Pinlet	1	0.00305	0.003052	5.96	0.018
a*s	1	0.00229	0.002288	4.46	0.039
a*Pinlet	1	0.00055	0.000549	1.07	0.305
s*Pinlet	1	0.00000	0.000001	0.00	0.961
Error	57	0.02921	0.000513		
Lack-of-Fit	56	0.02231	0.000398	0.06	1.000
Pure Error	1	0.00690	0.006904		
Total	72	1.25033			

Table 6. ANOVA results of T_m

Source	DF	Adj. SS	Adj. MS	F-Value	P-Value
Model	15	1099.01	73.267	158.84	0.000
Linear	5	784.51	156.902	340.15	0.000
ρ	1	48.78	48.776	105.74	0.000
μ	1	9.93	9.933	21.53	0.000
a	1	4.33	4.331	9.39	0.003
s	1	0.01	0.006	0.01	0.912
Pinlet	1	712.73	712.728	1545.15	0.000
Square	1	65.98	65.982	143.05	0.000
Pinlet*Pinlet	1	65.98	65.982	143.05	0.000
2-Way Interaction	9	57.80	6.422	13.92	0.000
ρ *a	1	0.11	0.105	0.23	0.635
ρ *s	1	0.62	0.624	1.35	0.250
ρ *Pinlet	1	40.47	40.466	87.73	0.000
μ *a	1	0.04	0.045	0.10	0.757
μ *s	1	0.34	0.341	0.74	0.393
μ *Pinlet	1	2.75	2.747	5.96	0.018
a*s	1	2.06	2.059	4.46	0.039
a*Pinlet	1	0.49	0.494	1.07	0.305
s*Pinlet	1	0.00	0.001	0.00	0.961
Error	57	26.29	0.461		
Lack-of-Fit	56	20.08	0.359	0.06	1.000
Pure Error	1	6.21	6.213		
Total	72	1125.30			

Table 7. ANOVA results of PEC

Source	DF	Adj. SS	Adj. MS	F-Value	P-Value
Model	15	0.587599	0.039173	241.49	0.000
Linear	5	0.472862	0.094572	583.01	0.000
rho	1	0.054982	0.054982	338.95	0.000
mu	1	0.000185	0.000185	1.14	0.290
a	1	0.050785	0.050785	313.07	0.000
s	1	0.022769	0.022769	140.36	0.000
Pinlet	1	0.344361	0.344361	2122.89	0.000
Square	1	0.036230	0.036230	223.35	0.000
Pinlet*Pinlet	1	0.036230	0.036230	223.35	0.000
2-Way Interaction	9	0.015621	0.001736	10.70	0.000
rho*a	1	0.000000	0.000000	0.00	0.987
rho*s	1	0.000053	0.000053	0.32	0.571
rho*Pinlet	1	0.002693	0.002693	16.60	0.000
mu*a	1	0.000709	0.000709	4.37	0.041
mu*s	1	0.000915	0.000915	5.64	0.021
mu*Pinlet	1	0.000981	0.000981	6.05	0.017
a*s	1	0.000325	0.000325	2.00	0.163
a*Pinlet	1	0.006573	0.006573	40.52	0.000
s*Pinlet	1	0.001788	0.001788	11.02	0.002
Error	57	0.009246	0.000162		
Lack-of-Fit	56	0.008367	0.000149	0.17	0.981
Pure Error	1	0.000879	0.000879		
Total	72	0.596845			

While the increase in the gap between the blocks seen in the horizontal arrangement has a positive effect on PEC, it is also seen in the vertical arrangement that it has a negative effect on R_{th} and T_m , that is, it increases.

6. Conclusion

In this study, the RSM method was applied to the data obtained with the effect of using three different fluid types (water, CuO, and CuO+Fe/Water) in heat sinks designed in different thicknesses and cavity block types. The findings obtained are as follows:

1. The R^2 values obtained in the horizontal arrangement are 99.21%, 99.21%, and 99.37% for R_{th} , T_m , and PEC, and 97.66%, 97.66%, and 98.45%, in the vertical arrangement. It is a remarkable result that all data are higher than 99%.
2. It was observed that increasing the distance between the blocks increased the PEC, i.e., had a positive effect but had a negative effect on R_{th} and T_m .
3. It is seen that increasing the block thickness has a very serious effect on R_{th} and T_m ; that is, it increases the cooling capacity and uniformizes the temperature distribution.

7. Author Contribution Statement

Taha Tuna Göksu: Conceptualization, Data curation, Formal analysis, Investigation, Methodology, Validation, Visualization, Writing – original draft, Writing - review & editing.

8. Ethics Committee Approval and Conflict of Interest

“There is no conflict of interest with any person/institution in the prepared article”

9. Nomenclature

C_p	specific heat, (J/kg·K)
D_h	hydraulic diameter, (m)
f	friction factor
h	convection heat transfer coefficient, (W/m ² ·K)
k	thermal conductivity, (W/m.K)
q''	heat flux, (W/m ²)
R_{th}	effective thermal resistance (K/W)
T	temperature, (K)

Greeks

μ	dynamic viscosity, (Pa·s)
ρ	density, (kg/m ³)
φ	concentration (%)

Abbreviations

CFD	computational fluid dynamics
CPU	central processing unit
PEC	performance evaluation criterion
RSM	response surface method

10. References

- [1] J. Ajayan, D. Nirmal, S. Tayal, S. Bhattacharya, L. Arivazhagan, A.S. Ausgustine, P. Murugapandiyann and D. Ajitha, “Nanosheet field effect transistors-A next generation device to keep Moore’s law alive: An intensive study”, *Microel. Jour.*, vol. 114, p. 105141, Aug. 2021.
- [2] A. Matallana, E. Ibarra, I. Lopez, J. Andreu, J. I. Garate, X. Jorda and J. Rebollo, “Power module electronics in HEV/EV applications: New trends in wide-bandgap semiconductor technologies and design aspects,” *Renew. and Sust. Ener. Reviews*, vol. 113, p. 109264, Oct. 2019.
- [3] R. R. L, P. Jayaramu, S. Gedupudi, and S. K. Das, “Experimental investigation of the influence of boiling-induced ageing on high heat flux flow boiling in a copper microchannel,” *International Journal of Heat and Mass Transfer*, vol. 181, p. 121862, Dec. 2021.
- [4] Gholami,A. and Bahrami, M., “Thermal spreading resistance inside anisotropic plates with arbitrarily located hotspots”.
- [5] K.-S. Yang, C.-H. Chung, C.-W. Tu, C.-C. Wong, T.-Y. Yang, and M.-T. Lee, “Thermal spreading resistance characteristics of a high power light emitting diode module,” *Appl. Ther.Eng.*, vol. 70, no. 1, pp. 361–368, Sep. 2014.
- [6] A. F. Al-Neama, N. Kapur, J. Summers, and H. M. Thompson, “Thermal management of GaN HEMT devices using serpentine minichannel heat sinks,” *Appl. Ther. Eng.*, vol. 140, pp. 622–636, Jul. 2018.
- [7] H.-C. Chiu, R.-H. Hsieh, K. Wang, J.-H. Jang, and C.-R. Yu, “The heat transfer characteristics of liquid cooling heat sink with micro pin fins,” *Inter. Commun.in Heat and Mass Transfer*, vol. 86, pp. 174–180, Aug. 2017.
- [8] H.-C. Chiu, M.-J. Youh, R.-H. Hsieh, J.-H. Jang, and B. Kumar, “Numerical investigation on the temperature uniformity of micro-pin-fin heat sinks with variable density arrangement,” *Case Stud.in Ther. Engi.*, vol. 44, p. 102853, Apr. 2023.
- [9] A. Shahsavar, M. Shahmohammadi, and I. Baniasad Askari, “The effect of inlet/outlet number and arrangement on hydrothermal behavior and entropy generation of the laminar water flow in a pin-fin heat sink,” *Inter. Commun. in Heat and Mass Transfer*, vol. 127, p. 105500, Oct. 2021.
- [10] A. Shahsavar, M. Shahmohammadi, and I. B. Askari, “CFD simulation of the impact of tip clearance on the hydrothermal performance and entropy generation of a water-cooled pin-fin heat sink,” *Intern. Commun. in Heat and Mass Transfer*, vol. 126, p. 105400, Jul. 2021.
- [11] R. Fattahi and M. Saidi, “Numerical investigation of curved shape fins height effect on heat transfer and flow characteristics in open microchannel heat sink,” *Inter.Jour. of Thermal Sci.*, vol. 185, p. 108060, Mar. 2023.
- [12] Y. Xia, L. Chen, J. Luo, and W. Tao, “Numerical investigation of microchannel heat sinks with different inlets and outlets based on topology optimization,” *Appl. Ener.*, vol. 330, p. 120335, Jan. 2023.
- [13] O. A. Ismail, A. M. Ali, M. A. Hassan, and O. Gamea, “Geometric optimization of pin fins for enhanced cooling in a microchannel heat sink,” *Intern. Jour.of Ther., Sci.*, vol. 190, p. 108321, Aug. 2023.
- [14] F. Koca and T. B. Güder, “Numerical investigation of CPU cooling with micro-pin-fin heat sink in different shapes,” *Eur. Phys. J. Plus*, vol. 137, no. 11, p. 1276, Nov. 2022.
- [15] R. B. Gurav, P. Purohit, P. K. Tamkhade, and S. P. Nalavade, “Computational and analytical study on CPU heat sink cooling by single and double stack air-foil micro pin fins,” *Mater. Today: Procee.*, p. S2214785323011719, Mar. 2023.








- [16] F. N. Ghadhbhan and H. M. Jaffal, "Numerical and experimental thermohydraulic performance evaluation of multi-minichannel heat sinks considering channel structure modification," *Inter. Commun.s in Heat and Mass Transfer*, vol. 145, p. 106847, Jun. 2023.
- [17] A. J. Obaid and V. M. Hameed, "An experimental and numerical comparison study on a heat sink thermal performance with new fin configuration under mixed convective conditions," *South African Jour. of Chem. Eng.*, vol. 44, pp. 81–88, Apr. 2023.
- [18] M. Fathi, M. M. Heyhat, M. Zabetian Targhi, and S. Bigham, "Bifurcated divergent microchannel heat sinks for enhanced micro-electronic cooling," *Inter. Commun. in Heat and Mass Transfer*, vol. 146, p. 106868, Jul. 2023.
- [19] G. Sung, D.-Y. Na, and S.-J. Yook, "Enhancement of the cooling performance of a pin fin heat sink based on the chimney effect using aluminum tape," *Inter. Jour. of Heat and Mass Transfer*, vol. 201, p. 123613, Feb. 2023.
- [20] M. W. Uddin and N. S. Sifat, "Comparative study on hydraulic and thermal characteristics of minichannel heat sink with different secondary channels in parallel and counter flow directions," *Inter. Jour.of Thermof.*, vol. 17, p. 100296, Feb. 2023.
- [21] V. Arumuru, K. Rajput, R. Nandan, P. Rath, and M. Das, "A novel synthetic jet based heat sink with PCM filled cylindrical fins for efficient electronic cooling," *Jour. of Ener. Stor.*, vol. 58, p. 106376, Feb. 2023.
- [22] T. T. Göksu and F. Yılmaz, "Numerical comparison study on heat transfer enhancement of different cross-section wire coils insert with varying pitches in a duct," *Jour. of Ther. Eng.*, vol. 7, no. 7, Art. no. 7, Nov. 2021.
- [23] İ. H. Yılmaz and T. T. Göksu, "Enhancement of heat transfer using twisted tape insert in a plain tube," *Bitlis Eren Üni. Fen Bilim. Derg.*, vol. 8, no. 1, Art. no. 1, Mar. 2019.
- [24] Kavitha. C, M. P.C., and A. K. C.M, "Numerical study on the performance of Al₂O₃/water nanofluids as a coolant in the fin channel heat sink for an electronic device cooling," *Mater. Today: Procee.*, p. S221478532300901X, Mar. 2023.
- [25] Choi, S. U. S., Singer, D. A., and Wang, H. P., "Developments and applications of non-Newtonian flows," vol. 66, no. 99–105, 1995.
- [26] Chol, S., "Enhancing thermal conductivity of fluids with nanoparticles," *ASME*, vol. 231, 1995.
- [27] Xinyu, W., Huiying, W., and Ping, C., "Pressure drop and heat transfer of Al₂O₃-H₂O nanofluids through silicon microchannel," *Jour.of Micromec. and Microeng.*, vol. 19, p. 105020.
- [28] S. S. Ghadikolaei, S. Siahchrehghadikolaei, M. Gholinia, and M. Rahimi, "A CFD modeling of heat transfer between CGNPs/H₂O Eco-friendly nanofluid and the novel nature-based designs heat sink: Hybrid passive techniques for CPU cooling," *Ther. Sci. and Eng.Progress*, vol. 37, p. 101604, Jan. 2023.
- [29] M. Khoshvaght-Aliabadi, P. Ghodrati, H. Mortazavi, and Y. T. Kang, "Numerical analysis of heat transfer and flow characteristics of supercritical CO₂-cooled wavy mini-channel heat sinks," *App. Ther. Eng.*, vol. 226, p. 120307, May 2023.
- [30] M. D. Massoudi and M. B. Ben Hamida, "Combined impacts of square fins fitted wavy wings and micropolar magnetized-radiative nanofluid on the heat sink performance," *Journal of Mag. and Mag. Mater.*, vol. 574, p. 170655, May 2023.
- [31] H. R. Seyf and M. Feizbakhshi, "Computational analysis of nanofluid effects on convective heat transfer enhancement of micro-pin-fin heat sinks," *Inter.Jour.of Ther. Sci.*, vol. 58, pp. 168–179, Aug. 2012.
- [32] T. Ambreen, A. Saleem, and C. W. Park, "Pin-fin shape-dependent heat transfer and fluid flow characteristics of water- and nanofluid-cooled micropin-fin heat sinks: Square, circular and triangular fin cross-sections," *App. Ther.Eng.*, vol. 158, p. 113781, Jul. 2019.

- [33] W. Cai et al., “Eulerian-Lagrangian investigation of nanoparticle migration in the heat sink by considering different block shape effects,” *App. Ther. Eng.*, vol. 199, p. 117593, Nov. 2021.
- [34] M. Yasir, M. Khan, A. S. Alqahtani, and M. Y. Malik, “Numerical study of axisymmetric hybrid nanofluid MgO-Ag/H₂O flow with non-uniform heat source/sink,” *Alex. Eng. Jour.*, vol. 75, pp. 439–446, Jul. 2023.
- [35] S. Mukherjee, S. Weislik, V. Khadanga, and P. C. Mishra, “Influence of nanofluids on the thermal performance and entropy generation of varied geometry microchannel heat sink,” *Case Stud. in Ther. Eng.*, vol. 49, p. 103241, Sep. 2023.
- [36] O. Ozbalci, A. Dogan, and M. Asilturk, “Performance of discretely mounted metal foam heat sinks in a channel with nanofluid,” *App. Ther. Eng.*, vol. 235, p. 121375, Nov. 2023.
- [37] I. Karaaslan and T. Menlik, “Numerical study of a photovoltaic thermal (PV/T) system using mono and hybrid nanofluid,” *Solar Ener.*, vol. 224, pp. 1260–1270, Aug. 2021.
- [38] C. J. Ho, J.-K. Peng, T.-F. Yang, S. Rashidi, and W.-M. Yan, “On the assessment of the thermal performance of microchannel heat sink with nanofluid,” *Inter. Jour. of Heat and Mass Transfer*, vol. 201, p. 123572, Feb. 2023.
- [39] G. Sriharan, S. Harikrishnan, and H. F. Oztop, “Performance improvement of the mini hexagonal tube heat sink using nanofluids,” *Ther. Sci. and Eng. Prog.*, vol. 34, p. 101390, Sep. 2022.
- [40] S. E. Ghasemi, A. A. Ranjbar, and M. J. Hosseini, “Forced convective heat transfer of nanofluid as a coolant flowing through a heat sink: Experimental and numerical study,” *Jour. of Mol. Liq.*, vol. 248, pp. 264–270, Dec. 2017.
- [41] S. E. Ghasemi, A. A. Ranjbar, and M. J. Hosseini, “Thermal and hydrodynamic characteristics of water-based suspensions of Al₂O₃ nanoparticles in a novel minichannel heat sink,” *Jour. of Mol. Liq.*, vol. 230, pp. 550–556, Mar. 2017.
- [42] M. Bahiraei, S. Heshmatian, and M. Keshavarzi, “Multi-criterion optimization of thermohydraulic performance of a mini pin fin heat sink operated with ecofriendly graphene nanoplatelets nanofluid considering geometrical characteristics,” *Jour. of Mol. Liq.*, vol. 276, pp. 653–666, Feb. 2019.
- [43] W. Guo, G. Li, Y. Zheng, and C. Dong, “Numerical study of nanofluids thermal and hydraulic characteristics considering Brownian motion effect in micro fin heat sink,” *Jour. of Mol. Liq.*, vol. 264, pp. 38–47, Aug. 2018.
- [44] M. Bahiraei, M. Jamshidmofid, and M. Goodarzi, “Efficacy of a hybrid nanofluid in a new microchannel heat sink equipped with both secondary channels and ribs,” *Jour. of Mol. Liq.*, vol. 273, pp. 88–98, Jan. 2019.
- [45] N. Abbas, W. Shatanawi, and K. Abodayeh, “Computational Analysis of MHD Nonlinear Radiation Casson Hybrid Nanofluid Flow at Vertical Stretching Sheet,” *Symmetry*, vol. 14, no. 7, Art. no. 7, Jul. 2022.
- [46] B. Cabir and A. Yakın, “Evaluation of gasoline-phthalocyanines fuel blends in terms of engine performance and emissions in gasoline engines,” *Jour. of the Ener. Inst.*, vol. 112, p. 101483, Feb. 2024.
- [47] M. Yetkin, Ö. F. Taş, and E. Sayın, “Comparison of equivalent earthquake load method for TEC-2007 and TBEC-2018: Adiyaman province example,” *Firat Univ. Jour. of Exper. and Comp. Eng.*, vol. 2, no. 2, Art. no. 2, Jun. 2023.
- [48] T. T. Göksu, “Investigation of pin and perforated heatsink cooling efficiency and temperature distribution,” *J Therm Anal Calorim*, Apr. 2024.
- [49] J. Zhou, M. Hatami, D. Song, and D. Jing, “Design of microchannel heat sink with wavy channel and its time-efficient optimization with combined RSM and FVM methods,” *Inter. Jour. of Heat and Mass Transfer*, vol. 103, pp. 715–724, Dec. 2016.

- [50] M. Rahimi-Gorji, O. Pourmehran, M. Hatami, and D. D. Ganji, “Statistical optimization of microchannel heat sink (MCHS) geometry cooled by different nanofluids using RSM analysis,” *Eur. Phys. J. Plus*, vol. 130, no. 2, p. 22, Feb. 2015.
- [51] M. Shanmugam and L. Sirisha Maganti, “Multi-objective optimization of parallel microchannel heat sink with inlet/outlet U, I, Z type manifold configuration by RSM and NSGA-II,” *Inter. Jour. of Heat and Mass Transfer*, vol. 201, p. 123641, Feb. 2023.
- [52] F. Pourfattah, M. F. Kheryabadi, and L.-P. Wang, “Coupling CFD and RSM to optimize the flow and heat transfer performance of a manifold microchannel heat sink,” *J Braz. Soc. Mech. Sci. Eng.*, vol. 45, no. 3, p. 178, Mar. 2023.
- [53] T. T. Göksu, “Enhancing cooling efficiency: Innovative geometric designs and mono-hybrid nanofluid applications in heat sinks,” *Case Stud. in Ther. Eng.*, vol. 55, p. 104096, Mar. 2024.
- [54] S. Lineykin and S. Ben-Yaakov, “Mod. and Anal. of Therm. Modules,” *IEEE Transactions on Industry Applications*, vol. 43, no. 2, pp. 505–512, Mar. 2007.
- [55] R. L. Webb, “Performance evaluation criteria for use of enhanced heat transfer surfaces in heat exchanger design,” *International Journal of Heat and Mass Transfer*, vol. 24, no. 4, pp. 715–726, Apr. 1981.
- [56] K. Martin, A. Sözen, E. Çiftçi, and H. M. Ali, “An Experimental Investigation on Aqueous Fe–CuO Hybrid Nanofluid Usage in a Plain Heat Pipe,” *Int J Thermophys*, vol. 41, no. 9, p. 135, Sep. 2020.



Microsoft Teams ve Skype’ın Uzaktan Eğitim Araçları Olarak Adli Bilişim Açısından İncelenmesi

Tugce KELES^{1*} , Yunus Emre COLAK² , Nurcan ILHAN³ , Kubra YILDIRIM⁴ ,
Arif Metehan YILDIZ⁵ , Turker Tuncer⁶ , Sengul Dogan⁷ 

^{1,2,3,4,5,6,7}Adli Bilişim Mühendisliği Bölümü, Teknoloji Fakültesi, Fırat Üniversitesi, Elazığ, Türkiye.

¹keles@firat.edu.tr, ²yunusemrecolak@outlook.com, ³ilhannc@gmail.com, ⁴kubra.yildirim@firat.edu.tr,
⁵a.metehanyildiz@gmail.com, ⁶turkertuncer@firat.edu.tr, ⁷sdogan@firat.edu.tr

Geliş Tarihi: 01.03.2023

Kabul Tarihi: 20.05.2024

Düzeltilme Tarihi: 04.09.2023

doi: <https://doi.org/10.62520/fujece.1462073>

Araştırma Makalesi

Alıntı: T. Keleş, Y. E. Çolak, N. İlhan, K. Yıldırım, A. M. Yıldız, T. Tuncer ve Ş. Doğan, “Microsoft teams ve skype’ın uzaktan eğitim araçları olarak adli bilişim açısından incelenmesi”, Fırat Üni. Deny. ve Hes. Müh. Derg., vol. 3, no 2, pp. 204-215, Haziran 2024.

Öz

Günümüz toplumunda internet, teknolojinin yaygın kullanımı nedeniyle her yerde bulunan bir ihtiyaç haline geldi. Bu gereklilik geleneksel normları alt üst etmiş ve hayatın her alanını etkilemiştir. Teknolojinin etkilediği en önemli alanlardan biri de kuşkusuz eğitim sektörüdür. Nüfus oranı arttıkça eğitimin önemi ve gerekliliği de artmaktadır. Bu eğitim ihtiyacına karşılık olarak çağın koşullarına göre yeni eğitim modelleri ortaya çıkmaktadır. Bu yeni modellerin ortaya çıkmasına neden olan kritik faktörlerden biri de Mart 2020’de tüm dünyayı etkisi altına alan COVID-19 salgınıdır. Bu salgın sonucunda ülkeler eğitim ve öğretim alanında çeşitli yöntemleri benimsemiştir. Bazı ülkeler eğitim faaliyetlerine ara vermiş, bazıları ise süreci uzaktan eğitim yoluyla sürdürmüştür. Uzaktan eğitim, ağırlıklı olarak bilgi ve bilgi araçlarının aktif kullanımına dayanan bir öğretim yöntemidir. Uzaktan eğitim araçlarının yaygın kullanımı, bu hizmetlere doğrudan veya dolaylı olarak erişmeye çalışan kötü niyetli kişilerin dikkatini çekebilir. Bu çalışma, Microsoft Teams ve Skype tarafından depolanan trafik bilgilerinin veya ağ üzerinden gelen ve giden trafik bilgilerinin izole bir ortamda analiz edilmesiyle elde edilen veri ve bilgilerin sunulmasını amaçlamaktadır. Çalışma, Windows 10 işletim sistemi ve web client uygulamaları kurulu bilgisayarlarda gerçekleştirilmiştir. Bu çalışmanın öncelikli amaçlarından biri gelecekte uzaktan eğitim araçlarını araştırarak olan araştırmacılara yardımcı olmaktır.

Anahtar kelimeler: Uzaktan eğitim, Microsoft teams, Skype, Wireshark

*Yazışılan Yazar








İntihal Kontrol: Evet – Turnitin

Şikayet: fujece@firat.edu.tr

Telif Hakkı ve Lisans: Dergide yayın yapan yazarlar, CC BY-NC 4.0 kapsamında lisanslanan çalışmalarının telif hakkını saklı tutar



Investigation of Microsoft Teams and Skype as Distance Education Tools in Terms of Digital Forensics

Tugce KELES^{1*} , Yunus Emre COLAK² , Nurcan ILHAN³ , Kubra YILDIRIM⁴ ,
Arif Metehan YILDIZ⁵ , Turker TUNCER⁶ , Sengul DOGAN⁷ 

^{1,2,3,4,5,6,7}Department of Digital Forensics Engineering, College of Technology, Firat University, Elazig, Türkiye.

¹keles@firat.edu.tr, ²yunusemrecolak@outlook.com, ³ilhannrc@gmail.com, ⁴kubra.yildirim@firat.edu.tr,
⁵a.metehanyildiz@gmail.com, ⁶turkertuncer@firat.edu.tr, ⁷sdogan@firat.edu.tr

Received: 01.03.2023

Revision: 04.09.2023

doi: <https://doi.org/10.62520/fujece.1462073>

Accepted: 20.05.2024

Research Article

Citation: T. Keleş, Y. E. Çolak, N. İlhan, K. Yıldırım, A. M. Yıldız, T. Tuncer and Ş. Doğan,, “Investigation of microsoft teams and skype as distance education tools in terms of digital forensics”, Firat Univ. Jour.of Exper. and Comp. Eng., vol. 3, no 2, pp. 204-215, June 2024.

Abstract

In today's society, the internet has become a ubiquitous necessity due to the widespread use of technology. This necessity has disrupted traditional norms and has affected all aspects of life. Undoubtedly, the education sector is one of the most significant areas affected by technology. As the population rate increases, the importance and necessity of education also increase. In response to this need for education, new educational models emerge based on the contemporary conditions. One of the critical factors that lead to the emergence of these new models is the COVID-19 outbreak that affected the entire world in March 2020. As a result of this epidemic, countries have adopted various methods in the field of education and training. Some countries suspended their educational activities, while others have continued the process through distance education. Distance education is a teaching method that relies heavily on the active use of information and information tools. The extensive use of distance education tools can attract the attention of malicious individuals who may seek to access these services directly or indirectly. This study aims to present the data and information obtained from analyzing the traffic information stored by Microsoft Teams and Skype or incoming and outgoing traffic information over the network in an isolated environment. The study was conducted on computers with the Windows 10 operating system and web client applications installed. One of the primary goals of this study is to assist researchers who will study distance education tools in the future.

Keywords: Distance Eeducation, Microsoft teams, Skype, Wireshark

*Corresponding author

1. Introduction

The growth of societies is significantly influenced by education, making it a key element. The accessibility of education to individuals within a society and the value that education provides are directly correlated with the level of development of the educational system [1]. Throughout the history of humanity, education has served as an essential foundation for personal and societal development, with early education typically starting within the family unit [2].

Education is increasingly necessary and important, especially in the information society [3]. As the population grows, there is a greater demand for education. New educational models have arisen to meet the societal conditions and demands that make this process necessary. The COVID-19 epidemic prevalent in our era is one such demand that has significantly contributed to the birth of new models [4]. In March 2020, the first coronavirus case occurred in Turkiye, leading to several challenges, including disruptions and interruptions in schooling. In response to decisions made by the Ministry of National Education and The Council of Higher Education training was suspended for a period, and traditional face-to-face education was switched to distance education [5].

Distance education involves trainees and providers in various locations and at different times. This teaching strategy uses informatics and tools to facilitate learning [6]. Instruments used to implement these models include satellite TV channels, terrestrial TV channels, radio frequencies, computers, and the Internet. Online services such as shopping, job interviews, consultations, and educational services require internet use. However, frequent use of remote learning resources may attract malicious individuals who attempt to access user accounts. Hackers can use novel tactics and strategies to harm services used during distance education. In providing distance education services, procedures such as data preparation, analysis, and reporting may have evidentiary value in case of a crime [7]. Specialized forensic techniques, such as digital forensics, can access digital evidence by examining information systems and data storage devices [8].

Digital forensics provides different types of evidence depending on the crime committed. Data gathered by information system components are evidence in crimes involving computers [9]. Crime problems that once occurred in physical locations are now relocated to virtual environments as the use of distance education tools expands. Electronic evidence can be gathered from crimes committed with electronic tools such as computers, portable devices, network devices, and storage devices [10]. Distance learning systems and applications include Microsoft Teams, Microsoft Skype for Business, Zoom, Google Meet, Whatsapp, Slack, and Discord. Each of these systems and applications may require different procedures and techniques for analysis and processing in digital forensics. Bayındır et al. [11] used document analysis to present a descriptive analysis of crimes involving violations of the right to education and training during the 2019-2020 academic year. The issues of defamatory writing, insult, privacy, right to education, freedom and limits of communication were addressed and conclusions were drawn. The study is important to increase educational stakeholders' understanding of potential legal and administrative wrongdoings involving educational rights and freedoms in web-based applications. The findings reveal that teachers and students can misbehave by interfering with children's access to education, restricting their freedom of expression, violating their families' privacy, and using offensive language. Kamysbayeva et al. [12] conducted a study examining contemporary e-learning challenges, analysis of the learning process, problems related to online learning and opportunities offered by online learning. The study used a qualitative approach consisting of a two-stage procedure. The interview gave the participants a chance to talk about and compare their individual learning experiences, mostly those related to the COVID-19 problem. The findings of the study showed that developing soft skills requires more effort than developing hard skills, while at the same time identifying key elements of professional staff training that should be taken into account when creating a plan to integrate on-campus and online learning, as well as diversifying the curriculum using various pedagogical technologies and digital tools. Garcia and colleagues [13] endeavored to compare nine different aspects of nine video conferencing programs, to determine the most suitable option. In this paper, we conducted a comprehensive analysis utilizing questionnaires to gather data from two distinct samples at the national and international levels. The CDIO methodology was employed, which comprises four phases which are (1) conception, (2) design, (3) implementation, and (4) operation designed to tackle challenging issues. Our primary objective is to evaluate the best live-streaming alternative based on selected standards, with popular platforms such as

Jitsi, Zoom, Microsoft Teams, Google Meet, and Big Blue Button serving as examples. The evaluation of these platforms against predefined criteria is further enhanced by employing multi-criteria analysis. Our study provides an in-depth analysis of the various aspects of video conferencing programs, facilitating the identification of the best option based on the user's needs and preferences. Mahr and colleagues [14] investigate the Zoom video conferencing application through a primary disk, network, and memory forensic analyses. The researchers utilize network intercepts, forensic imaging of digital devices, and forensic memory to uncover users' critical information, including chat messages, names, e-mail addresses, passwords, and more, in plain text or encrypted/encoded formats. The findings reveal the app's vulnerability to digital forensic investigations, allowing for the retrieval of sensitive data. The authors also delve into the fascinating anti-forensic strategies the Zoom application employs when contacts are removed from the contact list, highlighting the app's efforts to conceal user information. Al-Saleh and colleagues [15] aimed to investigate the artifacts generated by Skype, one of the most popular VoIP applications, during calls and chats on Android devices. They conducted a thorough analysis of the RAM and NAND flash memories under various conditions and durations. Their findings demonstrate that while Skype offers secure internet communication, artifacts of calls and chats can be detected on the device. Remarkably, this study is the first to investigate Skype on Android devices, making it an important contribution to the field of digital forensics. Paligu et al. [16] conducted a meticulous investigation into the artifacts produced by Microsoft Teams and stored in the IndexedDB. The research team executed a single-case pretest-posttest quasi-experiment to establish artifacts in the Microsoft Teams repository and observed that these artifacts could be extracted without requiring user credentials, a phenomenon that gives rise to potential security issues. The researchers employed signature models to ascertain the relevance of the extracted artifacts and presented the findings in a conventional database format featuring related queries and grouping by relevance. They also utilized time frame analysis to scrutinize the material, rendering it appropriate for fellow researchers. The study's findings indicate that the artifacts contained in Microsoft Teams IndexedDB harbor the vast potential for digital investigations since they facilitate the extraction of private chat messages, voice messages, and team extensions, among other data. The cybersecurity company McAfee published a blog post titled "Top 10 Microsoft Teams Security Threats" where they identified some of the major security risks associated with Microsoft Teams [6]. The study used the McAfee MVISION Cloud and analyzed data from over 40 million users worldwide. The research found ten significant security issues with Microsoft Teams, including the possibility of malware uploads, data loss from file sharing, and guest users who may accidentally join calls with confidential information. Bowling [17] tested the app on both the Windows 10 operating system and mobile operating systems such as iOS and Android. Key features of Teams, including messaging, file sharing, video conferencing and other features, were tested in a closed environment. Both automated forensic techniques and manual analysis were used to examine these devices. Cellebrite UFED and Magnet AXIOM were used for mobile and Windows devices, respectively. The majority of the artifacts on all three devices were obtained, at least in part, through manual or non-automated interrogation. In their study, many of the objects discovered through manual examination could not be recovered by the forensic tools used. Iqbal et al. [18] undertook a digital forensic examination of Google Meet, a task that entailed the probing of the platform's efficacy on sundry browsers and operating systems, including but not limited to Windows 10 and Linux, Mozilla Firefox, Google Chrome, and Microsoft Edge. The research team, in the course of the study, collected artifacts or traces of possible evidence from the client's computer, including data sourced from the Random Access Memory (RAM) and the browser. These artifacts included many data points, ranging from meetings, conversations, e-mails, profile pictures, browsing history, downloads, bookmarks, cache, and cookies. The team also sought to scrutinize the effects of RAM size on the persistence and form of the extracted memory artifacts, a feat achieved by developing an extraction tool designed to automate the process. The study, in its full magnitude, seeks to underscore the precarious nature of user data protection, even with several privacy and security measures in place. Yang et al. [19] present the results of a forensic analysis of two well-known Windows Store instant messaging applications (IMs), Facebook and Skype. Installing, uninstalling, logging in, logging out, discussing, sharing data, and other private IM operations for the analyzed programs constituted the study. The findings showed that the use of instant messaging applications from the Windows Store can leave evidence on the hard disk, memory dumps and network captures that may be important or valuable for an investigation.

In April 2021, Microsoft Teams had 145 million daily active users, a platform that can be used as a tool for distance learning. In June 2022, the company's CEO announced increased daily active users to more than 250 million [20].

The Microsoft Teams app is widely used, as evidenced by the rising number of daily active users. Even though it hasn't been the focus of any lawsuits yet, it might soon require forensic analysis as a case. Additionally, it may be assumed that the rate of use of white-collar workers is similarly high due to its institutional framework [17].

In this study, the effectiveness of distant learning resources for digital forensics was investigated. This study includes facts and information gleaned through a solitary examination of the inbound and outbound traffic records kept by Skype and Microsoft Teams. The results highlight these technologies' significance in modern digital forensics.

1.1. Objective and motivation

Distance education, as described in the literature, refers to learning activities not restricted by time or place. The COVID-19 pandemic has forced many countries to adapt their teaching processes to distance education, resulting in its widespread acceptance among educational institutions. As we transition into the post-COVID era, distance education models are likely to remain prevalent, with many companies utilizing such systems to facilitate remote working environments. However, with the increasing digitization of education and work, electronic crimes are also becoming more common. Experts are required to handle electronic evidence obtained from devices such as computers, portable devices, network devices, and storage devices.

Popular distance education applications and platforms such as Microsoft Teams, Microsoft Skype for Business, Zoom, Google Meet, Whatsapp, Slack, and Discord are increasingly being used. However, examining and handling these platforms in terms of forensic informatics may require different methods and techniques. Microsoft Teams is an example of a platform that has seen significant growth in popularity. Despite only being released recently, in April 2021, it reached 145 million daily active users, nearly twice as many as the previous year. By June 2022, Satya Nadella, the CEO of Microsoft, announced that the number of daily active users had surpassed 250 million. Although it has not been the subject of any lawsuits to date, the increasing number of daily active users of the Microsoft Teams application suggests that it may require forensic examination in the future.

2. Analyzed Distance Education Tools

2.1. Microsoft Teams

Microsoft Teams is a comprehensive platform that combines chat, meetings, note-taking, and plugins, making it a crucial distance work and education tool. Its infrastructure can be integrated with fixed telephone (PSTN) services, and while Microsoft 365 services can be used, other PSTN services can also be preferred [21]. However, supporting services such as PSTN can broaden Microsoft Teams' attack surface, attracting malicious individuals. Furthermore, Microsoft Teams features can be enriched with numerous add-ons, some developed by Microsoft, while other companies or individuals create others. Microsoft Teams benefits from three primary categories of services available on computers and mobile devices: meeting needs, real-time communication needs, and other services customized with applications [22].

In meeting scenarios, Microsoft Sharepoint and Microsoft OneDrive enable users to collaborate on content and files, and store files with version numbers. Integration with Microsoft Exchange simplifies sending mail to calendar-enabled channels, assigning tasks, and availability notifications. Microsoft Teams also allows up to 10,000 people to attend live events simultaneously. Its text-to-text translation feature can translate speeches into different languages with the help of artificial intelligence integration. However, Turkish to text translation is currently not supported [21].

Regarding real-time communication, Microsoft Teams employs VOIP technology to enable simultaneous online voice, video, or data-sharing communication between internal and external users. With the help of applications, Microsoft Teams enables capacity building according to various needs. These applications can be produced by Microsoft or created by other companies, and there are hundreds of them available [23].

Microsoft Teams can be reviewed through the management center on corporate platforms. In accordance with the working logic of Microsoft Teams, the entire communication center rotates over the server. The examinations made on this corporate management center provide very productive information. As a result of a two-way dialogue within the organization, a lot of information is available, such as messages sent by users to each other, in-channel conversations, last activity time, operating system type of device used by users, etc. [23].

In some cases, in-house users can also communicate with external Skype users in line with the organizational settings. However, the data obtained from this management panel may be limited since the relevant user is outside, and communication is performed via Skype. In such cases, it may be necessary to analyze the traffic with network listening and different analysis methods of computer content with the installation of the SCB server. In this context, Windows applications usually store their own data in the AppData directory [24]. This AppData directory is usually located at C:\Users\\AppData\Roaming. The username in the path address differs depending on the current user. Although the AppData path may vary in Windows versions, it can be pointed to with the %AppData% variable. For example, the Teams AppData folder is located in the C:\Users\\AppData\Roaming\Microsoft\Teams folder path. The Cache folder in the Teams AppData folder contains the Chromium Cache format files belonging to Teams. The fact that the files are in chromium format shows that the Microsoft Teams desktop application was developed with the open source electron [16]. This is also similar to the format of the Google Chrome app. Therefore, the CromeCashView application is very easy to examine the cache folder of Microsoft Teams.

2.2. Skype

Skype is a widely used communication application that has been available since 2003. It enables users to make free one-to-one video or voice calls, group calls, send instant messages, and share files over the internet [25]. Previous studies have shown that useful data can be retrieved from Skype in iOS and Android operating systems [15]. Additionally, research has been conducted on Skype for Windows desktop environments and Microsoft's enterprise solution, Skype for Business [19].

Although Skype, Skype for Business, and Microsoft Teams are separate applications, the research results on where and how these applications stored data in the past can give an idea to our work.

3. Investigation of Microsoft Teams and Skype Distance Education Tools in Terms of Digital Forensics

This section explains the hardware and software materials used in the examination of Microsoft Teams and Skype Distance Education tools and the examination methods of these tools. Each application is presented within the framework of the method used uniquely. The hardware and software materials used in the applications are listed in Table 1.

Table 1. Hardware and software materials used in applications

Hardware Materials	Software Materials
1 Dell brand 7300 model laptop computer with Windows 10 20H2 version operating system, x64 bit architecture, 512 GB disk capacity and 32 GB RAM	1 Windows Operating System 1 VMware Workstation 16 Virtualization Solution 2 virtual computers with 2 GB RAM, 2 Virtual Processors, 50 GB Storage Space, Network Interface with NAT, Windows 10 21H2 x64 Operating System 2 Microsoft Teams Desktops with App Ver:1.5.00.11163 2 Microsoft Skype Web Applications 1 Chrome Cache Viewer Application 1 Skype Application 1 Fiddler Application 1 WireShark Application 1 Teams Admin Account 2 Independent User E-mail Accounts 1 Enterprise Office 365 and Office 365 E1 License

3.1. Extracting user data through network analysis of skype

In the first step, we defined the "Environment Variables" on the Windows 10 client to allow for the decryption of encrypted traffic before recording the network traffic of the Skype Web Client while it was running on the Chrome browser. This process involved running "sysdm.cpl" from regedit and creating a new environment variable named "SSLKEYLOGFILE" in the "Environment Variables" section. Once Wireshark was installed on the target computers, we initiated network recording on both user computers and performed user logins on the Skype Web application using the address <https://www.skype.com/tr/features/skype-web/>. We used usernames such as "test1forensic," "test2forensic," "test1," and "test2" to identify e-mail addresses and passwords that could be obtained by searching and analyzing network records.

After successfully logging in, we initiated a message chat between test1 and test2 users, utilizing various multimedia features such as sending pictures, emojis, and GIFs and adding reactions. A "Voice Call" was made between the same users that lasted for 25 seconds, and a "Video Search" was performed to examine all features while analyzing the network recording. During the "Video Call," the camera and microphone were turned on, and audio and visual data were streamed on the network.

Once we finished using the "Message Chat," "Voice Call," and "Video Call" features, we stopped network recording via Wireshark and saved the captured data for further analysis.

3.2. Extracting user data through network analysis of microsoft teams

In the initial phase, the "Environment Variables" were defined on the Windows 10 client to enable the decryption of encrypted traffic before network registration on the Microsoft Teams Web Client, which runs on the Chrome browser. This was accomplished by launching "sysdm.cpl" from regedit and setting up a new environment variable named "SSLKEYLOGFILE" within "Environment Variables". Subsequently, Wireshark was installed on the relevant machines, and network recording was commenced on both user computers. The Microsoft Teams Web application was accessed via the address <https://www.microsoft.com/tr-tr/microsoft-teams/log-in>, and user logins were performed using the usernames "test1forensic", "test2forensic", "test1", "test2", "forensic1", and "forensic2". The aim was to extract e-mail addresses and passwords through an analysis of the network records. Once a successful login was achieved, a message conversation was initiated between users "test1" and "test2", and an array of multimedia features, such as sending pictures, emojis, GIFs, and adding reactions, were employed. After the message exchange, a "Voice Call" was conducted, and data transmission continued over the network for a duration of one minute and 25 seconds.

4. Results and Findings

After the operations were completed, the network recording obtained via Wireshark was analyzed using specific filters and search queries. Firstly, the "HTTP" filter was applied in Wireshark to view the received HTTP packets. Then, the received HTTP objects were exported and subjected to further analysis.

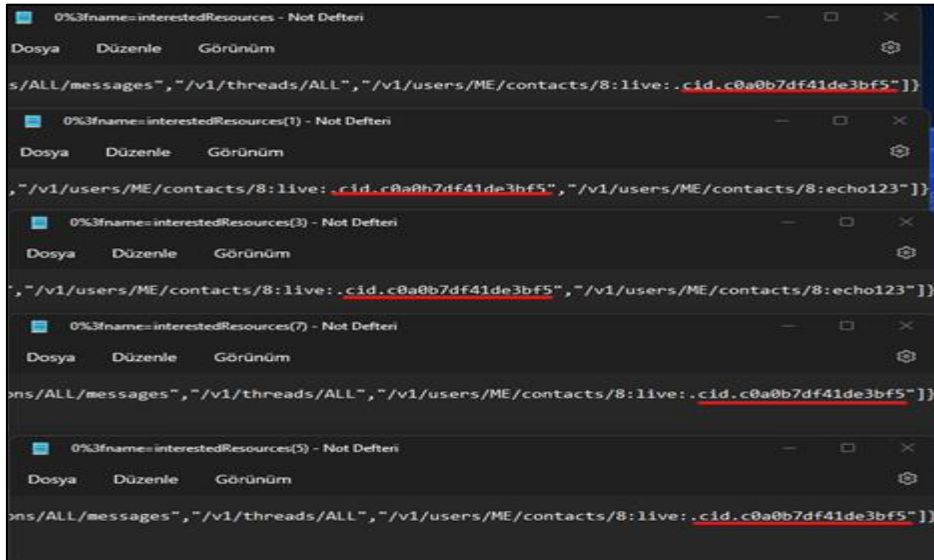


Figure 1. CID Values in Exported Files

Figure 1 clearly indicated that the exported file named "0%3fname=interestedResources" shared an identical caller identifier value (cid) with eight other files that had similar names.

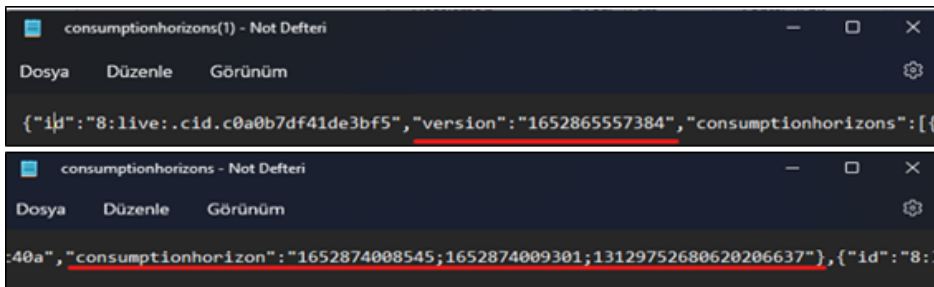


Figure 2. Timestamps of Received and Read Statuses

Figure 2 presented clear evidence that the file named "consumptionhorizons" contained timestamps of the received/read statuses. Moreover, the images/images that were exchanged during the messaging process were represented as thumbnails in files named "imgpsh_thumbnail_sx", "imgpsh_thumbnail_sx(1)", and "imgpsh_thumbnail_sx(2)".

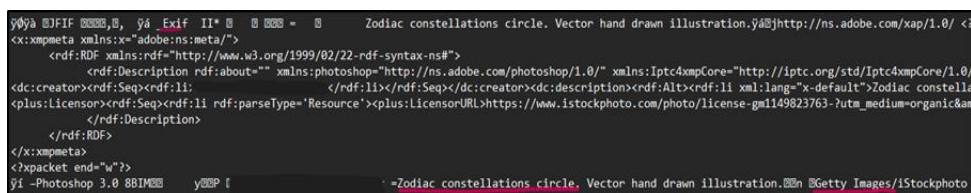


Figure 3. Exif information of the Image Sent via Chat

Figure 3 showed the exif information of the image saved as "moon.png" sent by Test1 user via chat. Exif information was the area where information about any file was small but could contain evidence in terms of digital forensics. As a result of examining the Exif information, the following details were obtained:

- Name of the person who created the image
- Name of the program used to draw the image
- The version of the program
- It was also found that the name of the image was "Zodiac Constalleions Circle" and what kind of drawing it was ("Vector hand illustration"). The name of the website from which the image was taken was also clearly visible.

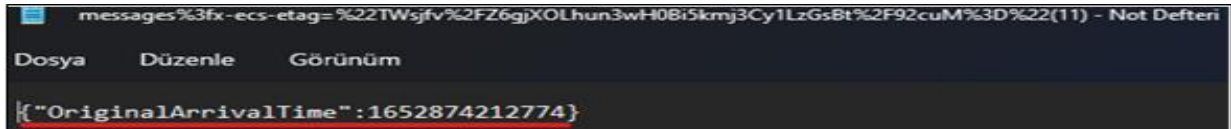
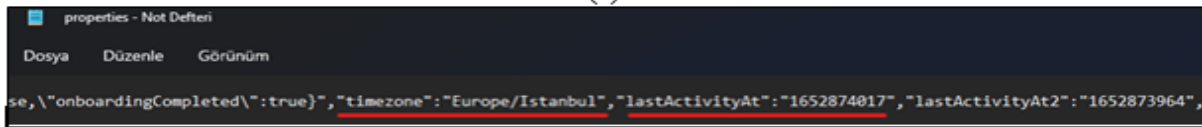


Figure 4. The arrival time of the message to the recipient

Messages sent were clear and concise in text form. The usernames of both the sender and receiver, "Test Forensic" and "Testt Forensic", were displayed along with the message ID and time. Upon examination, it was observed that all other messages were as clearly visible as the aforementioned ones. The file named "messages%3fx-ecs-etag=%22TWsjfv%2FZ6gjXOLhun3wH0Bi5kmj3Cy1LzGsBt%2F92cuM%3D%22(11)" displayed the arrival time of the message to the recipient in epoch format, as shown in the figure. Additionally, the caller identifier ID (cid) values of both users were stored and visible in video and voice calls.



(a)



(b)

Figure 5. CID and Timezone values (a) "cid" Values Retained in Voice and Video Calls, (b) Timezone and Last Active Time

In Figure 5, the "cid" values kept, the "timezones" of the users, and the last active times are marked. The method applied on Skype Web Client was also applied on Microsoft Teams Web Client, and as a result, the following findings were found;

While examining the exported objects, the first finding was "skypetoken". Since both applications belong to the same producer, it can be said that this is because they use the same infrastructure.

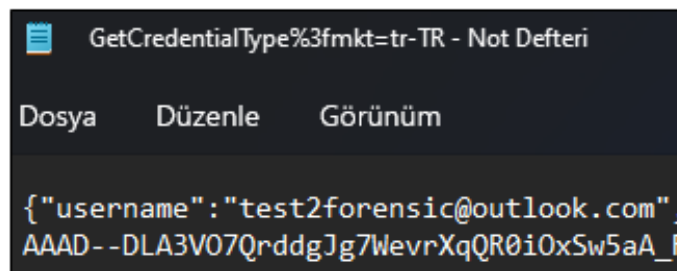


Figure 6. User Credential/ User Mail Information

It was seen in Figure 6 that the e-mail address used by the Test2 user when logging into Microsoft Teams was among the exported objects and could be read clearly.

```
102.0.5005.63@DeviceInfo.OsName Windows@DeviceInfo.OsVersion NT 10.0
DeviceInfo.Id$6a5dd49e-f0bd-4e78-833e-5e81f802804e
Session.Id$a763c0c0-a568-fddb-f20b-34fcb3f8da5b@AppInfo.ClientType@web@AppInfo.ProcessArchitecture@x64@AppInfo.WebVersion@1415/1.0.0.2022050105@
multi-window@DeviceInfo.OsFamily Windows@EventInfo.isNS@true
Panel.Context@iFrame
startReason
userInitiated@UserInfo.Language@tr-TR
UserInfo.Ring
life-general userAgentsMozilla/5.0 (Windows NT 10.0; Win64; x64) AppleWebKit/537.36 (KHTML, like Gecko) Chrome/102.0.5005.63 Safari/537.36
Window.Type@MW
Tenant.Mode@Session.TelemetryContext@web@AppInfo.BootType Unknown@UserInfo.UserLocale@tr-tr@UserInfo.OSorBrowserLocale@tr-TR@UserInfo.HostETag
```

Figure 7. Device ID, Session ID, Architecture and Language Information

In the exported file named "%3fqsp=true&content-type=application%2Fbond-compact-binary&client-id=NO_AUTH&sdk-version=ACT-Web-JS-2.5(2)", it is marked in Figure 7, and the architecture information of the device is x64., it could be inferred that the location of the user was "tr". There was an ID of the device used by the user in the format 8-4-4-4-12, and this ID is kept with the "Id" variable in the DeviceInfo class.

```
@EventInfo.Source@JS_default_source@EventInfo.InitId$190c261d-c1e4-3430- ea55-c0112008799f@EventInfo.Sequence@1@EventInfo.Name session@EventInfo.Time@2022-06-01T10:35:30.088Z
ession.Id$a763c0c0-a568-fddb-f20b-34fcb3f8da5b
ession.State Started@Session.FirstLaunchTime@2022-06-01T10:35:29.999Z@UserInfo.TimeZone@+03:00@DeviceInfo.BrowserName@Chrome@DeviceInfo.BrowserVersion
02.0.5005.63@DeviceInfo.OsName Windows@DeviceInfo.OsVersion@10
eviceInfo.Id$6a5dd49e-f0bd-4e78-833e-5e81f802804e
```

Figure 8. Session Start Time, Operating System Information, Timestamp

A timestamp of when the session was started, the session ID, the "Time.Zone" (UTC0+03:00) the user was in, the information that the user was using the "Chrome" browser and the browser version was "102.0.55005.63" Figure 8' was also clearly visible.

While examining the exported objects, the following information was obtained:

- The user's e-mail address,
- The user was running a Windows operating system, and the operating system version was "10",
- Session Id,
- The Id of the user's device, specified as "DeviceInfo",
- That the grammar of the user's location was "TR",
- Timestamps were kept in epoch and normal time format with different variables.

5. Discussions

We present a digital forensics analysis of Skype and Microsoft Teams distance education platforms. Our work includes a security analysis of both platforms, which makes us the first team to present such findings. In this paper, we discuss our analysis, findings, advantages, and limitations.

Our findings show that most distance education platforms do not use cryptographic protocols, relying solely on network security methods. This creates a significant security gap. Specifically, Skype's information security is relatively low. To acquire data from Skype and Microsoft Teams, we present two models.

Our research has several advantages. Firstly, we provide a digital forensics guide for these platforms. Secondly, we gather evidence from two distance education platforms using our model. Our primary objective is to present common digital investigation steps for distance platforms. However, since companies use different software development techniques and database structures, each platform requires different approaches. Our approach detects folder paths, which enables digital forensics analysis. Moreover, we provide the gathered information from Skype in Section 4.

The main limitation of this work is the use of only two platforms. Future work will involve investigating more distance education platforms such as Zoom and Google Meet. We plan to write a book on digital forensics analysis of distance education platforms.

6. Conclusions

The proliferation of distance education platforms has expanded the range of computer interactive crimes. Efficient case analysis requires the expertise of digital forensics professionals, who must possess knowledge of the platforms, including their APIs, background processes, and protocols.

The COVID-19 pandemic has led to a surge in the number of tools used in distance education systems, making them an essential part of people's lives. However, these platforms are vulnerable to computer interactive crimes. Digital forensics experts may encounter difficulties in investigating these crimes if they are not familiar with the components involved.

Our research offers a guide for digital forensics analysis of distance education platforms. The study employed Wireshark to record network traffic, filter it with predetermined keywords, and focus on objects that could serve as evidence. In this study, we conducted digital forensics analysis on Microsoft Teams and Skype Web Client. Information about users and devices can be obtained from network traffic and directories on these platforms.

In conclusion, digital forensics analysis of distance education tools is crucial in investigating potential computer interactive crimes. Digital forensics professionals can effectively collect evidence to assist in case analysis with the appropriate expertise and knowledge of the platforms involved.

7. Author Contribution Statement

Tugce KELES: Conceptualization, Methodology, Software, Investigation, Resources, Data Curation, Writing - Original Draft, Writing - Review & Editing. Yunus Emre COLAK: Conceptualization, Methodology, Investigation, Visualization, Writing - Original Draft, Writing - Review & Editing. Nurcan İLHAN: Methodology, Software, Resources, Data Curation. Kubra YILDIRIM: Software, Data Curation, Visualization. Sengul DOGAN: Validation, Formal Analysis, Investigation, Writing - Original Draft, Writing - Review & Editing, Supervision, Project Administration. Turker TUNCER: Validation, Formal Analysis, Investigation, Writing - Original Draft, Writing - Review & Editing, Supervision, Project Administration. Arif Metehan YILDIZ: Resources.

8. Ethics Committee Approval and Conflict of Interest

There is no need for an ethics committee approval in the prepared article. There is no conflict of interest with any person/institution in the prepared article.

9. References

- [1] Y. Akyüz, Türk eğitim tarihi. Ankara Üniv. Eğitim Bilimleri Fak., 1982.
- [2] L. Malaguzzi, C. Edwards, L. Gandini, and G. Forman, "History", Ideas and Basic Philosophy, 1993.
- [3] E. Alampay, "Beyond access to ICTs: Measuring capabilities in the information society", Inter.Jour. of Educ. and Devel. Using ICT, vol. 2, no. 3, pp. 4-22, 2006.
- [4] Y. Zhao and J. Watterston, "The changes we need: Education post COVID-19", Jour. of Educ. Chan., vol. 22, no. 1, pp. 3-12, 2021.
- [5] A. E. Al Lily, A. F. Ismail, F. M. Abunasser, and R. H. A. Alqahtani, "Distance education as a response to pandemics: Coronavirus and Arab culture", Techn. in Soci., vol. 63, p. 101317, 2020.
- [6] P. P. Wilson, D. Valentine, and A. Pereira, "Perceptions of new social work faculty about mentoring experiences", Jour. of Social Work Educ., vol. 38, no. 2, pp. 317-332, 2002.

- [7] K. Conlan, I. Baggili, and F. Breitingner, "Anti-forensics: furthering digital forensic science through a new extended, granular taxonomy", *Dig. Inves.*, vol. 18, pp. S66-S75, 2016.
- [8] A. Agarwal, M. Gupta, S. Gupta, and S. C. Gupta, "Systematic digital forensic investigation model", *Inter. Jour. of Comp. Sci. and Secur.(IJCSS)*, vol. 5, no. 1, pp. 118-131, 2011.
- [9] E. AkbaL, Ş. Doğan, T. Tuncer, and N. S. Atalay, "Adli bilişim alanında ağ analizi", *Bitlis Eren Üni. Fen Bil. Derg.*, vol. 8, no. 2, pp. 582-594, 2019.
- [10] Y. Korkmaz and A. Boyacı, "Adli bilişim açısından ses incelemeleri," *Fırat Üni. Müh. Bil. Derg.*, vol. 30, no. 1, pp. 329-343, 2018.
- [11] N. Bayindir and S. Levent, "An Awareness Study on Judicial/Administrative Crimes That May Occur During Web-Based Education Process," *Osmangazi Jour.of Educ. Res.*, vol. 8, no. 2, pp. 149-164.
- [12] A. Kamysbayeva, A. Koryakov, N. Garnova, S. Glushkov, and S. Klimenkova, "E-learning challenge studying the COVID-19 pandemic," *Inter. Jour. of Educ.Manag.*, vol. 35, no. 7, pp. 1492-1503, 2021.
- [13] N. O. García, M. D. Velásquez, C. T. Romero, J. O. Monedero, and O. Khalaf, "Remote academic platforms in times of a pandemic", *Inter. Jour. of Emer. Tech. in Learning (iJET)*, vol. 16, no. 21, pp. 121-131, 2021.
- [14] A. Mahr, M. Cichon, S. Mateo, C. Grajeda, and I. Baggili, "Zooming into the pandemic! A forensic analysis of the Zoom Application", *Fore. Sci. Intern.: Digital Inves.n*, vol. 36, p. 301107, 2021.
- [15] M. I. Al-Saleh and Y. A. Forihat, "Skype forensics in android devices," *Inter. Jour. of Comp. Appl.*, vol. 78, no. 7, 2013.
- [16] F. Paligu and C. Varol, "Microsoft Teams desktop application forensic investigations utilizing IndexedDB storage", *Jour. of Foren. Scie.*, vol. 67, no. 4, pp. 1513-1533, 2022.
- [17] H. R. Bowling, "A Forensic Analysis of Microsoft Teams", *Purdue University Graduate School*, 2021.
- [18] F. Iqbal, Z. Khalid, A. Marrington, B. Shah, and P. C. Hung, "Forensic investigation of Google Meet for memory and browser artifacts", *Foren. Scie. Inter.: Digital Inves.*, vol. 43, p. 301448, 2022.
- [19] T. Y. Yang, A. Dehghantanha, K.-K. R. Choo, and Z. Muda, "Windows instant messaging app forensics: Facebook and Skype as Case Studies", *PloS one*, vol. 11, no. 3, p. e0150300, 2016.
- [20] E. M. Osiakwan, "The KINGS of Africa's digital economy", *Digital Kenya*, pp. 55-92, 2017.
- [21] Z. Kristóf, "International trends of remote teaching ordered in light of the Coronavirus (COVID-19) and its most popular video conferencing applications that implement communication," *Central Europ. Jour. of Educ. Res.*, vol. 2, no. 2, pp. 84-92, 2020.
- [22] D. Pal and V. Vanijja, "Perceived usability evaluation of Microsoft Teams as an online learning platform during COVID-19 using system usability scale and technology acceptance model in India", *Child. and Youth Serv. Revi.*, vol. 119, p. 105535, 2020.
- [23] M. Nicoletti and M. Bernaschi, "Forensics for Microsoft teams", *arXiv preprint arXiv:2109.06097*, 2021.
- [24] R. Brewer, "Ransomware attacks: detection, prevention and cure", *Net. Secu.*, vol. 2016, no. 9, pp. 5-9, 2016.
- [25] V. Lo Iacono, P. Symonds, and D. H. Brown, "Skype as a tool for qualitative research interviews", *Sociol. Resea. Online*, vol. 21, no. 2, pp. 103-117, 2016.



T Bağlantılarda Deltoit Yarıçapının Çekme Yüküne Etkisinin Sayısal Olarak İncelenmesi

Mustafa ALBAYRAK^{1*}

¹Makine ve Metal Teknolojileri Bölümü, Malatya OSB Meslek Yüksekokulu, İnönü Üniversitesi, Malatya, Türkiye.
¹mustafaalbayrak@inonu.edu.tr

Geliş Tarihi: 17.04.2024

Kabul Tarihi: 21.05.2024

Düzeltilme Tarihi: 29.04.2024

doi: <https://doi.org/10.62520/fujece.1469580>

Araştırma Makalesi

Alıntı: M. Albayrak, "T bağlantılarda deltoit yarıçapının çekme yüküne etkisinin sayısal olarak incelenmesi", Fırat Üni. Deny. ve Hes. Müh. Derg., vol. 3, no 2, pp. 216-226, Haziran 2024.

Öz

Bu çalışmada farklı deltoit yarıçaplarına sahip kompozitlerden T şeklinde birleşimler tasarlanmıştır. Bu amaçla takviye elemanı olarak karbon elyaf dokuma kumaşlar tercih edilmiştir. Daha sonra bu kompozit T-eklemleri üzerinde çekme analizleri yapılmıştır. Deltoit yarıçapının yapının maksimum çekme kuvvetine ve hasar davranışına etkisi incelenmiştir. Analizler sonucunda kuvvet-deplasman grafiği ile birlikte her deltoit yarıçap için yapıda meydana gelen fiber çekme-basma hasarı görüntüleri elde edilmiştir. Hasar başlangıcı için Hashin hasar kriteri tercih edilmiştir. Aşamalı hasar analizinde hasar ilerlemesi için Malzeme Özelliklerinin Bozulması (MPDG) yöntemi kullanılmıştır. Deltoit yarıçapının 6 mm'den 12 mm'ye çıkarılmasıyla maksimum temas kuvveti yaklaşık %10 artmıştır. 18 mm'ye çıkarılmasıyla ise yaklaşık %20.11 yükseldiği belirlenmiştir. Flanşın ağ ile temas etmediği alt yüzeyinde geniş bir alana yayılan fiber basma hasarının baskın hasar tipi olduğu belirlenmiş ve deltoit yarıçapın artmasıyla bu hasarın azaldığı tespit edilmiştir. Deltoit yarıçapı arttıkça T bağlantılı kompozit yapının daha rijit malzeme davranışı sergilediği görülmüştür.

Anahtar kelimeler: T-bağlantıları, Deltoit yarıçapı, Karbon fiber, Sürekli hasar mekaniği, Malzeme özelliklerinin bozulması

*Yazışılan Yazar

İntihal Kontrol: Evet – Turnitin

Şikayet: fujece@firat.edu.tr

Telif Hakkı ve Lisans: Dergide yayın yapan yazarlar, CC BY-NC 4.0 kapsamında lisanslanan çalışmalarının telif hakkını saklı tutar.



Numerical Investigation of the Effect of Deltoid Radius on Tensile Load in T-joints

Mustafa ALBAYRAK ^{1*}

¹Department of Machine and Metal Technologies, Malatya Organized Industrial Zone Vocational School, Inonu University, Malatya, Türkiye.

¹mustafaalbayrak@inonu.edu.tr

Received: 17.04.2024

Accepted: 21.05.2024

Revision: 29.04.2024

doi: <https://doi.org/10.62520/fujece.1469580>

Research Article

Citation: M. Albayrak, "Numerical investigation of the effect of deltoid radius on tensile load in t-joints", *Firat Univ. Jour. of Exper. and Comp. Eng.*, vol. 3, no 2, pp. 216-226, June 2024.

Abstract

In this study, T-shaped joints were designed from composites with different deltoid radius. For this purpose, carbon fiber woven fabrics were preferred as reinforcement elements. Then, tensile analyzes were performed on these composite T-joints. The effect of the deltoid radius on the maximum tensile load and damage behavior of the structure was examined. As a result of the analyses, fiber tensile-compression damage images occurring in the structure for each deltoid radius were obtained along with the load-displacement graph. The Hashin damage criterion was preferred for damage onset. Material Property Degradation (MPDG) method was used for damage progression in progressive damage analysis. By increasing the deltoid radius from 6 mm to 12 mm, the maximum contact load increased by approximately 10%, and by increasing it to 18 mm, the maximum contact load increased by approximately 20.11%. Fiber compression damage, spread over a wide area on the lower surface of the flange where it does not come into contact with the web, was determined to be the dominant damage type, and it was determined that this damage decreased with the increase of the deltoid radius. it was observed that as the deltoid radius increases, the T-jointed composite structure exhibits more rigid material behavior.

Keywords: T-joints, Deltoid radius, Carbon fiber, Continuum damage mechanics, Material property degradation

*Corresponding author

1. Introduction

In recent years, fiber-reinforced composite structures have been widely used in many areas, such as the marine, aviation, and space industries. Composites are lightweight and have high strength and rigidity. In addition, the fact that they can be produced in desired geometries and sizes and provide the intended strength properties by using different fiber/matrix components causes these structures to be widely used. Large fiber reinforced plastic (FRP) structures have many connection points in their topology due to design and manufacturing constraints [1]. The most important connection type applied in structural applications is the composite T-connection. T-joints are designed to meet bending loads in structures such as aircraft fuselage-wing connections, marine and road vehicles [2]. Thin-walled composite structures are used in some wing panels and fuselage sections of aircraft. These structures need to be strengthened with internal reinforcements, especially to increase buckling strength. The most suitable design for this is the T-shaped hardened connection. The purpose of the T-stiffener is to prevent buckling of the surface during wing loading [3]. Material and geometry changes have a significant impact on the stress distribution, damage mode and performance of T-joints [4]. Improper design of a connection increases the likelihood of structural damage or even disaster. Therefore, understanding the damage mechanism and mechanical behavior of composite joints is a very important issue [5]. When the static tests and analyzes performed on T-connected composite structures are examined: Trask et al. carried out studies on the damage mechanisms that occur in structures with laminated composite T-joint structures under tensile load. They investigated the effect of process-induced defects in the deltoid area on the damage load by focusing on the effect [6]. Philips and shenoi [1]. proposed an approach to evaluate the damage tolerance of fiber-reinforced composite structures in critical regions of single-wall T-joints. They examined the sequence of damage initiation and progression at T-joints under loading and boundary conditions and characterized the stress patterns in the connections under these loads. Khor et al. presented a new approach to improve the structural properties and damage tolerance of fiber-reinforced polymer composite joints by tufting using shape memory alloy (SMA) filaments. By strengthening the T-shaped connections made from carbon-epoxy composite material with thin SMA (Ni-Ti nitinol) tufts, they determined the ultimate load, ultimate displacement and absorbed energy capacity of the reinforced T connection [7]. Stickler and Ramulu produced cross-stitched T-joints using fiber splicing process and PR520 hardened epoxy resin and investigated their mechanical behavior. They carried out experimental and numerical analyzes under bending loading and carried out preliminary experiments under tensile loading [8]. Dharmawan et al. investigated the structural integrity and damage tolerance of typical composite T-joints found in ships constructed from glass fiber reinforced plastic. They determined the effect of T-joint geometry on strain distribution using finite element analysis [9]. Koh et al. conducted an experimental study on the effect of carbon/epoxy T-joints reinforced with z-pins on the structural properties and strengthening mechanisms. By increasing the volumes of z-pins, they determined the effects of T-connections on elastic stiffness, failure onset stress, ultimate strength, damage limit and absorbed energy capacity [10]. Heimbs et al. carried out a study on the mechanical behavior and damage status of T-joints under dynamic and static loads. They created a new reinforcement technique in the thickness direction using metallic arrow pins to increase the damage. They then performed T-bending tests on the composite connections to evaluate potential loading rate effects along with resistance and damage tolerance [11]. Yan et al. modeled T-joints from new generation 3D woven fabrics. Afterwards, they numerically investigated the mechanical behavior by performing tensile analysis. As reinforcement architecture, two new design models have been proposed that explain the weft yarn geometric properties based on the classification of production knitting patterns[12]. Barzegar et al. defined the adhesive region in the composite structure with a T-shaped profile and examined its behavior under bending load. They examined the changes in properties such as adhesive thickness, curve radius, etc. in the adhesive region they designed by using different adhesives [5]. Yang et al. investigated a new healing repair process for T joints by implanting a three-dimensional repairable polymer network using a fiber suture technique. For this, they sewed continuously repairable thermoplastic filaments into the T-junction to promote interlayer hardening as well as self-healing ability and examined its mechanical behavior under tensile load[13]. In this study, unlike the literature, T-shaped joints with different deltoid radius were designed from carbon-epoxy composite material. Then, by performing tensile test analysis on these structures, the effect of the deltoid radius on the maximum tensile load and the type of damage occurring in the T-shaped joints was determinate. As a result of the analyses, fiber tensile-compression damage images occurring in the structure for each deltoid radius were obtained and interpreted, along with the load-displacement graphs.

2. Material Method

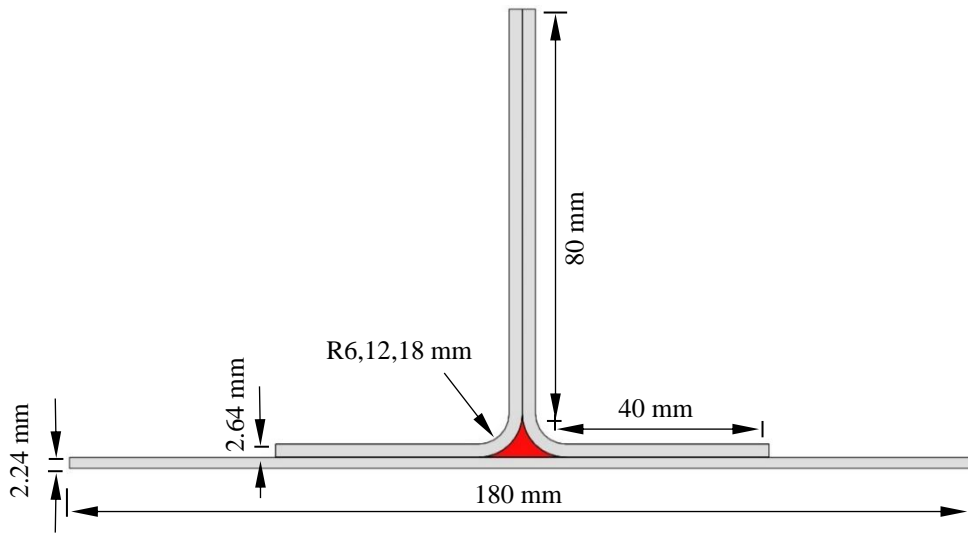


Figure 1. T-joint geometric dimensions.

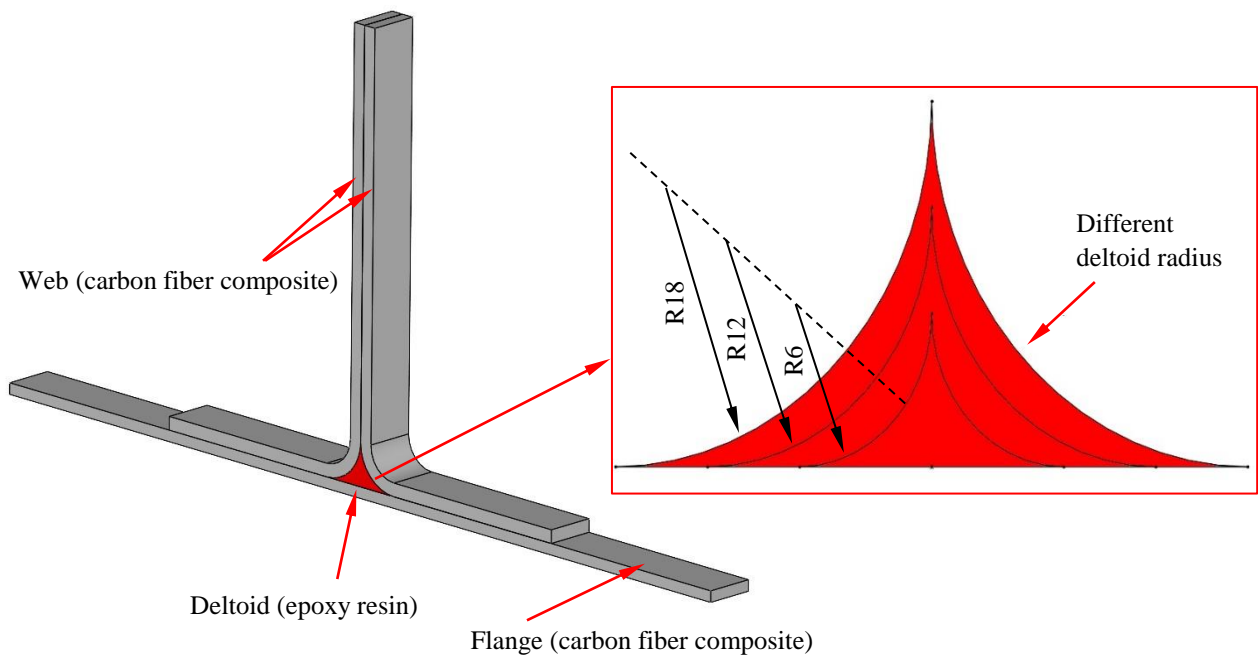


Figure 2. Design details for different deltoïd radiuses.

The model whose dimensions are given in Figure 1 was designed to perform tensile analyzes on the T-jointed carbon fiber composite structure. Modeling in the design was done in the Solidworks program. Here, the Flange and Web parts are modeled at 10 mm width. T-joint design details for different deltoïd radius are given in Figure 2. In this study, the effect of deltoïd radius was examined. For this purpose, deltoïd radius of 6mm, 12mm and 18mm were used, respectively.

2.1. Numerical analysis

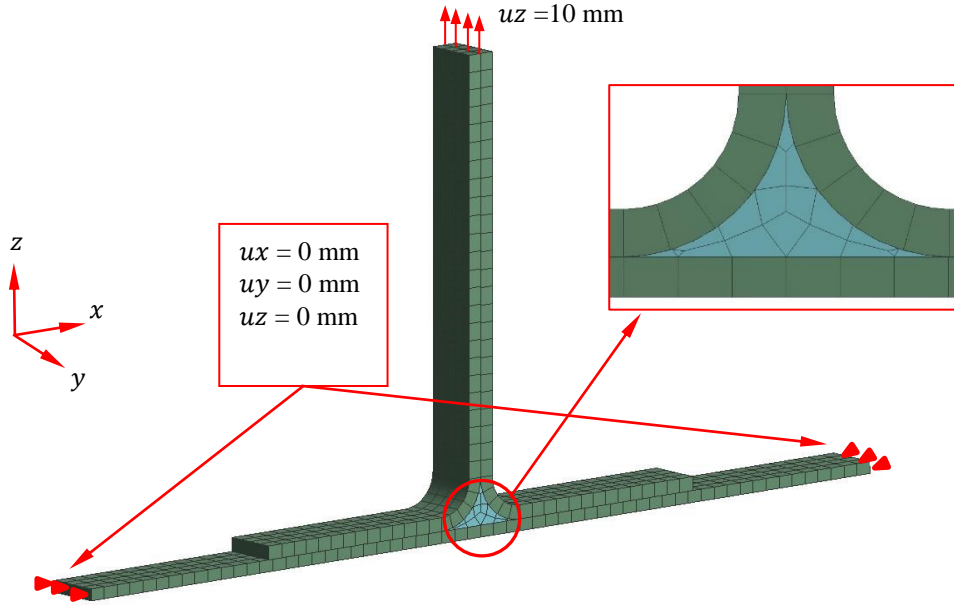


Figure 3. Finite element model of T-joint composite.

In the numerical part, the analyzes were carried out in the Ansys Workbench 2020R1 program. The Flange and Web parts that make up the T-joint were modeled as separate volumes and transferred to the Workbench program with the "Parasolid" extension. After the necessary material assignments were made, the solid models were divided into finite elements. Here, 8-node element type is preferred and Multizone mesh type is used. In the model divided into finite elements, the number of elements was determined as 5820 and the number of nodes was determined as 33175. The mesh structure of the finite element model are presented in Figure 3. The two side surfaces of the Flange model were selected as fixed supports and the web part was given a displacement in the z direction.

2.1.1. Damage model

Orthotropic properties of carbon fiber are presented in Table 1. In order to define the beginning of damage in progressive damage analysis, Hashin damage initiation criteria must be entered into the program. The hash initiation criteria include the following four damage initiation modes. Here the damage initiation indices are I_f^t ; I_f^c ; I_m^t and I_m^c represent fiber tensile, fiber compression, matrix tensile and matrix compression damage, respectively. When any of these indices exceeds 1, damage onset occurs. Four different damage cases belonging to the Hashin criteria are evaluated according to the following formulas in Equations (1)-(4)

Table 1. Mechanical properties of carbon fiber reinforced composite [14].

Symbol	Properties	Value	Unit
ρ	Density	1500	kg/m ³
E_x, E_y	Elasticity modulus x and y direction	43.7	GPa
E_z	Elasticity modulus z direction	14.57	GPa
ν	Poisson	0.21	-
G_{xy}	Modulus of rigidity in xy plane	14.18	GPa
G_{yz}	Modulus of rigidity in yz plane	14.65	GPa
G_{zx}	Modulus of rigidity in zx plane	14.65	GPa

Fiber failure for tension ($\sigma_{xx} \geq 0$):

$$I_f^t = \left(\frac{\sigma_{xx}}{F_{xt}} \right)^2 + \alpha \left(\frac{\sigma_{xy}}{F_6} \right)^2 \quad (1)$$

Fiber failure for compression ($\sigma_{xx} < 0$):

$$I_f^c = \left(\frac{\sigma_{xx}}{F_{xc}} \right)^2 \quad (2)$$

Matrix failure for tension ($\sigma_{yy} \geq 0$):

$$I_m^t = \left(\frac{\sigma_{yy}}{F_{yt}} \right)^2 + \left(\frac{\sigma_{xy}}{F_6} \right)^2 \quad (3)$$

Matrix failure for compression ($\sigma_{yy} < 0$):

$$I_m^c = \left(\frac{\sigma_{yy}}{2F_4} \right)^2 + \left[\left(\frac{F_{yc}}{2F_4} \right)^2 - 1 \right] \frac{\sigma_{yy}}{F_{yc}} + \left(\frac{\sigma_{xy}}{F_6} \right)^2 \quad (4)$$

Table 2. Orthotropic stress limit values of carbon fiber composite [14].

Symbol	Properties	Value (MPa)
X_T	Tensile strength in X direction	859
Y_T	Tensile strength in Y direction	859
Z_T	Tensile strength in Z direction	859
X_C	Compression strength in X direction	109.6
Y_C	Compression strength in Y direction	109.6
Z_C	Compression strength in Z direction	373.5
S_{XY}	Shear strength in plane $X - Y$	108.2
S_{YZ}	Shear strength in plane $Y - Z$	105.5
S_{XZ}	Shear strength in plane $X - Z$	105.5

Here σ_{ij} are the components of the stress tensor; F_{xt} and F_{xc} are the tensile and compressive strengths of a sheet in the longitudinal (fiber) direction; F_{yt} and F_{yc} are the tensile and compressive strengths in the transverse direction; F_6 and F_4 are in-plane and inter-layer shear strengths. α is the contribution of the in-plane shear stress according to this criterion and is taken as 0 in this study. In order to evaluate the damage initiation criteria in the composite structure, it is necessary to define the maximum stresses or strains that the material can tolerate before damage occurs. Stress limit values are presented in Table 2.

2.1.2. Damage evolution

MPDG was used for damage progression. Stiffness reductions used for the four damage cases in the study are given in Table 3.

Table 3. Stiffness reduction coefficients for the MPDG method.

Properties	Value
Reducing fiber tensile stiffness	0.46
Reducing fiber compressive stiffness	0.46
Reducing matrix tensile stiffness	0.4
Reducing matrix compressive stiffness	0.4

3. Results and Discussion

Tensile analyzes were performed on T-joined specimens made of carbon fiber reinforced composites. The problem was solved and evaluated according to the Material Property Degradation method for different deltoid radius. The effect of deltoid radius changes on the maximum load and damage type that the composite structure can carry was evaluated. Figure 4 shows the reaction load-displacement curve of the sample. Considering the graph, it was determined that the structure exhibited linear material behavior for all deltoid radiuses. However, it has been observed that as the deltoid radius increases, the T-joined composite structure exhibits more rigid material behavior. Maximum contact loads for different deltoid radius are compared in Figure 5. When the graph is examined, the maximum contact load for R6 is determined as 121.86 N. For radius R12 and R18, these values are 133.15N and 146.36N, respectively. It was calculated that by increasing the deltoid radius from 6mm to 12mm, the maximum contact load increased by approximately 10%, and by increasing it to 18mm, it increased by approximately 20.11%. In their study, Trask et al obtained similar results by determining that the maximum contact load increased parallel to the deltoid radius. When the study is examined, Trask et al. performed tension pull-off test on the T-joined structure they produced from carbon epoxy unidirectional pre-preg and according to the results they obtained: They determined that a 50% decrease in the deltoid area caused a 33% loss of strength in the structure. Fiber tensile and compression damage images occurring in the specimens for different deltoid radius are presented in Figures 6-8. A color scale appears next to the numerical damage images. Here, the red area indicates that the sample is damaged, and the blue areas indicate the undamaged parts of the sample. Fiber reinforced materials exhibit linear elastic behavior and their damage behavior is more complex than isotropic materials. Especially due to the brittle structure of damaged composites, fiber tensile damages can be observed in the damage area of the fibers carrying the main load under tensile load. When the fiber tensile damage images of all specimens were examined (Figure 6a-8a), fiber tensile damage was observed at each edge ends of the flange, which were kept fixed. However, fiber compression damages spread over a wide area were detected on the lower surface of the flange, where it did not come into contact with the web (Figure 6b). However, as the deltoid radius increased, fiber compression damage in this region was gradually reduced and even completely prevented (Figures 7b and 8b). This is related to ensuring continuity between web and flange a more linear geometry by increasing the radius value. In this way, the peak stress occurring in the web-to-flange transition connections are reduced [15].

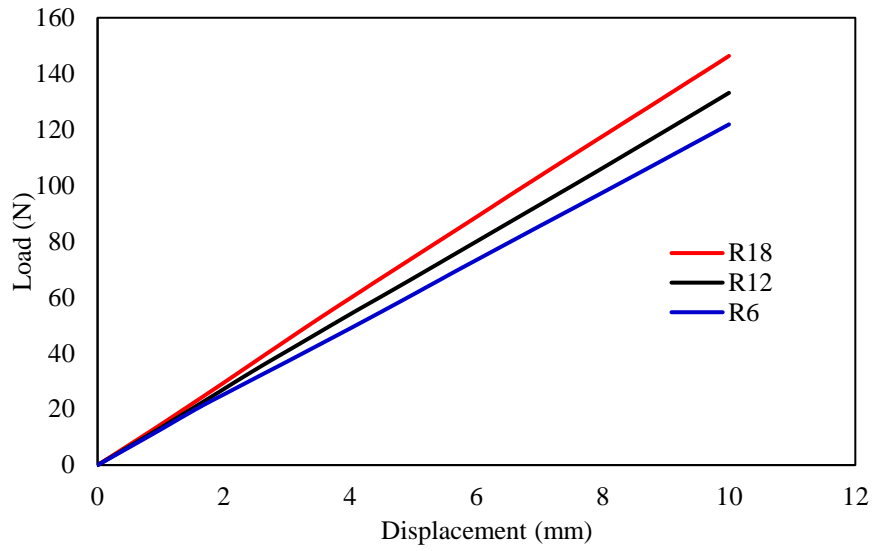


Figure 4. Comparison of load-displacement graphs for different deltoid radius.

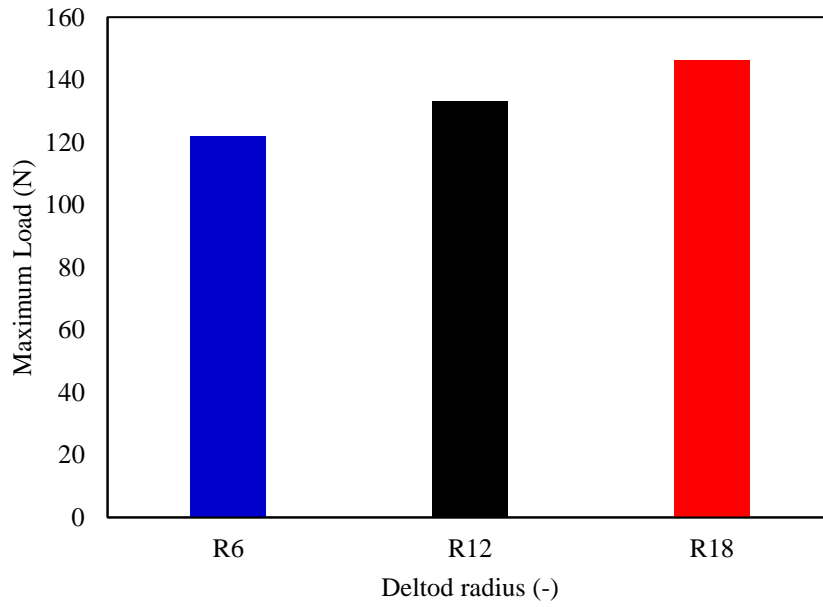


Figure 5. Numerical comparison of maximum load values.

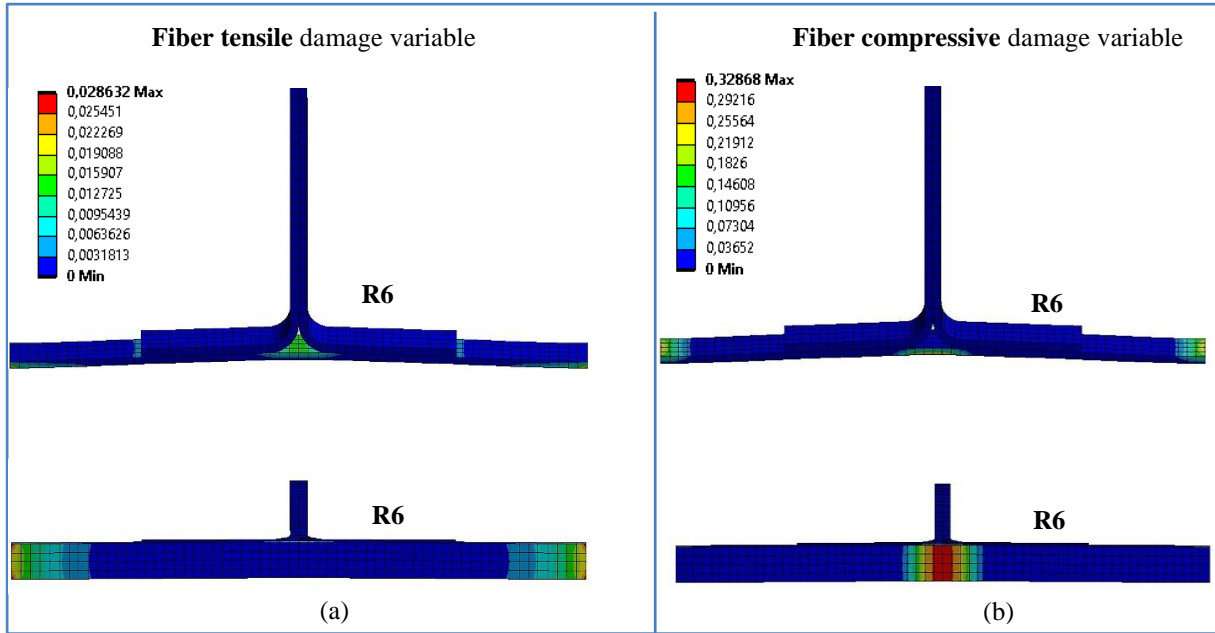


Figure 6. Comparison of (a) fiber tensile damage and (b) fiber compression damage images in the T-joint composite for specimen R6.

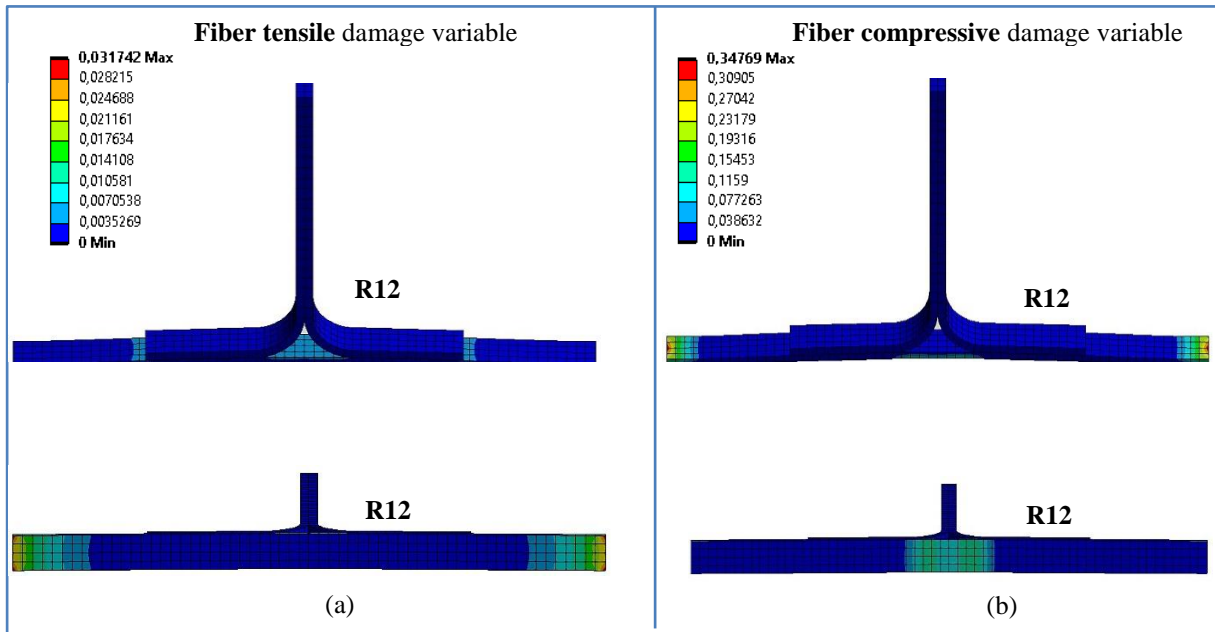


Figure 7. Comparison of (a) fiber tensile damage and (b) fiber compression damage images in the T-joint composite for specimen R12.

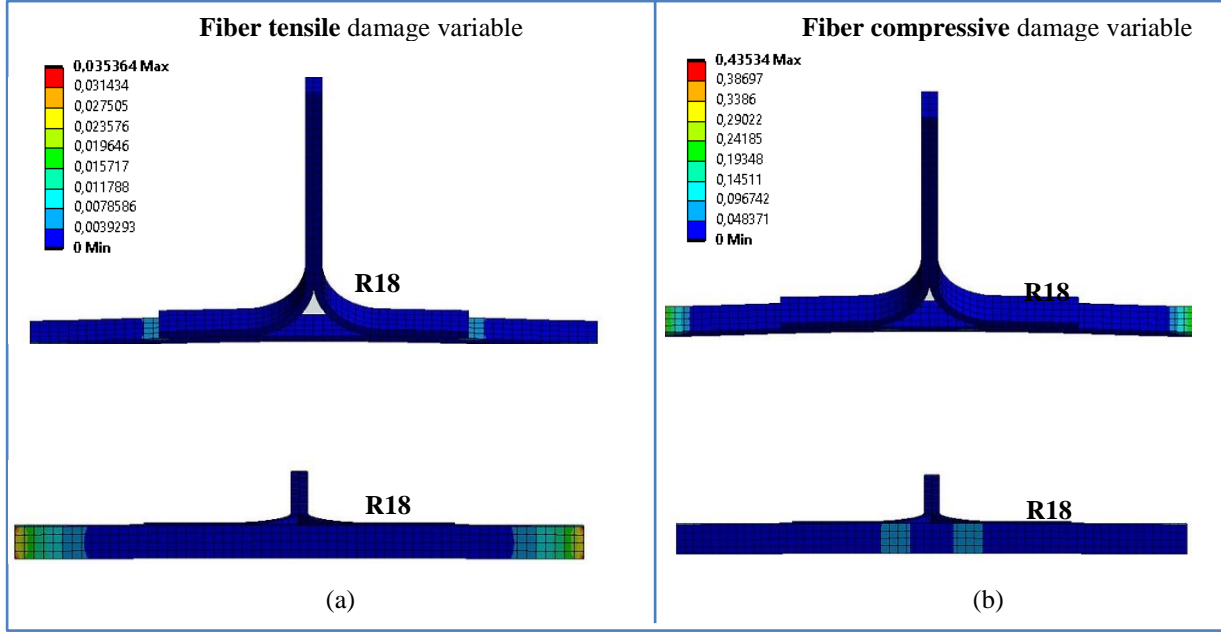


Figure 8. Comparison of (a) fiber tensile damage and (b) fiber compression damage images in the T-joint composite for specimen R18.

4. Conclusion

Tensile test analysis was carried out on T joints with different deltoid radius made of carbon-epoxy composite material, and the effect of deltoid radius on the maximum tensile load and damage behavior of the composite structure was examined. The results were compared and summarized as follows.

- By increasing the deltoid radius from 6 mm to 12 mm, the maximum contact load increased by approximately 10%, and by increasing it to 18 mm, the maximum contact load increased by approximately 20.11%.
- it was observed that as the deltoid radius increases, the T-jointed composite structure exhibits more rigid material behavior.
- With the increase in the deltoid radius, both higher contact loads were obtained in the structure and the peak stresses occurring in the web-flange transition connections were reduced as the continuity between the web and the flange provided a more linear geometry.
- It is recommended to increase the deltoid radius in the design of T joints, which is one of the most important connection types for structural applications. In this way, connections that are resistant to tensile load and less damaged are obtained.

5. Author Contribution Declaration

In the study carried out, Author 1 contributed to the formation of the idea, design and literature review, evaluation of the results, procurement of the materials used and examination of the results, and checking the article in terms of spelling and content.

6. Ethics Committee Approval and Conflict of Interest Declaration

There is no need to obtain ethics committee permission for the article prepared. There is no conflict of interest with any person/institution in the prepared article.

7. References

- [1] H. J. Phillips and R. A. Shenoı, “Damage tolerance of laminated tee joints in FRP structures” *Compos. Part A Appl. Sci. Manuf.*, vol. 29, no. 4, pp. 465–478, 1998.
- [2] Y. Wang, C. Soutis, A. Hajdaei, and P. J. Hogg, “Finite element analysis of composite T-joints used in wind turbine blades” *Plast. Rubber Compos.*, vol. 44, no. 3, pp. 87–97, 2015.
- [3] P. Stickler and M. Ramulu, “Entwicklung von textilen halbzeugen für faserverbunde unter verwendung von stickautomaten” *Compos. Struct.*, vol. 52, no. 3–4, pp. 307–314, 2001.
- [4] R. Akrami, S. Fotouhi, M. Fotouhi, M. Bodaghi, J. Clamp, and A. Bolouri, “High-performance bio-inspired composite T-joints” *Compos. Sci. Technol.*, vol. 184, p. 107840, 2019.
- [5] M. Barzegar, M. D. Moallem, and M. Mokhtari, “Progressive damage analysis of an adhesively bonded composite T-joint under bending, considering micro-scale effects of fiber volume fraction of adherends” *Compos. Struct.*, vol. 258, no. October 2020, p. 113374, 2021.
- [6] R. S. Trask, S. R. Hallett, F. M. M. Helenon, and M. R. Wisnom, “Influence of process induced defects on the failure of composite T-joint specimens” *Compos. Part A Appl. Sci. Manuf.*, vol. 43, no. 4, pp. 748–757, 2012.
- [7] W. Khor et al., “Improving the damage tolerance of composite T-joints using shape memory alloy tufts” *Compos. Part A Appl. Sci. Manuf.*, vol. 168, p. 107474, 2023.
- [8] P. B. Stickler and M. Ramulu, “Damage progression analyses of transverse stitched T-joints under flexure and tensile loading” *Adv. Compos. Mater. Off. J. Japan Soc. Compos. Mater.*, vol. 15, no. 2, pp. 243–261, 2006.
- [9] F. Dharmawan, R. S. Thomson, H. Li, I. Herszberg, and E. Gellert, “Geometry and damage effects in a composite marine T-joint” *Compos. Struct.*, vol. 66, no. 1–4, pp. 181–187, 2004.
- [10] T. M. Koh, S. Feih, and A. P. Mouritz, “Experimental determination of the structural properties and strengthening mechanisms of z-pinned composite T-joints” *Compos. Struct.*, vol. 93, no. 9, pp. 2222–2230, 2011.
- [11] S. Heimbs, A. C. Nogueira, E. Hombergsmeier, M. May, and J. Wolfrum, “Failure behaviour of composite T-joints with novel metallic arrow-pin reinforcement” *Compos. Struct.*, vol. 110, no. 1, pp. 16–28, 2014.
- [12] S. Yan, X. Zeng, and A. Long, “Effect of fibre architecture on tensile pull-off behaviour of 3D woven composite T-joints” *Compos. Struct.*, vol. 242, no. January, p. 112194, 2020.
- [13] T. Yang, J. Zhang, A. P. Mouritz, and C. H. Wang, “Healing of carbon fibre-epoxy composite T-joints using mendable polymer fibre stitching” *Compos. Part B Eng.*, vol. 45, no. 1, pp. 1499–1507, 2013.
- [14] I. Bozkurt, M. O. Kaman, and M. Albayrak, “Low-velocity impact behaviours of sandwiches manufactured from fully carbon fiber composite for different cell types and compression behaviours for different core types” *Mater. Test.*, vol. 65, no. 9, pp. 1349–1372, 2023.
- [15] A. Mishra and R. Ray, “Alternative formats If you require this document in an alternative format , please contact ” *Festivals 2.0 Consum. Prod. Particip. Ext. Festiv. Exp.*, vol. 13/10, no. 1, pp. 97–114, 2010.